2016

Internal Cooling Using Novel Swirl Enhancement Strategies in A Slot Shaped Single Pass Channel

Del Alan Segura
Louisiana State University and Agricultural and Mechanical College

INTERNAL COOLING USING NOVEL SWIRL ENHANCEMENT STRATEGIES IN A SLOT SHAPED SINGLE PASS CHANNEL

A Dissertation

Submitted to the Graduate Faculty of the
Louisiana State University and
Agricultural and Mechanical College
in partial fulfillment of the
requirements for the degree of
Doctor of Philosophy

in

The Department of Engineering Science

by
Del Segura
M.S., Tulane University, 2004
B.S., University of Southwestern Louisiana, 1992
May 2016

Acknowledgements

I would like to thank my wife and daughter for being so patient with me, for allowing me time away from them, and their encouragement while I pursued my personal goal of earning a PhD. Additionally, there are many graduate and undergraduate students that have assisted me and encouraged me to continue during the hard times. In particular, I would like to thank Greg Kramer, Louis Moreaux, J. W. Post, Baine Breaux, and Brunet Breaux. I have made life-long friends with these upstanding gentlemen.

Several other friends and colleagues have assisted me along the way with writing Matlab code and fabrication of components used in my research. Dr. Liang Yi and Mr. Norbert Sigue were of invaluable assistance and well deserving of my utmost gratitude.

Of course, I could not have completed my PhD endeavor without the kind assistance of my faculty advisor, Dr. Shengmin Guo in the Mechanical Engineering department. He unselfishly agreed to take a leadership role in helping me through the final semesters of my time here at LSU. Others that deserve thanks include the department chair of Mechanical Engineering, Dr. Dimitris Nikitopoulos, who spent time with me and helped guide me as I neared the end of my studies. I also wish to thank my two other committee members, Dr. Mayank Tyagi in Petroleum Engineering and Dr. Murad Abu-Farsakh in Civil Engineering. These gentlemen have taken time from their busy schedules to lend assistance and guidance.

Table of Contents

List of Tables

List of Figures

Nomenclature

a	Width of slot channel, *mm*
b	Height of slot channel, *mm*
AR	Aspect Ratio, a/b
A/F	Air/Fuel Ratio
BR	Blowing Ratio (ratio of jet velocity to main channel velocity)
d	Jet hole diameter, *mm*
d_h	Channel Hydraulic Diameter, *m*
DR	Ratio of flow director diameter to inner pipe diameter
e	Trip strip height, *mm*
f	Friction coefficient
f_o	Normalized Friction coefficient
FDD	Flow director diameter
h	Convection Heat Transfer Coefficient, $W/m^2 K$
k	Coefficient of thermal conductivity, $W/m K$
L	Channel Length, *mm*
Nu	Nusselt number (ratio of convective to conductive heat transfer)
Nu_o	Nusselt number in a smooth channel with no heat transfer enhancements
Nu_{smooth}	Nusselt number in a smooth slot shaped channel
Nu_{90}	Nusselt number in a smooth slot shaped channel with a 90 degree entry
p	Pitch, *mm*
Pr	Prandtl Number
P	Pressure, *Pa*

P_m Pressure, Main Channel, *Pa*

P_o Pressure, Outer Jet Supply Channel, *Pa*

Re Reynolds Number

r_p Pressure Ratio

t time, *s*

T_f Firing Temperature, K

T_i Initial temperature, *K*

T_w Wall temperature, *K*

$\Delta T_{m,I}$ Temperature difference between each time step, *s*

U_m Mean Velocity, *m/s*

T_m Fluid temperature, *K*

Greek

α Coefficient of thermal diffusivity, m/s^2

ρ Density, kg/m^3

τ Time step for each temperature step, *s*

η Thermal Enhancement Factor $(Nu/Nu_o / f/f_o)^{1/3}$

η_c Compressor Efficiency

Acronyms

BFM Back Flow Margin

SOA State of the art

TLC Thermochromic Liquid Crystal

Abstract

A series of heat transfer tests using a single pass slot shaped channel utilizing varying configurations of trapezoid shaped turbulence enhancement strip or varying configurations of high velocity jets issuing from side channels are studied. Thermochromatic Liquid Crystal techniques are used to determine local heat transfer coefficients, which are converted to normalized Nusselt values. The results show a marked improvement over traditional heat transfer enhancements used in the mid-span region of first stage turbine blades.

Chapter 1 – Introduction and Background

From supplying 400 MW of electricity to power homes or propelling an advanced fighter jet to speeds in excess of 2100 miles per hour, the modern gas turbine engine plays a vital role in society. These prime movers are valued for their high power to weight ratio, but could not have realized such an important role in our daily lives without significant technological advancements. Operating at efficiencies greater than 58%, unheard of just a few short years ago, combustion temperatures of 1600^{o} C exceed the limits of current metal airfoil material. Various strategies have been developed to cool turbine blades since the inception of the first "jet" engine by Hero, an Egyptian scientist from Alexandria, around 100 BC. The birth of the modern gas turbine engine began in the late 1930's. The thrust output of gas turbines has increased from 7 kN for Whittle's W2 in 1939 to greater than 440 kN for modern engines. The evolution in performance is closely related to increases in turbine rotor inlet temperature as the performance of modern gas turbine engines improves with increased turbine inlet temperature.

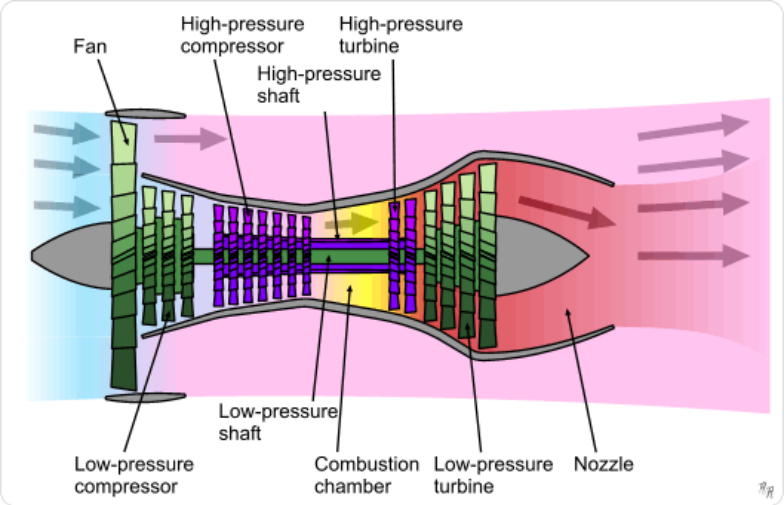

Figure 1-1 : Basic internal components of a gas turbine engine (courtesy of Rolls Royce).

Advancements in materials and various techniques to aid in cooling the turbine blades have resulted in an increase in turbine inlet temperatures of roughly 900^{o} C in 70 years.

In a typical modern turbine engine, a small percentage of air is extracted from the compressor portion of the engine (Figure 1-1) and directed into complex passages in the turbine blade (Figure 1-3).

A more detailed cross section view of a turbine engine can be seen in Figure 1-2. This GE turbojet engine is typical of gas turbine engines built in the 1970s. In this photo the flow enters the engine on the left and progresses through the multistage compressor. Combustion takes place in the center and the work is performed on the turbine blades on the right. The basic concept remains the same in modern gas turbine engines.

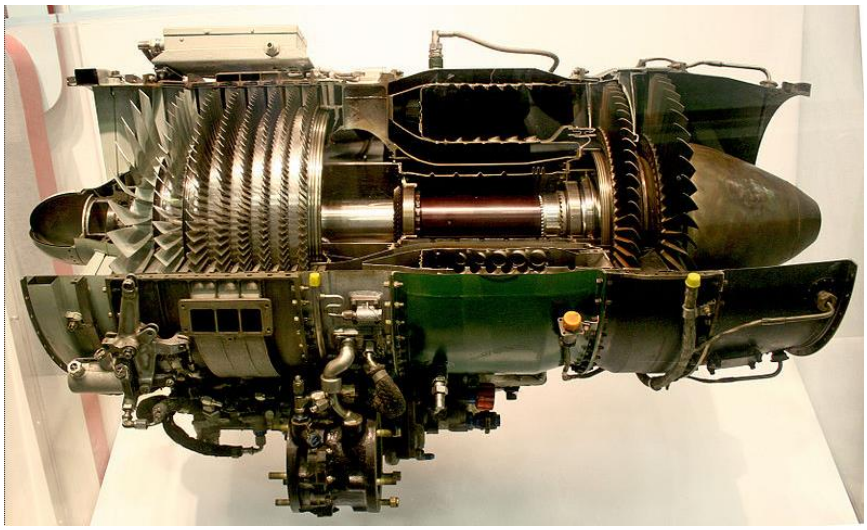

Figure 1-2 : A General Electric J85-GE-17A turbojet engine. (courtesy Sanjay Acharya)

This bypass air typically enters the blade at ~650^{o} C and cools the blade uniformly to a permissible temperature of ~1000^{o} C or less. The increases in turbine inlet temperature produce increased thrust

and increased specific impulse. If the designer is off by 30° C, the life of the blade can be reduced by 50%.

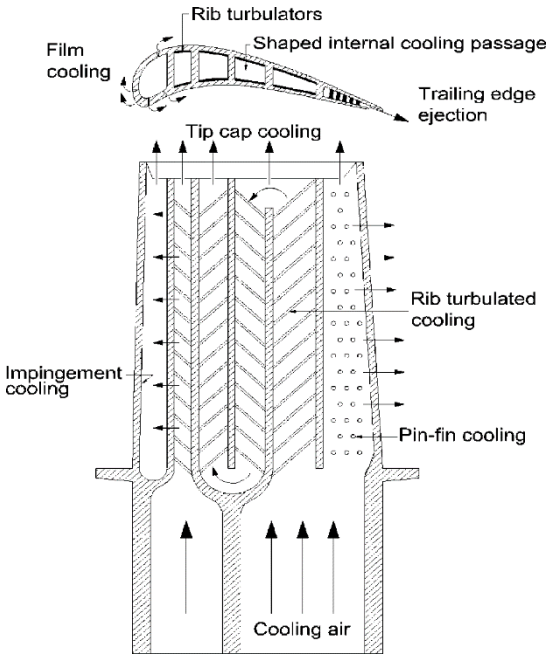

Figure 1-3 : Cross section of a typical modern turbine blade [1].

As shown in figure 1-3, the common configurations for airfoil cooling include ribs, pin-fins, impingement jets, and film cooling holes. These cooling strategies have fared well over the last few decades, but at a cost to the overall operating efficiency due to the amount of compressor bypass air needed. Recent studies have indicated that marked improvements to effective heat transfer can be gained by utilizing swirl/cyclone motion in the internal passages. Normalized heat transfer enhancement factors of four are not untypical. These values may yield as much as a 25% improvement over a similarly designed passage with ribbed turbulators. This study hopes to advance turbine blade mid-span internal cooling performance, utilizing new and innovative

methods to enhance gas turbine internal heat transfer by incorporating swirl and tumble cooling strategies.

Chapter 2 – Scope and Motivation

Since their inception in the late 1930's, the thrust output of gas turbines has increased from 7kN for Whittle's W2 to greater than 440kN for modern engines. This evolution in performance is closely related to increases in turbine rotor inlet temperature as the performance of modern gas turbine engines improves with increased turbine inlet temperature. For an ideal turbofan, for example, increases in turbine inlet temperature produce increased thrust and increased specific impulse [2]. Figure 2-3 shows that turbine inlet temperature has increased 700 K in 60 years. However, much of that improvement occurred during the middle of the twentieth century.

Table 2-1; Performance comparison of early and modern aircraft turbine engines. (Courtesy of Rolls Royce)

	Whittle W2 (turbojet engine)	**Rolls-Royce Trent 892 (turbofan engine)**
maximum thrust	7.1 kN (1600 lb)	407 kN (91,500 lb)
engine weight	3.8 kN (850 lb)	c. 72 kN (c.16,000 lb)
specific fuel consumption	0.115 kg/h/N (1.13 lb/h/lb)	0.0765 kg/h/N (0.575 lb/h/lb)
air mass flow rate	12 kg/s (26 lb/s)	1200 kg/s (2650 lb/s)
turbine entry temperature	1050 K	1750 K
overall pressure ratio	4.4	40.8
thrust-to-weight ratio	1.9	5.7

Figure 2-1 shows that the state-of-the-art in turbine rotor inlet temperature increased 1100° F between 1960 and 1980 (about 55° F/year), compared to only 100° F between 1980 and 1997 (about 6° F/year).

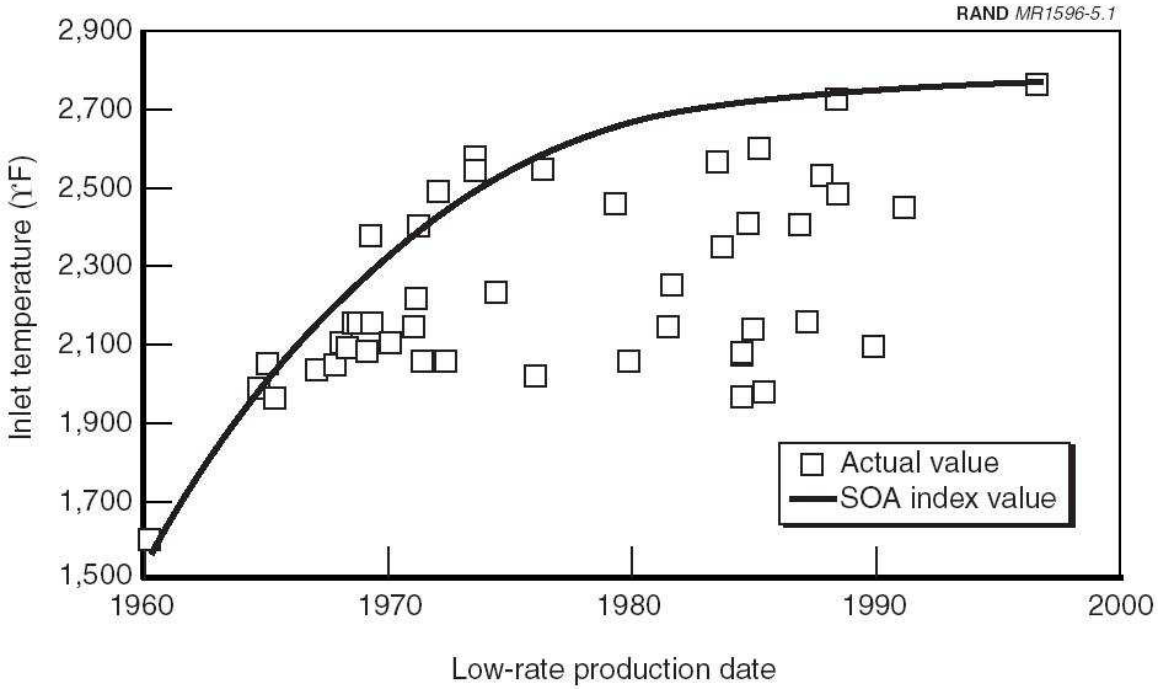

Figure 2-1 : Graph of actual and "state of the art" turbine rotor inlet temperature versus year of entry into service for military engines (courtesy of the RAND Corporation).[2]

The desire for better performance and improved efficiency will continue the trend toward higher turbine inlet temperatures, as current engine technology limits turbine temperatures to those well below stoichiometric combustion limits [2]. It has been stated that if you increased the turbine temperature by 200° C, a high performance turbofan engine would produce almost 20% more thrust [3]. The equation below shows that the cycle efficiency of a simple cycle turbine engine is determined by several factors, including the firing temperature (T_f) and the pressure ratio (r_p).

$$\eta_{\text{cycle}} = \left(\frac{\eta_t T_f - \dfrac{T_{\text{amb}} r_p^{\left(\frac{\gamma-1}{\gamma}\right)}}{\eta_c}}{T_f - T_{\text{amb}} - T_{\text{amb}} \left(\dfrac{r_p^{\left(\frac{\gamma-1}{\gamma}\right)} - 1}{\eta_c} \right)} \right) \left(1 - \frac{1}{r_p^{\left(\frac{\gamma-1}{\gamma}\right)}} \right)$$

The firing temperature is a function of the air/fuel ratio (A/F). Most turbine engines cannot operate at the stoichiometric ratio because the combustion temperatures would exceed the limits of the blade material. The pressure ratio is somewhat determined by the compressor efficiency (η_c), which are typically in the 87% range, but more so determined by the amount of bypass air that is needed to cool the blades and other associated components in the high temperature area of the engine. Figure 2-2 plots a few examples of cycle efficiency vs. pressure ratio for several firing temperatures. It becomes easy to see that the higher firing temperatures and higher pressure ratios are the key to improved cycle efficiencies.

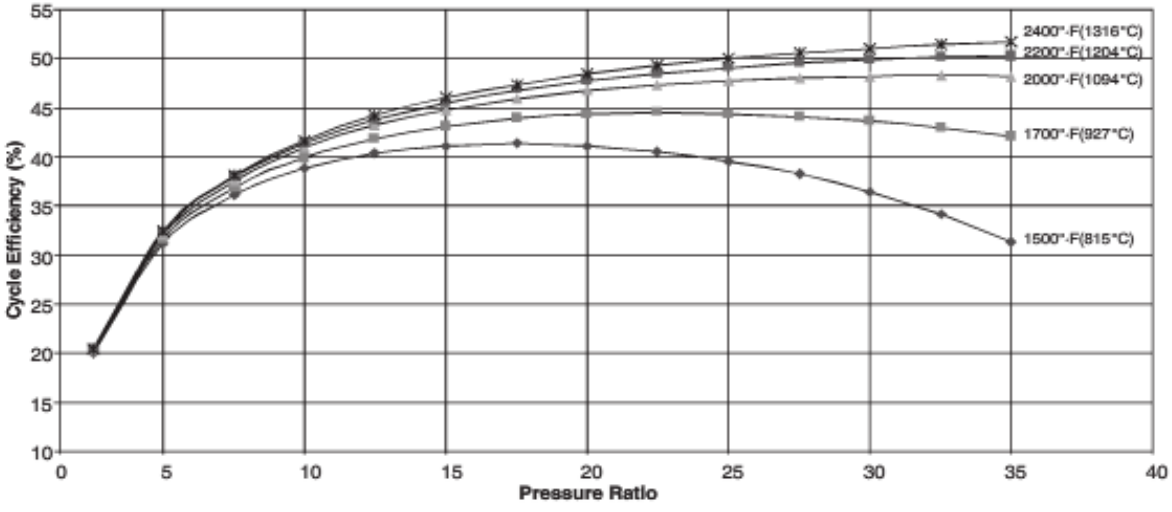

Figure 2-2 : Overall cycle efficiency as a function of firing temperature and pressure ratio. Plot based on a compressor efficiency of 87% and a turbine efficiency of 92%. [3]

High turbine inlet temperatures provide a challenging environment for turbine blades which are subjected to a variety of damage mechanisms, including high-temperature oxidation, creep, corrosion, and thermo-mechanical fatigue. Thus, engine designs must strike a balance between thermodynamic performance and component life. In response, turbine airfoil temperature capability has evolved on two fronts: materials and airfoil cooling. The metal temperature capability of turbine airfoil materials has improved more than 250^{o} C in the last 50 years [2]. Advancements in turbine blade cooling have allowed an even larger increase. Newer-generation turbine airfoils operate at turbine-rotor inlet temperatures that are 700^{o} C above those of comparable uncooled blades and 400^{o} C above the melting temperature of the alloys [2].

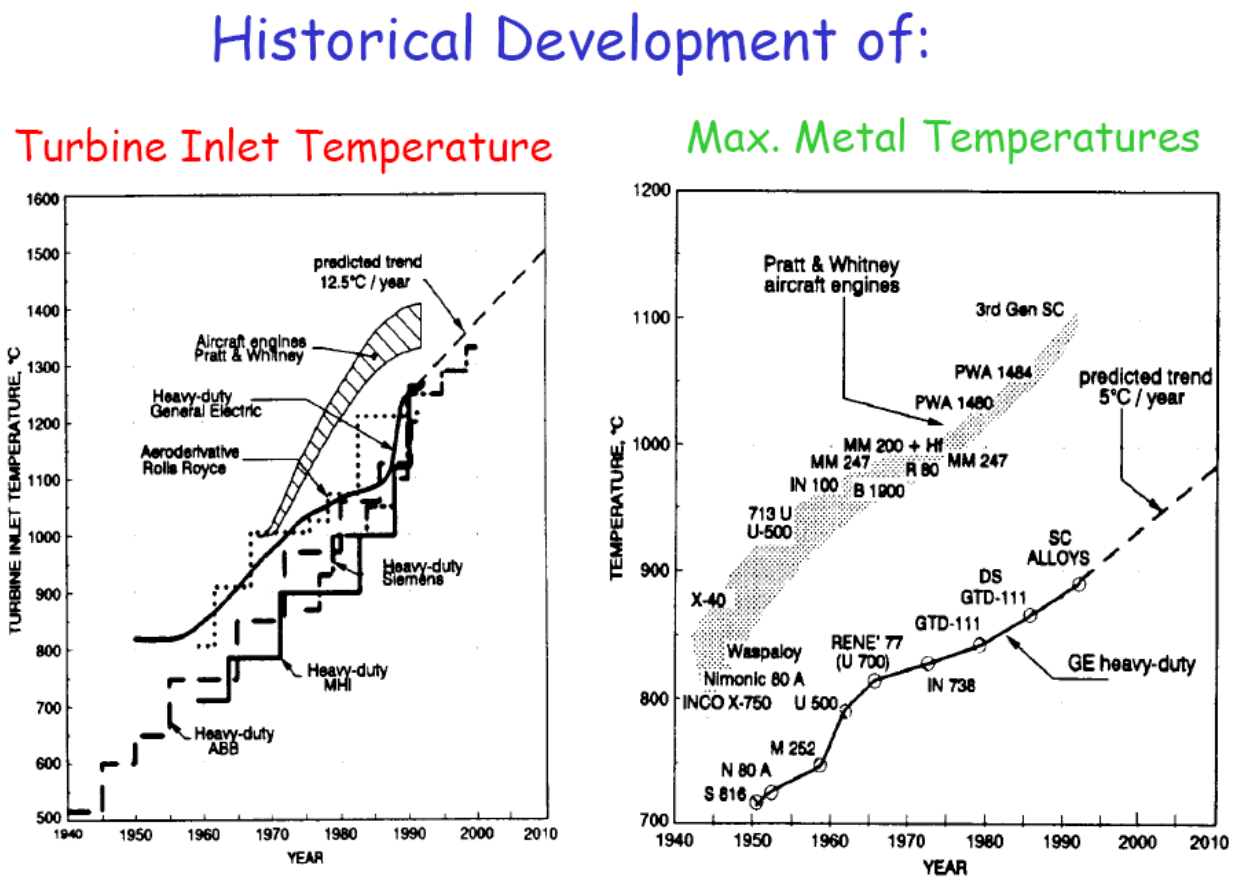

Figure 2-3 : Historical development of turbine inlet temperature and maximum metal temperature. [4]

Over the last decade the temperature has risen from 1500 K to 1750 K in some high-performance units. With this increase of the temperature only about 25% can be attributed to improved alloys. New materials, such as ceramics, could help increase this maximum temperature even more in the future.

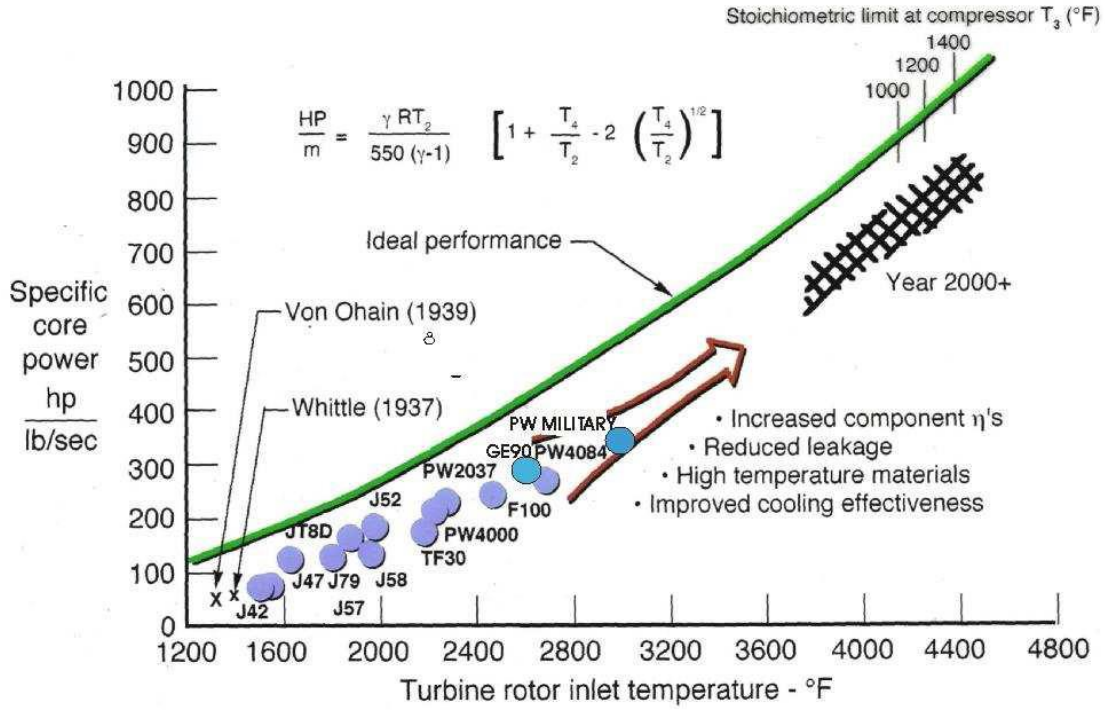

Figure 2-4 : Historical trend in specific core power and turbine rotor inlet temperature for a variety of military and commercial gas turbine engines [4].

However, most of the recent improvements in inlet temperature come from better cooling of the blades and a greater understanding of the heat transfer and the three dimensional temperature distribution in the turbine passage. Higher gas temperature generally causes increased blade temperature and greater temperature gradients, both of which can have a detrimental effect on service life.

The progression of pressure and temperature inside a typical gas turbine engine is shown in figure 2-4. It is not untypical for the various compressor stages to be able to compress the incoming air up to 40 times that of the inlet air in a high performance engine. That air leaves the compressor section at temperatures in the 200 to 550 C range, due to work done on the air by the compressor. However, all of the air that is compressed does not go into the combustion chamber. Some of the air is routed through the turbine blades and other components in the combustion area in order to prevent overheating.

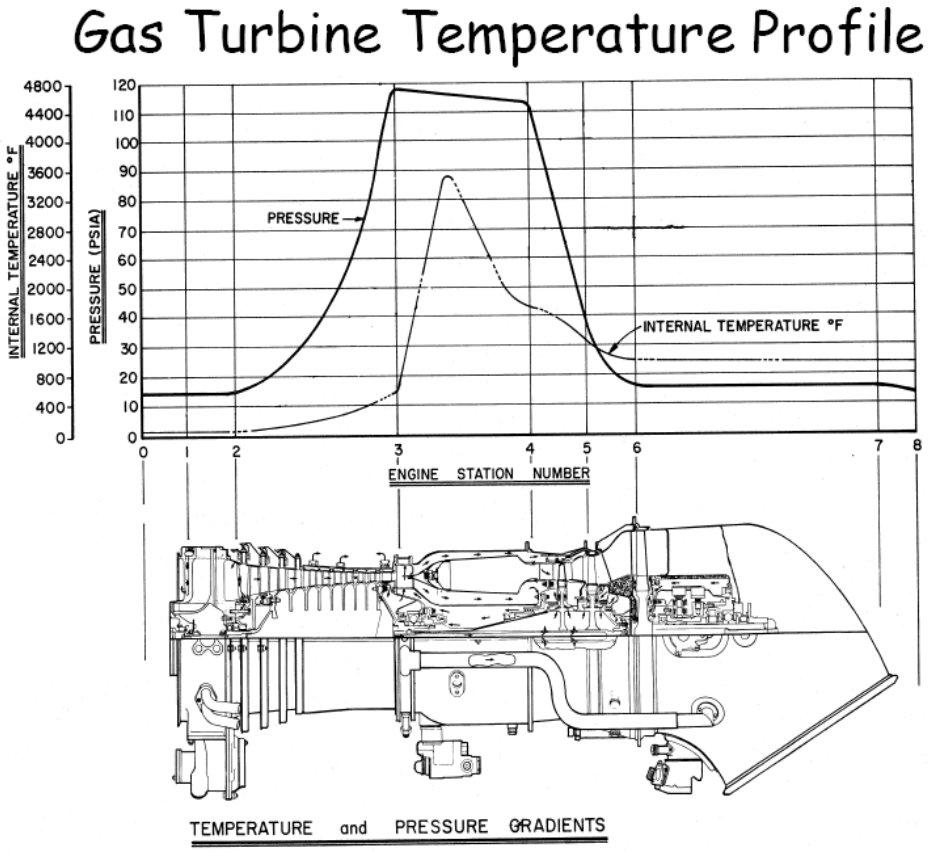

Figure 2-5 : Progression of internal temperature and pressure from inlet to exit of a typical gas turbine engine (courtesy of General Electric).

A summary of a host of recently published literature on gas turbine blade internal cooling performance verses friction loss is shown in figure 2-6. The value Nu/Nu_o indicates the Nusselt

number determined from a particular test, to the Nusselt number for the equivalent tests in a smooth channel (Nu_o) with no heat transfer enhancements added. The results of the normalized friction factor (f/f_o) use the same criteria. Although details of the specific tests are not known, tendencies can trends can be deduced from this graph. The majority of testing seems to be with ribbed turbulators.

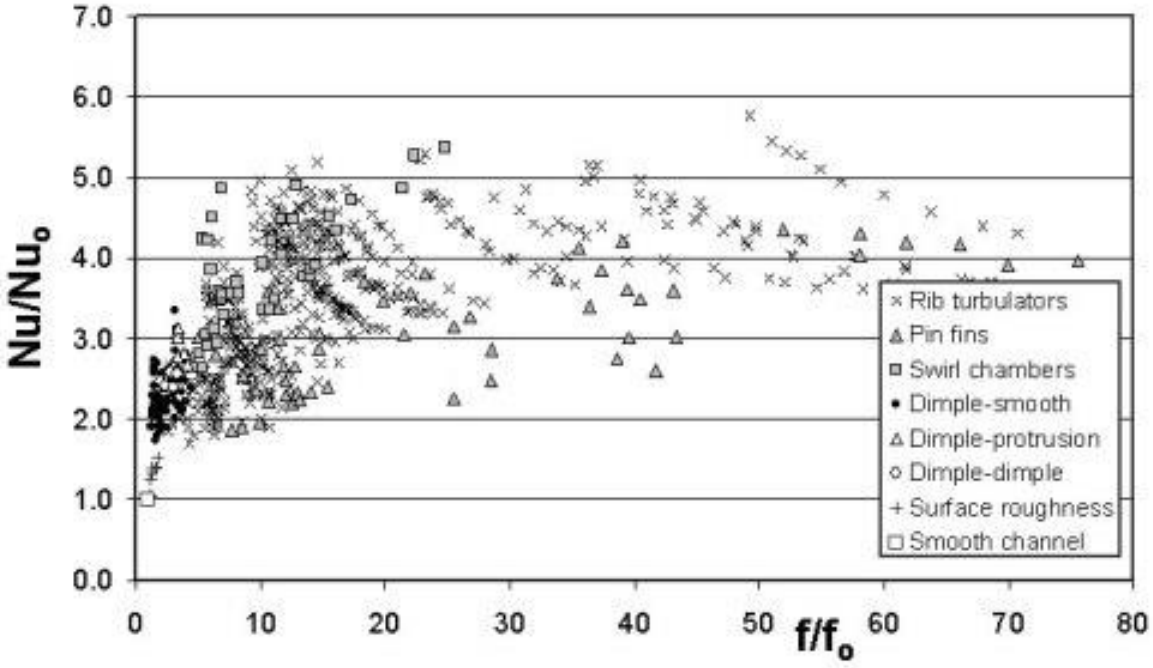

Figure 2-6 : Comparison of relative performance of rib turbulators, pin fins, swirl chambers, dimple-smooth arrangements, dimple-protrusion arrangements, dimple-dimple arrangements, surface roughness, and smooth-walled channels. Globally-averaged Nusselt number ratios are presented as dependent upon channel friction factor ratios.[5]

The values for ribbed turbulators span the entire graph with the vast majority of data points in the Nu/Nu_o range of 2 to 5. Normalized friction factors encompass the entire range of the graph. Pin fins show a similar tendency, but the average of all tests shown indicates the average value of Nu/Nu_o is less than ribs. Dimpled surfaces exhibit extremely low friction characteristics and the Nu/Nu_o values hover around 1.8 to 2.8 in most cases. A close examination of swirl chambers show that the normalized friction factor values congregate in the lower 1/3 of the graph and the

heat transfer enhancement values tend to be in the 3.0 to 5.0 range of the graph. Based on this graph, it is surprising to find that very few published studies are done on swirl generated heat transfer enhancement in gas turbine blades.

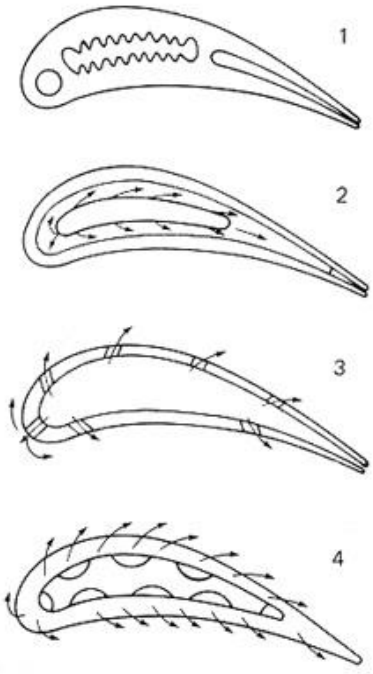

Figure 2-7 : Various methods used for internal airfoil cooling [6].

Figure 2-7 shows the various methods that are used to cool turbine blades. Sketch 1 shows convection cooling using turbulence enhancers in the mid-span section. Sketch 2 shows impingement jets directed at specific locations. The third sketch shows film cooling jets used to create a thin cool boundary layer on the outer surface of the blade. And in the fourth sketch, transpiration cooling is used. For obvious reasons this method cannot be used in aviation applications.

The complexity of the internal cooling passages of a typical first stage turbine blade is shown in Figure 2-8. Note the different aspect ratios of the channel on the two blades. The blade on the left is a two pass design in the mid-span portion and incorporates turning vanes at the end

of the first pass. Also note the pins located near the trailing edge. The complexity of this design can give some insight into the level of detail that is needed to provide adequate cooling.

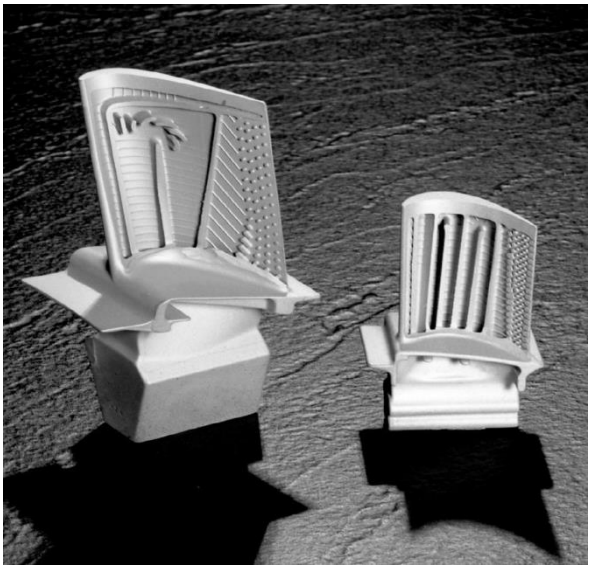

Figure 2-8 : A cut-away view of a typical first stage turbine blade (Courtesy of GE).

When adequate cooling is not achieved, the blade material overheats and begins to melt. Figure 2-9 shows two examples of blades that overheated and begin to melt.

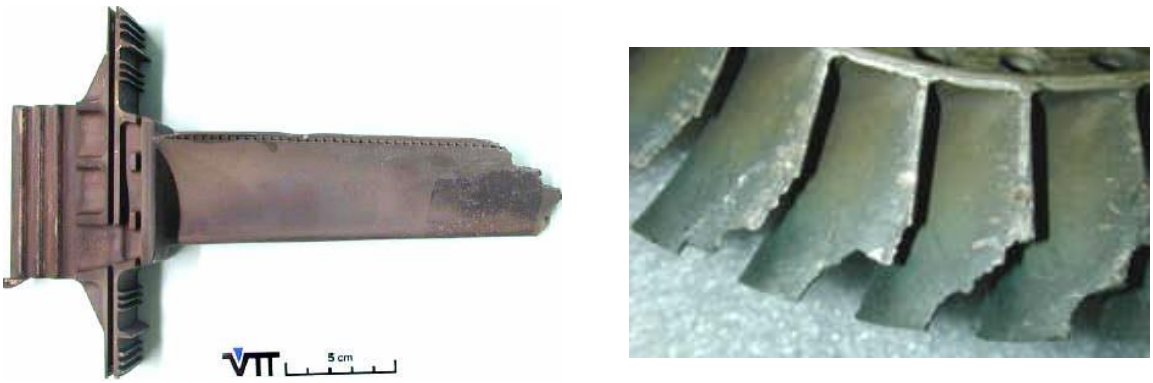

Figure 2-9 : Results of inadequate cooling [Courtesy of VTT Industrial Systems].

Internal cooling is studied under two basic scenarios, stationary testing and rotational testing. Each provides useful information to the designer.

Internal Cooling in Stationary Geometries

In a typical gas turbine internal cooling channel, ribs are cast on two opposite walls of the internal cooling channel to promote turbulence and enhance heat transfer. When air flows over a rib, it separates from the rib at the top and reattaches to the blade surface between the ribs. This separation and reattachment enhances turbulent mixing and as a result enhances heat transfer from the blade surface, as compared to a smooth surface. The schematic of a flow over a ribbed surface is shown in Figure 2-10. Extensive work has been done over the years studying different aspects of ribbed geometries under stationary and rotating conditions. Some key parameters studied include, a) rib angle of attack, b) rib pitch, c) rib height, d) channel AR effect on ribs, e) rib orientation and other innovative rib designs. The literature review portion of this paper will discuss the particulars of each of these parameters.

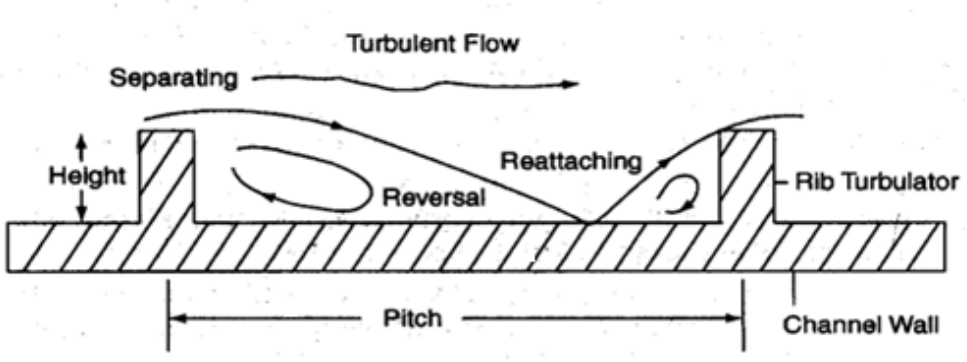

Figure 2-10 : Concept of flow over a ribbed surface [7]

Chapter 3 – Literature Review

A thorough literature review must include various peer reviewed journal and conference papers as well as patents issued. Many published papers were reviewed and the following were selected as being either representative of current state of the art technology or for being somewhat novel as compared to mainstream literature dealing with gas turbine blade cooling. Since limited information can be gleaned from patents, patent sketches will be reviewed to give insight into new concepts being explored in industry.

Published Literature

The following information was obtained from some of the most recent published papers regarding heat transfer in turbine blades and other types of heat exchangers commonly used in industry. An effort has been made to try and distinguish testing performed in a stationary environment and testing performed in a rotating environment. However, since some important papers have the results of stationary and rotation testing included together, it was difficult in some cases to separate them in the literature review.

Swirl Generation

Enhancing heat transfer by using swirl enhancement is not new. But recent published literature indicates that significant gains may be possible with the right swirl enhancement techniques. Most available literature involving swirl enhancement in turbine blades deals with the leading edge, which is usually a circular channel. This leading edge channel almost always has film cooling holes to allow the air to exit the channel. Since the proposed study deals with the mid-span portion of the blade and the channels in the mid-span are rarely ever round, a thorough review

of leading edge swirl cooling is not included. Instead the focus is on swirl cooling without “film cooling” exit holes.

Helical Inserts

Smith Eiamsa-ard, et-al [8] studied the effect of helical tape inserts in a round tube like that typically used in a shell and tube heat exchanger. Different helical pitches and designs were used, and water was the used as the fluid in the pipe. Although the study looks a Reynolds numbers of 10,000 or less, the graphical results of the study can be extrapolated to higher Reynolds numbers and may prove useful for turbine blade cooling using air instead of water.

A 160% increase in mean Nusselt number was obtained in one particular test with other tests showing slightly lower values.

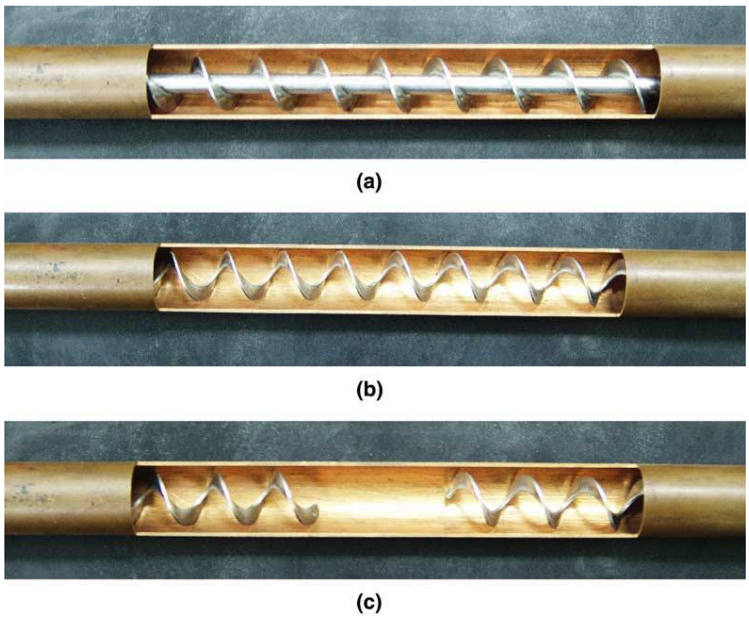

Figure 3-1 : The inner tube fitted with various helical geometries insert: (a) Full-length helical tape with a rod; (b) Full-length helical tape without a rod; (c) Regularly-spaced helical tape without a rod [8].

Pressure drops were as high as nine times that of a smooth pipe at the higher Reynolds numbers tested when a center rod was inserted and six times higher when the center rod was removed. At

the lower Reynolds numbers, the pressure drops reduced to approximately three times higher than a smooth pipe with a helical tape and no center tube. Helical tape pitch had a significant effect of the pressure drop as well at the higher Reynolds numbers tested. Photos of the various tests pieces can be found in figure 3-1.

This type of helical enhancers is not currently used in turbine blade, but a derivative of this design may be possible. In any case a thorough examination into heat transfer methods used in applications other than gas turbine blades can spark new ideas that can be investigated.

.

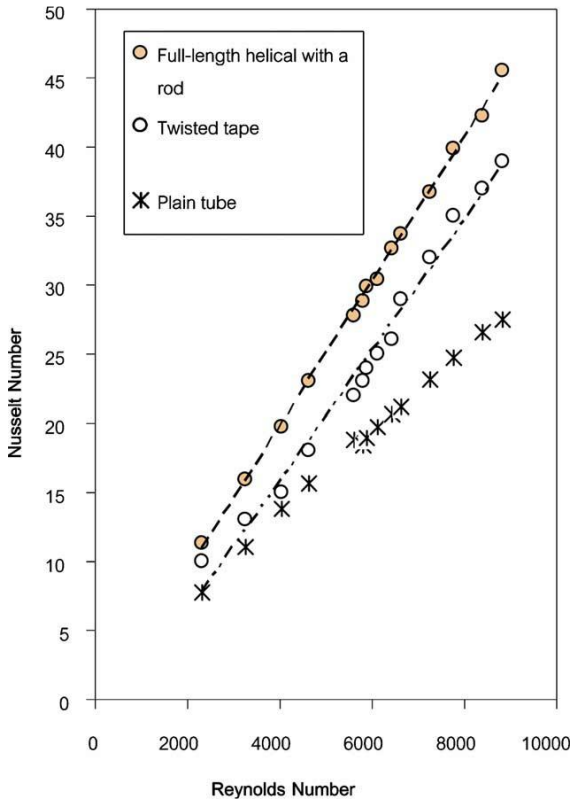

Figure 3-2 : Relationship between Nusselt number and Reynolds number for the tube with the helical-tape and twisted-tape inserts. [8]

Figure 3-2 shows the results of Nu verses Reynolds number for helical tape and twisted tape installed into a smooth pipe. As much as a 75% improvement in Nu is realized at the low Reynolds

numbers tested. Extrapolating the values to higher Reynolds numbers yields ~ 110% improvement at Re=45,000

Figure 3-3 shows the results of a test with and without the center rod added (see Figure 3-1-a). The results indicate that the center rod had little effect on improving heat transfer as compared to the removal of the rod.

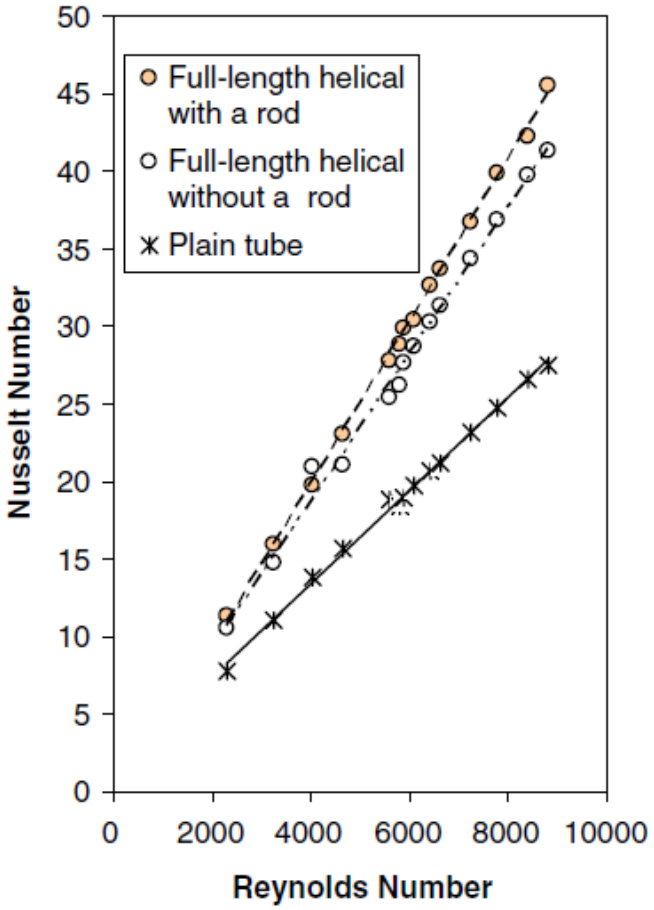

Figure 3-3 : Reynolds Number vs. Nusselt Number for tube with full length helical tape inserts. [8]

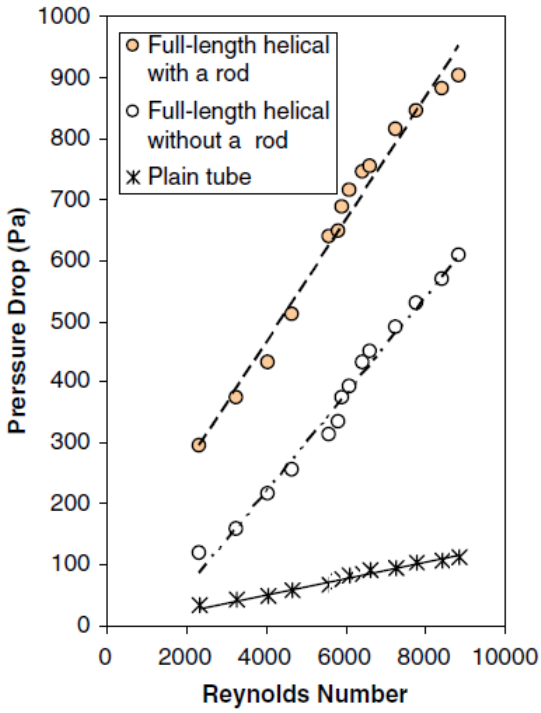

Figure 3-4 : Relationship between Reynolds number and pressure drop in a tube with full length helical tape strips. [8]

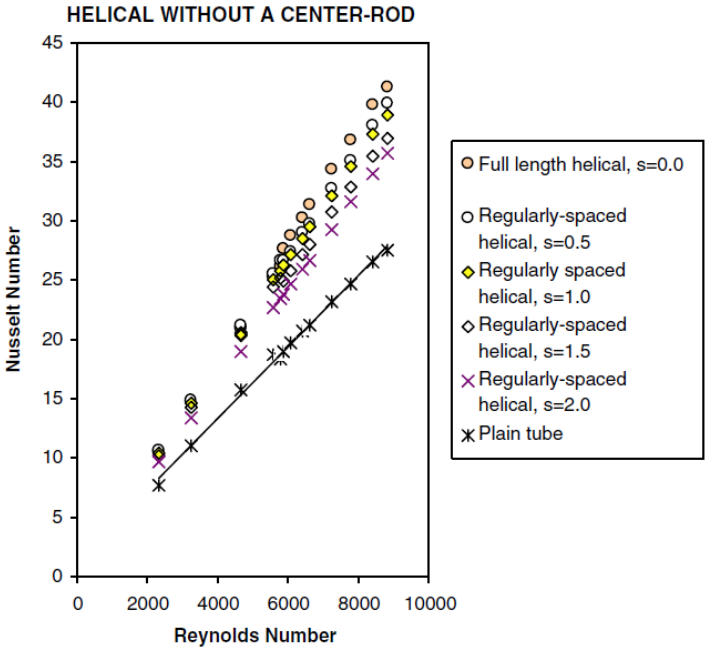

Figure 3-5 : Relationship between Nusselt number and Reynolds number for the tube with regularly-spaced helical tape inserts without rod. [8]

Flow visualization techniques were used to capture the swirl motion induced by the swirl tape. Figure 3-6 shows the results of the flow visualization study using swirl tape without a center rod. Note how the velocity vectors in the area of the tape are approaching a direction normal to the pipe length. As stated earlier, when rotational testing is performed, the Coriolis force is the cross product of the angular velocity of rotation and streamwise coolant fluid velocity. The flow condition should have a very positive effect on heat transfer in rotation.

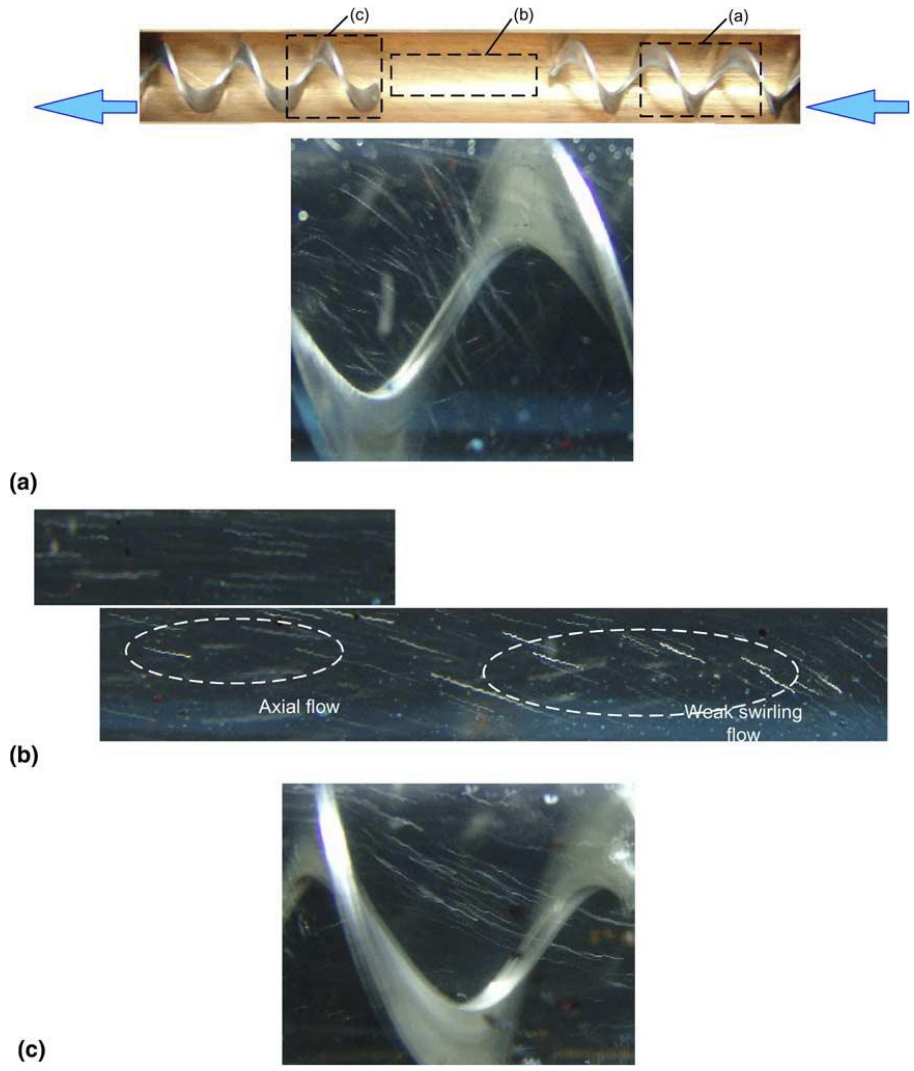

Figure 3-6 : Photograph of the flow in a circular tube fitted the helical tape without a rod:
(a) Swirling flow created by upstream helical tape; (b) Swirling flow decaying in the free-space; (c) Swirling flow recreated by downstream helical tape. [8]

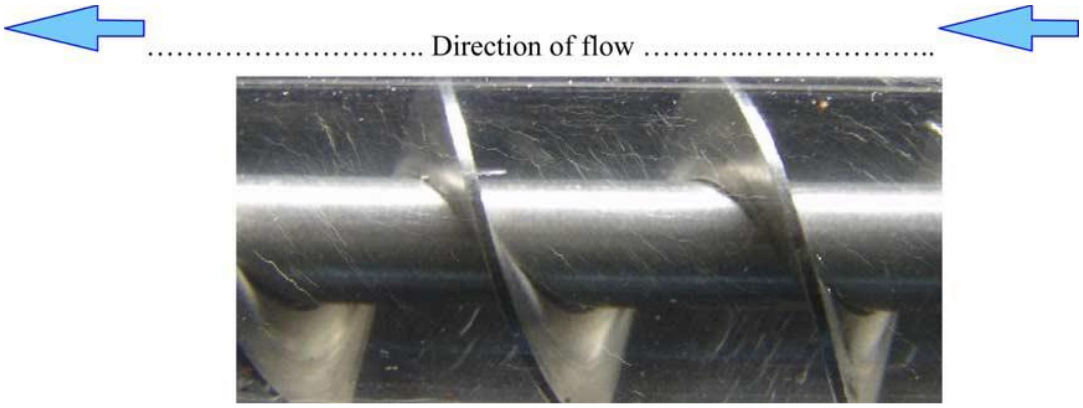

Figure 3-7 : Photograph of the flow in a circular tube fitted with the helical tape. [8]

Flow Directed Induced Swirl

Kurtbaş, et-al [9] studied the effects of inducing swirl into a smooth channel by using flow directed swirl generator nozzles at the inlet of a round channel with uniform heat flux. Cone insert angles of 30º, 45º, and 60º and flow director angles of 30º, 60º, and 90º were examined. Reynolds numbers of 9,400 to 35,000 were used throughout the various test performed. Pressure drop was also measured and finally an overall thermal performance value was determined. The general layout of the test piece is shown in figure 3-8.

Figure 3-9 is a graphical representation with a 30º cone and air introduced at different angles relative to the pipe. The value DR is defined as the ratio of the flow director diameter (FDD) to inner diameter of the pipe. No other swirl enhancement devices are used other than the flow generator nozzle.

Table 3-1 : Critical Dimensions and angles on the test piece [9].

Dimensions of the independent parameters (mm).

L_p	L_{sg}	L_{fd}	d	D	α (deg)	β (deg)
	60		4		30	30
1200	78.4	6	7	60	45	60
	116		10		60	90

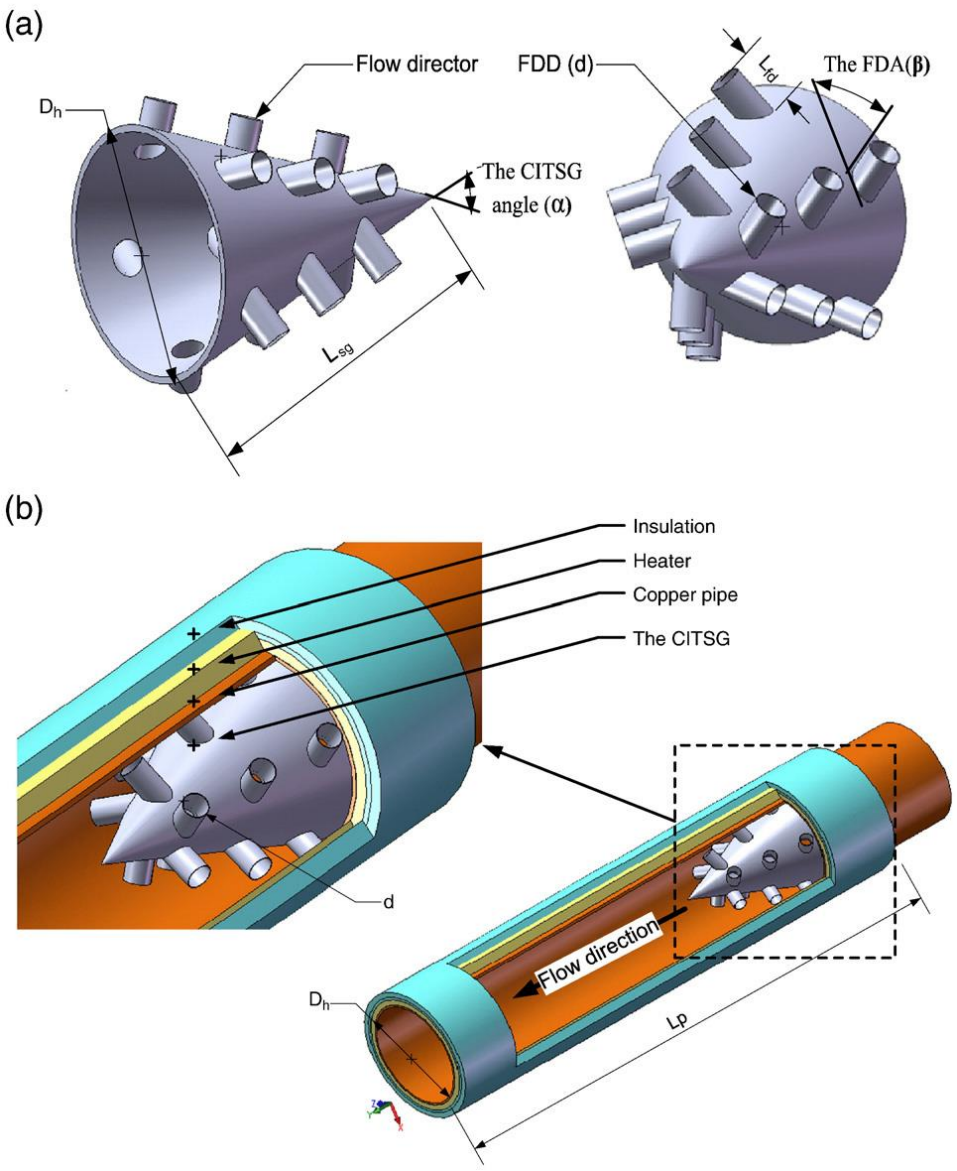

Figure 3-8 : Layout of test piece with swirl generators. [9]

The overall thermal performance at low Reynolds numbers fared the best when DR = 0.116 with a cone angle (α) of 30° and a flow director angle (β) was 30°. This changed as the Reynolds number increased. At higher Reynolds numbers the results were markedly higher with DR= 0.166, and α = 45°. The overall thermal performance shown in this study is typical to those using other heat transfer enhancements, such as trip strips, etc..

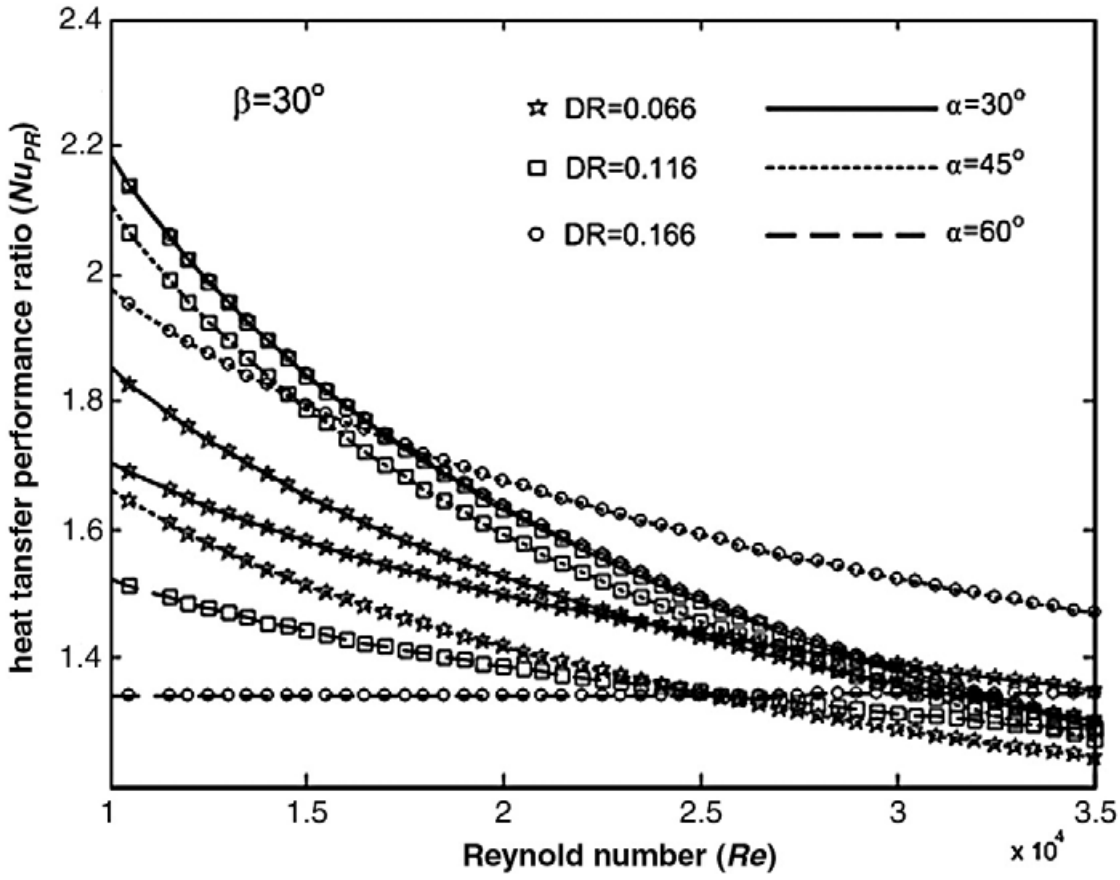

Figure 3-9 : Comparison overall thermal performance with varieties of Re for β=30°. [9]

Side Jet Induced Swirl

Ligrani, et-al studied the effects of swirl in a round channel with a single jet positioned tangent to the tube wall and issuing at an angle of 90 degrees to the normal flow direction. The jet was rectangular and suction was used at the exit of the channel to force air to enter the round channel through the rectangular shaped inlet jet. Figure 3-10 shows the basic set up. This round channel is typically found in the leading edge of a turbine blade.

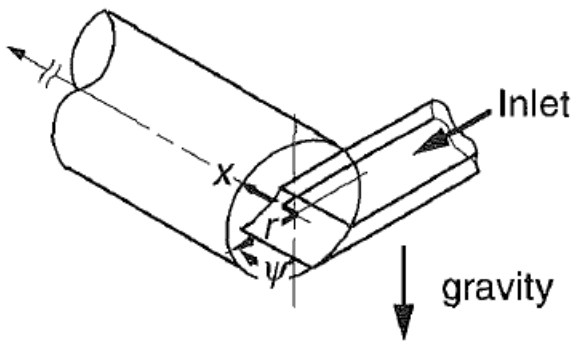

Figure 3-10 : Side Jet Issuing into Circular Channel used in Swirl Test [10]

The results of their tests are shown in Figure 3-11. The values of circumferentially averaged Nusselt numbers are presented as a function of x/r_o. The Re value is the Reynolds number in the jet and the Re_D value is the Reynolds number in the round channel. In all cases the value of Nu reaches a steady state value at $x/r_o \sim 12$. This can be expected as there are no additional mechanisms to cause the flow to continue swirling as it progresses through the channel. Although some details of pressure losses are given, the authors do not present an overall heat transfer enhancement value. The high Nu values presented in Figure 3-11 at x/r_o of 0 to 3 and x/r_o of 6 – 10 do indicate that the swirl induced flow heat transfer is substantial and significant.

As expected the higher Reynolds numbers performed better. A blowing ratio (jet velocity vs. tube velocity) based on the Reynolds numbers provided, indicate that the blowing ratio would be less than 3 for all cases tested. If Nu/Nu_o values were to be estimated, based on Nu_o in a smooth round channel of the same diameter as the round main channel in the tests, the highest Nu/Nu_o values would be approximately eleven for Re_D of 6537 located at $x/r_o \sim 8$. Considering that the friction factor is low the overall heat transfer performance can be expected to be very high, at least in these local areas.

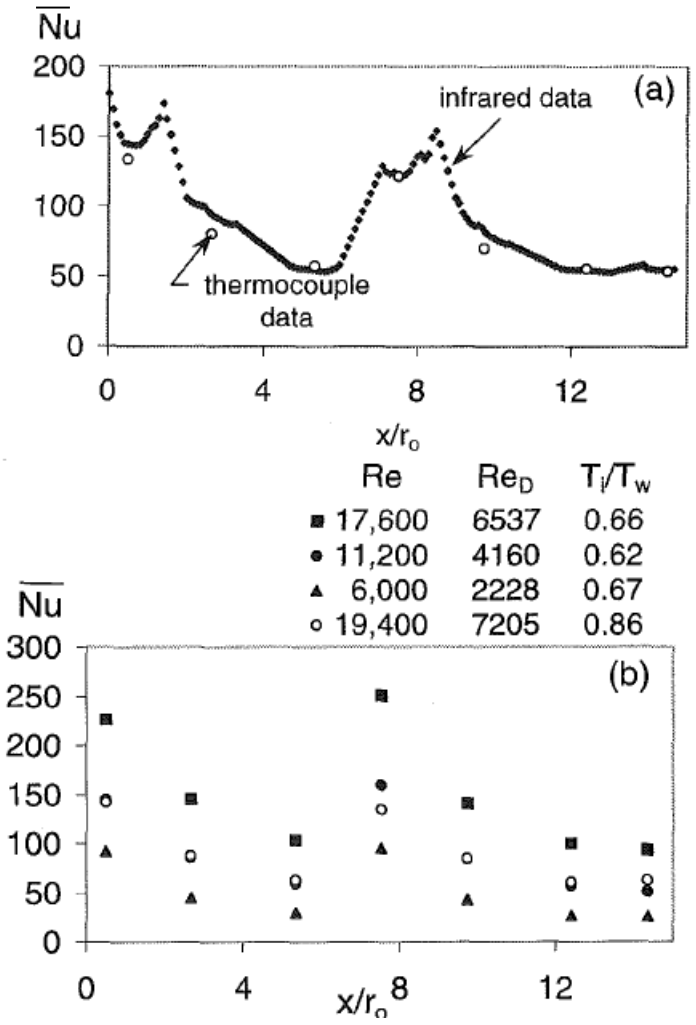

Figure 3-11 : Circumferentially averaged Nusselt numbers as dependent upon x/r_o: (a) Nusselt numbers for Re = 19,400 (Re_d = 7,205) and Ti,/Tw = 0.85; (b) Nusselt numbers for different Re and Re_d and for different Ti,/Tw.[10]

Ribbed Turbulators

Adding ribs to a smooth channel induces vortices and flow reattachment as the fluid passes over the rib. The concept can be seen in Figure 3-12. The shape, angle, height, pitch, and layout of the ribs in the flow channel can affect the local and regional heat transfer in many ways. A thorough understanding of how each of these parameters is needed in order to advance technology in the area of heat transfer in gas turbine blades when using ribbed turbulators.

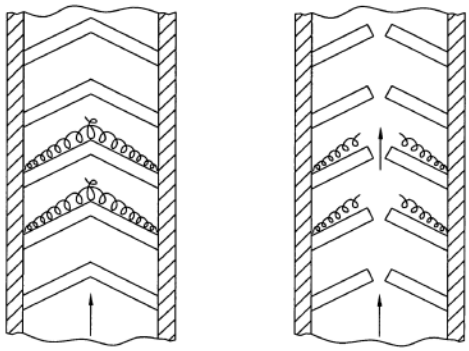

Figure 3-12 : Concept of turbulence induced by trip strips in rectangular channels [11].

Detailed studies of these various parameters have been published over the last few decades.

Several different layouts were reviewed and the results of a few key studies are presented.

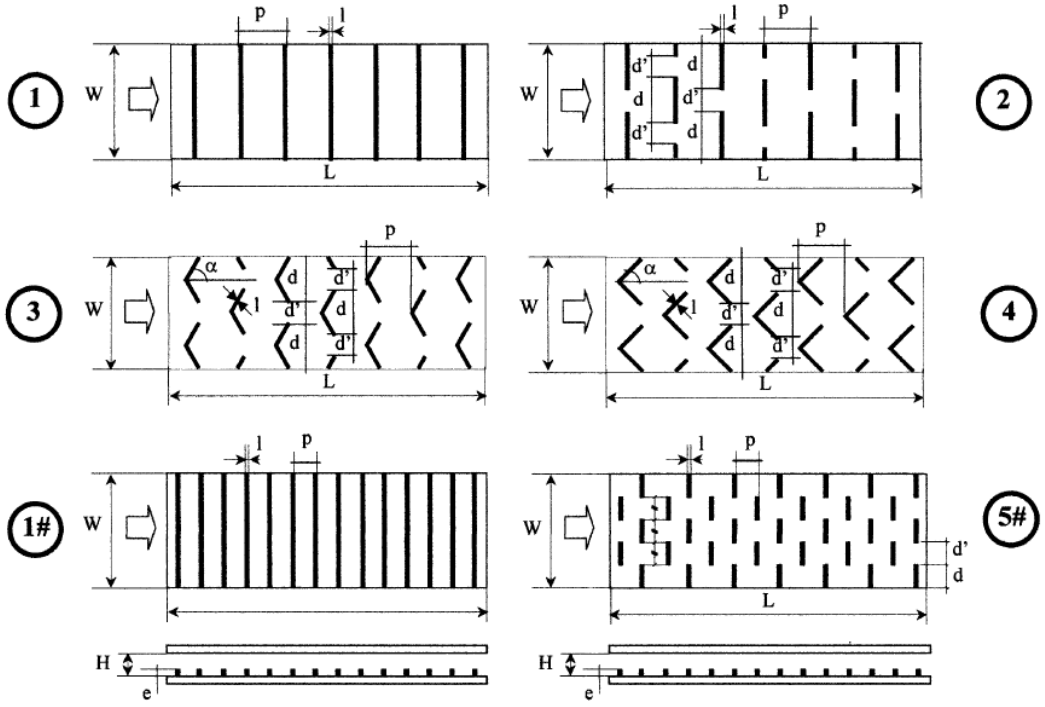

Figure 3-13 : Geometry of rib configurations studied: 1. Transverse continuous ribs (I,II), 2. Transverse broken ribs (I,II). 3. Broken 60 deg V-ribs (I,II). 4. Broken 45 deg V-ribs (I,II). 1-#. Transverse continuous ribs. 5-#. Transverse broken ribs. (I, II and # denote different rib pitch-to-height ratios). [11]

Rectangular Ribs at various angles and geometries in a single pass channel

A paper published by Tanda, et-al [11] in 2004 studied the thermal performance and friction losses of rectangular ribs angled at 90 degrees, 60 degrees, and 45 degrees to the main flow direction, as well as parallel and V-shaped configurations. The variety of tests also included what is referred to as a "broken" rib configuration. As expected, and seen in other published papers, the 90 degree ribs performed the worse, with 60 degree ribs performing the best. In this series of tests the 60° parallel broken ribs or 60° V-shaped broken ribs performed better than the 45° parallel broken ribs or 45° V-shaped broken ribs. Sketches of the various configurations are shown in figure 3-13.

Table 3-2 : Critical Dimensions of rib configurations [11].

Geometric characteristics of rib configurations

Configuration	e (mm)	l (mm)	α (deg)	d (mm)	d' (mm)	e/D	p/e	e/H
1-I continuous ribs	5	3	90	–	–	0.15	8	0.25
2-I broken ribs	5	3	90	40	20	0.15	8	0.25
3-I broken V-ribs	5	3	60	40	20	0.15	8	0.25
4-I broken V-ribs	5	3	45	40	20	0.15	8	0.25
1-II continuous ribs	3	3	90	–	–	0.09	13.3	0.15
2-II broken ribs	3	3	90	40	20	0.09	13.3	0.15
3-II broken V-ribs	3	3	60	40	20	0.09	13.3	0.15
4-II broken V-ribs	3	3	45	40	20	0.09	13.3	0.15
1-# continuous ribs[a]	5	3	90	–	–	0.15	4	0.25
5-# broken ribs[a]	5	3	90	20	20	0.15	4	0.25

A summary of the results are shown in the proceeding figures. Close examination of the color contour plots in figure 3-14 give insight to the effect of the convection heat transfer in various rib configurations. When traverse continuous ribs are used at this Reynolds number, recirculation and flow reattachment does not occur near the rib. The flow in this area is nearly stagnate and is the area that shows the least amount of heat transfer. The outer walls exhibit the greatest heat transfer. There are localized zones that make this layout undesirable. Contour map "b" in figure

3-14 shows 90 degree broken ribs. In this color plot there are small local cold zones at the four corners of the plot, but there is a good ring of high heat transfer that surround the broken rib in the middle of the plot. Recirculation zones form as the flow maneuvers around the center wall. The average Nusselt number is much higher than in map “a” and has a good distribution of heat transfer enhancement. Plot “c” is the same as plot “b” except for the height of the rib. The rib height changes from 5mm in plot “b” to 3mm in plot “c”. This causes the e/H and p/e values to change as shown in Table 3-2. The results are similar, but lower, and there is what appears to be a local flow stagnation area just in upstream of the center broken rib.

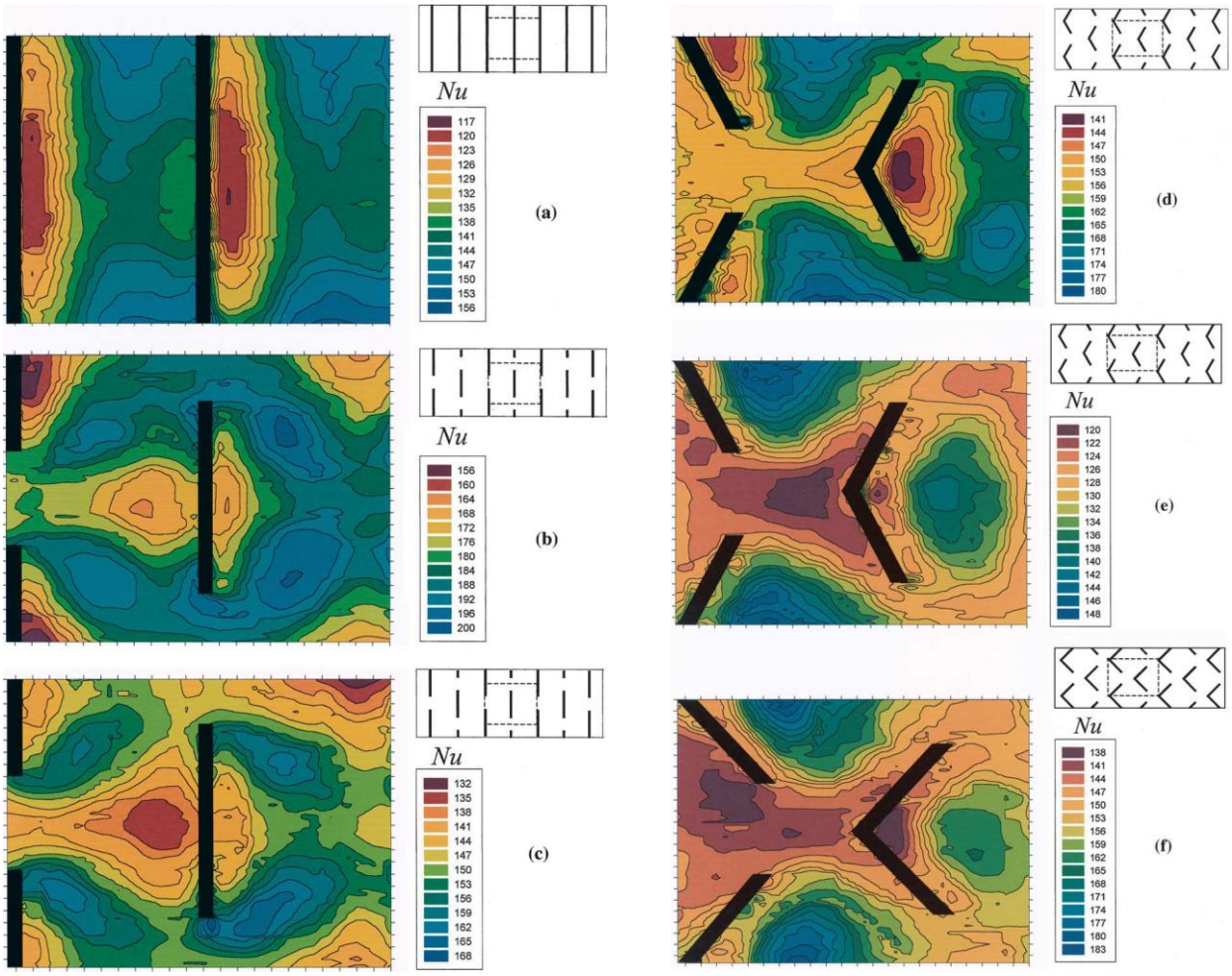

Figure 3-14 : Map of Nusselt number over the central (inline) region of the heated surface (Re = 28,500): (a) transverse continuous ribs 1-I, (b) 90 deg broken ribs 2-I, (c) 90 deg broken ribs 2-II, (d) 60 deg V-shaped ribs 3-I, (e) 60 deg V-shaped ribs 3-II, (f) 45 deg V-shaped ribs 4-I. [11]

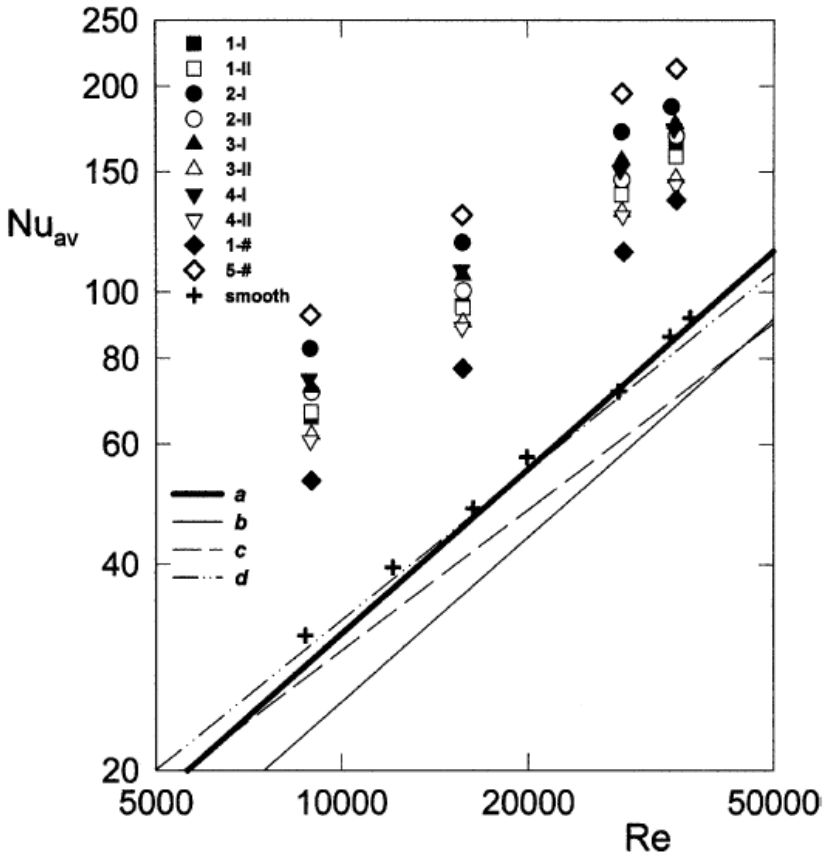

Figure 3-15 : Average Nusselt number for the rib configurations (open and closed symbols) and Nusselt number at x/D = 8 for the smooth channel (cross symbols). a–d: typical correlations for the fully developed flow Nusselt number in the smooth channel: a: $Nu_0 = 0.023Re^{0.8} Pr^{0.4}$; b: $Nu_0 = 0.019Re^{0.8} P r^{0.5}$; c: $Nu_0 = 0.055 Re^{0.684}$ (Pr = 0.7); d: $Nu_0 = 0.041 Re^{0.727}$ (Pr = 0.7). [11]

Plots “d”, “e”, and “f” use staggered V-shaped ribs and 60^o and 45^o, with plots “e” and “f” using the shorter 3mm ribs. The general contours are similar with plot “d” appearing to have the highest average values and the best heat transfer distribution.

Figure 3-16 shows the average Nusselt number verses Reynolds number for the full complement of tests. The 90^o traverse broken ribs with a p/e ratio of 4 performed the best by a substantial margin at all Reynolds numbers tested. Most published papers do not test 90^o traverse broken ribs with such a low p/e ratio, so this result is a little surprising.

Even when the average Nusselt number is normalized to a smooth channel as shown in figure 3-16, the 90° traverse broken ribs prevail over the other rib geometries tested. The worst performer is the 90° traverse continuous ribs.

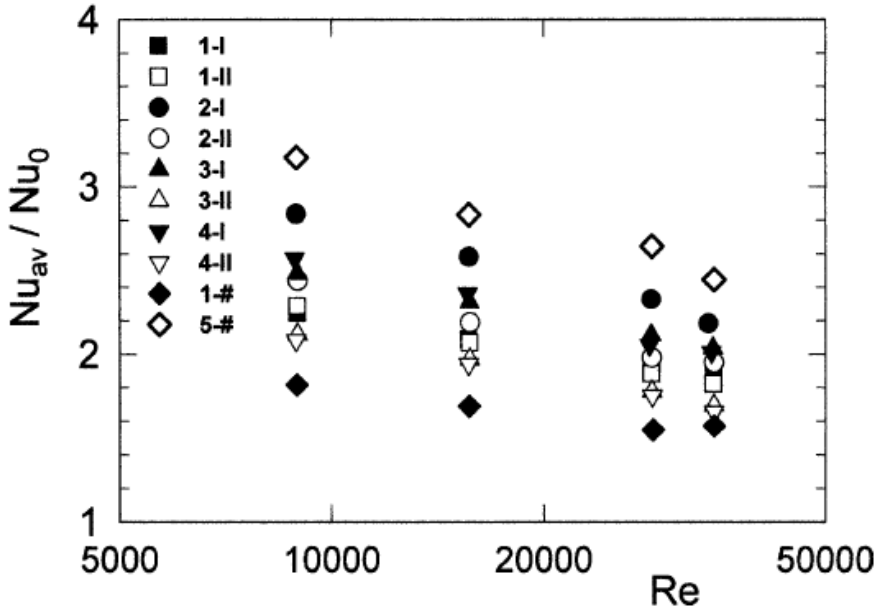

Figure 3-16 : Ratio of average Nusselt number with and without ribs against the Reynolds number for fixed mass flow rates.[11]

Rectangular 70° Angled Ribs in a 2:1 AR two pass channel

Kim, et-al [12] conducted a detailed study of the thermal performance and pressure losses in a 2:1 AR rectangular two pass duct with rectangular ribs positioned in various arrangements, oriented at 70 degrees. The Reynolds number was constant for all tests at 20,000. The static tests were repeated in a rotating environment with a rotation number of 0.1. The orientation of the ribs in each test is detailed in Figure 3-17. The ribs were positioned in a variety of PP (Positive-Positive) or NN (Negative-Negative) or combinations of PN/NP directions relative to the flow.

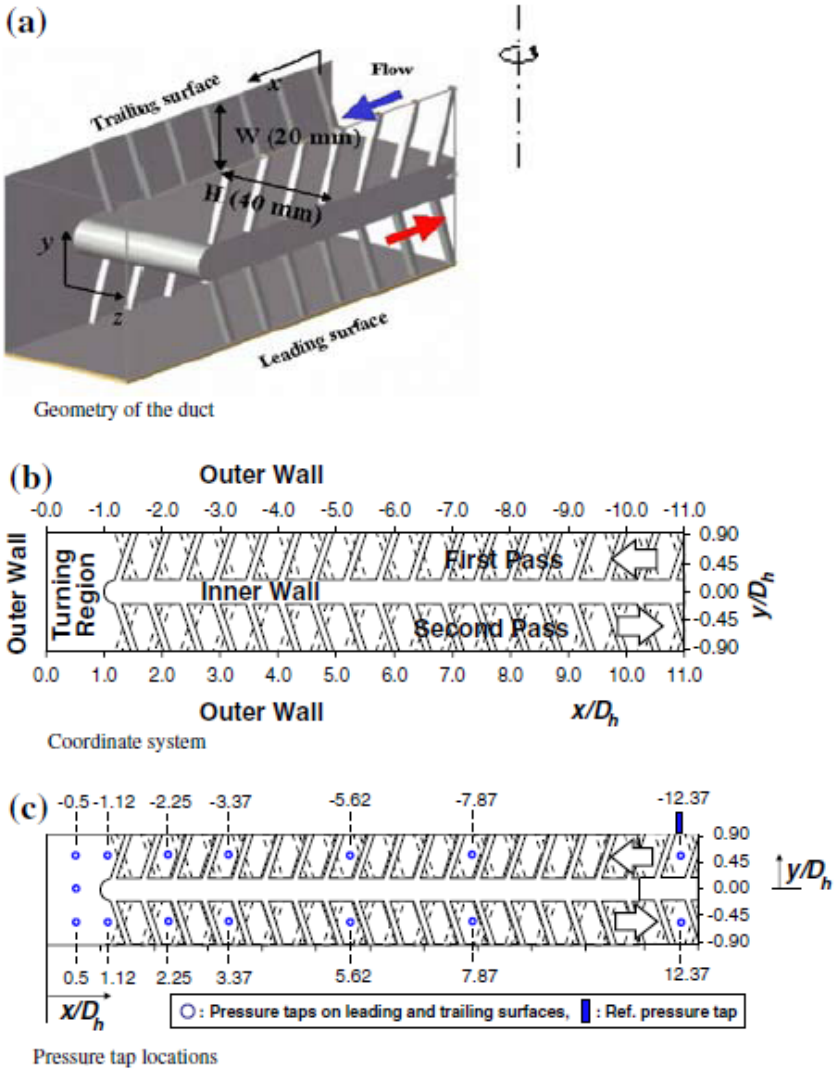

Figure 3-17 : Schematics of test duct (e.g., PN rib arrangement): a) geometry of the duct, b) coordinate system, c) pressure tap locations.[12]

Figure 3-18 depicts the regional thermal performance of the two pass duct during various static and rotating tests. Rib orientation does not seem to play a role in the first pass, whether in rotation or static arena. At the 180 degree turn all ribs performed nearly equally in the static test, but there was a notable increase with the NN and PP type ribs.

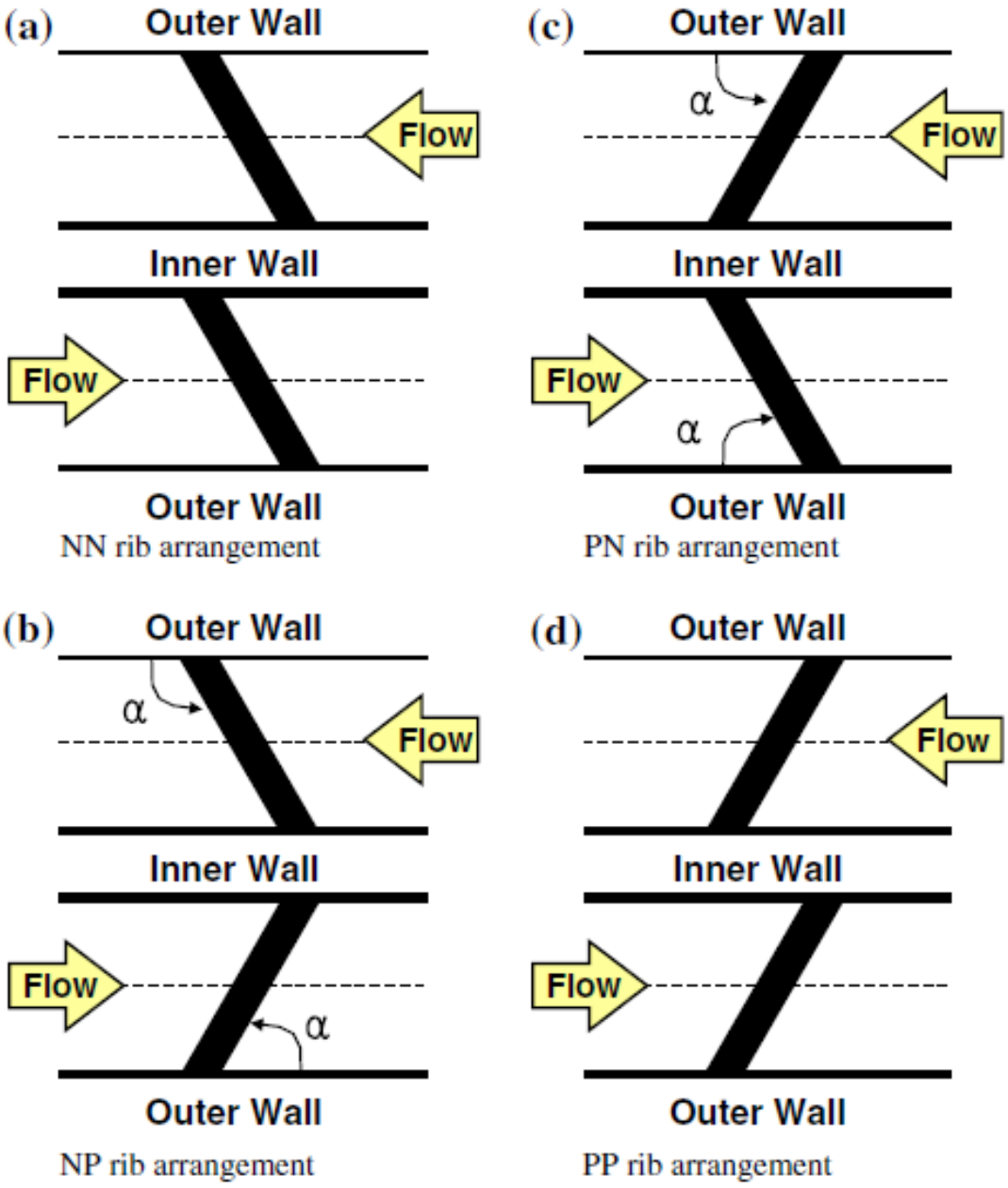

Figure 3-18 : Schematics of rib arrangements on leading surface in two-pass duct: a) NN rib arrangement, b) NP rib arrangement, c) PN rib arrangement, d) PP rib arrangement. [12]

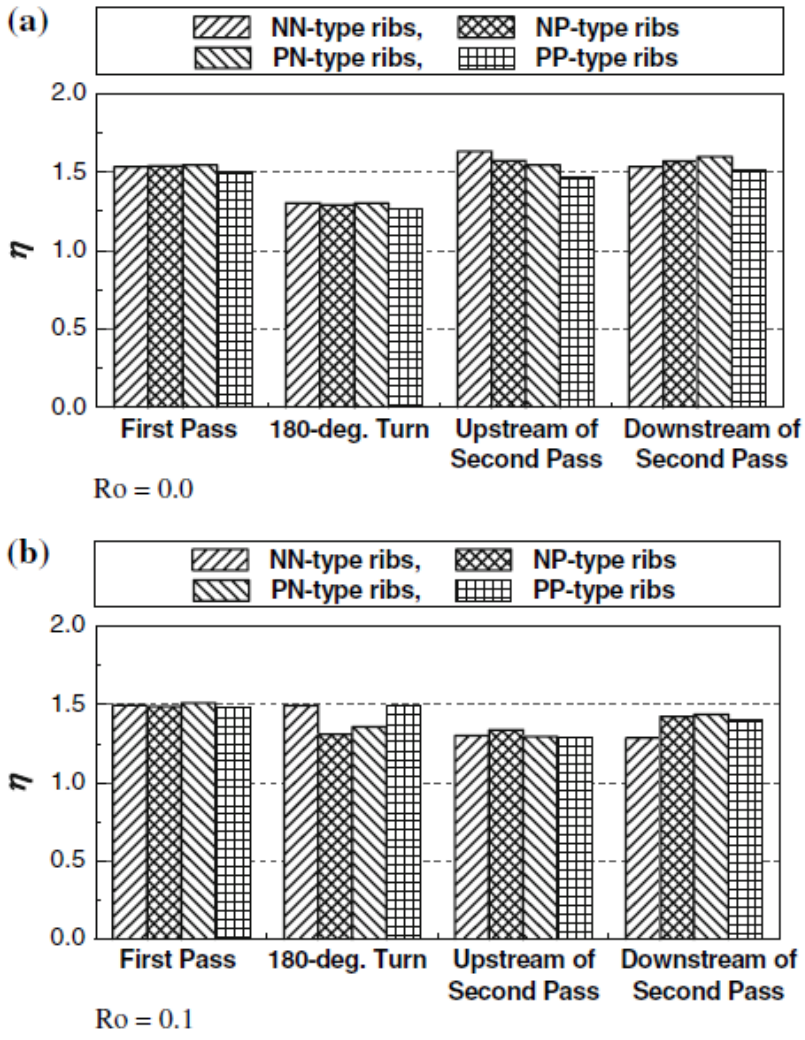

Figure 3-19 : Regional Thermal Performance: a) Ro=0.0, b) Ro=0.1[12]

The increase is likely due to the buoyancy effect and Coriolis forces induced during rotation and some impingement effects as the fluid turns. These same forces caused lower values upstream of the second pass in all rib types tested. This is consistent with other studies using two pass channels. The slightly lower values downstream of the second pass in the rotating test are carried over from the activity in the upstream portion of the second pass. The general trend of values of thermal performance is consistent with other studies of ribbed turbulators.

Thermal Performance in isosceles triangular shaped ribs

Thianpong, et-al [13] studied the effect of different height isosceles triangular shaped ribs in a rectangular shaped channel. Using e/b (noted as e/H in the study) ratios between 0.26 and 0.13 and Reynolds numbers from 5,000 to 22,000. Figure 3-20 shows the results of Nu/Nu_o verses Reynolds number. In this study the inline ribs with an e/b ratio of 0.26 with in line ribs resulted in Nu/Nu_o values of four or so throughout the range of Reynolds numbers. These results are quite high compared to similar studies of e/b ratios, where e/b values closer to 0.10 proved beneficial.

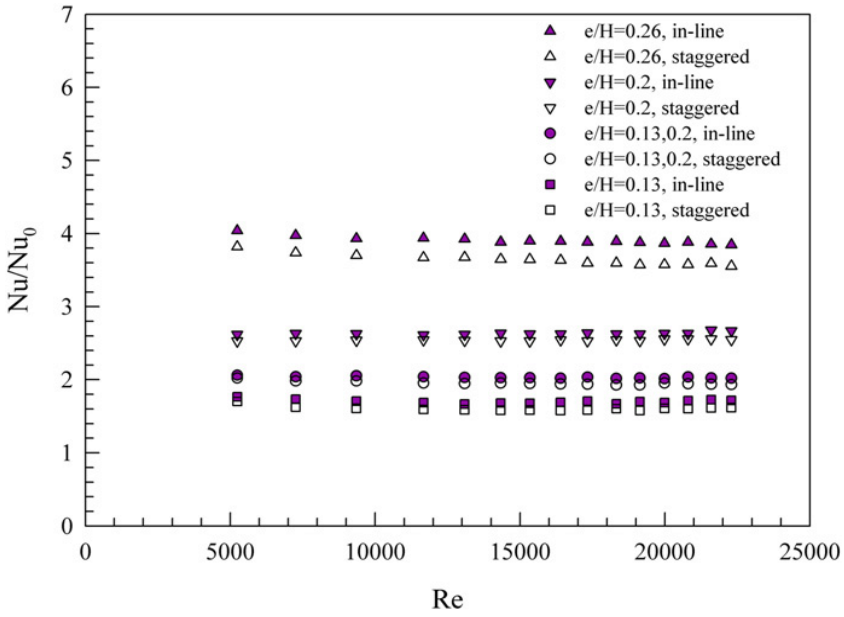

Figure 3-20 : Variation of Nusselt number ratio, Nu/Nu_0 with Reynolds number.[13]

This study did use a test piece with an aspect ratio (a/b) of 10, which is also not typically found in gas turbine blades. It will be shown in subsequent graphs that once friction is taken into account, the lower e/b ratios will prove beneficial in heat transfer enhancement.

Channel friction verses Reynolds number measurements were taken and plotted in Figure 3-21. Here it is easily seen that the higher e/b ratios are markedly higher throughout the range of

Reynolds numbers tested. It seems a little unusual that the severe drop in friction loss values when the e/b ratio is changed from 0.26 to 0.20 and yet the friction loss in the range of 0.20 to 0.13 are virtually the same as a smooth channel.

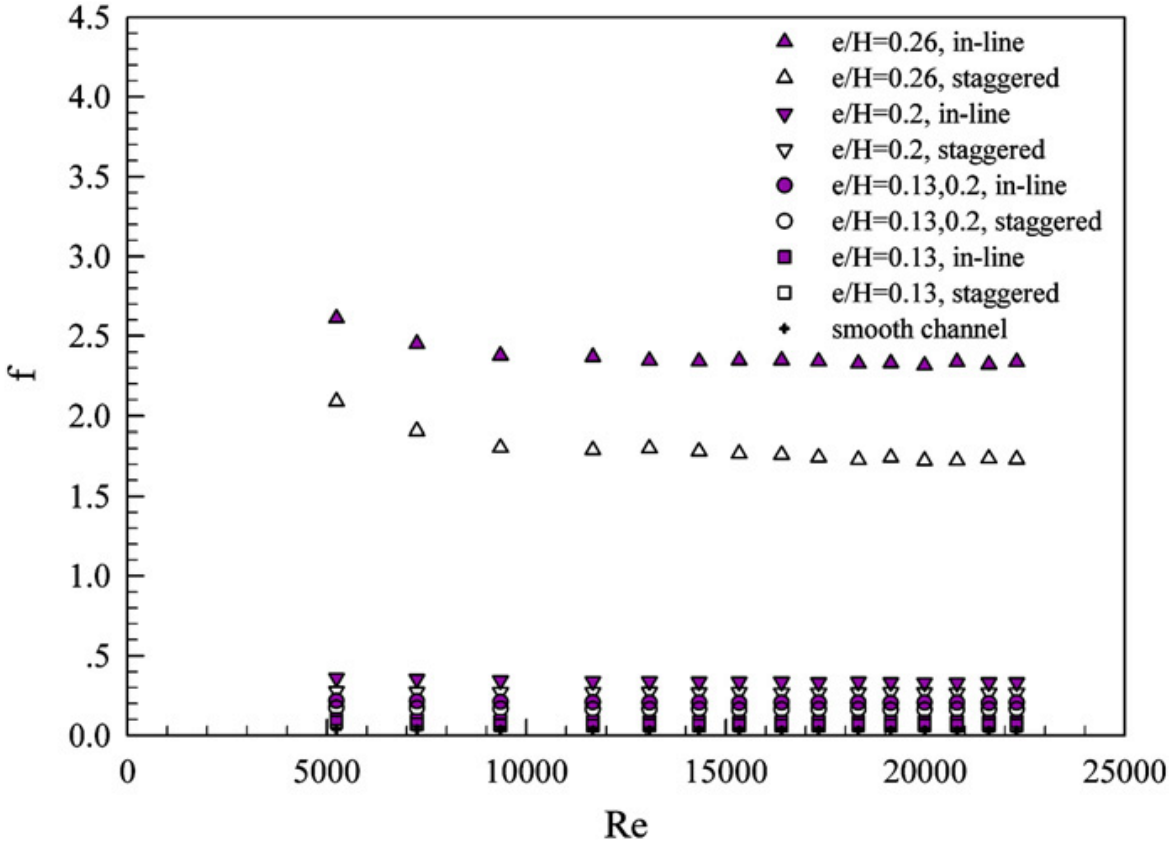

Figure 3-21 : Variation of friction factor with Reynolds number for various rib heights. [13]

Therefore, as expected, when a normalized friction value (f/f_o) is plotted against Reynolds number as in Figure 3-22 the results are proportional to values in Figure 3-21. The end user is primarily concerned with the overall Thermal Enhancement Factor, η, which related the normalized Nusselt number to the normalized friction factor.

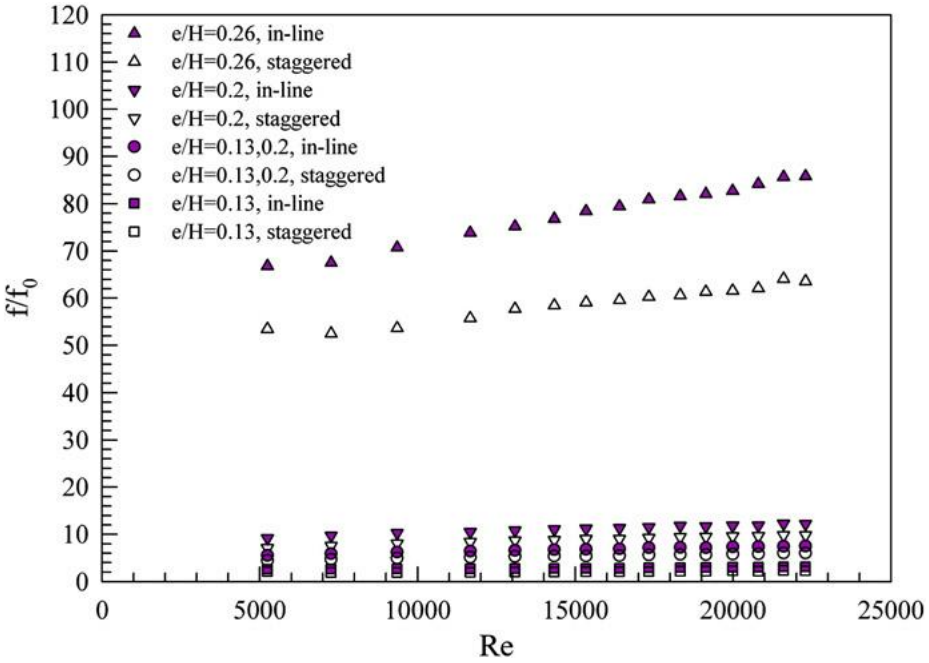

Figure 3-22 : Variation of friction factor ratio, f/f_0 with Reynolds number. [13]

Figure 1-39 shows a graph of the various triangular rib heights and orientation as they relate to the Thermal Enhancement Factor. This graph clearly shows the advantage of lower e/b ratios. Values in the 1.3 range are typical when compared to other published papers.

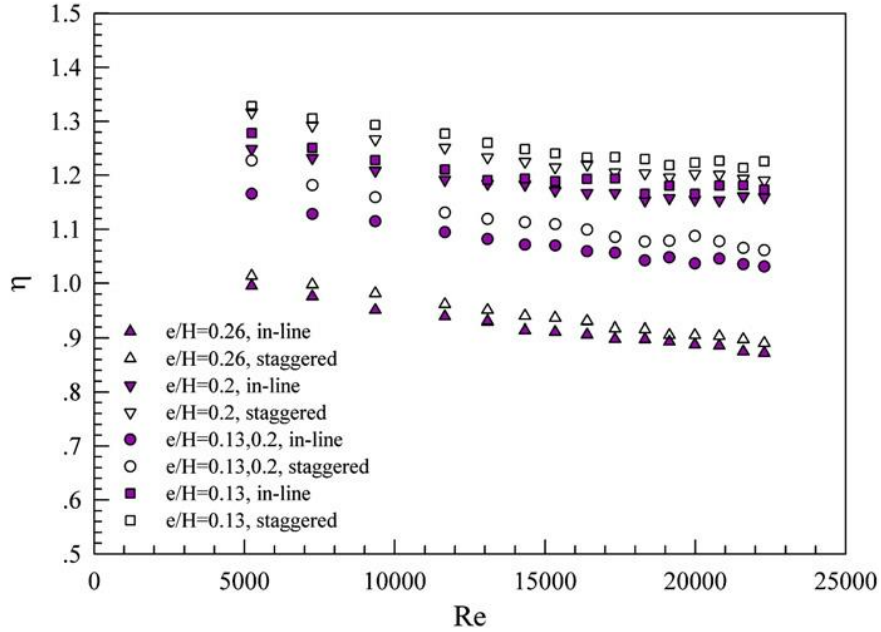

Figure 3-23 : Variation of thermal enhancement factor with Reynolds number. [13]

Comparison of triangular, wedge, and rectangular shaped ribs in a high aspect ratio channel

Reynolds numbers between 4,000 and 16,000 were tested by Promvonge, et-al [14] in a 15:1 aspect ratio channel with an e/b ratio of 0.3. Ribs were placed in staggered and inline for the various tests. A sketch of the general layout is shown in Figure 3-24. The pressure drop associated with this type of configuration is quite high, as e/b ratios of ~0.1 are more typical in gas turbine blades because of the lower pressure drop. The wedge ribs were shaped like a right triangle and the triangular shaped rib was isosceles. The P/e ratio along one wall was maintained at 6.67 for all tests.

Figure 3-24 : Staggered rib arrays, (a) wedge pointing upstream, (b) wedge pointing downstream, (c) triangular and (d) rectangular rib. [14]

When the Nusselt number is plotted in relationship to the Reynolds number as shown in Figure 3-25 it is easy to see that the rectangular ribs yield the worst performance, while the downstream facing wedge ribs performed the best.

Figure 3-26 shows the normalized Nusselt number of the rib configurations tested as related to Reynolds number. The downstream facing right triangular rib yielded impressive values in the 4.4 range throughout the Reynolds number values.

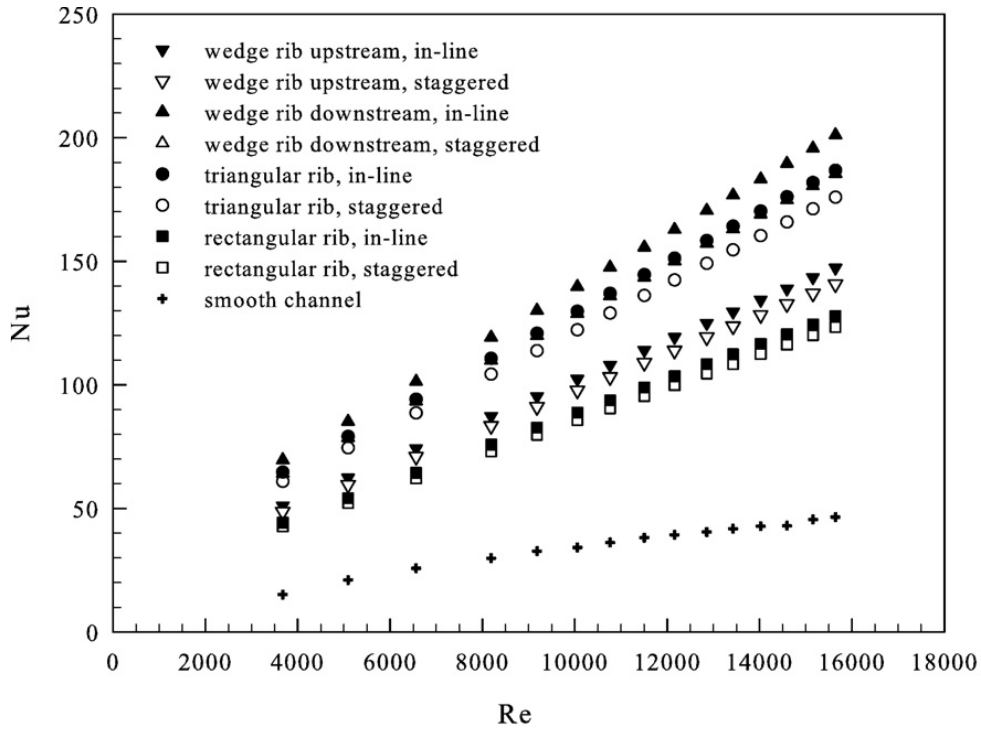

Figure 3-25 : Variation of Nusselt number with Reynolds number for various ribs. [14]

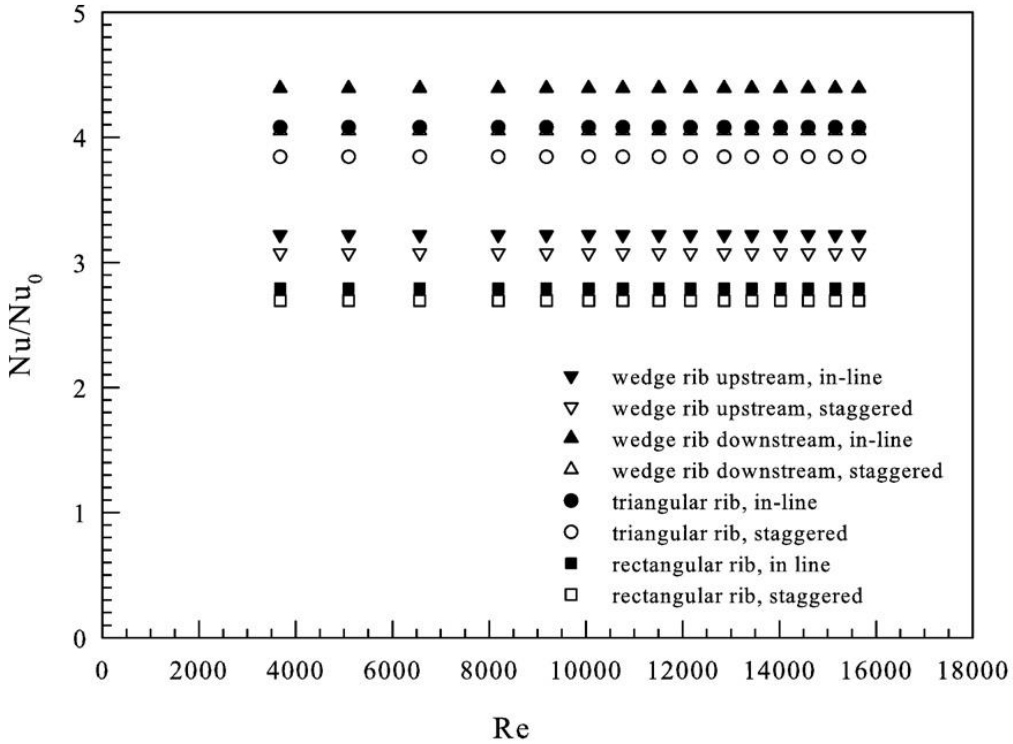

Figure 3-26 : Variation of Nusselt number ratio, Nu_a/Nu_0 with Reynolds number. [14]

Normalized friction factor values are shown in Figure 3-27. These values are high compared to most published data due to the high e/b ratio of 0.3. Not surprisingly, the downstream facing wedge shaped ribs performed the worst and the rectangular shaped ribs performed the best.

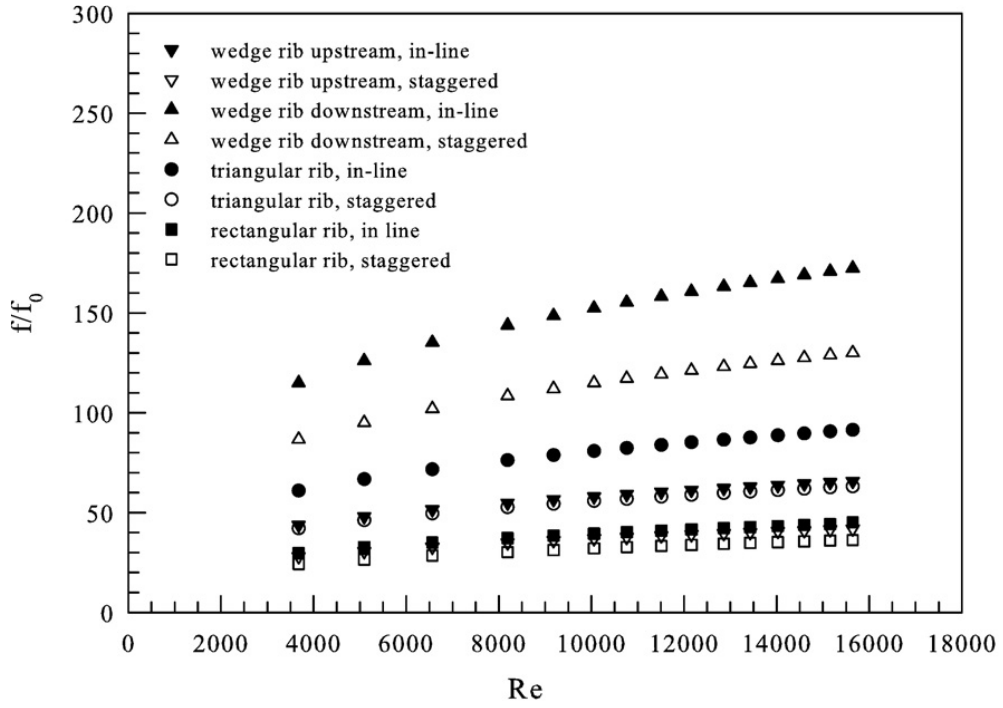

Figure 3-27 : Variation of friction factor ratio, f_a/f_0 with Reynolds number. [14]

Once these values are combined to determine the overall thermal performance the staggered triangular ribs lead the pack. The results are plotted in Figure 3-28. The performance of all of the rib configurations in this test are poor compared to other published papers. I suspect the reason is that the high aspect ratio (15:1) and low P/e ratio (6.67:1) are the major contributing factors. The author compares the smooth channel to the Dittus-Boelter equation, which is modeled off of a smooth round pipe. The author uses the hydraulic diameter in the various calculations. It is well understood and well published that the equation used to determine hydraulic diameter is limited to aspect ratios between 3.0 and 0.3. Since the aspect ratio used in this study is 15:1, the calculations that use the hydraulic diameter (i.e. Reynolds number) should be considered suspect.

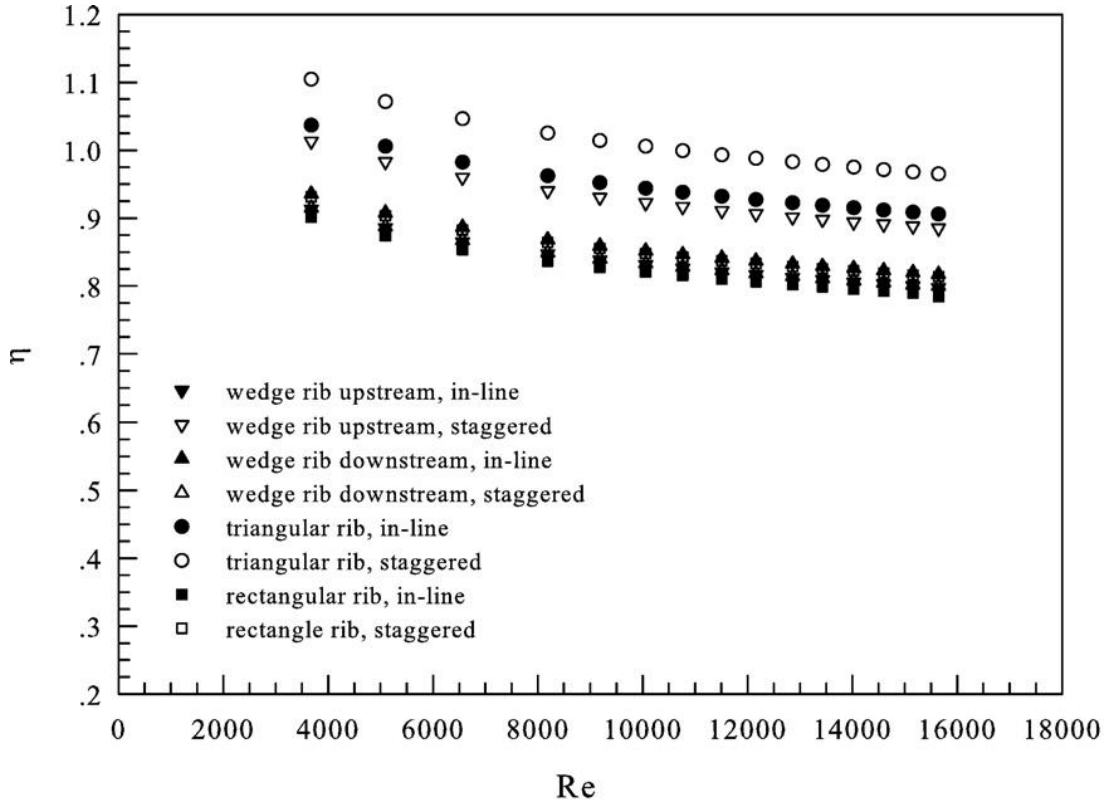

Figure 3-28 : Variation of enhancement factor with Reynolds number. [14]

The overall heat transfer enhancement values below 1.0 indicate that the configurations would not perform as well as a smooth pipe. This study should therefore only be used to track tendencies in performance and may not correlate well with studies using 2:1 aspect ratios, 10:1 P/e ratios, and 0.10 e/b ratios, which are more typically seen in gas turbine blade passages.

Square Duct with Various-shaped Ribs

Wang, et-al [15] performed a detailed study of various rib shapes in a square ducts with P/e ratios varying from 8 to 15 and $e/d_h = 0.1$. The range of Reynolds numbers tested was 8,000 to 20,000. Details of the rib configurations and other parameters are shown in Figures 3-29 – 3-32.

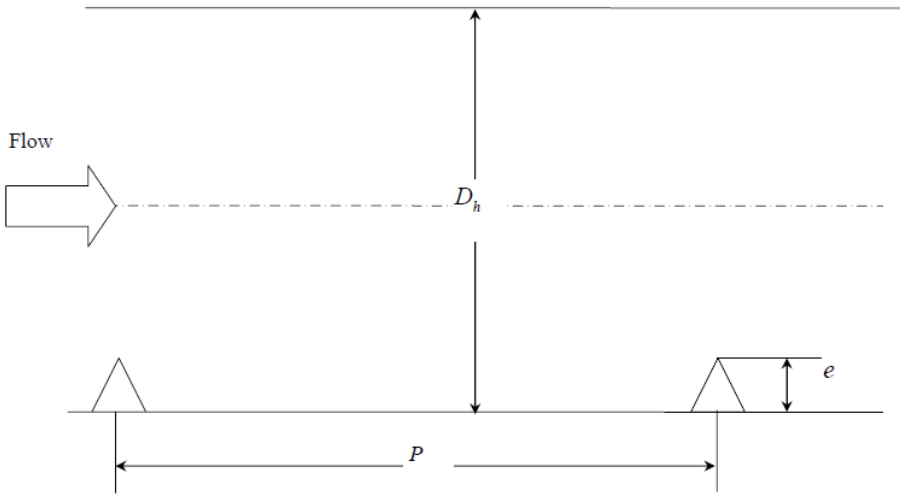

Figure 3-29 : Traverse triangular ribs, $e/d_h = 0.1$, $d_h = 50mm$, [15]

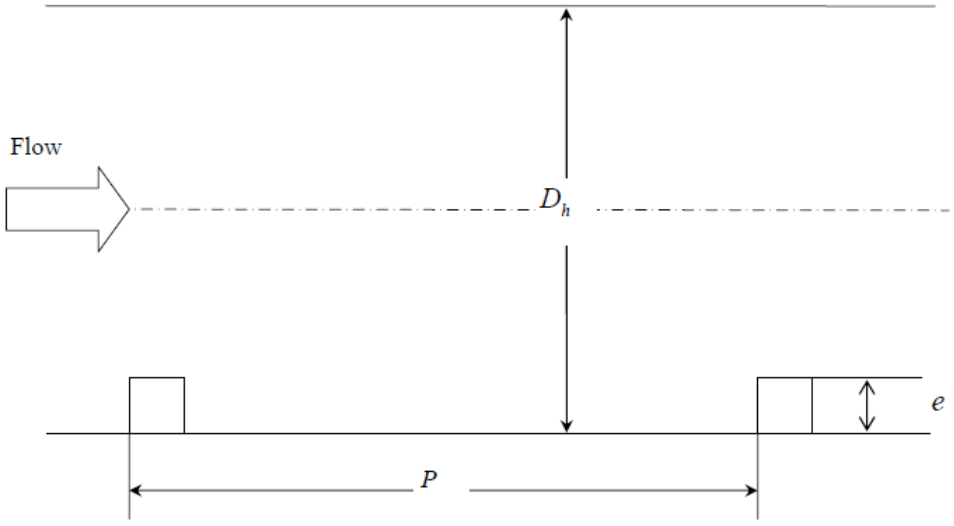

Figure 3-30 : Traverse square ribs, $e/d_h = 0.1$, $d_h = 50mm$, [15]

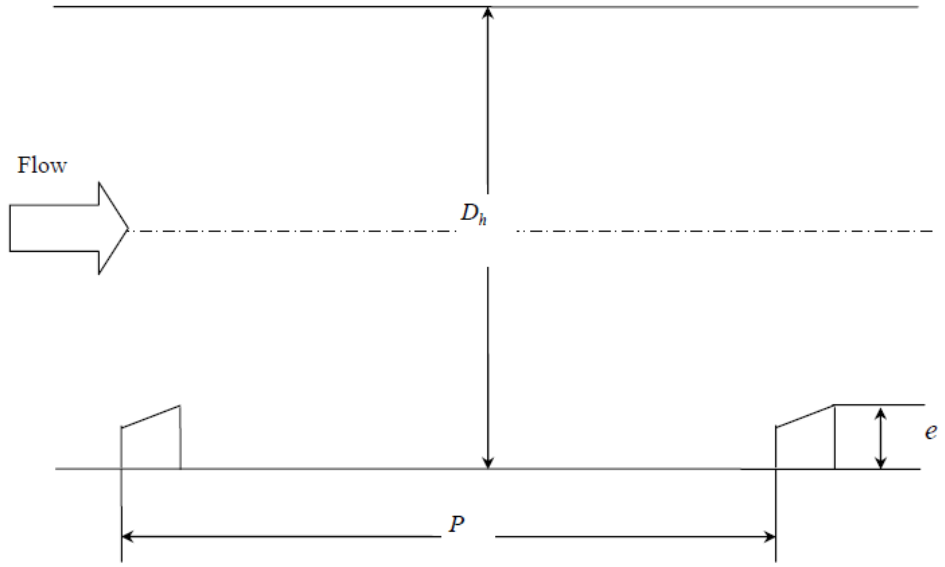

Figure 3-31 : Traverse trapezoid ribs, increasing height in flow direction, $e/d_h = 0.1$, d_h = 50mm, [15]

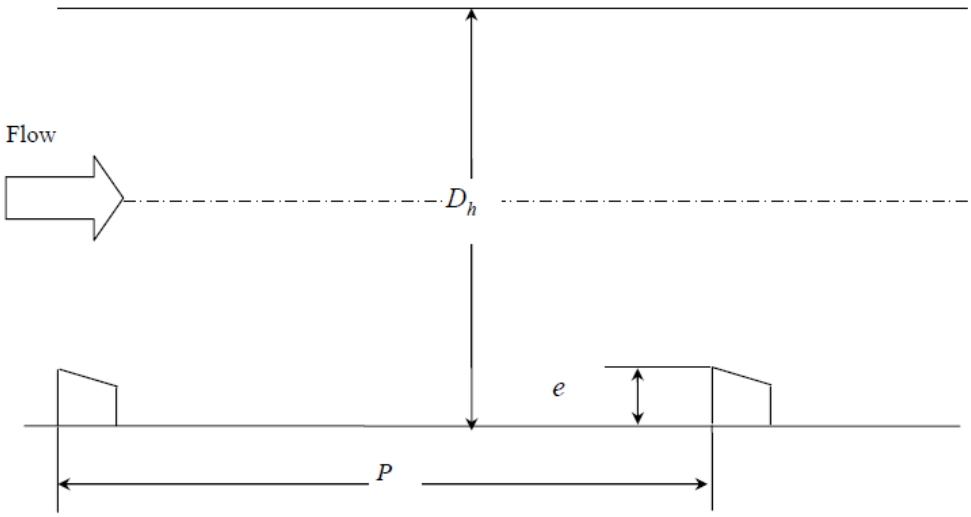

Figure 3-32 : Traverse trapezoid ribs, decreasing height in flow direction, $e/d_h = 0.1$, d_h = 50mm, [15]

Thermochromic Liquid Crystal (TLC) was used and the resulting color plots of Nu/Nu_o are shown in Figures 3-33 – 3-39.

The color plot of the square rib tested at Re=20k with a P/e=12 is shown in Figure 3-33. The average heat transfer enhancement is 1.75. A careful inspection of the color plot shows an area just past the rib that does not transfer heat very well. As the flow progresses between the ribs the color plot shows increasing values of Nu/Nu_o followed by diminishing values. Then the flow seems to impinge on the leading wall of the rib causing an increase in heat transfer. The uniformity and even distribution of heat transfer is critically important to the blade designer. As the remainder of the color plots are examined, attention to these factors will play an important role in deciding which shape performs best.

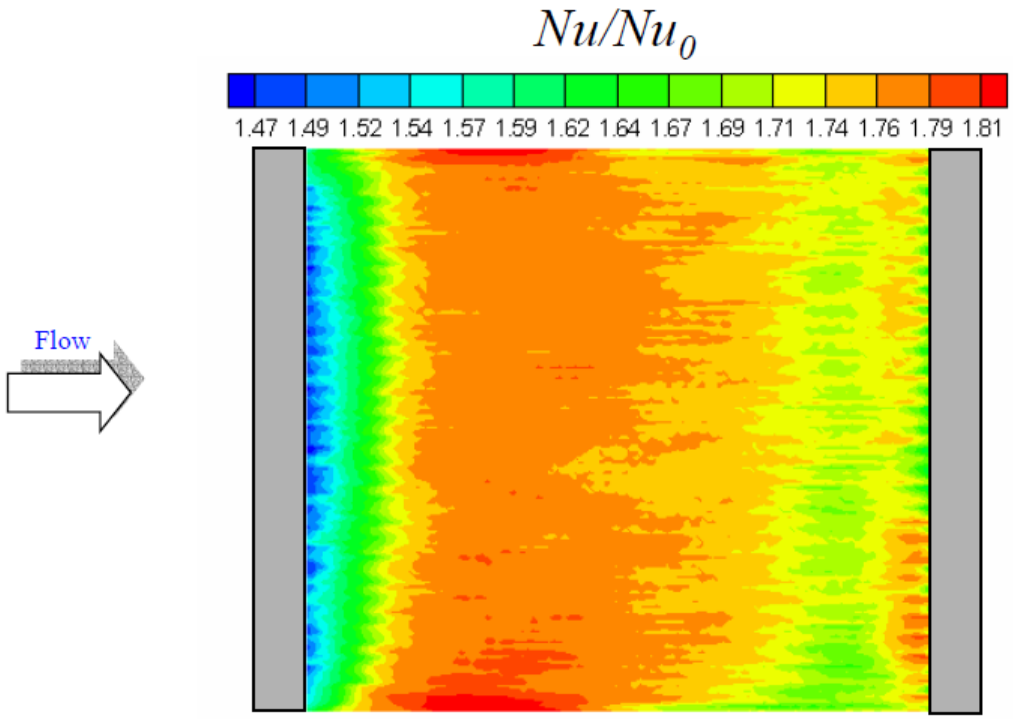

Figure 3-33 : Square Ribs, Re=20k, P/e = 12, Nu_{bar}/Nu_o = 1.75[15]

The triangular ribs performed similarly to the square rib with an average Nu/Nu_o value of 1.77 when tested with P/e = 12. A detailed look at this color plot in Figure 3-34 does not show the "impingement" region at the leading edge of the second rib.

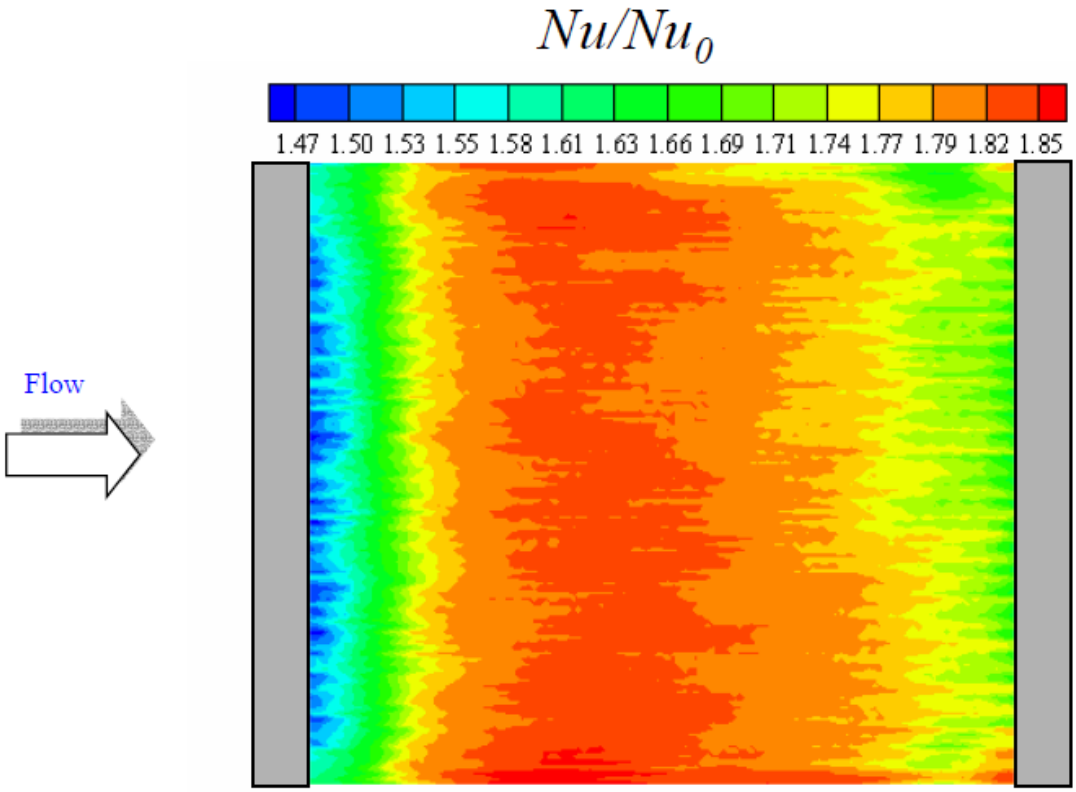

Figure 3-34 : Triangular Ribs, Re=20k, P/e = 12, Nu_{bar}/Nu_o = 1.77 [15]

The trapezoid rib shown in figure 3-35, tested under the same conditions as the previous two test shows a higher average Nu/Nu_o value of 1.85. The "dead" spot that immediately follows the first rib is still there, but the value of Nu/Nu_o is greater than the previous two color plots. The distribution of heat transfer is improved and the "impingement" on the leading edge of the second rib is present.

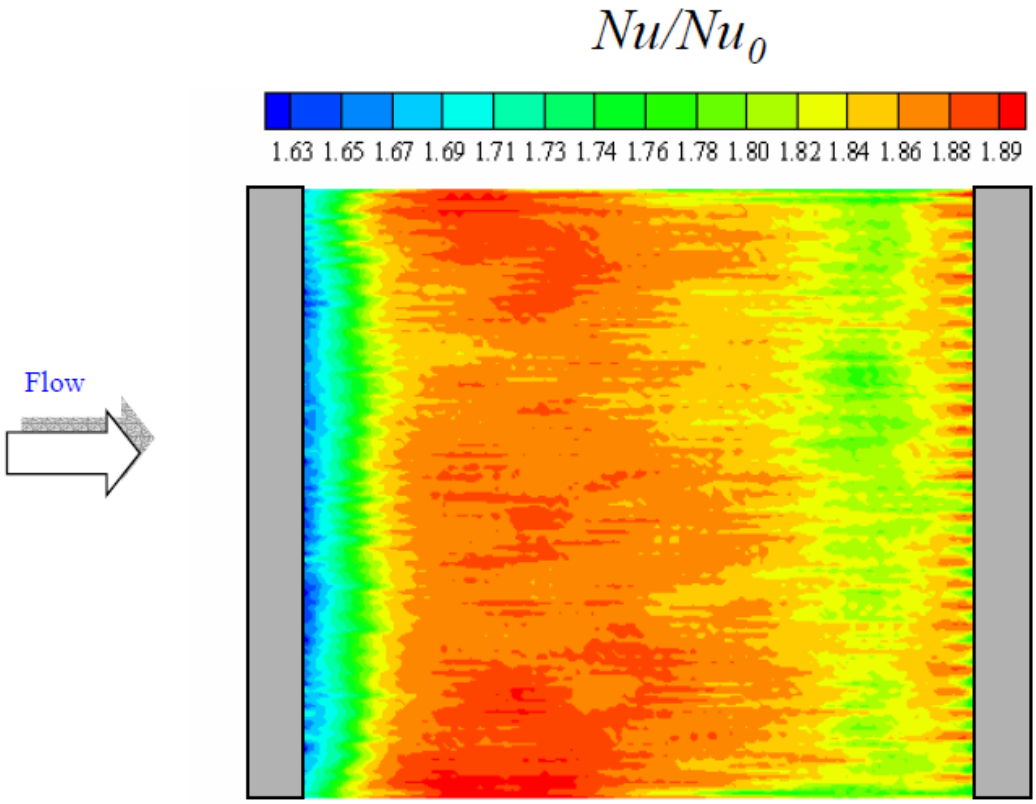

Figure 3-35 : Trapezoid Ribs w/ Decreasing Height in Flow Direction, Re=20k, P/e = 12, Nu_{bar}/Nu_o = 1.85 [15]

A thorough examination of the color plot of the trapezoid shaped rib with an increasing height in the flow direction is shown in figure 3-36. This configuration exhibited the worst average Nu/Nu_o value, 1.67. The "dead" area just past the first rib is much larger and the distribution of heat transfer is not nearly as uniform as the previous three contour plots. A blade with this rib configuration would exhibit on uniform cooling which may lead to premature failure. Other color plots are shown in the various figures below for comparison.

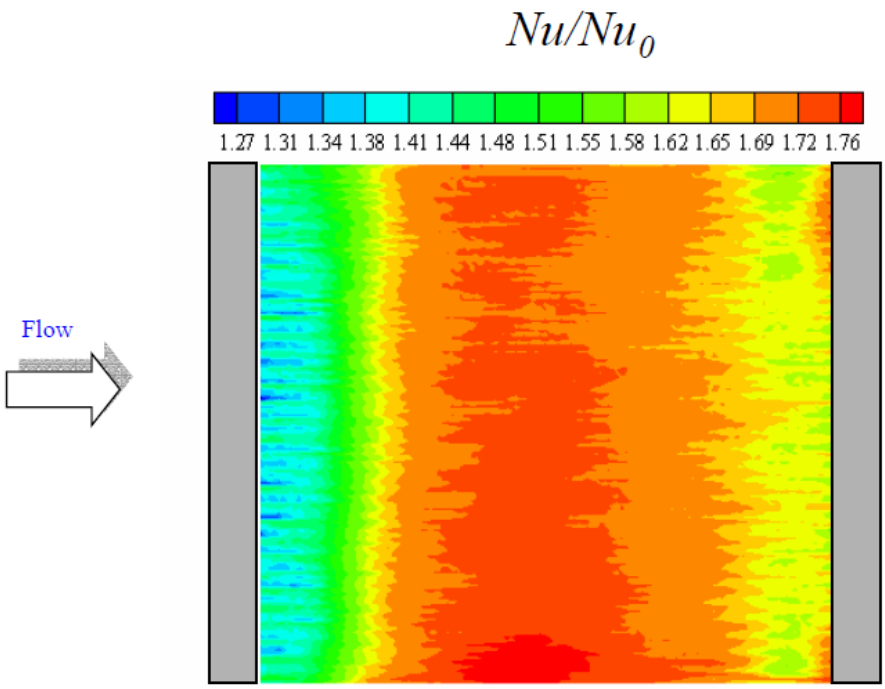

Figure 3-36 : Trapezoid Ribs w/ Increasing Height in Flow Direction, Re=20k, P/e = 12, Nu_{bar}/Nu_o = 1.67 [15]

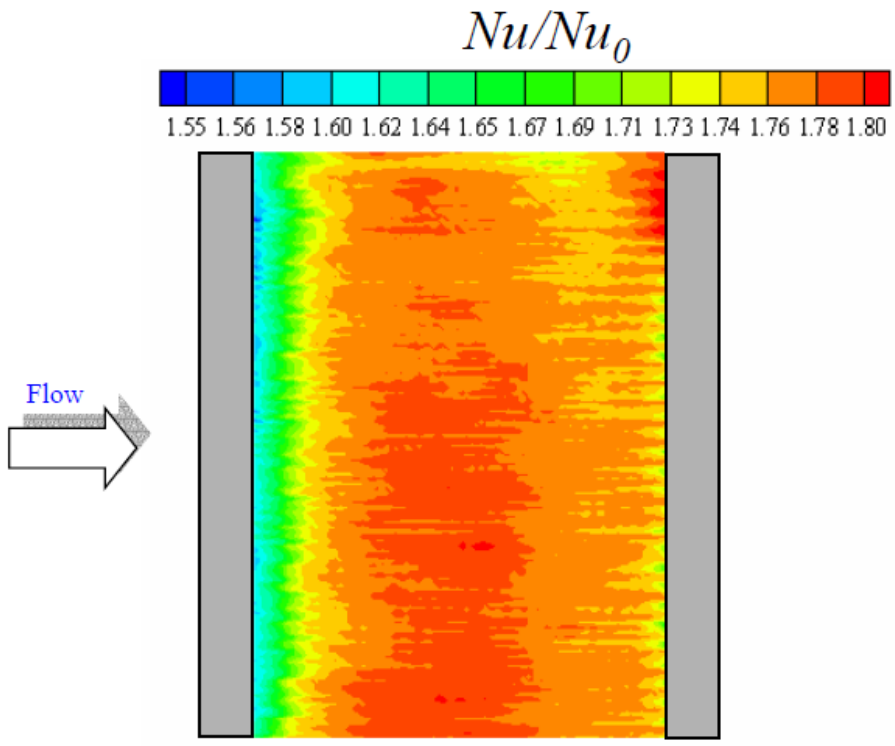

Figure 3-37 : Trapezoid Ribs w/ decreasing Height in Flow Direction, Re=20k, P/e = 8, Nu_{bar}/Nu_o = 1.77 [15]

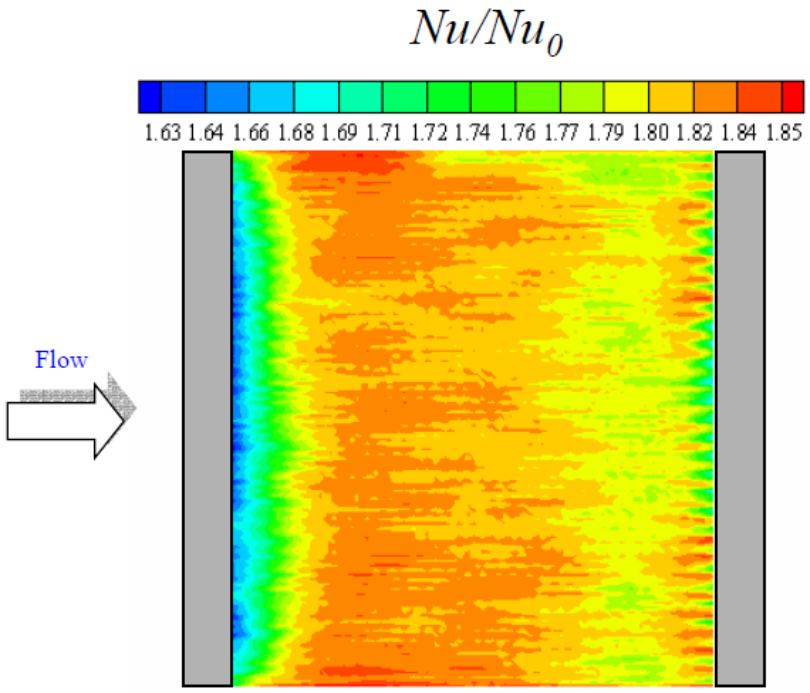

Figure 3-38 : Trapezoid Ribs w/ decreasing Height in Flow Direction, Re=20k, P/e = 10, Nu_{bar}/Nu_o = 1.81 [15]

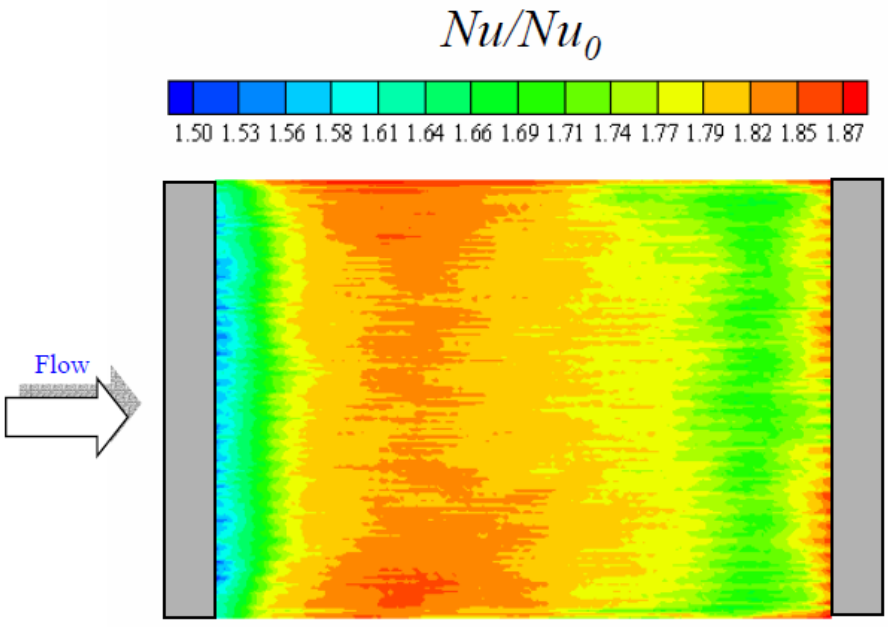

Figure 3-39 : Trapezoid Ribs w/ decreasing Height in Flow Direction, Re=20k, P/e = 15, Nu_{bar}/Nu_o = 1.76 [15]

Line plots of the normalized Nusselt numbers and the normalized friction factor are plotted against the P/e ratio are shown in Figures 3-40 and 3-41. While the trapezoid shape with decreasing height in the flow direction clearly seems superior with regards to heat transfer enhancement it should also be noted that the square rib performs as well when the P/e ratio is 10. Many other published papers conclude that a P/e ratio of 10 yield the best results.

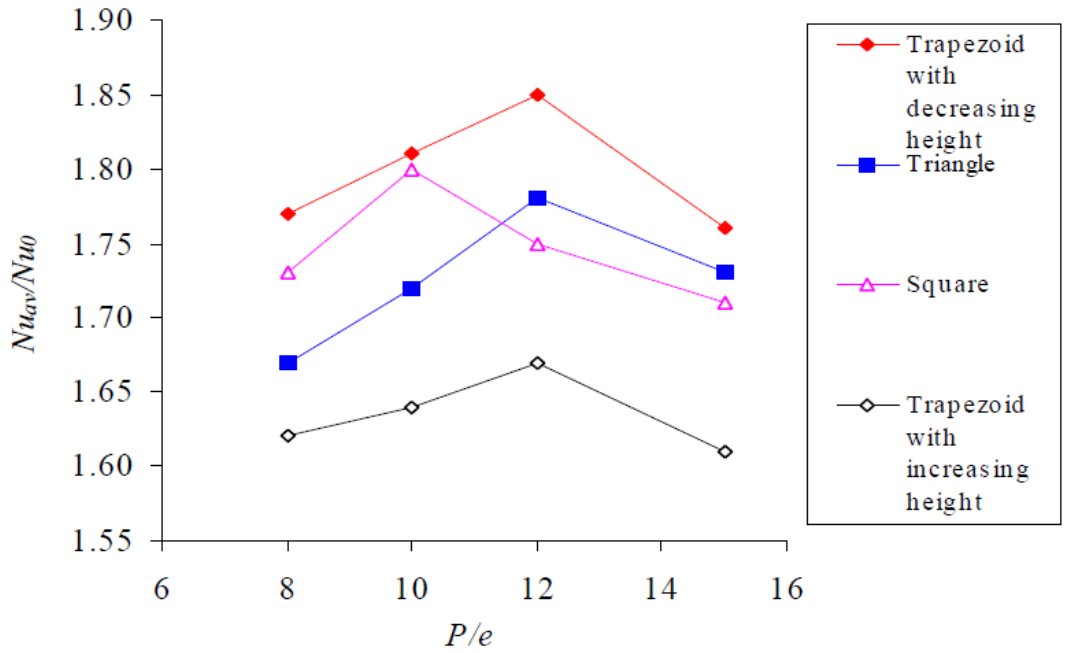

Figure 3-40 : Average Heat Transfer Enhancement for Various Shaped Ribs, Re=20k, [15]

A line plot of the normalized friction factor shows that the trapezoid shape with decreasing height in the flow direction yields the highest values with a slight dip in friction at a P/e ratio of 10. The square rib performed reasonably well as compared to the triangular and decreasing trapezoid rib.

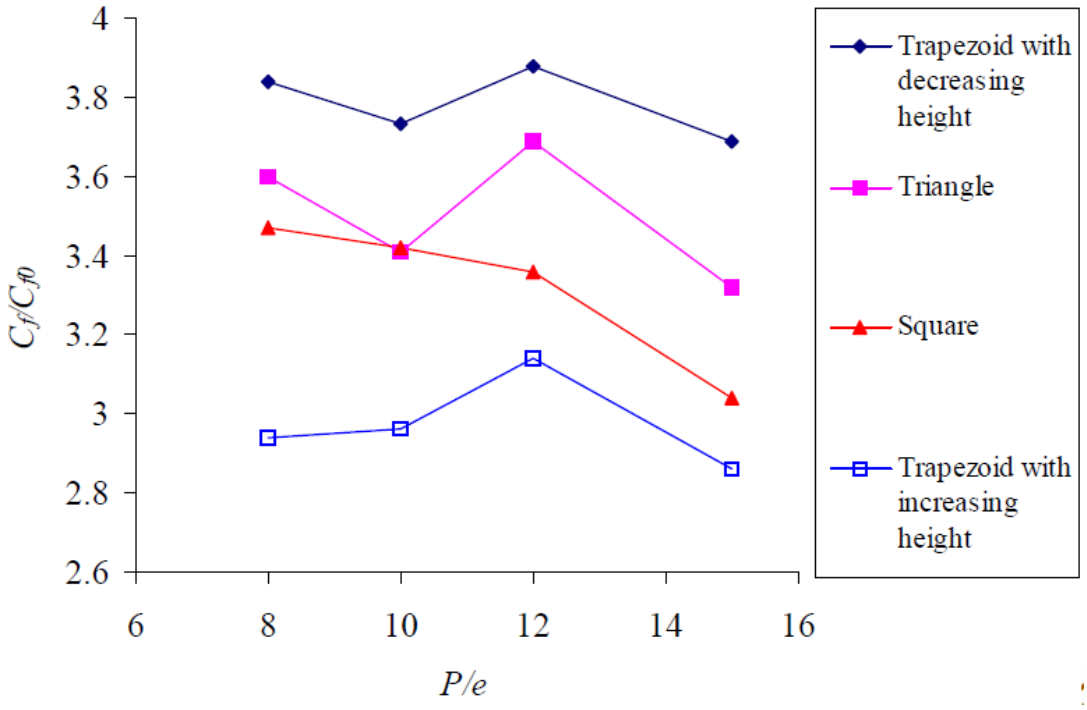

Figure 3-41 : Friction Factor for Various Shaped Ribs, Re=20k [15]

The results of both line plots are summarized in the table below.

Table 3-3 : Summary of test results showing: Nu_{avg}/Nu_o and C_f/C_{fo}

Rib Shape	Nu_{avg}/Nu_o				C_f/C_{fo}			
	P/e = 8	P/e = 10	P/e = 12	P/e = 15	P/e = 8	P/e = 10	P/e = 12	P/e = 15
Square	1.73	1.78	1.74	1.71	3.48	3.42	3.35	3.04
Triangle	1.66	1.72	1.78	1.73	3.60	3.42	3.37	3.05
Trapezoid w/ decreasing ht.	1.77	1.81	1.85	1.76	3.85	3.75	3.90	3.70
Trapezoid w/ increasing ht.	1.62	1.63	1.67	1.60	2.93	2.95	3.10	2.85

It is clear from this study that the shape of ribbed turbulators and the P/e ratio play an important role in the mean heat transfer enhancement and also in how evenly the heat is removed.

Jets

Jets can provide a local high heat transfer enhancement and are used in areas of the blade where high heat transfer is needed. The downside of using jets is the high pressure differential needed to create an effective impingement onto a surface. This is easy to accomplish in a lab, but may require specialized designs to be useful in an actual gas turbine engine. Film cooling holes are placed in many areas of a blade and use this concept to achieve localized cooling. However, this method is not popular in the mid-span region of the blade. There is very little published data that show impinging jets in the mid-span section.

When jets are used, a pressure differential must exist between the jet supply channel and the jet exit channel. The limiting factor with regards to this pressure differential is whether or not you can still meet 0% BFM (back flow margin). The back flow margin is an indicator of the likelihood that you would ingest hot gas into the blade instead of purging it out with cooling air.

The BFM at any point in the cooling circuit is the % coolant pressure above the gas static pressure at that point.

$$\%BFM = \frac{P_{int} - P_{ext}}{P_{ext}} * 100\%$$

P_{int} – Turbine blade internal pressure

P_{ext} – Turbine blade external pressure at the point of coolant exit (i.e. leading edge film cooling holes)

Controlling BFM can be a challenge to a designer. One method is to use a metering device in the main channel in order to decrease the pressure in that passage. This requires enough main cavity pressure to purge the rest of the blade and eventually exit the film holes. Minimum BFM can be set as low as 3%, with the engine operating in the worst case scenario, but generally the pressure coming into a stage one bucket is about 30% higher than the gas pressures coming into the leading edge of the bucket. As you move to the suction side and eventually the trailing edge, you may have as much as a 40% pressure margin.

Impinging Jets onto Dimpled Surfaces

One unique study performed by Kanokjaruvijit, et-al [16] tests the effect of using jets impinging on a recessed dimpled surface, subjected to cross flow. Dimples in cross flow have been studied in detail and are quite useful in gas turbine blades. Recessed dimples have very low friction losses and provide moderate heat transfer enhancement. Protruding dimples provided better heat transfer enhancement, but with much higher friction losses. In a simple dimpled duct with cross flow the dimpled surface caused the boundary layer to become detached from the surface and promotes turbulence. The ideal spacing of dimples is strongly dependent on the Reynolds number. Figure 3-42 shows the general layout of the coupled jet impingement/dimpled surface test.

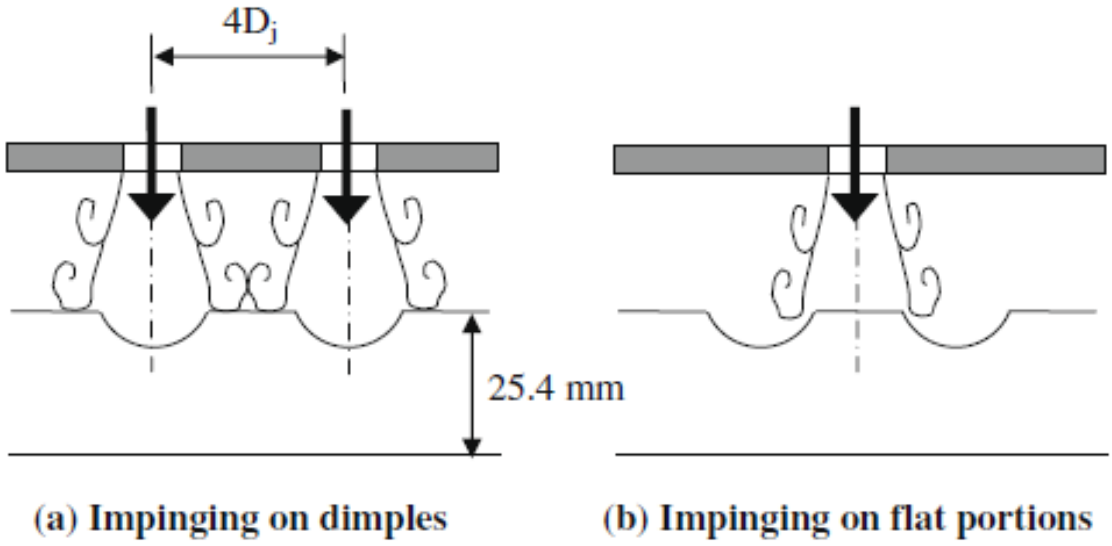

Figure 3-42 : Layout of impinging jets onto dimpled surfaces. [16]

Line plots of the stream wise average Nusselt number for two different dimple diameters verses dimple depths are shown in Figure 3-43. Whether the jet was directed into the dimple or between dimples the shallower dimples performed much better. The author suggested that this is due to better vortex source-sink features of the shallow dimples in crossflow.

Only one color contour plot was presented in the published paper. It is shown in Figure 3-44. The normalized average Nusselt number is not given for this plot, but a cursory examination would indicate that a mean Nu/Nu_o value in the range of 3.5 would be likely. The Nusselt number (Nu_o) value for a Reynolds number of 11,500 would be ~35. The location of the dimples are superimposed onto the color plot.

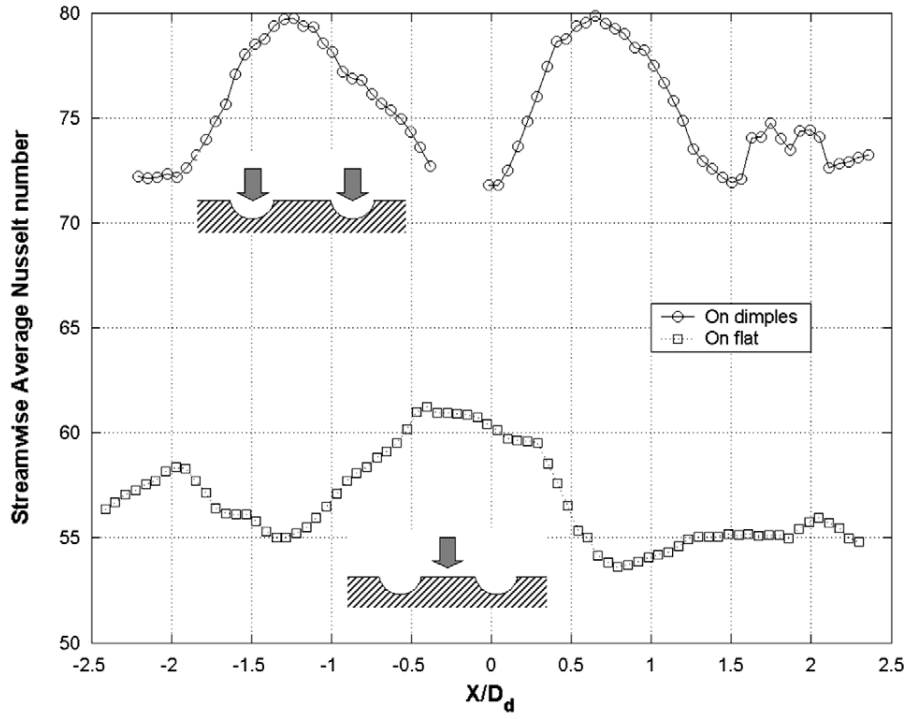

(a) $d/D_d = 0.25$

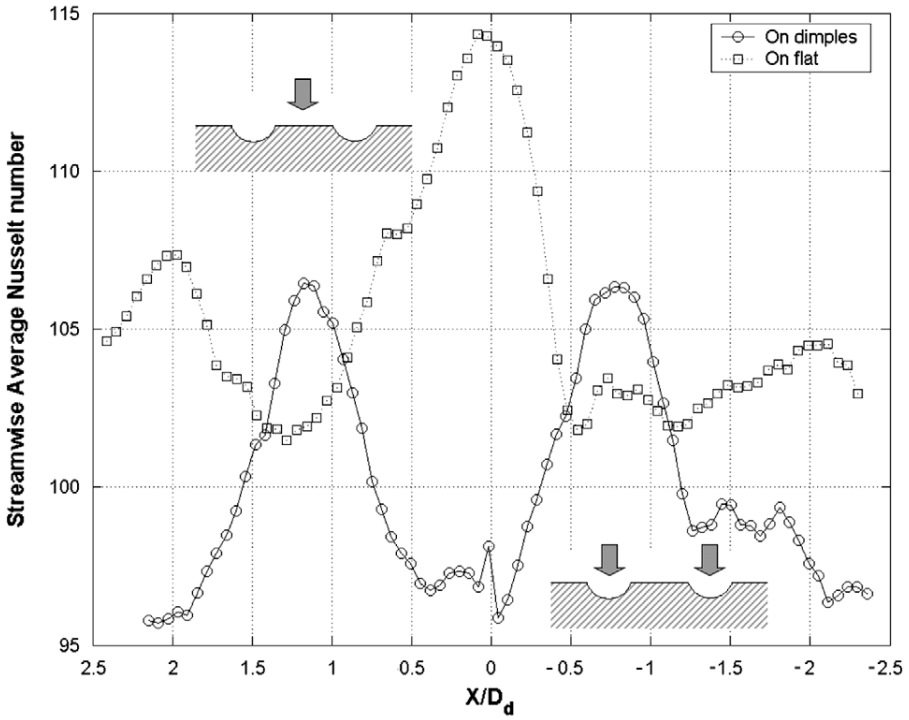

(b) $d/D_d = 0.15$

Figure 3-43 : Streamwise average Nusselt numbers of dimples at H/Dj = 2, ReDj = 11,500 and Dj/Dd = 0.50. [16]

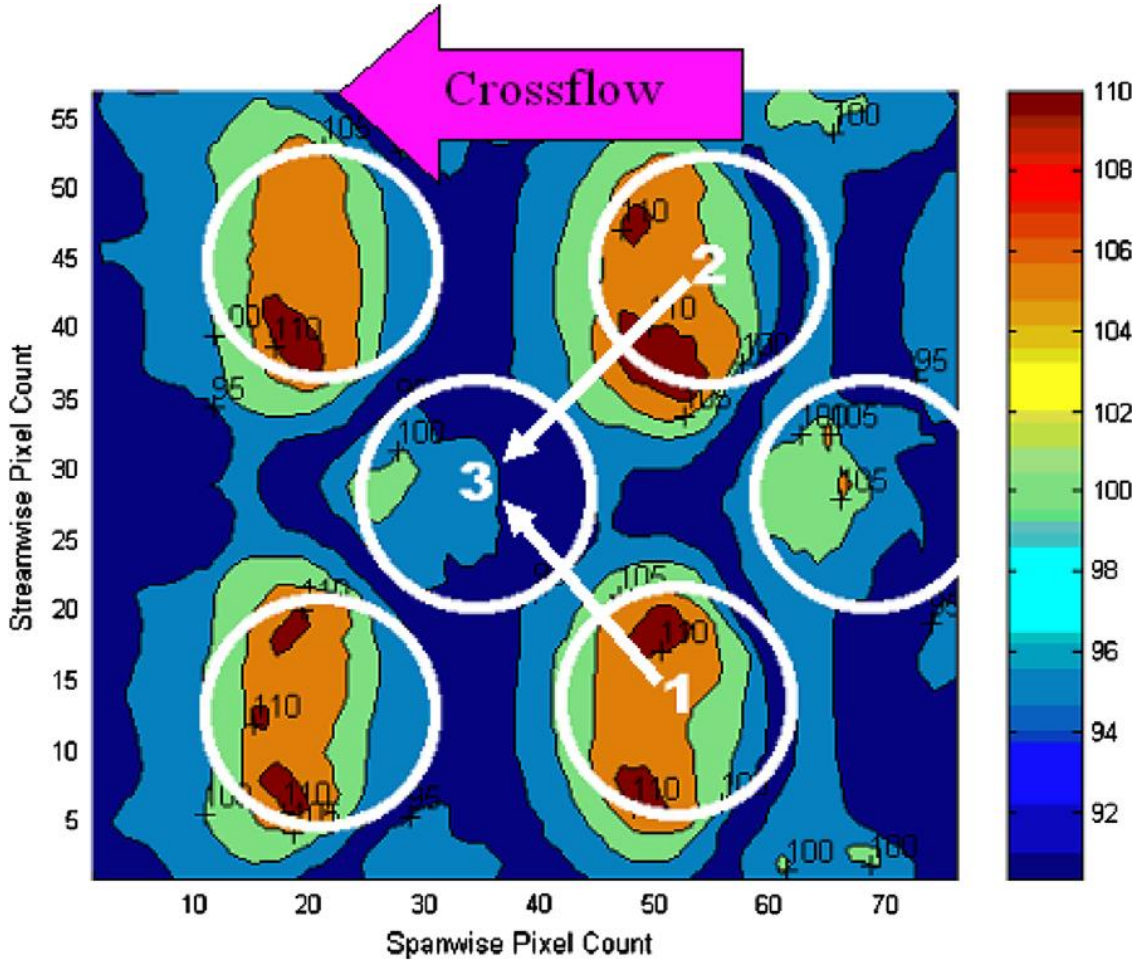

Figure 3-44 : Contour plot of Nusselt numbers of dimpled plate of 40 mm imprinted diameter and $d/D_d = 0.15$ at $Re_{Dj} = 11{,}500$, H/Dj = 2, impinging on dimples. [16]

Overall average Nusselt numbers are presented as a function of Reynolds number in Figure 3-45. The smaller H/Dj (channel height/jet diameter) performed better at all Reynolds numbers tested.

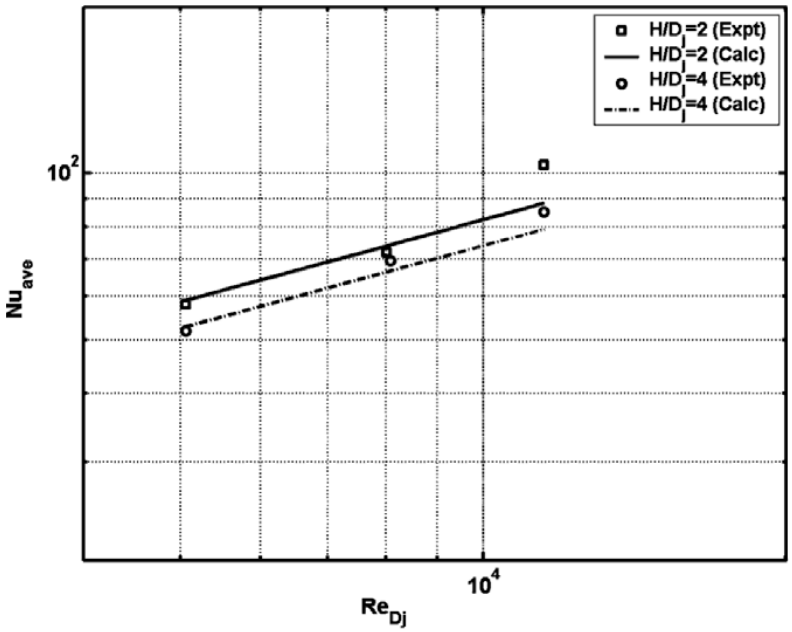

Figure 3-45 : Overall average Nusselt numbers as a function of Reynolds number for impinging on flat portions at H/Dj = 2 and 4 and d/Dd = 0.15. [16]

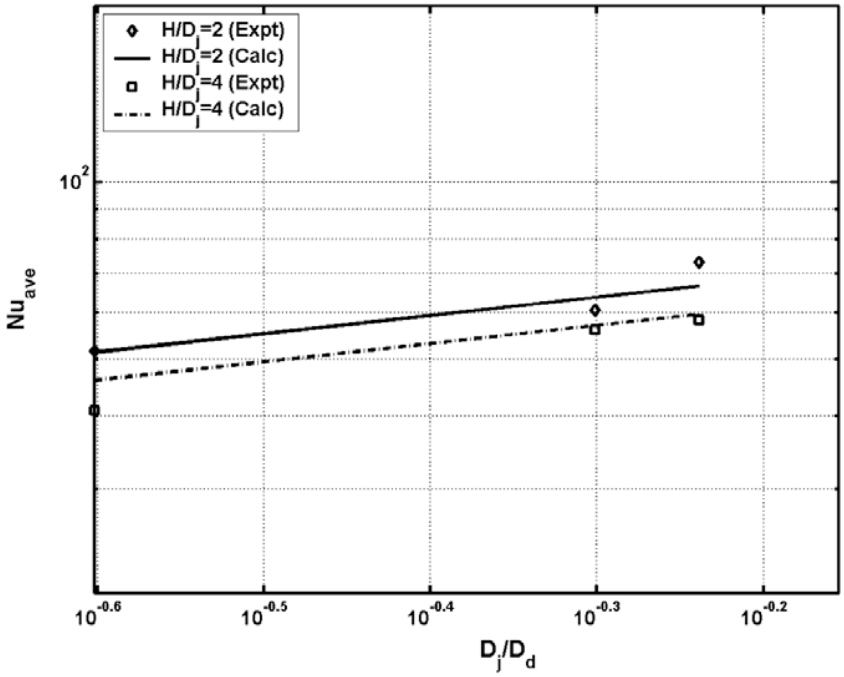

Figure 3-46: Overall average Nusselt number as a function of dimple curvature for dimple impingement at H/Dj = 2 and 4, ReDj = 11,500, d/Dd = 0.25, impinging on flat portions – both experimental data points and correlation curve are shown. [16]

The results presented in this paper are encouraging, but not enough information was provided regarding the blowing ratio or pressure losses to make an informed judgment as to the usefulness of this design.

Recent Patents

A detailed review of recently published patents was performed. Unlike the academic arena, there is no incentive in the private sector to publish the results of research. In most cases the internal research is purposely kept from the public and is considered proprietary. Some information can be gained by reviewing patents that are issued to private companies. Details of each patented designs performance is unknown. However, reviewing these patents can spark new ideas and promote discussion in the academic community that may lead to new and innovative designs. The patent sketches presented should do just that.

The vast majority of the patent sketches included were taken directly from patents that were issued in the past several years. A brief description of each is provided. The patentee is not required, and does not provide any information as to the effectiveness of the design or whether the design is actually being used in industry. An assumption has to be made that if the idea was patented by one of the major turbine engine manufacturers, the design must have some meaningful use and they chose to protect the rights to the design.

Only one patent drawing will be discussed and is shown in Figure 3-47. This patent takes advantage of several turbulence enhancements discussed in the previous sections. From the sketches provided it appears that the use of square shaped ribs are placed at an angle relative to the main stream flow. This style of rib, oriented at this angle has proved to be commonplace as superior

in many published papers. What is unique about this design is that in between the ribs, a series of small ribs of various shapes are inserted.

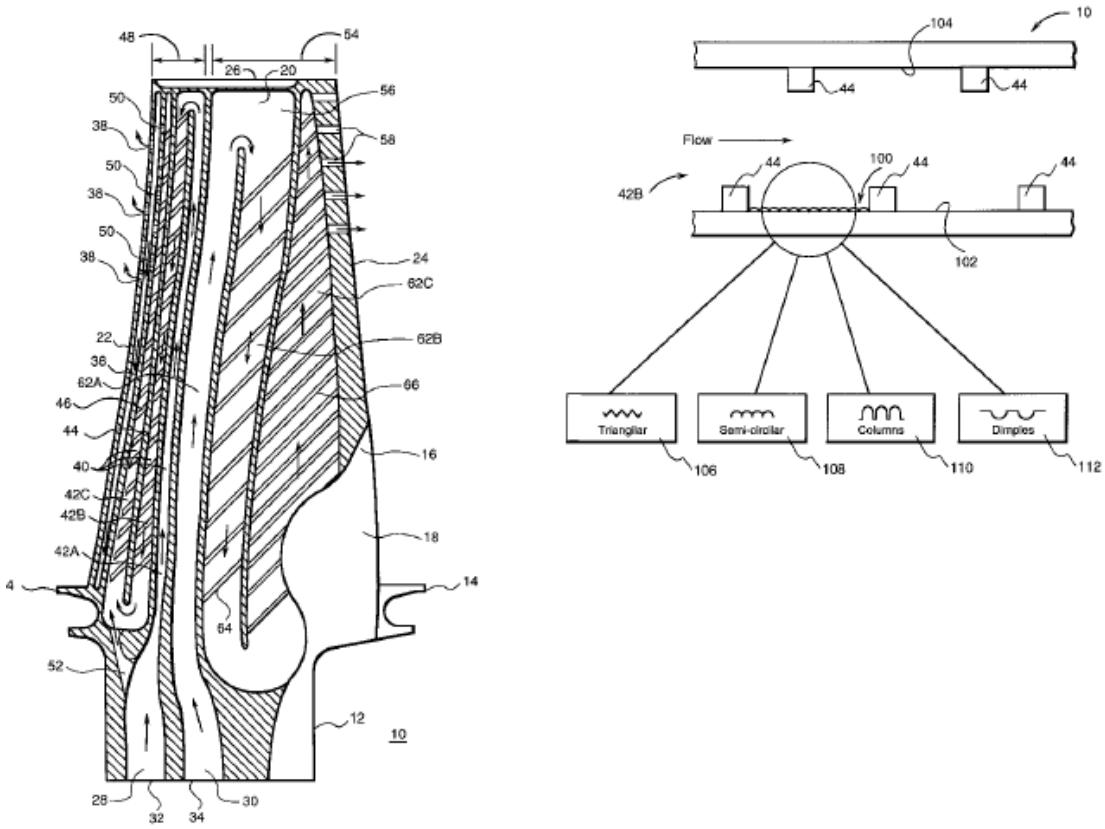

Figure 3-47 : United States Patent US5975850 showing multiple enhancements

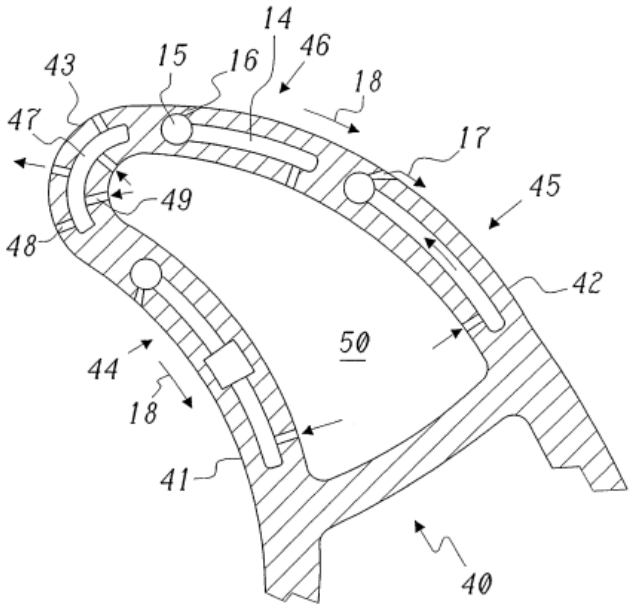

Figure 3-48 : Lutum, E. , US Patent 6,379,118, 2002, jet impingement into an outer channel

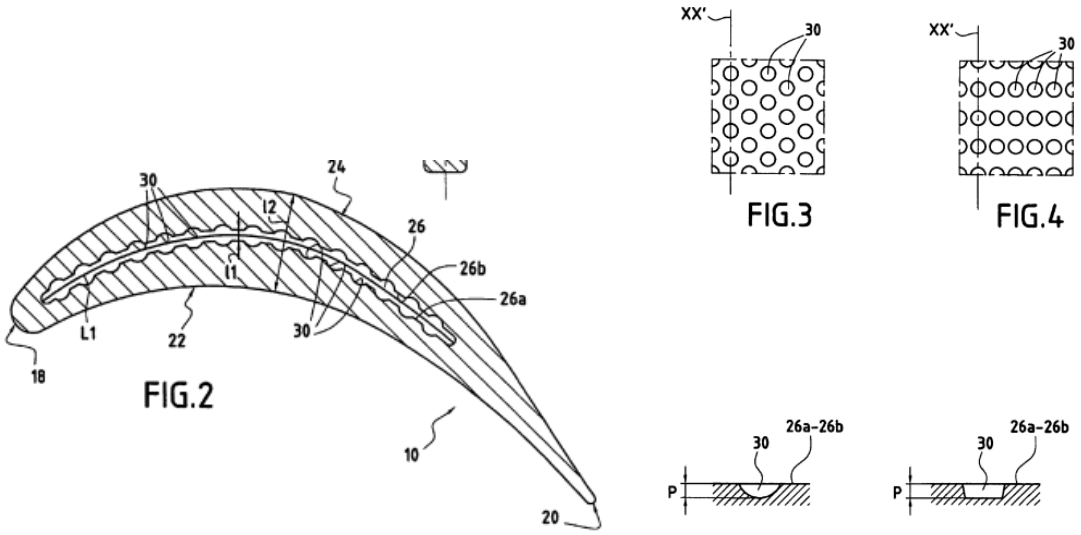

Figure 3-49 : High aspect ratio passage with dimples. Daux; Stephan, US Patent 7,513,737, 2009

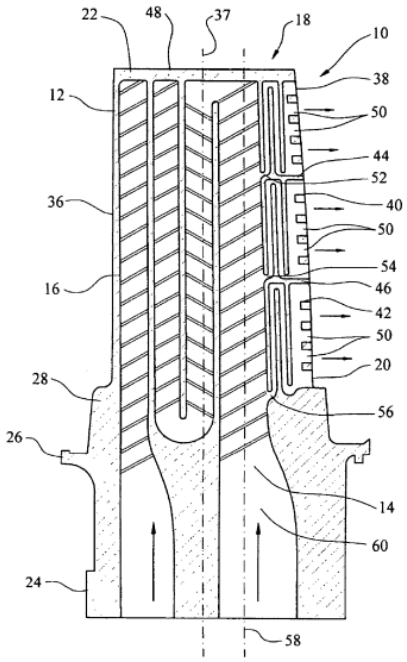

Figure 3-50 : Multiple channels with individual cooling controls. Liang; George, US Patent 7,435,053, 2008

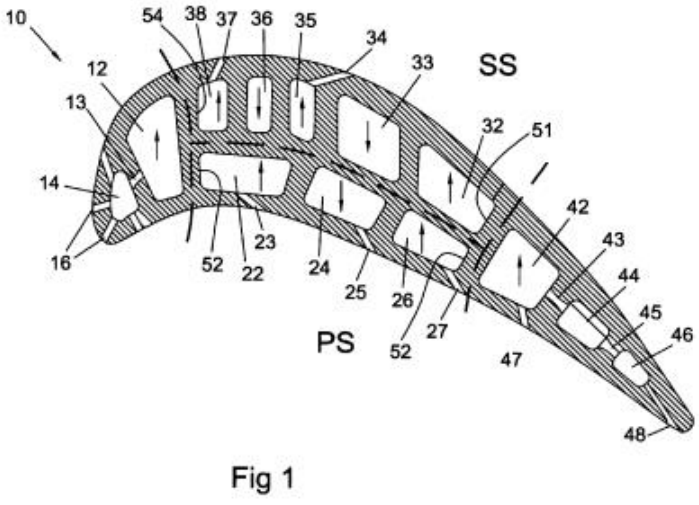

Fig 1

Figure 3-51 : Multiple channels with individual cooling controls.

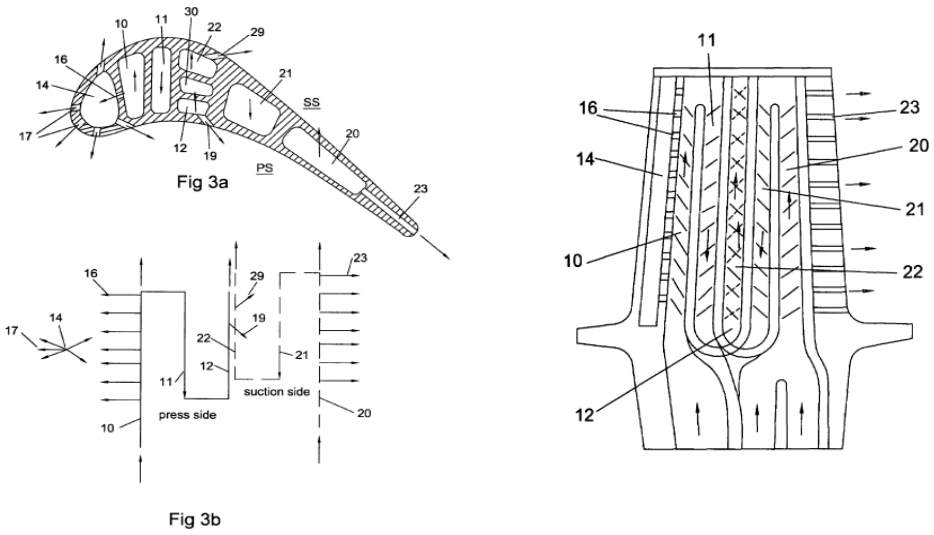

Figure 3-52 : Multiple channels with serpentine passages

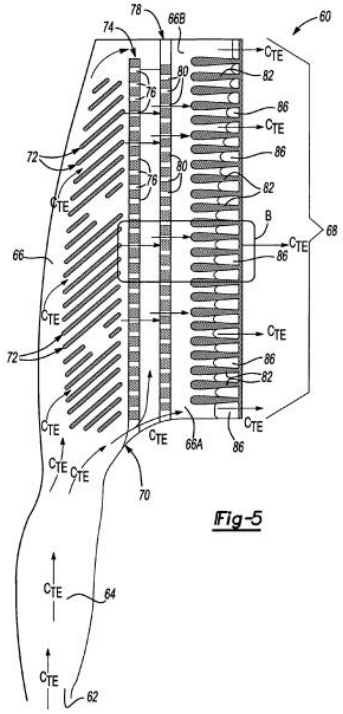

Figure 3-53 : Ribbed channels with impingement jets along the trailing edge.

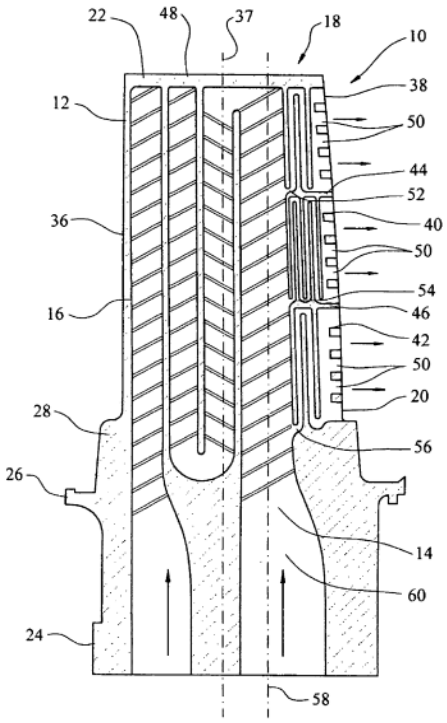

Figure 3-54 : Serpentine passages with trip strips

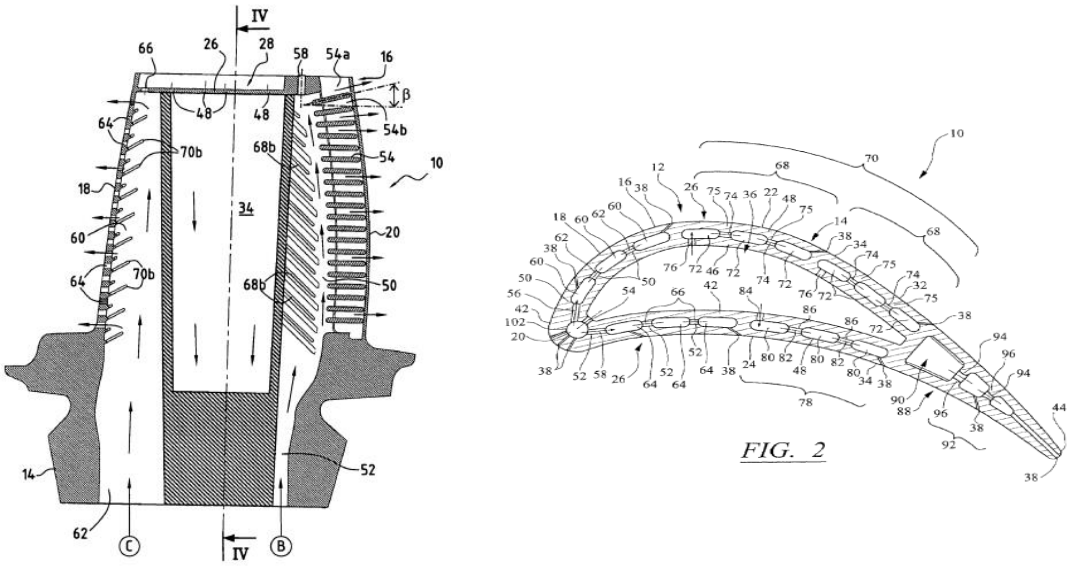

Figure 3-55 : Large high aspect ratio main channel with jets feeding small outer channels

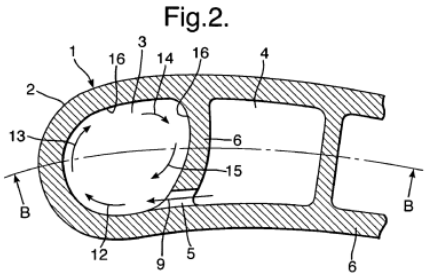

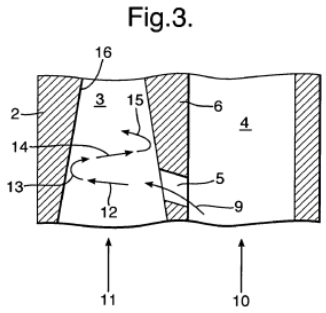

Figure 3-56 : Helical Swirl at leading edge.

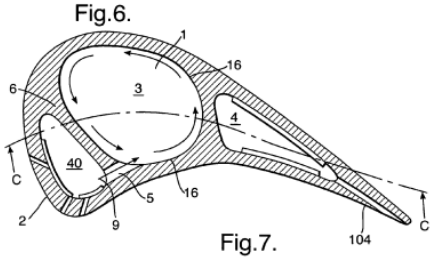

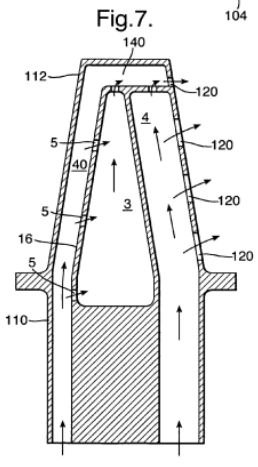

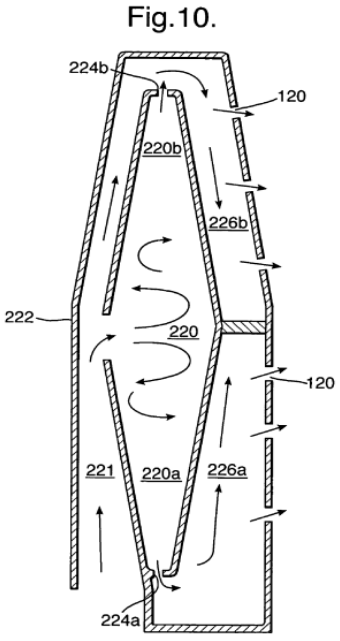

Figure 3-57 : Helical swirl at mid-chord.

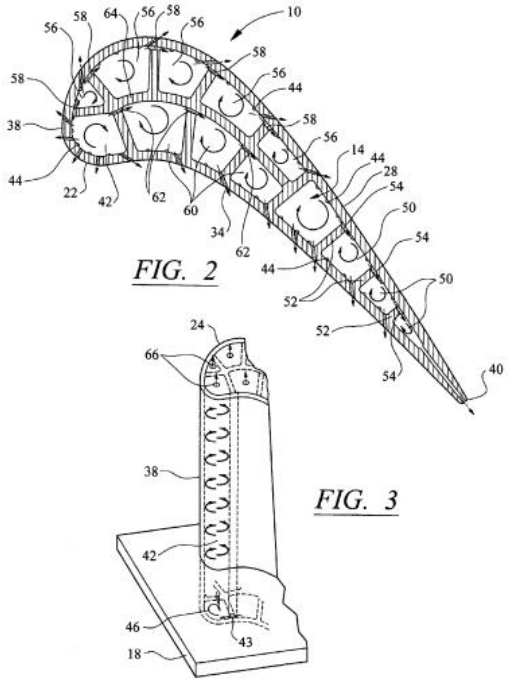

Figure 3-58 : Swirl enhanced cooling throughout

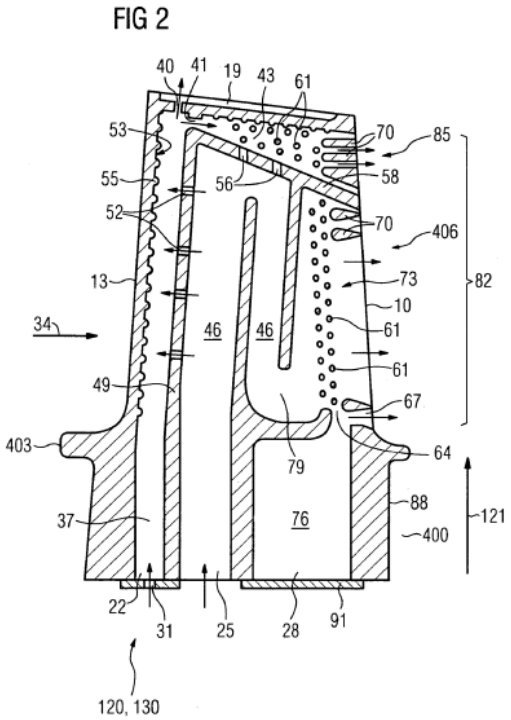

Figure 3-59 : Leading edge impingement cooling

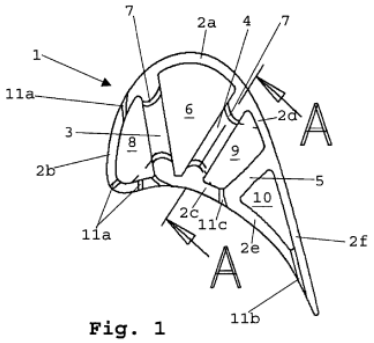

Fig. 1

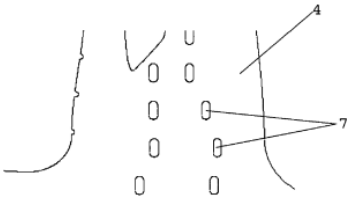

Fig. 2

Figure 3-60 : Impingement cooling using channel crossover jets

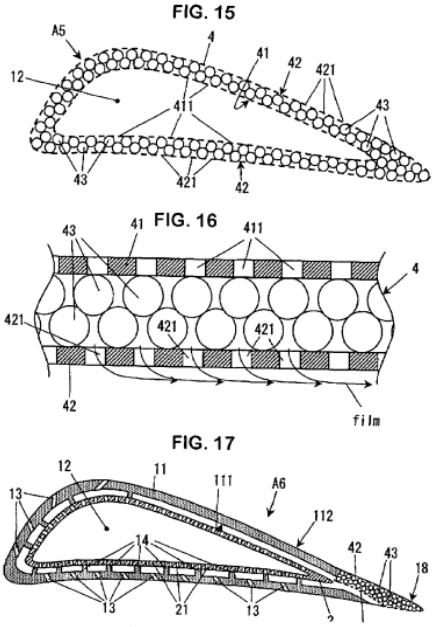

Figure 3-61 : Large Main Channel with impingement jets on outer channel.

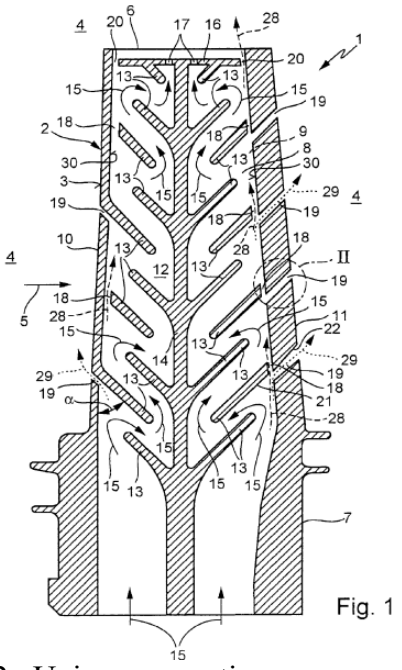

Figure 3-62 : Unique serpentine passage with trip strips

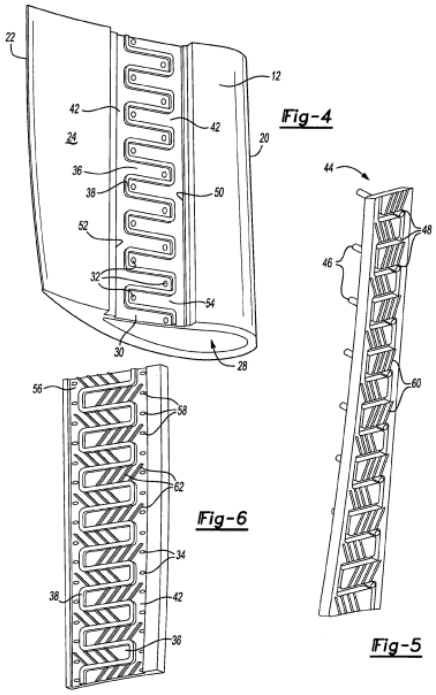

Figure 3-63 : Serpentine passage with saw tooth grid structure.

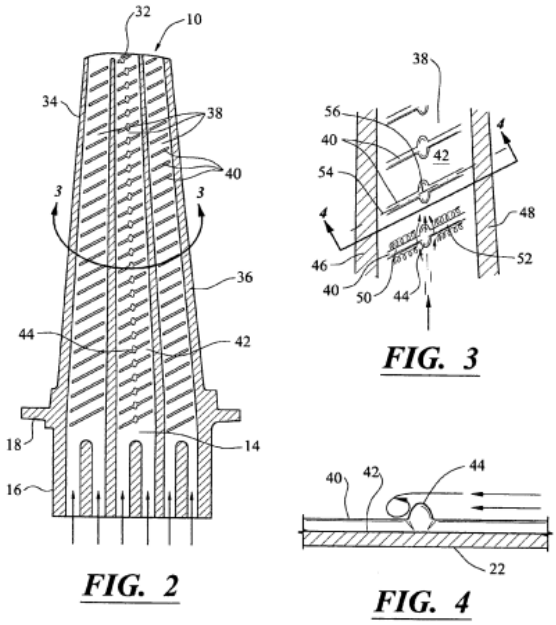

Figure 3-64 : Trip strips with vortex shedding devices.

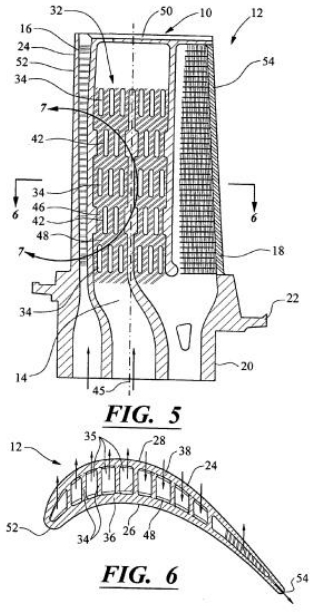

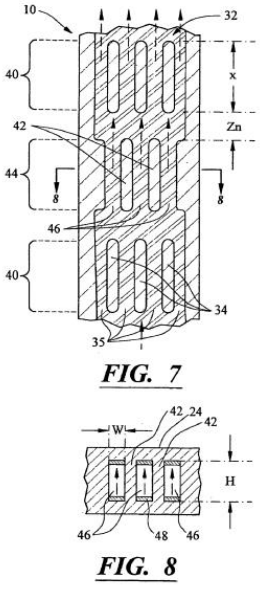

Figure 3-65 : Micro-channels with trip strips.

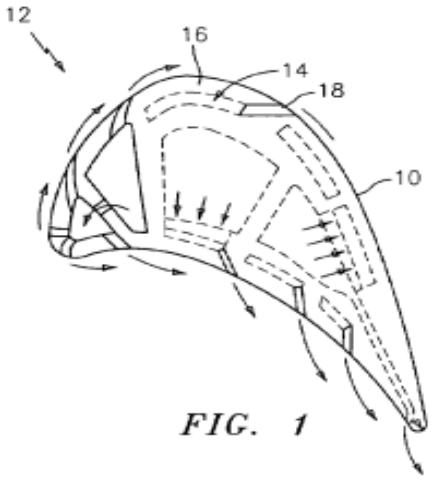

FIG. 1

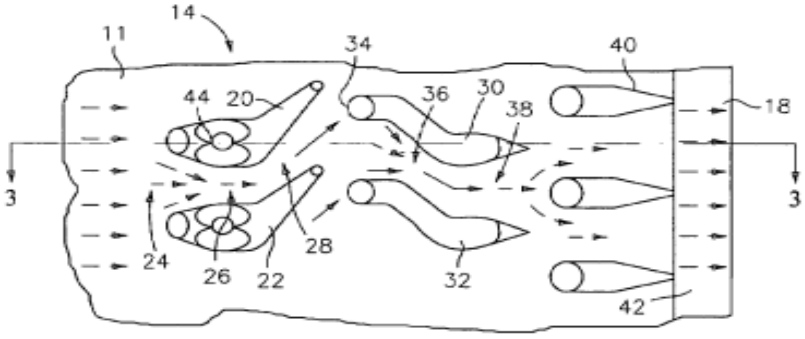

FIG. 2

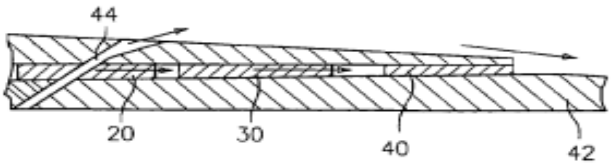

FIG. 3

Figure 3-66 : Low aspect ratio main channel feeding non-uniform micro-circuits.

A Rolls Royce publication provides a graphical representation of the number of patents issued by the turbine engine manufacturer. The bar charts are presented here in order to get insight into the number of patents issued and a sub-category showing the number of patents issued related to cooling or insulation in the turbine engines.

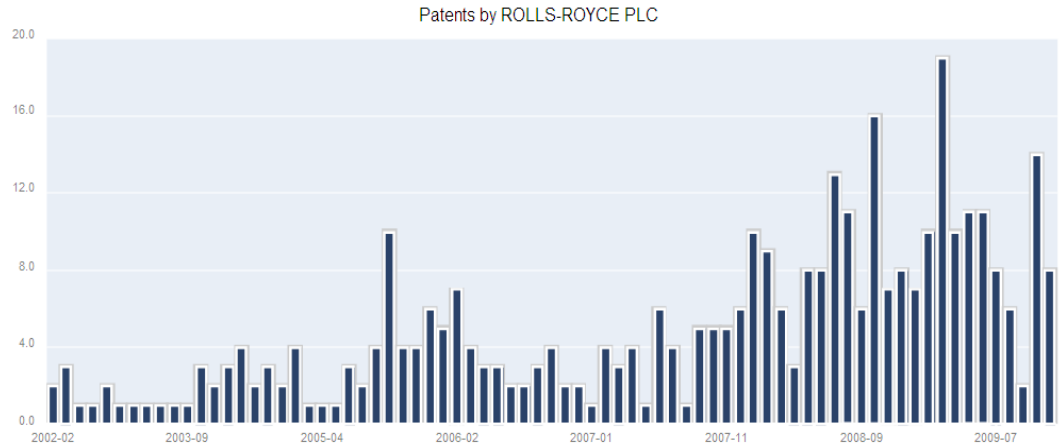

Figure 3-67 : Number of patents issued to Rolls Royce from 02/2002 – 07/2009 [Courtesy of Rolls Royce].

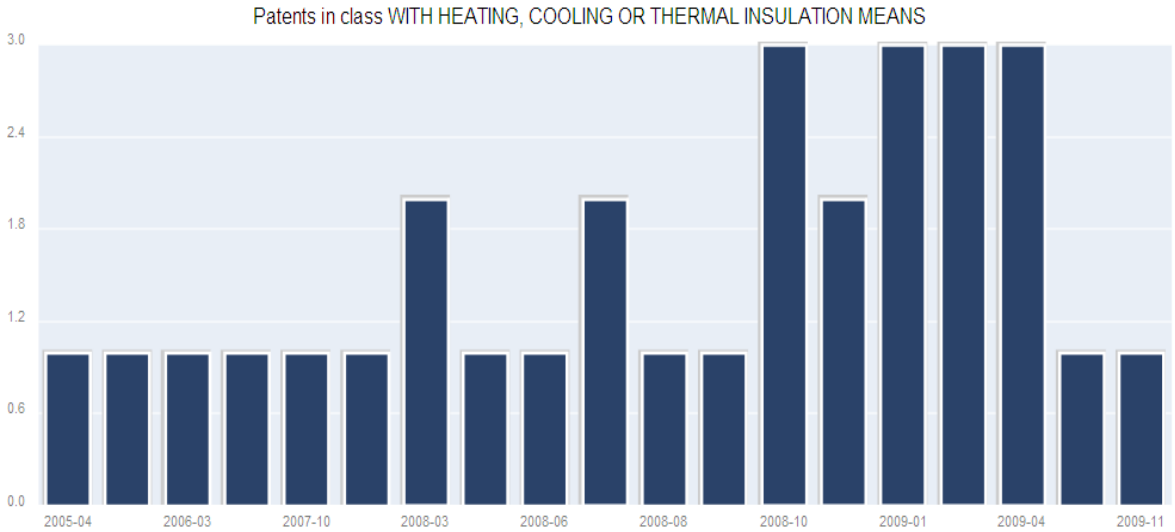

Figure 3-68 : Patents pertaining to heating, cooling, and insulation issued to Rolls Royce from 04/2005 – 11/2009 [Courtesy of Rolls Royce].

Chapter 4 – Goals

After careful examination of a wide variety of recent methods and configurations used in mid-span cooling of first stage turbine blades it was decided that two different new and innovative methods would be investigated.

Figure 2-6 made clear the benefits of using swirl enhancer, as these tended to have high Nusselt values while displaying low friction factors. It was also apparent from recently issued patents that mid-span cooling passages were seldom rectangular. Unfortunately, most published literature performed test using either rectangular channels when studying cooling enhancements in the mid-span of the blade or used round cross-sections when studying leading edge cooling enhancement strategies. The literature also made it clear that the shape (aspect ratio, etc.) of the passage was a sensitive to small changes.

In order to build on the latest technological advancements and to more closely simulate actual mid-span cooling passages a slot shaped passage was chosen. Heat transfer enhancements would come as one of two different approaches. The first would be the application of trapezoid shaped trip strips that progressed along the walls of the slot channel in a helical fashion. The trapezoid shape proved beneficial in the study performed by Wang [15] in a rectangular passage when placed at a 90 degree angle to the flow direction. Other studies used square or triangular shaped trip strips at different angles to the flow direction and saw positive results with angles less than 90 degrees. It was hoped that the helical strips placed at varying angles to the crossflow air would generate two different scenarios inside the passage. The first being that the trip strip would interrupt the boundary layer being formed along the wall and cause a recirculation zone and flow reattachment

after contacting the trip strip. This is a typical situation observed in rectangular channels with trip strips oriented in various configurations. In most studies performed in rectangular channels there are no trip strips placed on two of the four walls of the channel. In the proposed slot shaped channel the helical trip strip would be attached continuously to all walls as the trip strips progressed along the channel. The other condition that may occur is that the helical strips would change the direction of the flow as the air contacted the angled strip and cause the flow to swirl as it progressed through the passage. The combination of air tumbling as the crossflow air encounters the protruding trapezoid shaped trip strip and the air swirling as it contacted the angled helical strips could be the magic combination that brings turbine blade cooling enhancements to the next level of technological advancement.

The second strategy is to use jets issuing from side channels along the floor of the slot shaped channel to introduce a high velocity shear condition. The issuing jets would be angled into the crossflow air in such a fashion as to introduce a continuous swirling motion as the jet air progresses through the channel. Previous graduate students at LSU have studied this phenomenon in a rectangular passage with positive results. It is proposed that the jets issuing along the floor of the passage could act like a trip strip and cause the main channel air to tumble as it comes in contact with the high velocity jets. The situation would then be similar to the helical trip strips in that the main channel air would tumble as it contacted the high velocity jets along the floor of the passage and the angle of the jets would cause the air to swirl as it progressed along the slot shaped passage.

In keeping with known values that have yielding positive results the pitch between trip strips and the height of the trip strips/jet hole diameter will provide a P/e ratio of 12. Other common attributes

such as channel aspect ratio (AR) and channel height to trip strip height (e/b) will be kept at 3:1 and 0.1 respectively. Reynolds numbers will be in the range of 10,000 to 50,000. These are in line with the majority of published literature on internal turbine blade cooling.

Figure 4.1 shows a transparent view of the fluid passages and other features used in various tests. The green and red lines show locations of passages used to transfer high pressure air to the main slot shaped channel. The yellow spirals show a typical placement of trip strips. The grey spiral lines show the anticipated swirl and tumble pattern of the air as it encounters the various turbulence enhancing mechanisms.

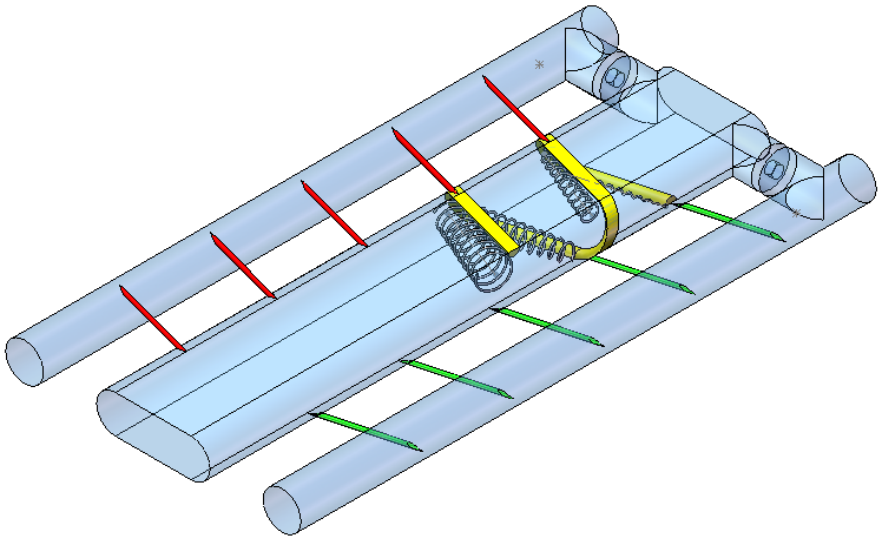

Figure 4-1: A generic 3-D transparent view of the fluid passages used in the various test.

Chapter 5 – General Methodology and Procedures

Facility

All testing to date was performed in the Engineering Research and Development Building, Room 240. The facility is supplied with compressed air at rates up to 5 lb/sec (2.27 kg/s) and 146 psig (10 bar). Dwyer's rotometers are used for flow measurements and calibration procedures per Dwyer's recommendations are followed. Pressure measurements are made using Dwyers hand held pressure gauges for pressure in excess of 5" H_2O. Pressure readings less than 5" H_2O are taken with an inclined manometer which is properly leveled and zeroed per the manufacturer's requirements. Both digital cameras are Sony model 430 SD and are capable of taken video images at 15 Hz or 30 Hz. The thermocouples used are listed as "fine wire" and "foil type" type K thermocouples. The maximum resolution is 20 Hz. All test performed were performed at 15 Hz in order to coincide with the camera and thermocouple limits and capabilities. A National Instruments Data Acquisition system is used to read thermocouple data. This data is written to an Excel file and stored for use during analysis. The video files are downloaded to a Virtual Dub software program where the video file is converted to individual image files. The image files are stored for processing. Two separate AC power supplies are used to power two inline "torch" style air heaters. The power supplies are capable of each supplying approximately 1500 W to the torch heaters.

Procedure

Before the test procedure can be described in detail a thorough understanding of the Thermochromic Liquid Crystal technique will be presented.

Liquid Crystal Technique

Liquid crystal is thought to have been discovered about 150 years ago. Sometime in the middle of the 19th century researchers discovered that nerve fibers excreted a fluid substance that exhibited a strange behavior when viewed through a polarized lens. This phenomenon occurred as the substance went through a phase change from liquid to a crystalline solid. It took almost 100 years before scientist realized the benefit of liquid crystals.

Liquid crystals are also not quite liquid and not quite solid. They are flow like liquids, but they have some properties of crystalline solids. Liquid crystals can be considered to be crystals which have lost some or all of their positional order, while maintaining full orientational order. The most common types of liquid crystal are nematic and smectic liquid crystals. Each possesses slightly different properties.

Nematics are polarized rod-like organic molecules on the order of 20 Angstroms in length. Smectic Liquid crystals are different from nematics in that they have one more degree of orientational order than do the nematics. Smectics generally form layers within which there is a loss of positional order, while orientational order is still preserved.

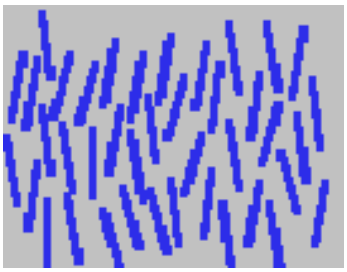

Nematic Liquid Crystals

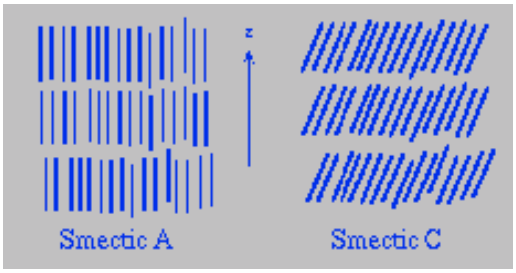

Smectic Liquid Crystals

Figure 5-1 Orientation order of various types of liquid crystals.

There are several different categories to describe smectics. The two best known of these are Smectic A, in which the molecules align perpendicular to the layer planes, and Smectic C, where the alignment of the molecules is at some arbitrary angle to the normal.

Liquid crystals are useful because they exhibit mechanical properties of a liquid, but have the optical properties of a single crystal. Temperature changes can affect the color of a liquid crystal, which makes them useful for temperature measurement.

The simplified definition of liquid crystal thermography (LCT) is that it correlates a color response of a heated surface treated with Thermochromic Liquid Crystal (TLC) to a change in temperature. Thermochromic Liquid Crystals (TLC) are materials that change their reflected color as a function of temperature when illuminated by white light. They reflect visible light at different wavelengths. The resolution of liquid crystal sensors is in the 0.1°C range.

Heat Transfer Measurement and Thermal Mapping

The most popular method is to use microencapsulated TLC applied directly to the surface of the test specimen. An alternate method is to use coated polyester sheets containing microencapsulated TLC mixtures; with or without adhesive backing.

Basic Procedure

One advantage of TLC is the simplicity of use when measuring surface temperature. The basic test procedure is as follows.

- Select the optics suitable for the spatial resolution required.

- Select the appropriate liquid crystal and calibrate it.
- Coat the test specimen with black paint.
- Spray the test specimen with liquid crystal.
- Invoke a temperature gradient to the test specimen and start the measurement.

A more detailed explanation of an actual test will be discussed later.

Basic Analysis

Cursory measurement can be done by visual observations. A more detailed scientific measurement requires the color/temperature relationship. To obtain a temperature measurement with LC, we must know the relationship between temperature and color response (calibration).

Types of Liquid Crystals

TLC is available in several forms and each has its advantages and disadvantages. Encapsulated liquid crystal material is encapsulated in a 5-10 micron sphere suspended in a water based binder material. This is the most popular type of TLC used. Because each droplet is encased in its own sphere, it prohibits crystallization of the mixture. The microcapsules of different TLCs can be mixed together to produce a formulation that displays color changes in multiple temperature ranges.

Another type of TLC is unencapsulated. The material is in its native form and is susceptible to contamination, however, once applied, produces brilliant colors. TLC is also available in coated (printed) sheets. These sheet contain the TLC applied to a polymer sheet

Designation of Thermochromic Liquid Crystals

When purchasing or using TLC, there is a standardized method of identification. The system utilizes a two color/temperature nomenclature. An example is given below.

Example:

– R40C5W , implies, activation (red color) temperature at 40ºC, a 5W implies start of Blue at 5ºC above Red.

– 5W can be a crude estimate of bandwidth of the liquid crystal

i.e., a 40 to 45ºC compound. Beyond the rated range the material will not exhibit any colors to the naked eye.

TLC is available in “narrow-band” and “wide-band” formulations. When the formulation range is 2º C or less it is designated as “narrow-band”. More than 2º C is designated as “wide-band”.

Example:

– R35C1W describes a TLC with a red start 35°C and a bandwidth of 1°C

i.e. a blue start 1°C higher, at 36°C; G100F2W describes a TLC mixture with green start temperature at 100°F and a bandwidth (red start to blue start) of 2°F.

Temperature Range

TLC is available from -30° C to 120° C, and bandwidths from 0.1° C to 30° C. According to Advanced Thermal Solutions, with a Liquid Crystal Thermography (LCT) system, the range is expanded to 180° C. The resolution of liquid crystal sensors is in the 0.1°C range.

Temperature Color Relationship

The following chart shows the temperature/color relationship of a particular TLC.

Table 5-1 : Temperature/Color Relationship for 40.5 C TLC (chart courtesy of Advanced Thermal Solutions)

T(C)	Red	Green	Blue	Hue	Saturation	Intensity
39.9	107.881	115.662	93.13	81.92725	30.02203	105.5577
40.2	97.013	194.411	73.189	137.7078	101.4411	121.5377
40.3	82.043	195.849	82.042	138.7264	80.62878	119.9767
40.4	77.524	183.403	103.029	129.9105	92.05212	121.3187
40.5	76.838	167.748	126.139	118.8215	96.44293	123.575
40.6	77.547	152.984	149.791	108.3637	99.01782	126.774
40.7	78.146	143.139	161.472	101.3901	98.81294	127.585
40.8	79.067	132.841	175.107	94.09571	98.71083	129.005
40.9	80.288	119.712	188.993	84.796	97.10431	129.664

A temperature, 39.9° C, is recognized by a system with RGB values as 107.9, 115.7 and 93.1. Hence, for qualitative measurement, a system is required to translate the RGB values into actual temperature.

Measurement Process

The following steps highlight the procedure for using TLC in thermal mapping.

Calibration

Clean the surface of sample test piece. Apply a uniform coat of the TLC to the surface. Apply a black paint over the TLC coated surface. Subject the treated surface to known temperature levels, then measure and record the color response of the TLC.

Additional Requirements

A uniform white light source must be available and focused on the specimen.

Specimen preparation

To ensure good measurement, the goal is to have a smooth and contaminant free calibration and the test specimen surfaces. This results in more brilliant colors and accurate measurement.

Preparation Process

Clean calibration and the test specimen surfaces (if possible) with alcohol and ensure that surfaces are dry. Apply a “thin and uniform” coat of black paint to the test specimen and the calibration surface (place them side by side). Dry the surfaces with a hot air gun at a mild temperature. Spray or apply the desired TLC material to both surfaces simultaneously.

Lighting and Light Source

A bright and stable white light source is required to obtain accurate and reliable reflected light intensity from a TLC coated surface. The light source must be void of infrared (IR) and ultra-violet (UV) radiation. Any IR energy present in the incident light will cause radiant heating of the test surface. Extended exposure to UV radiation can cause rapid deterioration of the TLC surface. This causes the surface to produce unreliable color-temperature response performance. Consistent light source settings and lighting-viewing arrangements between calibration and actual testing are essential to minimize color-temperature interpretation errors.

Table 5-2 : Comparison of Narrow-Band and Wide-Band Techniques [Courtesy of Image Therm Engineering, Inc.]

Comparison of Narrow-Band and Wide-Band Techniques		
	Advantages	**Disadvantages**
Narrow-band	High Accuracy absolute and relative temperature measurements can be readily obtained	Construction of an isotherm pattern can be tedious and time-consuming.
	Inexpensive implementation requires simple image processing systems	Full-field capabilities of the TLC coating are not utilized.
Wide-band	Uses the TLC's bandwidth to map the entire isotherm pattern of a surface from a single image	Robust TLC color-temperature response calibration is necessary for high accuracy measurements.
	Preferred in applications having large temperature variations which require high spatial resolution	More expensive to implement because more sophisticated image processing systems are required.

Advantages and disadvantages of using narrow- and wide-band TLC formulations in LC thermography systems.

Ref. Image Therm Engineering, Inc.

Experimental Set-up

The sketch below shows the basic components and layout for a static TLC test.

Air enters the system and is heated. Initially, the heated air is diverted away from the test piece. The temperature of the test piece is allowed to normalize prior to the start of the test. Thermocouples inside the test piece are available to monitor the air temperature as heated air is routed through the test piece. A digital camera is positioned on each side to capture the image as the wall temperature of the test piece changes through the temperature "band" of the TLC. Cold cathode fluorescent lamps (CCFL) are placed in front of the test piece to illuminate the TLC coated surface. The data acquisition board captures the thermocouple data and merges it with the images captured by the digital camera software.

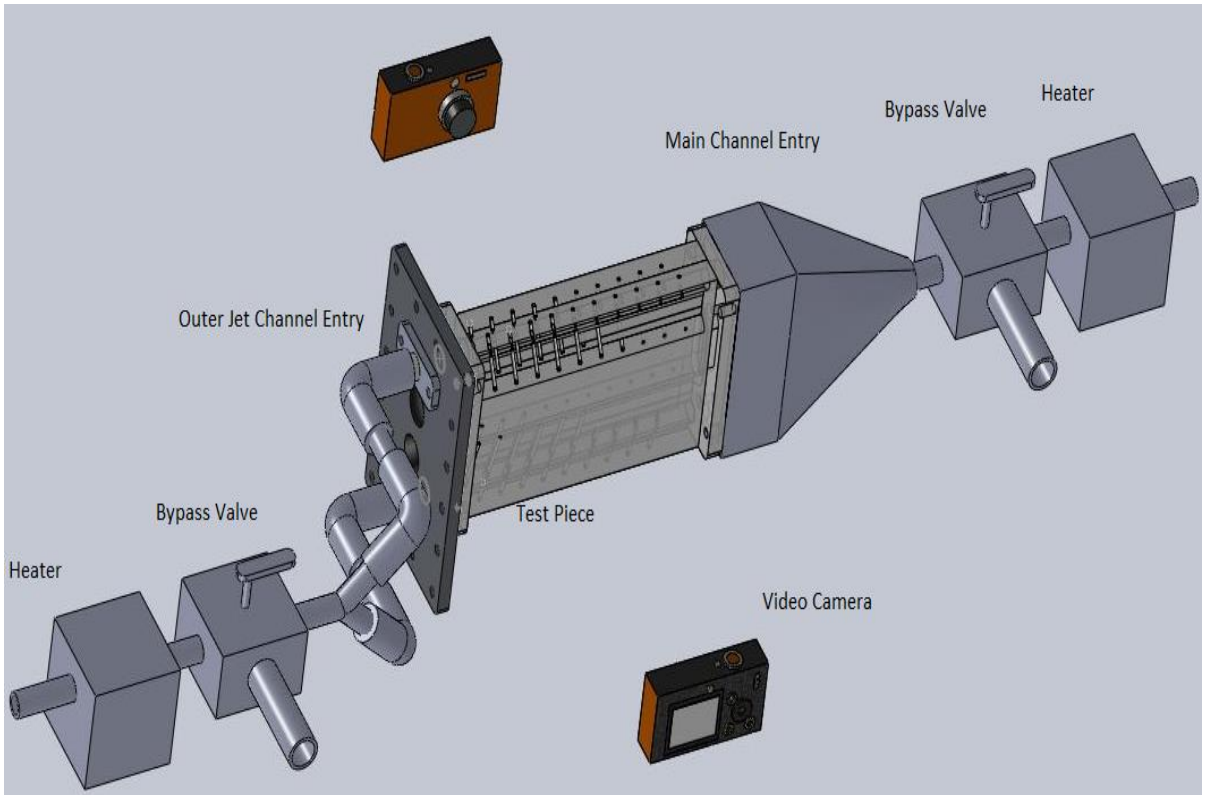

Figure 5-2 : Test set-up for stationary test with center inlet flow into the main channel.

Capturing the Images

The following images show an actual captured image superimposed onto the CAD model of the test piece.

The images are captured by the Digital camera software and each pixel is stored for analysis.

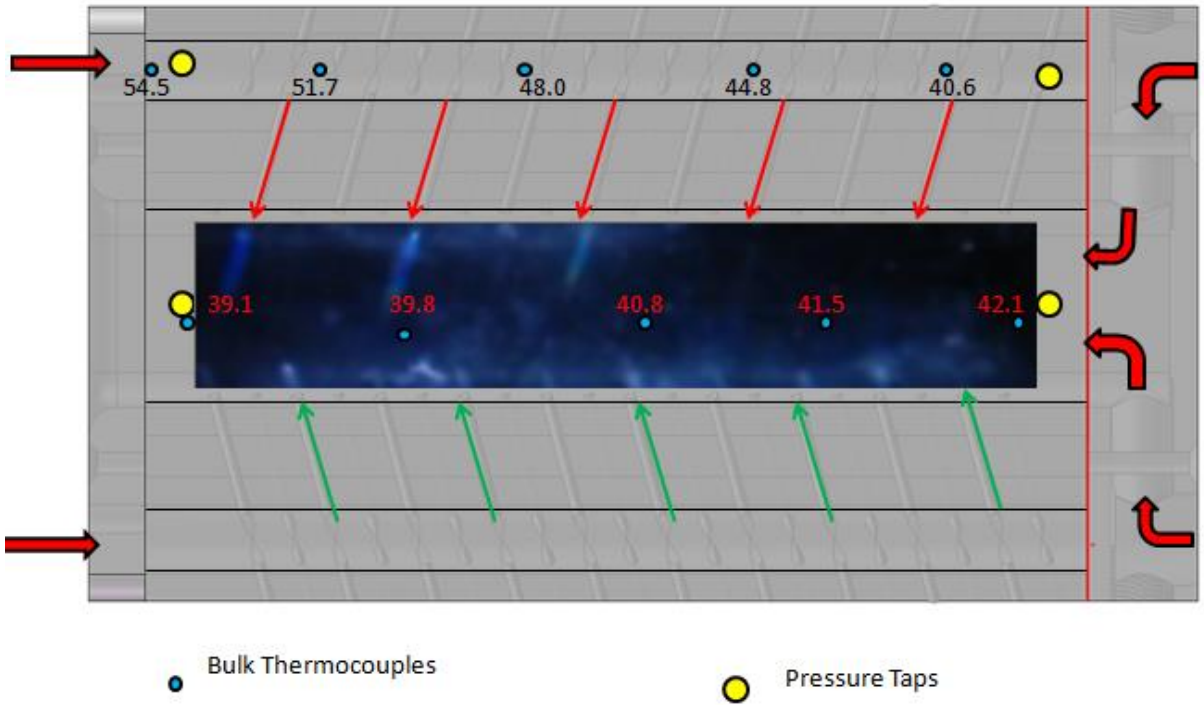

Figure 5-3 : Video image superimposed onto CAD drawing of test piece showing temperature of bulk thermocouples as related to TLC image. Jet Configure “B”, Re=25k, Blowing Ratio = 17.5, time = 5 sec

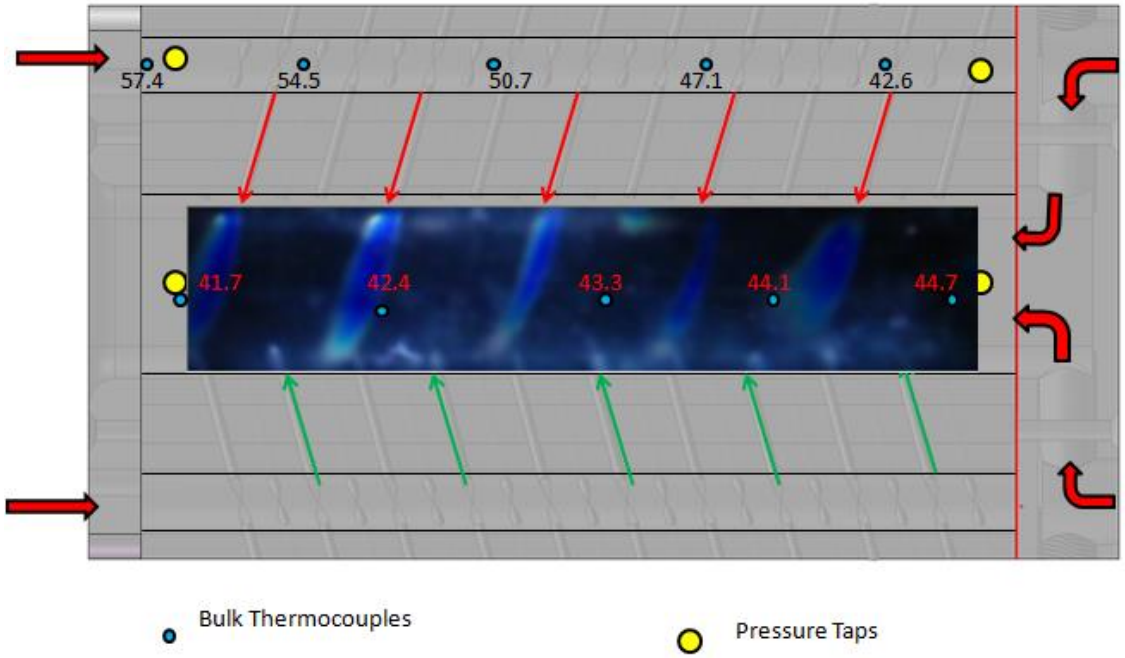

Figure 5-4 : Same as Figure 5-1, except time = 10 sec..

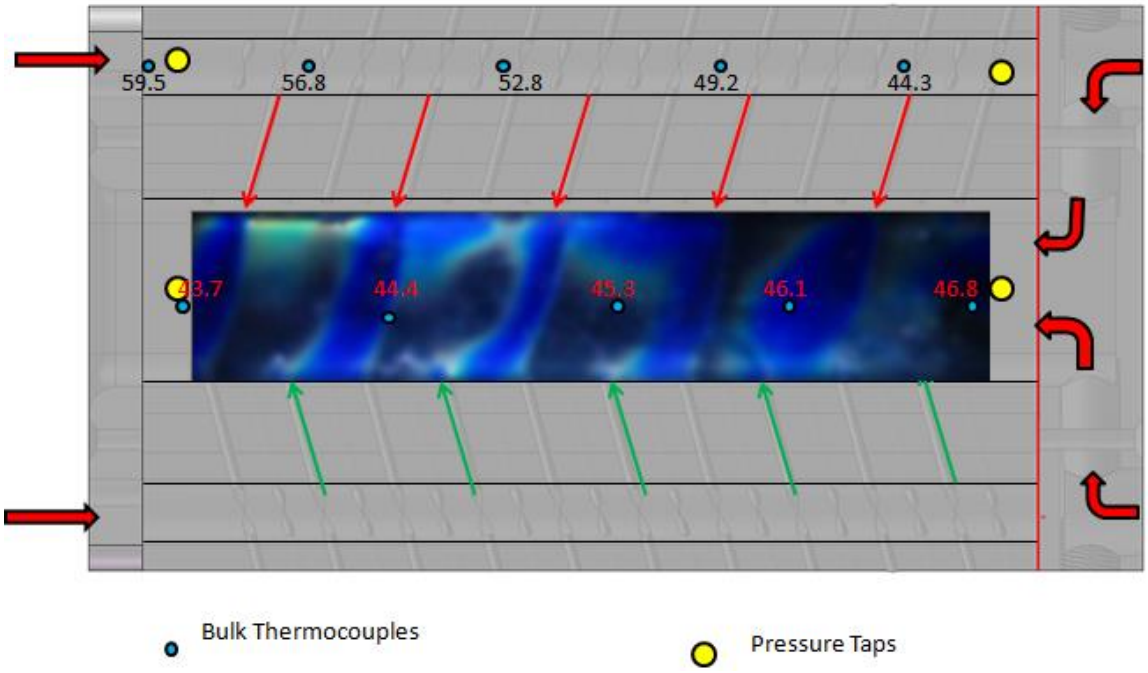

Figure 5-5 : Same as Figure 5-1, except time = 15 sec..

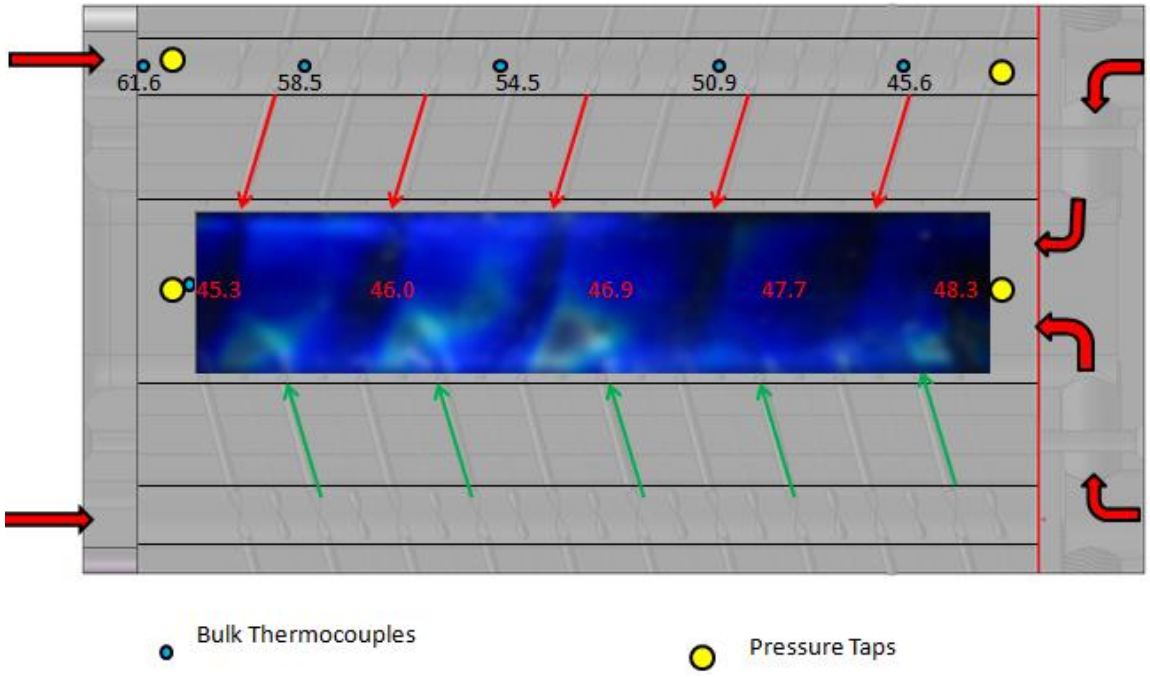

Figure 5-6 : Same as Figure 5-1, except time = 20 sec..

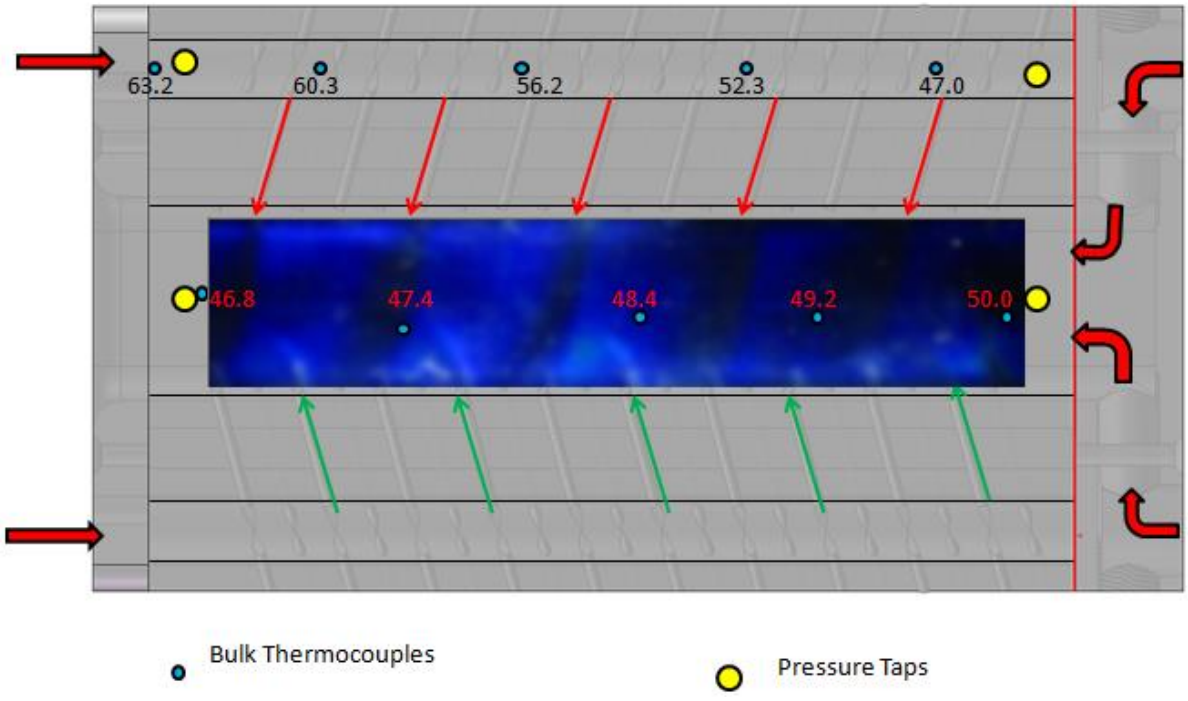

Figure 5-7 : Same as Figure 5-1, except time = 25 sec..

Processing the Images

1D Transient conduction equation with semi-infinite boundary condition is solved to get the heat transfer coefficient. The equation and the boundary conditions are:

$$k\frac{\partial^2 T}{\partial x^2} = \rho C_p \frac{\partial T}{\partial t}$$

$$at\ t = 0, T = T_0$$

$$at\ x = 0, -k\frac{\partial T}{\partial x} = h(T_w - T_\infty)$$

$$at\ x = \infty, T = T_0$$

When the 1 D transient conduction equation is solved with the given boundary conditions an equation is obtain and used to determine the heat transfer coefficient. The solution is:

$$\frac{(T_w - T_0)}{(T_\infty - T_0)} = 1 - \exp\left(\frac{h^2 \alpha\, t}{k^2}\right) erfc\left(\frac{h\sqrt{\alpha\, t}}{k}\right)$$

When the Mainstream air temperature T_∞ is a function of temperature, Duhamel's superposition theorem is used to solve for the heat transfer coefficient.

The local heat transfer coefficient is found by solving the following equation:

$$T_w - T_0 = \sum_{j=1}^{N}\left[1 - \exp\left(\frac{h^2 \propto (t - \tau_j)}{k^2}\right) \times erfc\left(\frac{h\sqrt{\propto (t - \tau_j)}}{k}\right) \times (\Delta T_{\infty(j,j-1)})\right]$$

The use of Duhamel's superposition equations require that convergence occurs to aquire an accurate solution. In order to select the right temperature band for the TLC testing was performed to establish at time/temperature relationship for the variety of test conditions that will be used for all testing. Figure 5-8 shows how the values of Nu/Nu_o vary for a single thermocouple cominbation located near the exit of the channel. The exit of the channel had the greatest variation in Nu/Nu_o values, once a stable convergence occurred.

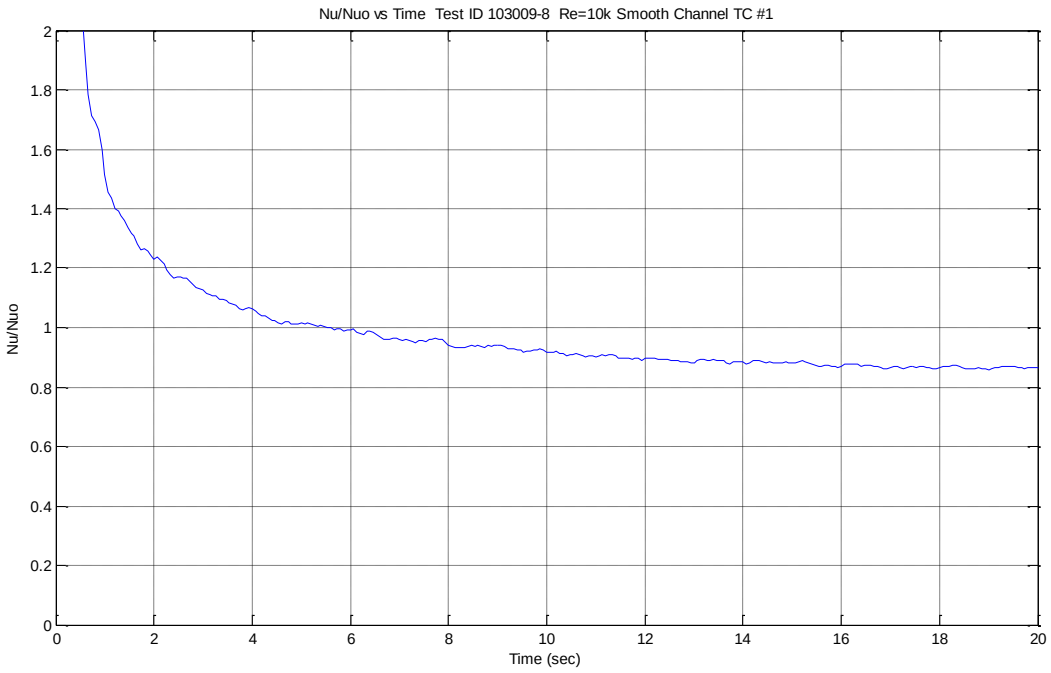

Figure 5-8 : Time vs. Nu/Nu_o for a single thermocouple located near the exit of the channel.

Figure 5-9 shows the Nu/Nu_o convergence for several different thermocouple combinations vs. time. This information was used to help select the proper TLC temperature range that would be used for all testing. Also note that three different Nu_o equations were used in the calculations to see how the results would vary. The more popularly accepted Dittus-Boelter equation for

turbulent flow was selected over the less commonly used Petukhov and Gnielinski equations for calculating turbulent flow Nu_o values.

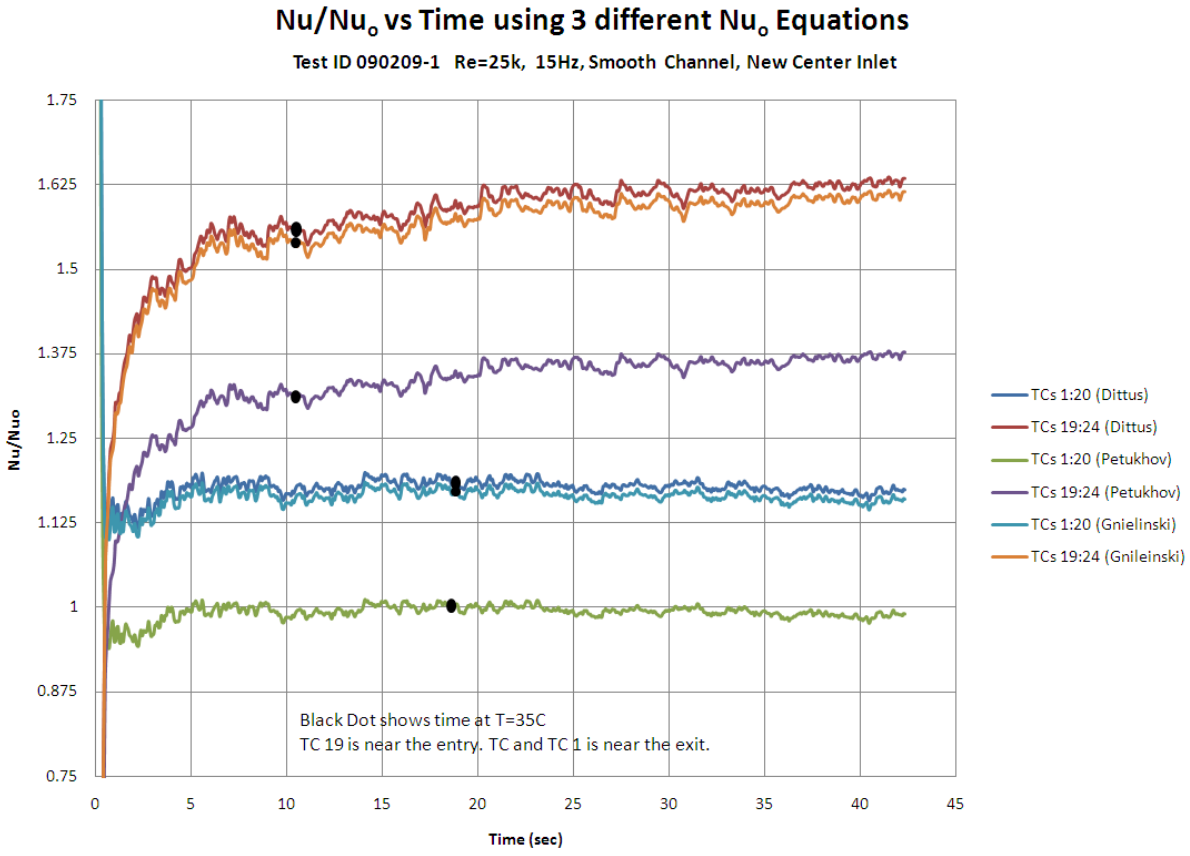

Figure 5-9 : Nu/Nu_o vs. Time, 3 different Nu_o equations

Analyzing the Images

Once the equations are solved for the local heat transfer coefficient (h) values at each pixel, the calculated values of "h" can be used to calculate the Nu/Nu_o values. The results can be plotted as a function of the heat transfer enhancement factor as shown in figures 5-10 – 5-11 below.

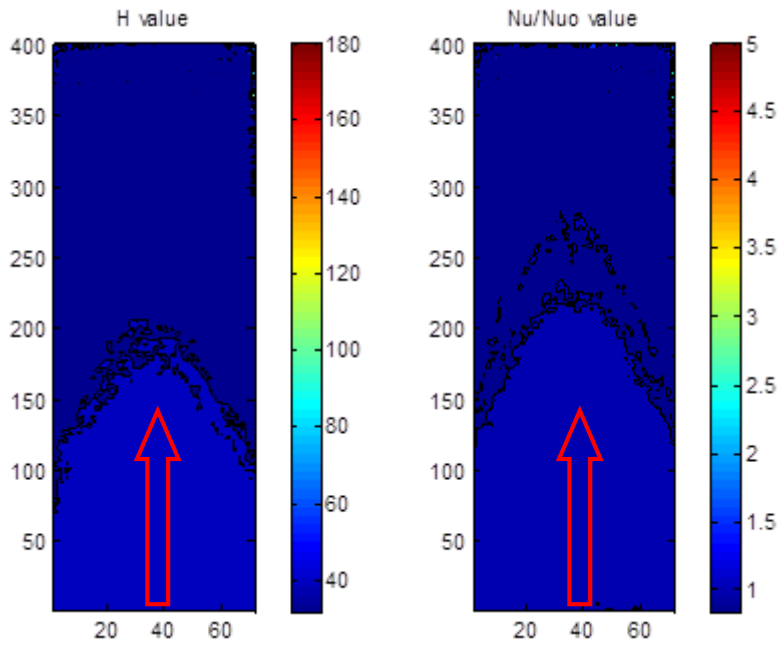

Figure 5-10 : Heat Transfer Coefficient (h) in units of W/m^2 K, and Heat Transfer Enhancement (Nu/Nu$_o$) for a Smooth Slot Channel, Re = 10k (Note: Nu$_o$ ~ 40 in this case)

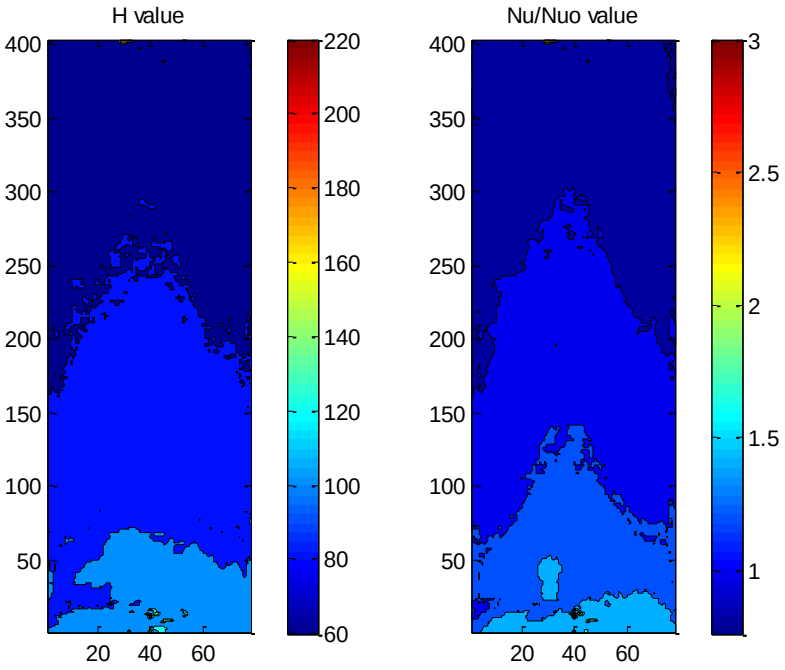

Figure 5-11 : Heat Transfer Coefficient (h) and Heat Transfer Enhancement (Nu/Nu$_o$) for a Smooth Slot Channel, Re = 25k (Note: Nu$_o$ ~ 65 in this case)

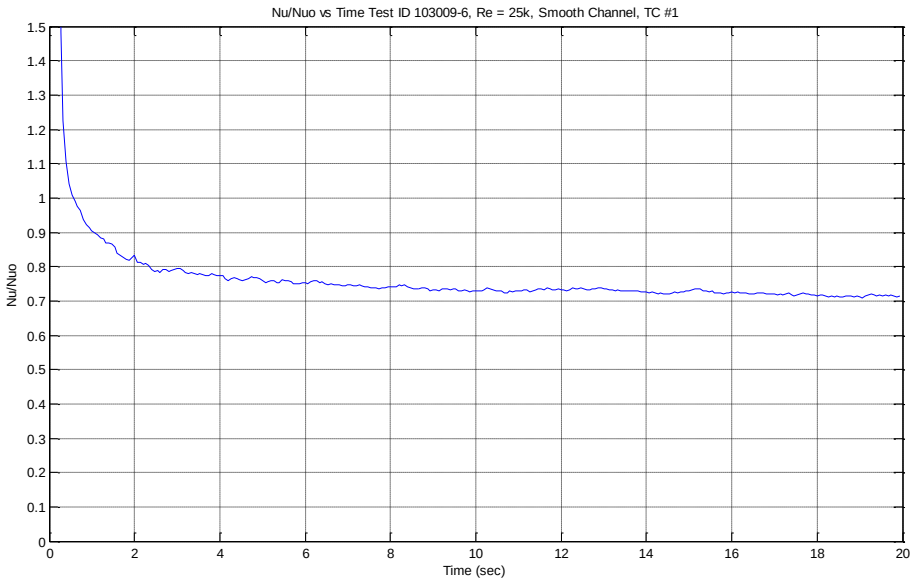

Figure 5-12 : Line Plot of Nu/Nuo in a Smooth Channel, Re=25k, TC #1 located near exit of channel.

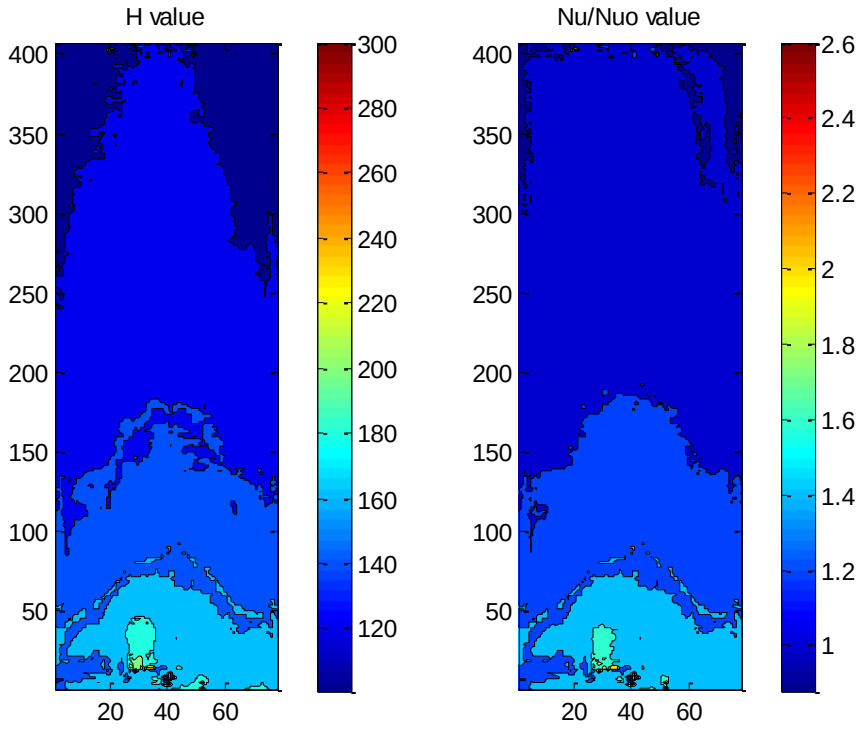

Figure 5-13 : Heat Transfer Coefficient (h) and Heat Transfer Enhancement (Nu/Nu_o) for a Smooth Slot Channel, Re = 50k (Note: $Nu_o \sim 121$ in this case)

Optional Multi-Band Liquid Crystal

In multi-band TLC testing several aggregates of TLC are mixed together. Each must be calibrated independently and analyzed independently to obtain accuracy results. Two methods are briefly described.

Preferred Method - A multi-band liquid crystal film for visual observation of two or more patterns is prepared by laminating at least two polyurethane films, each containing discrete aggregates of liquid crystals against a black film such that the visual response of the liquid crystals of each succeeding polyurethane film is different than that of the liquid crystals in the other film or films.

Alternate Method – This method requires that several aggregates of liquid crystal become mixed in a single solution and applied against a black film.

In the case of the testing that was performed, it was determined that multi-band TLC was not needed. The single band TLC that was best suited for the testing was 35ºC TLC with a temperature band of 1ºC.

Chapter 6 – Jets and Helix Strips with Various Blowing Ratios

Introduction

Heat transfer results for a given slot shaped channel with a 3:1 aspect ratio are presented using various methods to enhance swirl in the channel including helical shaped-trip-strips and swirl-jets issuing from the side walls. Four different configurations of the swirl jets and one configuration of the helical trip strips were studied. The Reynolds numbers investigated range from 10,000 to 50,000 and are based on the mean velocity of the fluid at the channel inlet, or when swirl-jets are used, the equivalent mass flow rates at the exit of the main channel. Independently these heat transfer enhancement strategies have proven to be effective in either round channels, in the case of swirl jets and helical protrusions, or rectangular channels, in the case of trip strips.

A transient technique combined with Duhamel's superposition theorem was used to obtain the heat transfer coefficient distributions. Narrow-band liquid crystals were used to map the transient surface temperatures and were combined with thermocouples that measured the bulk-air temperatures along the flow path in the main channel. The results for the tests reported in this paper show mean heat transfer enhancement values (Nu/Nu_o) greater than 4.5 and low normalized friction factors. Thermal performance factors ranged from 1.1-3.3 for the various configurations studied. These results show significant improvements over other types of heat transfer enhancement methods currently used in the mid-span section of turbine blades.

Configurations Studied

A 3:1 single passage channel with a hydraulic diameter d_h of 0.0248m and a L/d_h of 8.7 is chosen for this study. The various configurations investigated to enhance heat transfer include a

helical shaped-trip-strip (Fig. 6-1 and 6-2) and several fluidic-swirl-generation configurations where the swirl is generated by introducing tangential jets along the side walls of the main coolant passage (Fig. 6-5).

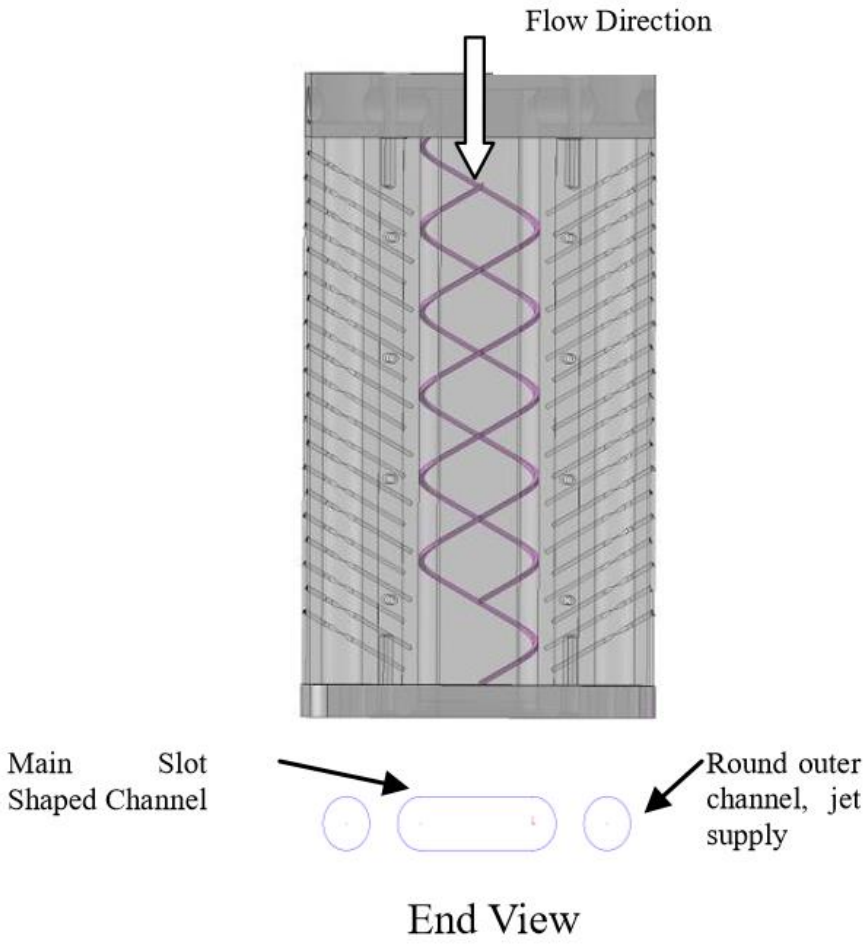

Figure 6-1: Transparent view of the test piece with double helix trip strips in main channel and available jet passages.

The helical trip-strip concept has been well explored in the heat exchanger community and is an accepted practice for heat exchangers such as tube-in-shell heat exchangers. However, its use in gas turbine cooling has not been extensively investigated. In the present study, the helical trip-strip concept is combined with trip-shaping to obtain added benefits. As noted by Wang, et al [15], a trapezoidal-cross-section trip-strip with a sloping face at 11 degrees provides increased heat

transfer coefficients when compared to square, hemispherical, triangle, and trapezoid shape with decreasing height. Wang also studied the effect of these various shapes with regard to the pitch to height (e) ratios between 8 and 15. The study concluded that the pitch to height ratio of 12 provided the greatest heat transfer enhancement in the Reynolds number range used in this study. The e/d_h value used in Wang's study was 0.1 and the channel shape was rectangular. This rectangular channel shape and e/d_h value is typical of what is found in current published literature. In this study, a double-helix trip-strip, as shown in figure 6-1, with a trapezoid cross-section as in [15], is used. The e/d_h value is 0.1. A cross section of the trapezoid shaped trip is shown in figure 6-2. The 11 degree sloping face is normal to the main stream air flow direction.

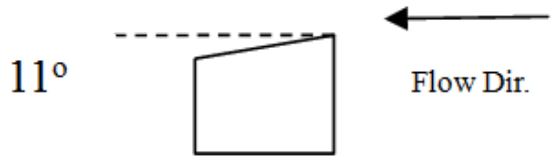

Figure 6-2: Cross section shape of trip strip.

The fluidic swirl-generation configurations are shown in figure 6-4, where four different configurations are shown and labeled as A through D.

In all these configurations, air enters the main channel through tangential side jets introduced through several holes placed axially along the neighboring (side) channels. Flow through the side-channels feeding the jet-holes was opposite to the main channel flow direction. The side-jets are introduced tangential to the main flow to produce a swirling motion, and are oriented at a 15 degree angle to the streamwise direction. In addition to the swirl, the jets are angled towards the main flow to generate counter-shear and associated turbulence. In figure 6-3, the red and green lines indicate the location of the jets entering the main channel. The pitch and offset of the jets are

described in detail in the experiments section. In configurations A and B, the tangential jet from the left is introduced along the bottom surface of the channel while the tangential jet from the right is introduced at the top of the channel. The two configurations differ in the relative offset between the left and right jets. In configurations C and D, the side jets are introduced along the top and bottom from both sides; thus the lower (upper) jets from either side can interact with each other depending on the relative pitch. In configuration D, the top and bottom jets on either side are relatively closely spaced, while in configuration C, they are further apart (as shown in figure 6-3).

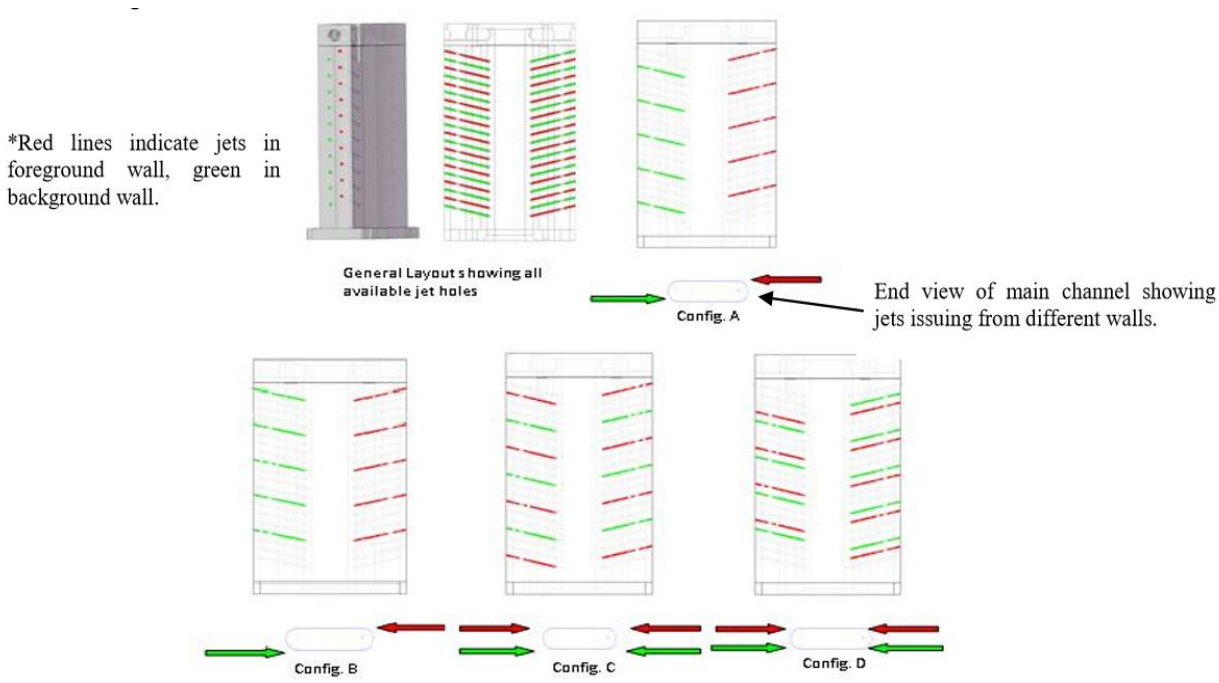

Figure 6-3: Various Jet Configuration Schemes

A channel-average blowing ratio, jet velocity to main channel velocity, of 17.5 was maintained throughout each test. The average blowing ratio was calculated based on the measured mass flow rates in the main channel and the side channels, and is an average value across all the

jet-holes. The individual jet-blowing ratio may vary from hole to hole depending on the pressure drop across the holes.

The large value of blowing ratio was selected to ensure that the jet penetrates the main flow field to the other side, and potentially creates an impingement effect. As a basis for comparison and normalization, an equivalent smooth-channel case with no swirl-enhancement was considered, with a mass flow rate equivalent to the sum of the main and side channel mass flow rates exiting the main channel for the swirl-enhanced cases. The total mass flow rate combined with the hydraulic diameter of the main channel was used to define the Reynolds number of the flow. The results of all tests presented in this study are compared (normalized) with the non-enhanced smooth channel designated by $Nu_{o\ smooth}$.

Experiments

Experimental Apparatus

A simulated clear polycarbonate airfoil was built that incorporates two strategies for inducing swirl motion in the internal passages of an airfoil. The main cooling channel is slot shaped with and aspect ratio of 3:1, with a height of 15.9 mm and a width of 47.6 mm. The overall length of the slot channel is 216 mm, not including the radiused entry and exit portion of the channel. As noted earlier, one method uses a trapezoid shaped rib that protrudes into the coolant flow stream. This trapezoid shaped rib spirals along on the wall of the passage for its entire length. The trapezoid cross section (1.6mm x1.6mm) incorporates an 11^{o} downward trailing edge along the top surface of the rib. This shape has proven to be beneficial in ribbed passages without swirl [15]. The trapezoid shaped ribs and coolant jets can be situated at various pitches and angles to order to

achieve the optimum cooling through a range of Reynolds numbers from 10,000 to 50,000. In the present paper, d_h/e is 15.5:1 and p/e is 24:1. Two separate strips traversed the length of the channel forming a helix. The pitch of each helix is 38 mm and the helix angle is 15 degrees relative to the flow path (figure 6-3). When the two sets of helical strips are combined the resultant pitch to height ratio is 12. The strips were fixed to the smooth channel using Loctite 4203 Ethyl cyanoacrylate adhesive. This adhesive can withstand high temperatures and has a thermal conductivity of 0.2073 W/m K, which is nearly identical to the properties of polycarbonate and should not affect the results when TLC is used.

The side-jets that produce swirl are fed through outer passages that run parallel to the main slot shaped channel. These passages are 15.9 mm in diameter and the diameter of the jet at the entrance to the main channel is 1.6 mm. The flow into the jet supply channels was not through flow and could only exit through the jets. In configurations “A” and “B” the jets were spaced 38 mm apart along one side. In configuration “A”, the jets located on the opposite wall were offset by 19 mm relative to each other. In configuration “B” the jets were aligned (no offset) relative to each other along both walls of the main channel. In jet configuration “C” jets enter from the upper and lower portion of each of the two sides of the slot shaped channel. They are spaced 38 mm apart and staggered 9.5 mm relative to one another on one side. Configuration “D” had similar spacing, but the stagger between sides was different. Figure 6-3 shows the jet spacing and stagger. The red and green lines indicate jet locations and sides. In each case the temperature at the entry of the respective channels at the beginning of the tests was maintained within two degrees Celsius of each other.

Initial static testing was performed using 25 thermocouples strategically placed in the passage of the channel. A smooth channel with no swirl inducement strategies was tested first, and the results of normalized heat transfer enhancement and pressure losses were used to compare against all tests with swirl enhancements. Testing with thermocouples as well as liquid crystal techniques will provide a more detailed account of heat transfer enhancement in the passage.

Heated air enters the test piece via a long diffuser section through a 13 mm radiused entry and exits the single flow slot shaped channel in an identical fashion. Upon exiting the channel the air is routed through a small plenum, then finally exits through two 18 mm holes to the atmosphere. The main channel inner walls are coated with a specially prepared thermochromic liquid crystal (TLC) substance which turns green at a nominal temperature of 35^0C. Two thin film thermocouples are attached to the walls, one near the entry and one near the exit of the main channel. These will be used to confirm the accuracy of the TLC. Five fine wire thermocouples are placed, equally spaced, in the flow stream. The thermocouples are wired directly to a Labview thermocouple data acquisition system. The thermocouples have a resolution of 20 Hz and the data acquisition system is set to read thermocouple data at 15 Hz.

Two Canon SD430 wireless cameras are securely mounted on each side of the test piece. The cameras are set to record video images at 15 Hz. The thermocouple data acquisition system and the video cameras are synchronized via cold cathode fluorescent lamps (CCFL) that are used to illuminate the TLC and are triggered by a switch attached to an air bypass valve.

Prior to the start of a test, heated air is allowed to bypass the test section. Once the bypassed heated air temperature has stabilized at approximately 80^{o} C preparations for the start of a test begins. The test piece is also maintained at room temperature for an extended period prior to the start of a test to ensure a uniform initial temperature.

In the case where air enters the outer jets channels and the main slot channel two separate heaters are used. One heater was used to heat the main slot channel and the other was used to heat air entering the two outer jet supply channels. Two separate flow meters were used to control the mass flow rate of air entering each channel. As stated, the combined mass flow rate at the exit of the test piece is used to determine an equivalent Reynolds number for comparison with tests that do not utilize jets. The heated air from each heater is bypassed and allowed to stabilize prior to the start of a test. It is desirable to have the air entering each channel to be the same throughout the entire test. This is quite a difficult task due to heat losses in the apparatus being somewhat different as the heated air travels from the individual heaters to the channel inlets. Thermocouples located at the entry of each channel monitor the temperature of the air entering the channel. Temperature differences of two degrees Celsius between the main and outer channel inlets were considered to be in the acceptable range for testing. Repeat testing using inlet air temperature differences as high as ten degrees Celsius were performed to better understand this effect. The results of this will be discussed in detail in the results and discussion section.

To begin a test, the thermocouple data acquisition system is activated and the cameras begin recording. Then a bypass valve(s) is closed allowing heated air to enter the test piece. Video images and thermocouple temperature readings are stored for post-test processing. The basic layout of the test apparatus is shown in figure 6-5.

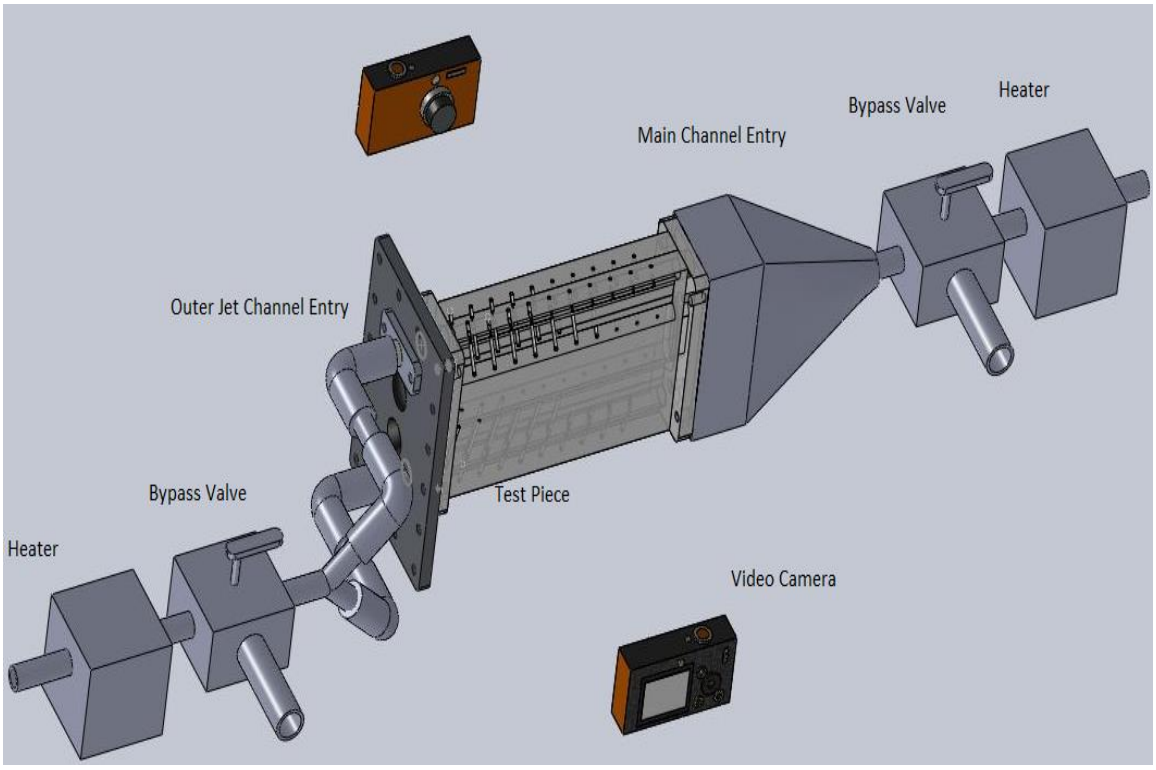

Figure 6-4: Basic Layout of Test Apparatus

The local heat transfer coefficients across a liquid crystal coated target surface can be obtained using the 1-D transient heat conduction model of a semi-infinite solid with a convective boundary condition as given by:

$$\frac{\partial T}{\partial t} = -k\frac{\partial^2 T}{\partial x^2} \tag{1}$$

with boundary and initial conditions:

$$T(x = o, t = 0) = T_i$$

$$T(x = 0, t \to \infty) = T_m \tag{2}$$

$$T(x \to \infty, t) = T_i$$

$$-k \frac{dT}{dx} \Big|_{x \to 0} = h(T_w - T_\infty)$$

where h is the surface heat transfer coefficient, T_w is the time-varying wall surface temperature and T_∞ is the time-varying local bulk (for internal flows) temperature. This is measured in the preset work using suspended centerline thermocouples at several axial locations. These suspended thermocouples acquire temperature changes throughout each test. The data is used to produce a curve fit of the centerline temperatures vs. time along the entire main channel. The temperature vs. time equation is then associated with each column of pixels in the video image. Therefore, each column of pixels (flow stream is along rows) has an associated time vs. temperature array of data.

The solution for the surface temperature response with time is:

$$\frac{T_w - T_i}{T_\infty - T_i} = 1 - exp\left(\frac{h^2 \alpha t}{k^2}\right) erfc\left(\frac{h\sqrt{\alpha t}}{k}\right) \qquad (3)$$

A single transient test using the liquid crystal method described earlier is used. Each pixel value is examined for its peak in local intensity. The intensity value is used in conjunction with a specifically written MATLAB program to determine the corresponding temperature. By measuring the corresponding time required for the surface temperature to reach this temperature, the local heat transfer coefficient can be determined.

The 1D semi-infinite solid assumption must be satisfied. In order to satisfy the semi-infinite assumption, the transient temperature must not penetrate through the thickness of the polycarbonate during the test duration. This is achieved by a sufficiently thick test piece of low thermal conductivity and diffusivity (0.201 W/mK and 0.1046 $x10^{-6}$ m^2/s for polycarbonate respectively). For the one-dimensional heat transfer assumption to be satisfied, conduction should only occur normal to the surface with all lateral conduction effects neglected. The test piece may actually experience some lateral conduction, but it is assumed that the dominant temperature gradient is in the direction perpendicular to the surface, and lateral effects are negligible.

Although the initial temperature of the polycarbonate is uniform at ambient temperature, the incoming fluid temperature is higher and not a linear step increase. This is accounted for through the modification of the previous equation by Duhamel's superposition theorem, which represents the temperature change as a series of steps described by:

$$T - T_i = \sum_{i=1}^{N} \left[1 - exp\left(\frac{h^2}{k^2} \alpha(t - \tau_i) \right) erfc\left(\frac{h}{k} \sqrt{\alpha(t - \tau_i)} \right) \right] \Delta T_{m,i} \qquad (4)$$

where τ is the time step for each temperature step, $\Delta T_{m,i}$ is the temperature difference between each temperature step and the initial temperature, T_i. α, and k are characteristic of the polycarbonate plate. In the cases where heat transfer enhancements using jets are incorporated, the air temperature at the entry of the main channel and the jet channel at the beginning of the tests were maintained within two degrees Celsius. The temperature of the fluid exiting the jets as expansion occurred is

not known, but is assumed to be taken into account when the main channel centerline temperature vs. time data is obtained.

Pressure Test

A pressure tap is located at each end of the main channel, and in the case of air flowing through the jet supply channels, additional pressure taps are located at each end of the outer jet channels. In order to obtain accurate and consistent results, pressure measurements were taken during steady state adiabatic tests.

Flow meters were positioned before the heaters each supply channel. The mass flow rate at the exit of each flow meter and pressure, temperature, and cross section area at the entry of each channel was used to determine velocities, densities, and associated Reynolds numbers, where applicable.

Pressure drops along the main channel and outer channels are recorded and used to determine friction losses. The following equation is used to determine friction loss in each channel:

$$f = 2\, d_h\, \frac{\Delta P}{L \rho U^2} \tag{5}$$

Velocities are calculated based on flow rates and channel cross section area. The friction losses in each channel are proportional to one over the square of the velocity as determined by the mass flow rate. When testing with jet enhancements the mass flow into each channel can be used to determine the total combined friction loss by using the following equation for friction loss in parallel flow:

$$1/\sqrt{f_{total}} = \frac{1}{\sqrt{f_1}} + \frac{1}{\sqrt{f_2}} + \frac{1}{\sqrt{f_3}} \quad (6)$$

where f_1 is the friction loss in the main channel and f_2 and f_3 are the losses in the two outer jet supply channels. Friction losses in the actual jet channels are not taken into consideration.

When jet configurations were used the combined overall mass flow rates were used to compare the plain smooth channel (no enhancements) to that of the jet enhanced channel. Table 6-1 below shows the mass flow rates when jet configurations "A" and "B" were used.

Pressure taps located at or near the entry and exit of the main channel as well as the entry and exit of the jet channels were used to determine the differential pressure at each jet. The values shown in Table 6-2 were calculated based on the actual jet locations with the test piece set up in configuration "A". Other configurations show similar results, depending on the mass flow rates for that particular configuration.

Table 6-1 : Mass Flow Rates for Jet Configurations "A" and "B"

	Mass Flow Rate (kg/s)	
Reynolds Number	Main	Outer (Both)
10,000	0.00402	0.00140
25,000	0.00825	0.00531
40,000	0.01658	0.00507
50,000	0.02085	0.00619

Table 6-2 : Pressure between outer (P_o) and main channel (P_m) at various jet locations, Configuration "A"

	$P_o - P_m$ (kPa)			
Jet Position	Re~10k	Re~25k	Re~40k	Re~50k
1 (Main Channel Entry)	11231	35529	60621	65547
2	10857	34562	59429	63659
3	10477	33582	57739	61969
4	10098	32605	56049	60183
5 (Main Channel Exit)	9716	31622	54358	58394
Max. Delta P (kPa)	1515	3907	6263	7154

Experimental Uncertainty and Error

An accurate assessment of uncertainty in liquid crystal measurement of heat transfer coefficients is essential because many factors affect the TLC results. A large number of studies have concluded that a properly performed test yields mean uncertainly of up to 11.0% for values of h, and up to 9% for temperatures. Smith [19], et al, compiled a table summarizing uncertainty studies of h and T when narrow band TLC methods were used. Thermocouple accuracy and repeatability are large contributors to uncertainty as well as illumination spectral effects. The wall mounted thermocouples were used to compensate for this effect and resulted in a 0.2° C temperature correction.

A minimum of two of each tests were conducted to evaluate the repeatability of tests. Heat transfer values typically were repeatable within 3% for tests where Reynolds numbers were moderate. As reported in the literature, current estimates of the uncertainty in the Nusselt number are approximately 10%.

Results and discussion

Overall Heat Transfer and Friction

The initial tests were performed with a smooth slot shaped channel with no heat transfer enhancements. The results of these tests showed heat transfer coefficients similar to the standard smooth pipe results noted by the Dittus-Boelter equation near the exit of the channel and somewhat higher values near the entrance of the channel, due to entry effect. The mean values of the heat transfer coefficient (h) and Nusselt number (Nu) over the entire channel were used as the standard for the remainder of testing. Thus, all references to h and Nu in this paper are listed as h/h_{smooth} and $Nu/Nu_{o\ smooth}$.

Values of mean $Nu/Nu_{o\ smooth}$ vs. Reynolds numbers for all five swirl-configurations are shown in figure 6-5. The results show the effectiveness of the jet configurations are extremely high ($Nu/Nu_{o\ smooth} \sim 4$) at low Reynolds numbers and become reduced at high Reynolds numbers, except for the case of Jet Configuration "A" which has the highest Nu ratio at Re=25k and 40k.

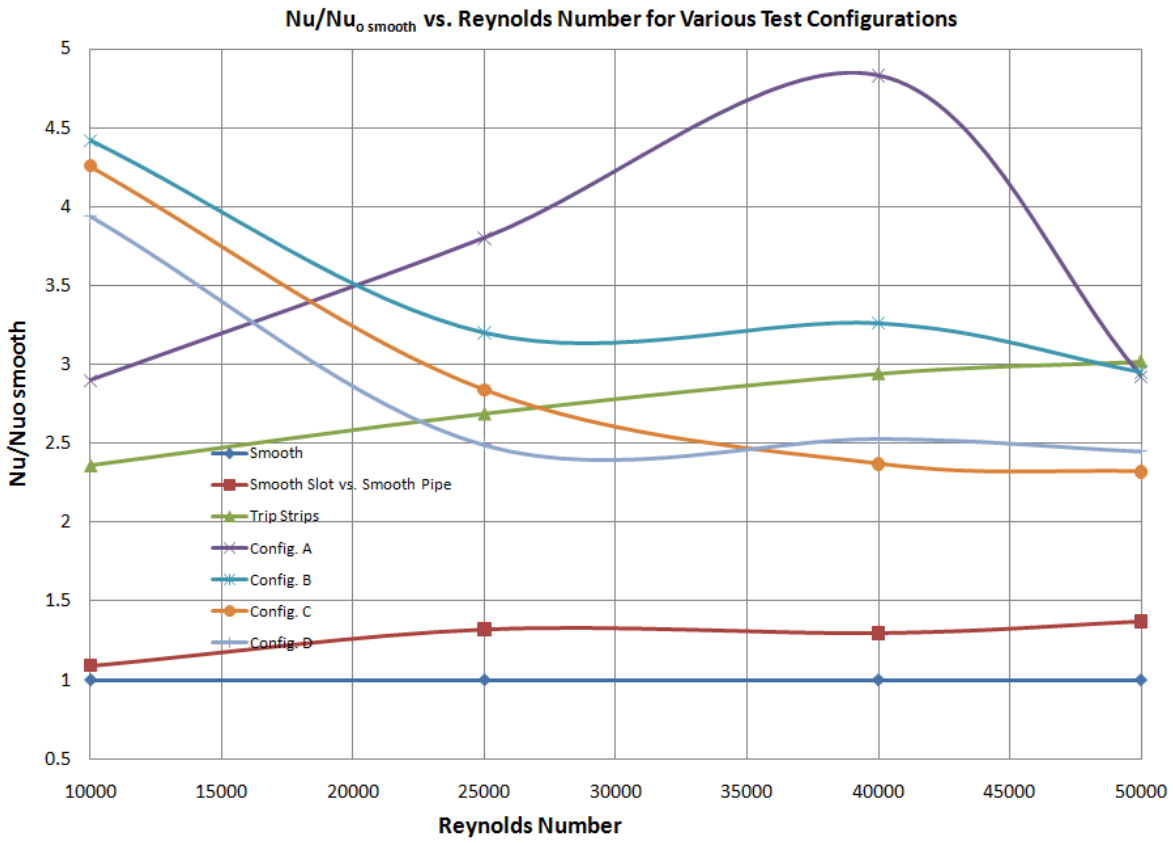

Figure 6-5: Normalized mean heat transfer enhancement vs. Reynolds number

The effectiveness at low Reynolds numbers is likely due to the lower mass and velocity of fluid entering the main channel at low Reynolds numbers compared to the high velocity impingement characteristics of the jets. These impingement regions contribute to high local heat transfer coefficients as compared to the smooth channel. As the Reynolds number increases the increased momentum of main channel fluid overcomes the momentum of fluid coming from each individual jets and tends to direct the fluid leaving the jet downstream. The opposing jets do not interact to increase turbulence. This is very apparent in the video images. Jet configuration "A" at Re=25k and 40k did not seem to be affected by this phenomenon or was affected in a positive way due to a more optimum jet configuration at this particular blowing ratio.

The normalized friction factor for all the swirl-jet cases are relatively low for all cases tested (figure 6-6) when compared to published data employing trip strips in rectangular channels, which are typically found to be in the 5-10 range for turbulated channels of turbine blades. The various swirl-jet case plots essentially overlap with each other, and appear to be insensitive to Reynolds numbers. Only the helical trip strips show friction factors that are more representative of turbulated trip-strips. It should be noted that the friction factor for the tests utilizing the jet enhancements is a combination of friction factors in the main channel and two outer jet supply channels (Eq. 6).

To determine the effectiveness of a trip-strip configuration, the Nusselt number ratio and friction factor ratios are often combined into an overall Thermal Performance Factor (TPF). Equation 7 is used to determine the thermal performance of each test. It is important to note that the values of Nu are an area averaged value that takes into account the entire test section between entry and exit pressure taps, not just the developed region.

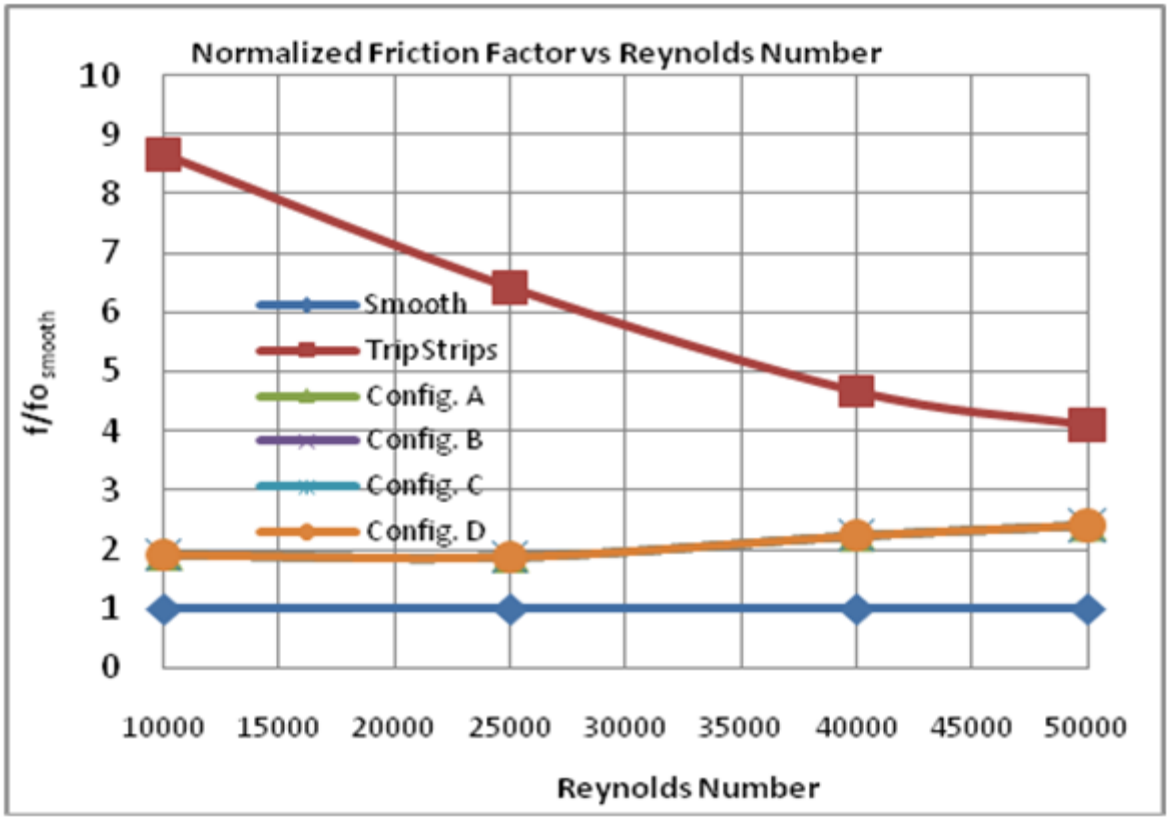

Figure 6-6: Normalized friction factor vs. Reynolds number

$$\frac{Nu}{Nu_{o\ smooth}} \div \left(\frac{f_{total}}{f_{o\ smooth}}\right)^{1/3} \tag{7}$$

A line plot of the calculated values summarizes the results in figure 6-7. As expected from the previous plots, the jet configuration "A" performs extremely well at Reynolds numbers of 40,000 and below.

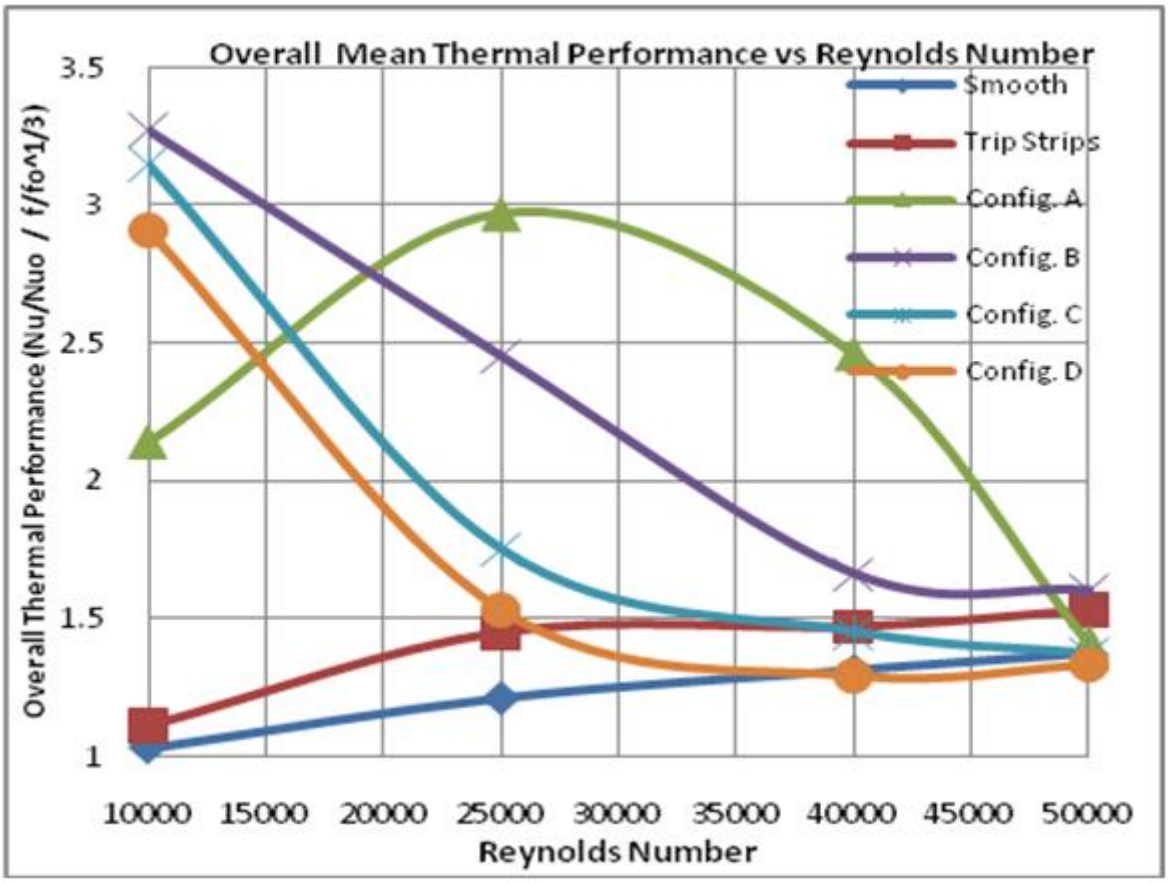

Figure 6-7: Overall Mean Thermal Performance vs. Reynolds number

The other jet configurations exhibit notably good results below Reynolds numbers of 40,000. It should be noted that typical values reported in the literature for turbulated channels range between 1-1.5, and values higher than 1.5 are considered to be very good configurations for enhancing heat transfer without the associated friction penalty. The swirl-jet configurations tested here lead to numbers in the 1.5-3 range over a reasonable Reynolds number range of 10000-50000. These configurations should therefore be considered promising.

Heat Transfer Contour Plots

Smooth channel with no heat transfer enhancements:

A smooth slot shaped channel with no heat transfer enhancements was used as a baseline for the remainder of the test. The resulting Nu/Nu_o color plots are shown below for reference.

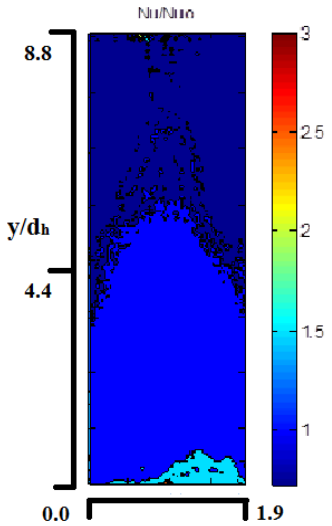

Figure 6-8: Heat Transfer Enhancement (Nu/Nu_o) for a Smooth Slot Channel, Re = 10k ($h_{avg.}$~40).

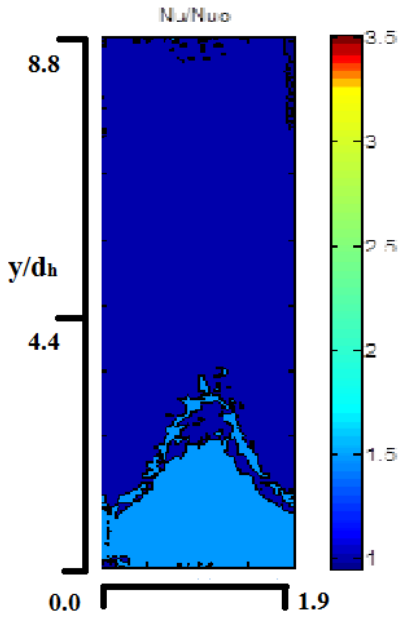

Figure 6-9: Heat Transfer Enhancement (Nu/Nu_o) for a Smooth Slot Channel, Re = 25k ($h_{avg.}$ ~ 75).

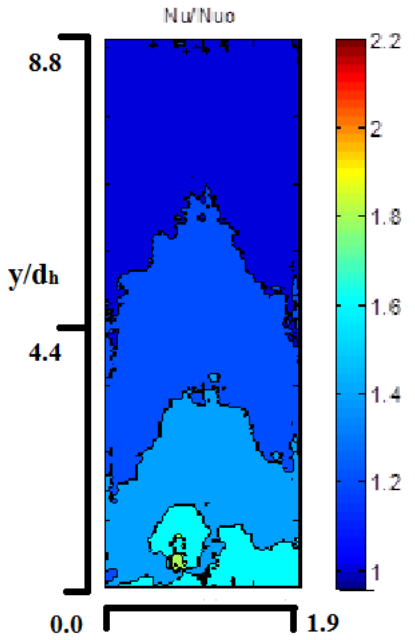

Figure 6-10: Heat Transfer Enhancement (Nu/Nu_o) for a Smooth Slot Channel, Re = 40k ($h_{avg.}$ ~ 127).

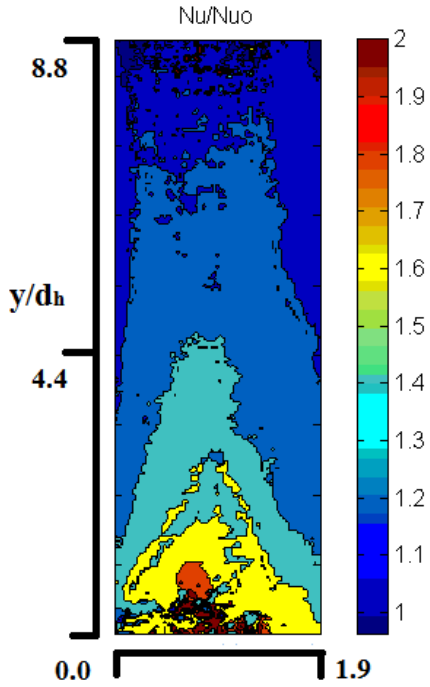

Figure 6-11: Heat Transfer Enhancement (Nu/Nu_o) for a Smooth Slot Channel, Re = 50k ($h_{avg.}$ ~ 160).

Helical Trip Strips:

For the helical trip strips, three $Nu/Nu_{o\ smooth}$ contour plots are shown in figure 6-8.

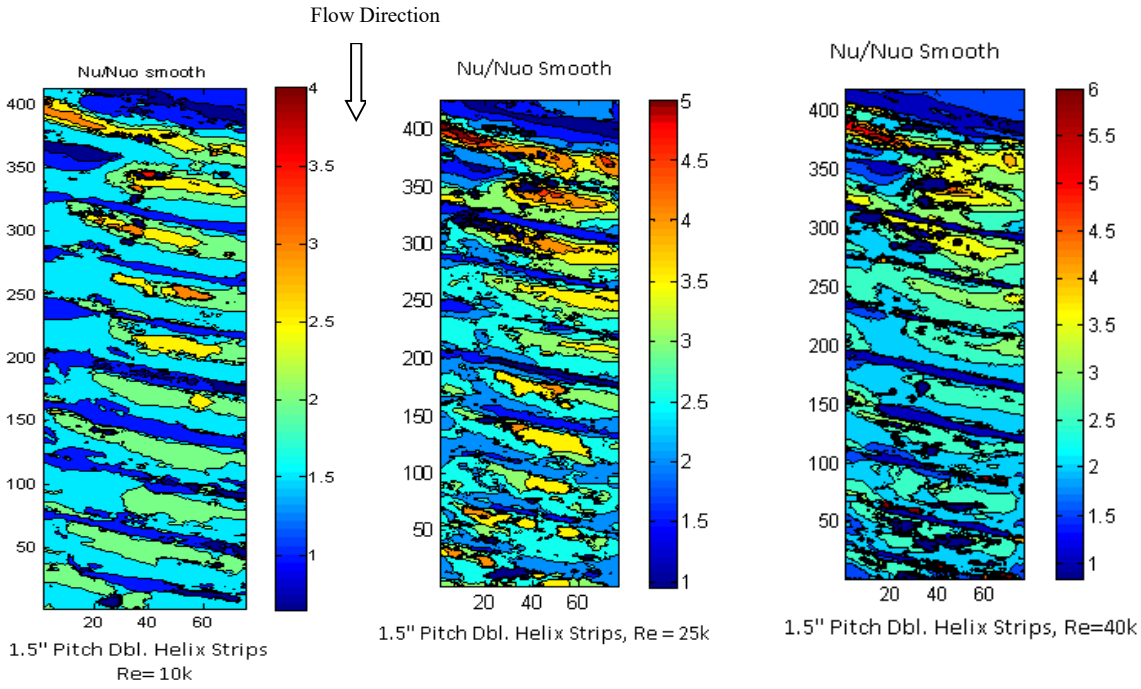

Figure 6-12: $Nu/Nu_{o\ smooth}$ with 38mm pitch double helix strips, Re = 10k, 25k, 40k

In reviewing the plot of Re = 10k, it is noted that as the fluid enters the channel minimal enhancement is apparent prior to the fluid contacting the first helix of the trip strip. The enhancement quickly improves once the first helical strip is encountered and values of $Nu/Nu_{o\ smooth}$ 2.5 to 4 are noted. As the flow progresses the effect of the enhancement is reduced and stabilize to a range of 1.3-2.3 near the exit of the channel. The mean $Nu/Nu_{o\ smooth}$ for this configuration is 2.36, with an overall thermal performance factor of 1.15 at Re=10000.

As the Reynolds number was increased to 25,000, the overall mean thermal performance increased to 1.45 with a mean heat transfer enhancement value of 2.04. As expected, the same lack

of significant enhancement is noted at the entry in the figure. The enhancement sharply increases following the first trip strip to values as high as 5 and maintain local values in excess of 3 throughout the channel to the exit, but these local areas diminish in size as the flow progresses through the channel. The normalized friction factor ($f/f_{o\ smooth}$) reduced from 8.66 at Re=10k to 6.42 at Re=25k.

As the Reynolds number is increased to 40,000 and 50,000 the increase in mean overall thermal performance only increases slightly to 1.47 and 1.53, respectively. As seen in figure 6-12, a small region of an enhancement value of 6 is noted after the first trip strip and diminishes as in previous plots. The normalized friction factor is 4.67 and 4.10 at Reynolds numbers of 40,000 and 50,000 respectively. Very small regions of high $Nu/Nu_{o\ smooth}$ values are noted near the exit. These are not seen in previous plots and may be due to the configuration of test piece exit and small exit plenum causing a small recirculation zone at the exit.

Jet-Swirl Configuration A:

The next series of test examined the heat transfer enhancement characteristics when high blowing ratio jets were introduced into the main channel flow. As noted earlier, four different configurations were examined at Reynolds numbers ranging from 10,000 to 50,000. The diameter of each jet was 1.6 mm and provided a p/d ratio of 12:1, which is the same as the p/*e* ratio used in the trip strip tests. In all these configurations, air enters the main channel through tangential side jets introduced through neighboring channels. Each of the four jet configurations differ in jet spacing and jet offset. The minimum offset of jet on any single side of the test piece is 19 mm. Jet

holes on the opposite side are staggered by 9.5 mm. Detail of each configuration is shown in figures 6-3.

Jet configuration A showed the most favorable results. Figure 6-13 shows the $Nu/Nu_{o\ smooth}$ plots of jet configuration A at an equivalent total mass flow to that of a Re = 10k, 25k, & 40k, respectively, in the smooth non-enhanced slot shaped channel. The plots depict samples of flow from only one channel side. The pitch of the jets in this configuration is 38mm along each side, with the jets on the side not shown at the same pitch. However, the jets on the opposing side are staggered in relation to the jets as shown in figures 6-3. At Re = 10k, the jet flow impinges on the surface of the main channel and cause very high local heat transfer enhancement, up to twelve in the main channel entry region. The enhancement values adjacent to each jet stream are much lower, especially near the entry, but as the flow proceeds through the channel the mixing quality improves with increasing crossflow, and there exists a more even distribution of heat transfer enhancement along with high local impingement values. The jet flow tends to cause swirl motion of the jet fluid and the main stream fluid seems to tumble as it encounters the high velocity jet fluid. The combination of swirl and tumble leads to the high heat transfer enhancement in this configuration. It is important to note that the jets continue to add mass into the main channel as the fluid progresses from the entry to the exit and that the total mass does not equal to mass flow rate of the Re=10k flow of the smooth channel until near the exit of the channel. This explains why the enhancement levels are higher at the channel inlet where the local channel flow rate and average velocity are the lowest along the length of the channel. Therefore the local jet to channel flow velocity ratio is the highest at this entry location.

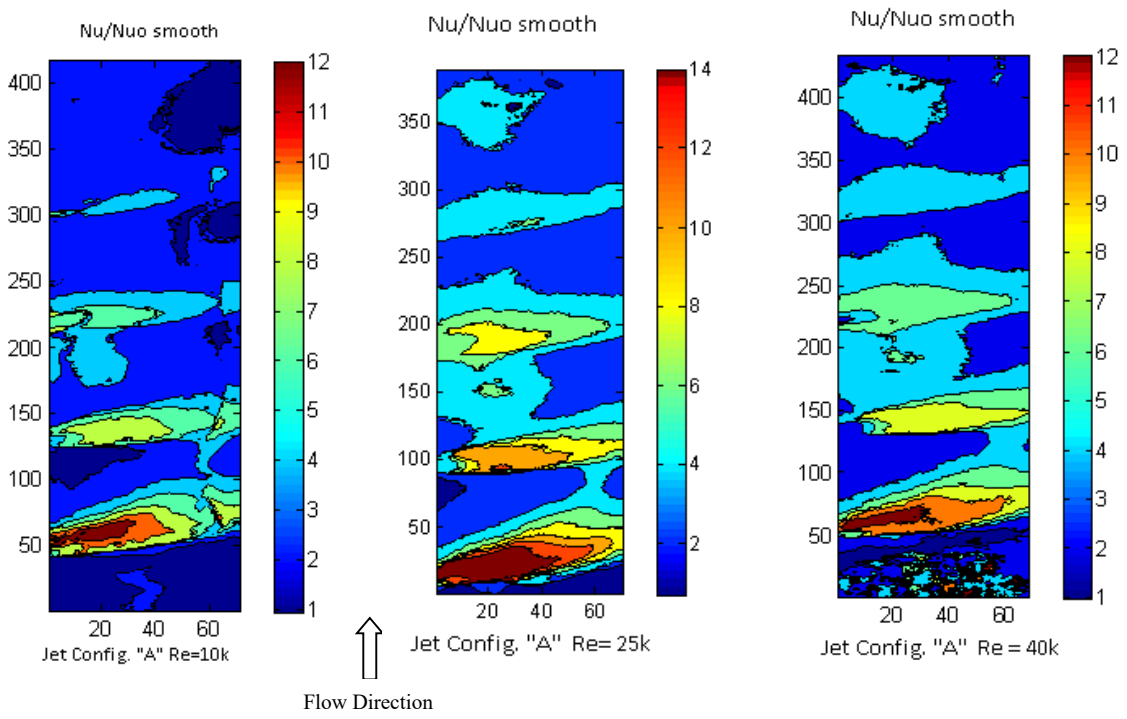

Figure 6-13: $Nu/Nu_{o\ smooth}$ with Jet Configurations "A", Re = 10k, 25k, 40k

At a Reynolds number of 25k and 40k, figure 6-13 displays similar attributes to those discussed for Re = 10k. Large local areas with $Nu/Nu_{o\ smooth}$ values exceeding 4 are noted throughout the channel and continue to the channel exit. At Re=25k, for example, the overall mean thermal performance value is 2.97 with a $Nu/Nu_{o\ smooth}$ value of 4.83. The normalized friction factor remains low at 1.87. These values offer a significant improvement over the helical trip strips and most other published data related to heat transfer enhancement in the mid-span region of turbine blades. The flow direction in these plots is from the opposing side from other plots presented.

Other Jet-Swirl Configurations:

Details of the tests results for the case with the helical trip-strips and tests with jet swirl enhancement for jet configuration A were discussed for three Reynolds number at all three Reynolds numbers. Contour plots for each of the three remaining enhanced test configuration performed at Re=40k (or equivalent mass flow rate in the case of jet enhancements) are shown in figure 6-14.

Configuration B performed the best of the three plots shown in figure 6-14. The aligned jets (refer to figure 6-3) created a slightly more even distribution of heat transfer enhancement than that shown in jet configuration A. The peak values were not as high as configuration A for the same Reynolds number tested. This configuration performed better than the helical trip strips in all reported categories.

A mean Nu/Nu_o value of 3.26 was noted along with a mean overall thermal performance value of 1.66. The normalized friction factor for all three tests in figure 6-10 was in the range of 2.25. The peak Nu/Nu_o value shown in the plot was 7.

Overall, configurations C and D did not perform as well as the helical trip strips or jet configurations A and B at the higher Reynolds numbers, but did show some rather impressive heat transfer enhancements at Re = 10k. These configurations results in values of Nu/Nu_o or 2.85 for configuration C and 2.54 for configuration D at Re=40k. There mean overall mean thermal performance values were 1.45 and 1.29 for C and D, respectively. It appeared that in configurations C and D, and particularly in D, that the jets were interacting with each other, and not necessarily in a supportive manner.

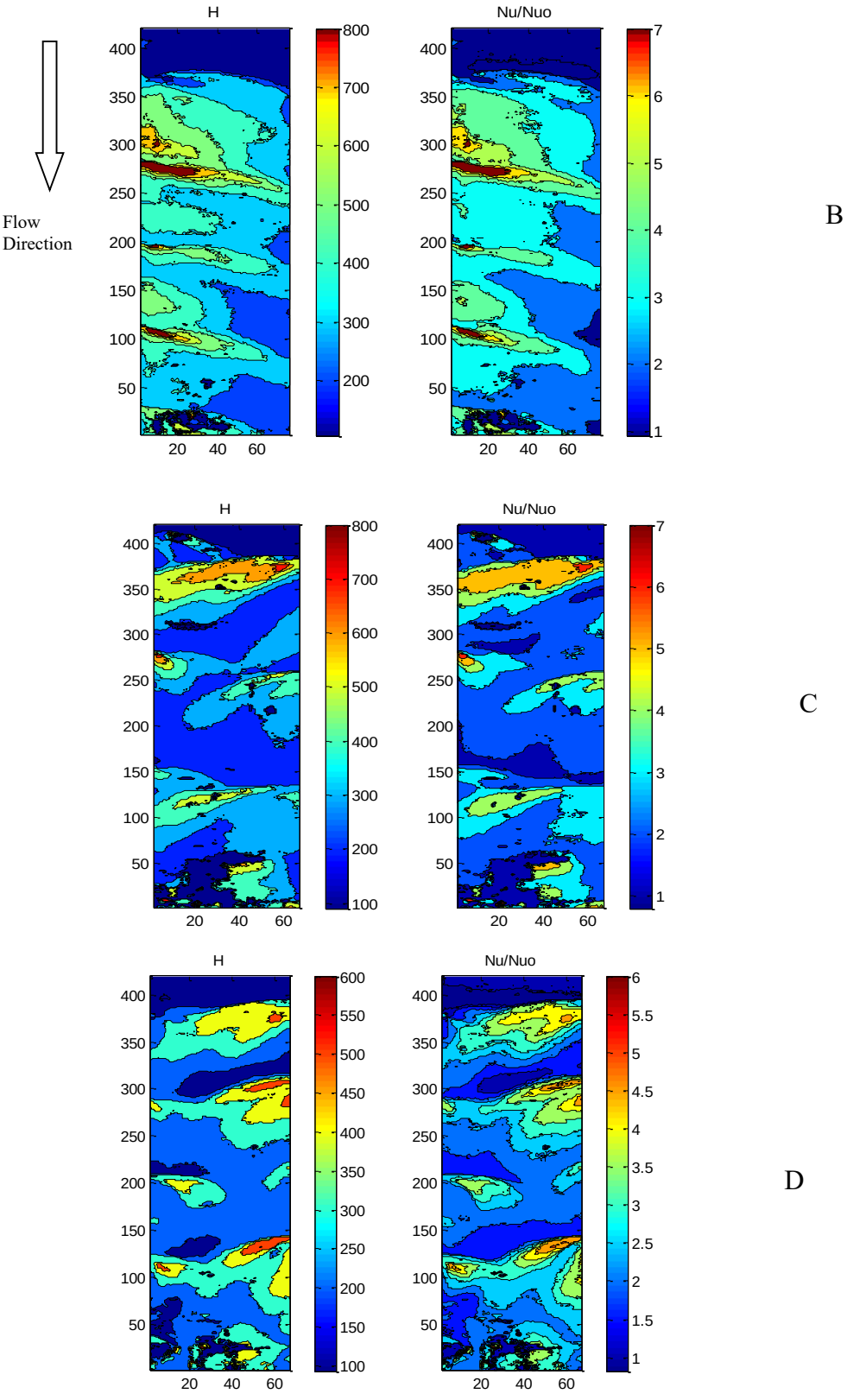

Figure 6-14: h and Nu/Nu_o plots for Jet Configuration B,C, and D at equivalent Re = 40k

Conclusion

A series of tests were performed in a slot shaped channel using two basic methods of heat transfer enhancement, helical trip strips and swirl-jets issuing from side walls. The resulting values of overall heat transfer enhancement, normalized friction factors, and overall thermal performance were compared to a smooth slot employing no enhancements.

The jet enhancement configurations show as substantial improvement in mean heat transfer enhancement values when compared to published results which utilize trip strips, but do not provide a uniform distribution of enhancement. This problem may be overcome by tailoring the jet hole sizes as the fluid progresses downstream. Configuration A in this study shows extremely good values for mean heat transfer enhancement with a value of 4.83 at Re = 40k. Local values of up to 14 in high impingement areas are noted for Re = 25k. The mean overall thermal performance for this same configuration was 2.97 at Re = 25k and 2.46 at Re = 40k. The normalized friction factor remained below 2.5 for all tests using jet enhancements.

The trapezoid shaped double helix trip strips provided a more uniform distribution of heat transfer, similar to trip strips used in rectangular channels. The overall heat transfer enhancement values ranged from 2.36 at Re = 10k to 3.02 at Re = 50k. Local values of up to 6 can be seen in Figure 9 at Re = 40k. These localized zones of high enhancement are much smaller than the localized zones of high enhancement when the jet enhancements are used. Even though these values are not as high as the jet enhanced passages, they are comparable to, or higher than, that of most published tests data where rectangular channels with trip strip are utilized. As expected, whenever heat transfer enhancements protrude into the main flow stream, the normalized friction factor values are much higher with the trip strips. A value of 8.66 is reported for Re = 10k and reduces to 4.1 at Re = 50k.

Chapter 7 – Single, Double, and Pentuple Helix Spiral Strips with Various Entry Configurations

Introduction

Heat transfer results for a given slot shaped channel with a 3:1 aspect ratio are presented using various configurations of a trapezoid shaped spiral wound strips to enhance swirl and tumble motion in the channel. The Reynolds numbers investigated range from 10,000 to 50,000 and are based on the characteristics of the fluid at the channel inlet. The ratio of absolute temperatures between the wall and fluid are on the order of 0.8 to 0.9. A combination of thermochromic liquid crystal techniques and thermocouples were used to create a temperature vs. time map. Duhamel's superposition theorem was then used to determine the local heat transfer coefficients (h) and heat transfer enhancement factors (Nu/Nu_o). In one series of testing a straight center inlet with a radiused entry was used to reduce entry effects.

In a second series of test a 90 degree inlet geometry was used to enhance turbulence at the entry. Three combinations of helical strips were tested using a single, double, and pentuple spiral design. The pitch of the helix remained constant in all tests at 0.75" (18 mm) as well as the height of the strip at 0.0625" (1.6 mm), yielding a p/e (pitch/rib height) ratio of 12. The resulting flow in the channel creates a tumble motion as the main channel fluid encounters the strips and a swirl motion as the fluid is directed through the spiraling helix. Many studies involving heat transfer using swirl enhancement have been presented in literature using round passages with wire spring inserts or twisted tapes, typically used in heat exchangers. In turbine aero foils, particularly in the mid-span region, rectangular channels with various configurations of trip strips are used to enhance heat transfer. The results of the tests presented in this paper show local heat transfer enhancement (Nu/Nu_o) values greater than seven and subsequent average values for the entire channel greater than three at the higher Reynolds numbers along with relatively low normalized friction factors.

Configurations Studied

A 3:1 single passage slot shaped channel with a hydraulic diameter d_h of 0.976 inch (0.0248 m) and a L/d_h of 8.8 is chosen for this study, due to limitations of the test vessel and to keep in line with typical turbine blade channel dimensions. The various configurations investigated to enhance heat transfer include three variations of helical shaped-trip-strips and two variations of entry geometries. The fluidic swirl-generation configurations are shown in Figure 7-1, one with a center entry flow into the channel and the other with a 90 degree entry flow into the channel.

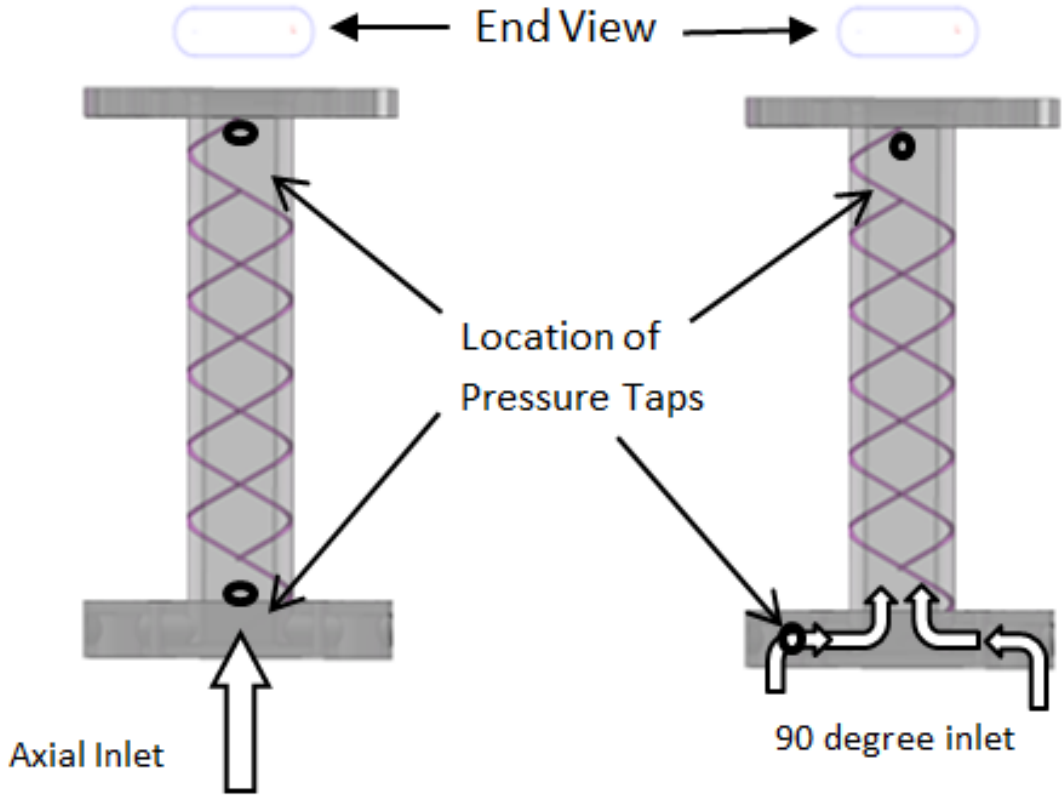

Figure 7-1: Transparent View of Test Piece with Double Helix Trip Strips in Main Channel

The helical insert concept has been well explored in the heat exchanger community and is an accepted practice for heat exchangers such as tube-in-shell heat exchangers. However, its use in gas turbine cooling has not been extensively investigated. In the present study, a helical trip-strip concept is combined with trip-shaping to obtain added benefits.

As noted by Wang, et al [15], a trapezoidal-cross-section trip-strip with a sloping face at 11 degrees provides increased heat transfer coefficients when compared to rectangular, triangular, round, or other various shapes. For this reason the trapezoid shaped helical trip strip shape was used for all testing. Figure 7-2 depicts the cross section shape used for this study.

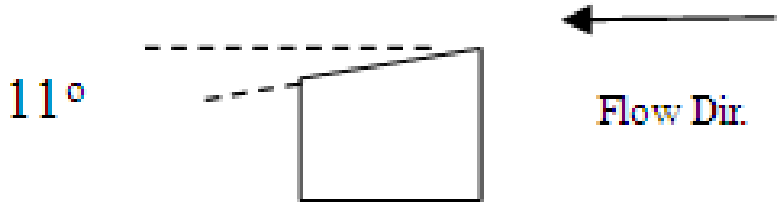

Figure 7-2: Cross Section Shape of Trip Strip

The strips are attached to the walls of the slot shaped channel in such a fashion as to form a helix. Figure 7-3 shows two views of the single helix strip. The image on the left shows the helical strips atttached to one side of the channel. The image on the right is a transparent view showing the strips on both sides of the test piece. The helical pattern is clearly visible in this image. Note also that the pitch is maintained at 0.75 inches (18 mm) for this test setup as well as the others.

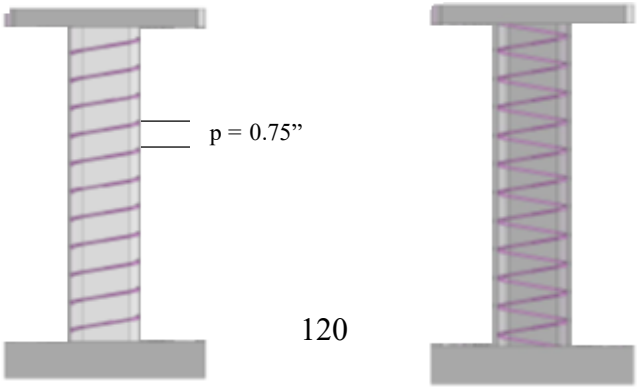

Figure 7-3: A slot channel with a single helix trip strip: (LH): as viewed from one side, (RH) a transparent view showing helix on both sides.

In Figures 7-4 and 7-5 it becomes clear that the angle of the trip strips relative to the incoming flow becomes more pronounced. The transparent view details the complexity of the trip strip arrangement that is not so easily realized by the image of one side only.

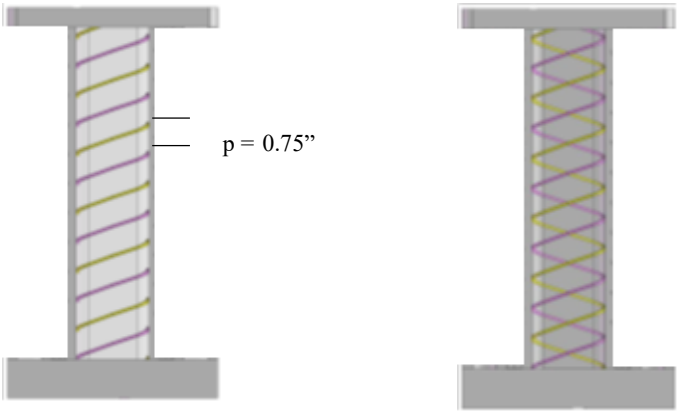

Figure 7-4: A slot channel with a double helix trip strip: (LH): as viewed from one side, (RH) a transparent view showing helix on both sides.

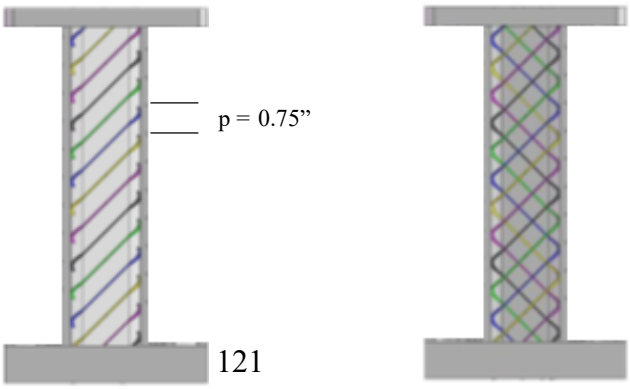

Figure 7-5: A slot channel with a pentuple helix trip strip: (LH): as viewed from one side, (RH) a transparent view showing helix on both sides.

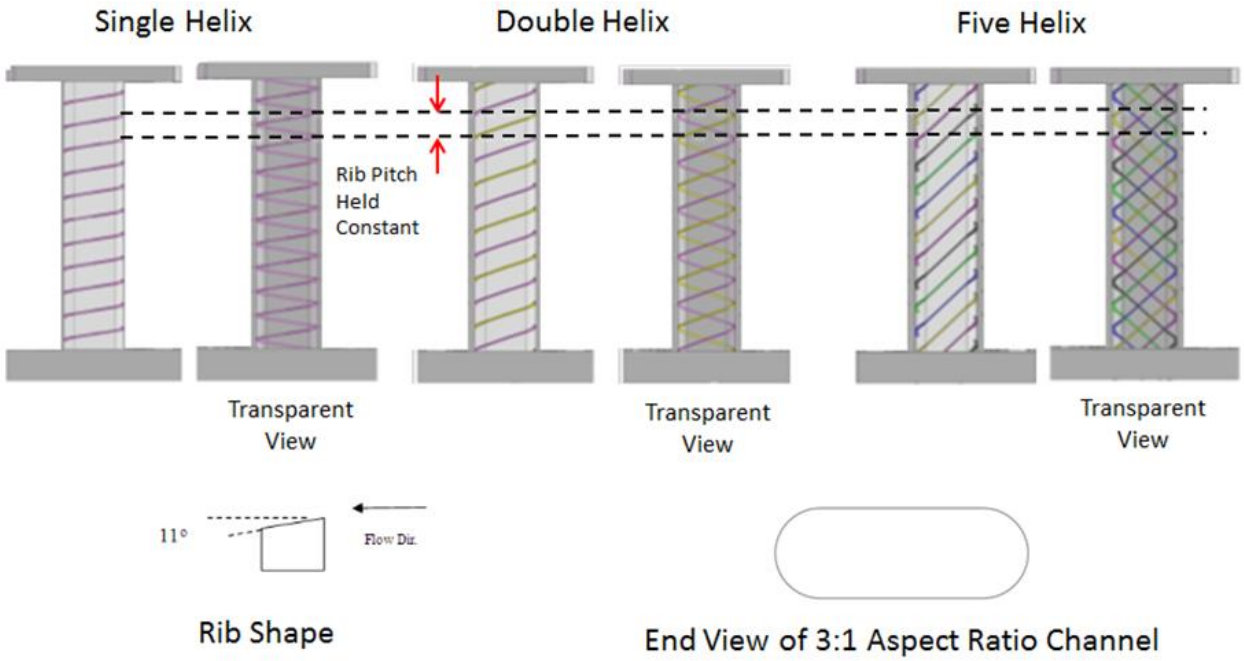

Figure 7-6: A side by side view of all six configurations studied.

Experiments

A simulated clear polycarbonate test piece was built that incorporates two strategies for inducing swirl motion in the internal passages of a heat transfer channel. The main cooling channel is slot shaped with an aspect ratio of 3:1, with a height of 0.625 inches (15.9 mm) and a width of 1.875 inches (47.6 mm). The overall length of the slot channel is 8.6 inches (218 mm), not including the entry and radiused exit portion of the channel. As noted earlier, one method uses a trapezoid shaped rib that protrudes into the coolant flow stream with axial flow entering the channel through a 0.5 inch (13 mm) radiused entry. This trapezoid shaped rib spirals along on the

wall of the passage for its entire length. The trapezoid cross section incorporates an 11° downward trailing edge along the top surface of the rib and has an overall height of 0.0625 inches (1.6 mm). This shape has proven to be beneficial in ribbed passages without any swirl enhancements [2]. The trapezoid shaped ribs are arranged in either a single helix, a double helix, or a pentuple helix configuration. Reynolds numbers ranged from 10,000 to 50,000 for each of the two entry shapes and three helical designs.

Initial static testing was performed using 25 thermocouples strategically placed in the passage of the channel. A smooth channel with no swirl inducement strategies was tested first, and the results of normalized heat transfer enhancement and pressure losses were used to compare against all tests with swirl enhancements as well as a smooth round pipe with an equivalent hydraulic diameter. Testing with thermocouples as well as thermochromic liquid crystal techniques will provide a more detailed account of heat transfer enhancement in the passage.

In the case of the axial entry, heated air enters the test piece via a long diffuser section through a 0.5 inch (13 mm) radiused entry and exits the single flow slot shaped channel in an identical fashion. The air exits the channel into the atmosphere. The main channel inner walls are coated with a specially prepared thermochromic liquid crystal (TLC) substance which turns green at a nominal temperature of 95 ºF (35C). Two thin film thermocouples are attached to the walls, one near the entry and one near the exit of the main channel. These will be used to confirm the accuracy of the TLC at those locations. Five fine wire thermocouples (0.005”) are placed, equally spaced, in the flow stream with the temperature sensing junction located in the center of the flow channel. These five thermocouples measure the centerline temperature of the air as it progresses through the channel. The thermocouples are wired directly to a Labview thermocouple data acquisition

system. The thermocouples have a maximum resolution of 20 Hz and the data acquisition system is set to read thermocouple data at 15 Hz.

In order to view the heat transfer characteristics on the interior of the channel the TLC is applied directly on to the inner wall of the clear polycarbonate channel. A black paint is applied over the TLC and the trip strips are applied over the black paint. The adhesive used to apply the trip strips have the same heat transfer properties as polycarbonate. This special adhesive allows for more accurate results under the trip strip, which act as thin fins to conduct heat. A concept sketch of the application of the TLC is shown in Figure 7-7.

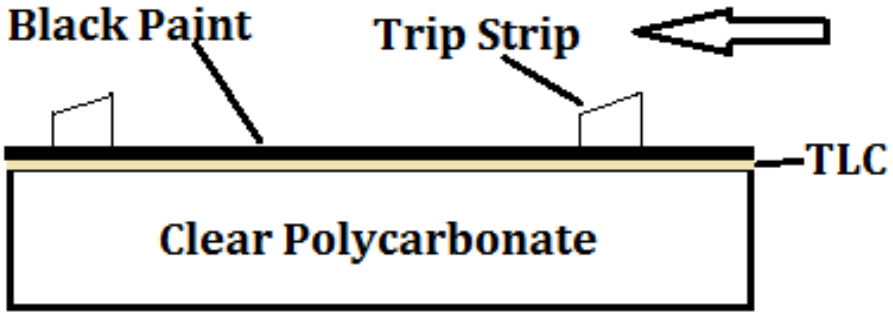

Figure 7-7: Detailed cross section of test piece showing application of thermochromic liquid crystal.

Two Canon SD430 wireless cameras are securely mounted on each side of the test piece. The cameras are set to record video images at 15 Hz. The thermocouple data acquisition system and the video cameras are synchronized via cold cathode fluorescent lamps (CCFL) that are used to illuminate the TLC and are triggered by a switch attached to an air bypass valve.

Prior to the start of a test, heated air is allowed to bypass the test section. Once the bypassed heated air temperature has stabilized at approximately 176 ºF (80 C) preparations for the start of a test begins. The test piece is also maintained at room temperature for an extended period prior to the start of a test to ensure a uniform initial temperature.

To begin a test, the thermocouple data acquisition system is activated and the cameras begin recording. Then a bypass valve is closed allowing heated air to enter the test piece. The operation of the bypass valve activates the CCFL lamps, which illuminate the test piece at the same time that the heated air enters the channel. Video images and thermocouple are stored for post-test processing.

In the case of the 90 degree entry, heated air exiting the bypass value is divided and enters the test piece as shown in Figure 7-8.

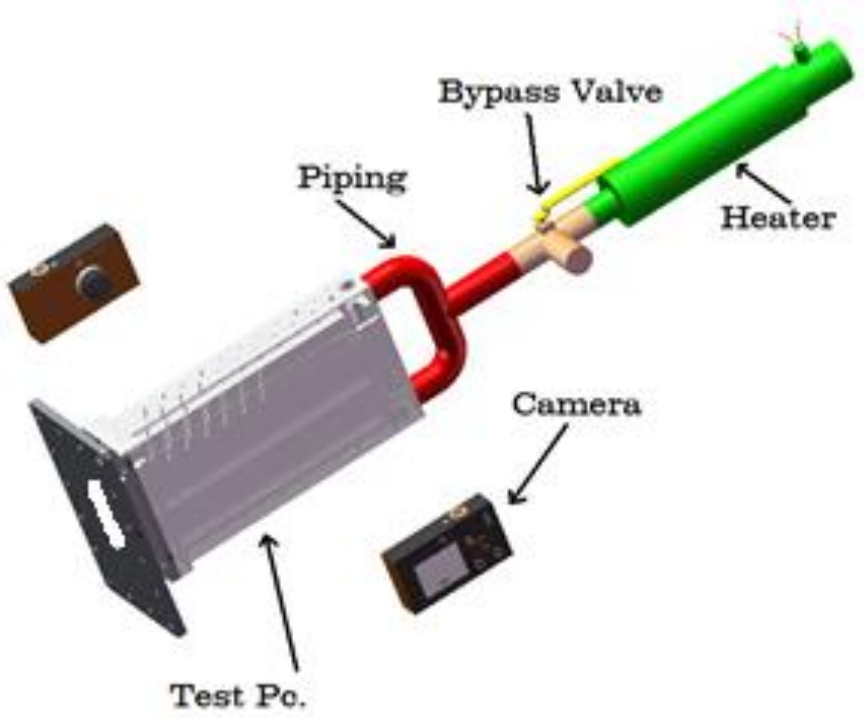

Figure 7-8: Concept sketch of test set up for the 90 degree entrance test.

Heat Transfer Coefficients

The local heat transfer coefficients across a liquid crystal coated target surface can be obtained using the 1-D transient heat conduction model of a semi-infinite solid with a convective boundary condition as given by:

$$\frac{\partial T}{\partial t} = -k\frac{\partial^2 T}{\partial x^2} \qquad \text{(Eq.1)}$$

with boundary and initial conditions:

$$T(x = 0, t = 0) = T_i$$

$$T(x = 0, t \to \infty) = T_\infty$$

$$T(x \to \infty, t) = T_i \qquad \text{(Eq. 2)}$$

$$-k\frac{dT}{dx}\bigg|_{x=0} = h(T_w - T_\infty)$$

The solution for the surface temperature response with regard to time suggested by Incropera [18] is:

$$\frac{T_w - T_i}{T_\infty - T_i} = 1 - exp\left(\frac{h^2\,\alpha t}{k^2}\right) erfc\left(\frac{h\sqrt{\alpha t}}{k}\right) \qquad \text{(Eq. 3)}$$

All variables shown in Equation 3 are available based on material properties or temperature data collected during the test, with the exception of the heat transfer coefficient (h). Duhamel's superposition theorem, Equation 4, can be applied and solved for the heat transfer coefficients at each pixel location of the video image.

$$T_w - T_0 = \sum_{j=1}^{N}\left[1 - \exp\left(\frac{h^2 \propto (t - \tau_j)}{k^2}\right) \times erfc\left(\frac{h\sqrt{\propto (t - \tau_j)}}{k}\right) \times (\Delta T_{\infty(j,j-1)})\right] \qquad \text{(Eq. 4)}$$

For turbulent fully developed flow inside a circular tube of diameter D and length L, the following relationship is suggested by Dittus.

$$Nu_D = 0.023\,\mathrm{Re}_D^{4/5}\,\mathrm{Pr}^n$$

$$\text{n = 0.3 for cooling the fluid and n = 0.4 for heating the fluid} \qquad \text{(Eq. 5)}$$

$$\left(0.6 < \mathrm{Pr} < 160, \mathrm{Re}_D > 10{,}000, \frac{L}{D} > 10\right)$$

The Nusselt number is the relationship between heat transfer caused by convection to those related to pure conduction. The Dittus solution for determining the Nusselt number in a round smooth pipe without any heat transfer enhancement provisions shown in Equation 5 will be the basis for normalizing the data obtained in this study. The Nusselt number for the smooth pipe relationship with an equivalent hydraulic diameter to the slot shaped test piece is referred in this paper as Nu_o. This value changes as the Reynolds number changes.

A single transient test using the liquid crystal method described earlier is used. Each pixel value is examined for its peak in local intensity. The intensity value is used in conjunction with a specifically written MATLAB program to determine the corresponding time at which the TLC turns green, indicating that the temperature at that particular pixel has reached the TLC specified value. By measuring the corresponding time required for the surface temperature to reach this temperature, the local heat transfer coefficient for each pixel in the image can be determined using Equation 4.

The heat transfer coefficient at each pixel is used to determine the Nusselt number at that pixel. The Nusselt number is defined as;

$$Nu = \frac{h\, d_h}{k_f} \qquad \text{(Eq. 6)}$$

where,

h = heat transfer coefficient

d_h = hydraulic diameter of the slot channel

k_f = the thermal conductivity of the fluid

The 1D semi-infinite solid assumption must be satisfied. In order to satisfy the semi-infinite assumption, the transient temperature must not penetrate through the thickness of the polycarbonate during the test duration. This is achieved by a sufficiently thick test piece of low thermal conductivity and diffusivity (0.201 W/mK and 0.1046 x10^{-6} m^2/s for polycarbonate, respectively). For the one-dimensional heat transfer assumption to be satisfied, conduction should only occur normal to the surface with all lateral conduction effects neglected. Although the test piece may actually experience some lateral conduction, it is assumed that the dominant temperature gradient is in the direction perpendicular to the surface, and lateral effects are negligible.

The initial temperature of the polycarbonate is uniform at ambient temperature, the incoming fluid temperature is higher and not a linear step increase. This is accounted for through the modification of Equation 3 by Duhamel's superposition theorem, Equation 4 which represents the temperature change as a series of steps where τ is the time step for each temperature step, $\Delta T_{m,i}$ is the temperature difference between each temperature step and the initial temperature, (T_i) The values of α, and k are characteristic of the polycarbonate plate.

Pressure Tests

A pressure tap is located at each end of the main channel, as shown in Figure 7-1. Inlet pressures and temperatures are used to determine air density values and used to determine Reynolds numbers and mass flow rates. Pressure drops along the main channel are recorded and used to determine the channel averaged Overall Thermal Performance (OTP). Equation 7 shows the relationship between the thermal enhancement value and the differential pressure loss.

$$\eta = \frac{\frac{Nu}{Nu_o}}{\left(\frac{\Delta P}{\Delta P_{\ smooth\ round\ pipe}}\right)^{1/3}} \qquad \text{(Eq. 7)}$$

Heat Transfer Contour Plots

Analyzing the Images

Once the equations are solved for the local heat transfer coefficient at each pixel the results can be plotted as a function of the heat transfer enhancement factor. To better understand the details of the heat transfer coefficient distributions, contour plots of the spatial distributions are presented.

Results and Discussion

Pressure Loss

The results of the pressure loss measurements are displayed in Figure 7-9. It is expected that the pressure loss would be significantly higher for the 90 degree entry cases. As seen in the chart, the pressure loss is approximately double when the 90 entry values are compared to the axial entry configurations.

The worst case occurs at the highest Reynolds numbers where the pressure loss more than triples for the 90 degree entry when the pentuple trip strips are compared to the axial entry case with pentuple trip strips, when values at Re = 50k are 9.35 H_2O" for the 90 degree case and 2.85 H_2O" for the axial enter case.

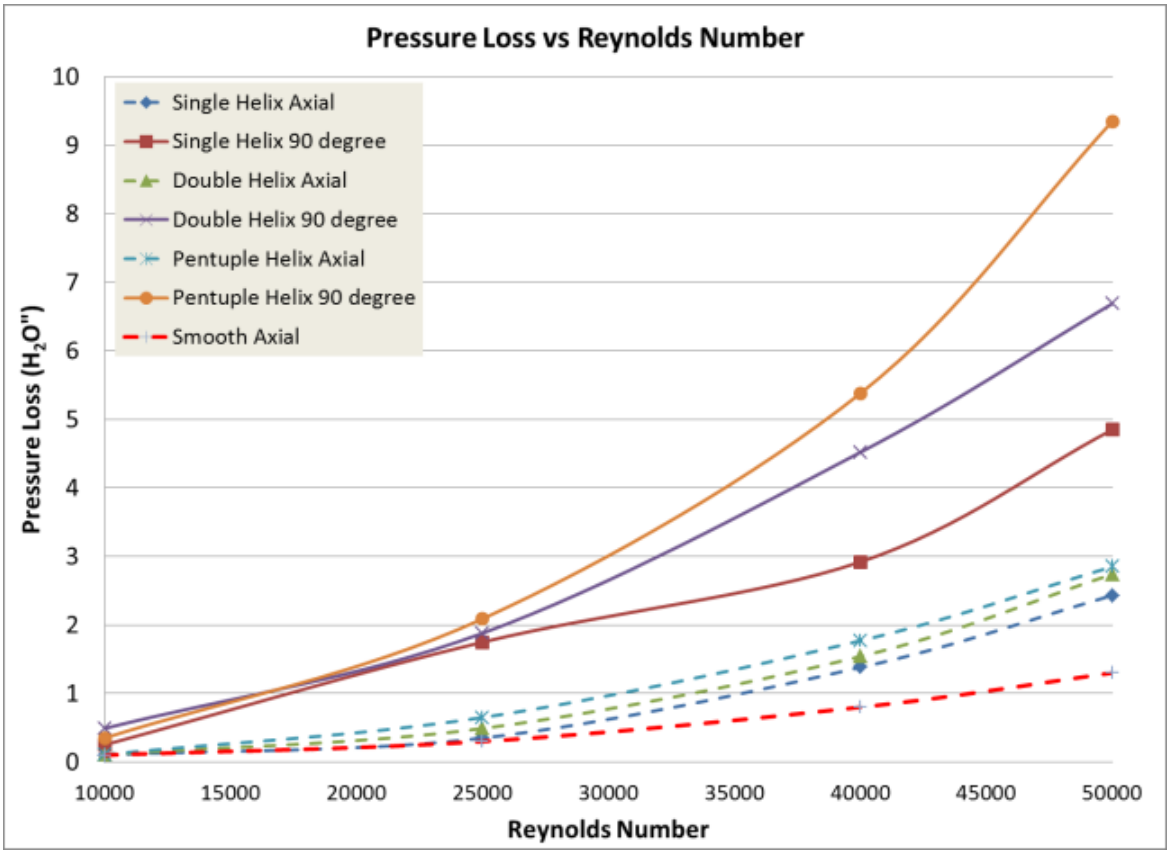

Figure 7-9: Pressure Loss vs. Reynolds Number for all Seven Configurations Tested.

Smooth Channel – Axial Inlet

For comparison purposes Nu/Nu_o plots of the slot shaped channel with a 0.5" (13 mm) radiused entry and air entering thorough a axial entry is shown in figures 7-10 – 7-13. The radiused entry reduces the turbulence at the entry, but does not eliminate heat transfer from occurring at the entrance. In all cases shown, the heat transfer enhancement becomes negligible near the exit.

The Nu/Nu_o values are 1.04, 1.11, 1.28, and 1.32 for Re=10k, 25k, 40k, and 50k respectively. In all four cases presented, the smooth channel with no heat transfer enhancement strategies show some high Nu/Nu_o values at the entrance to the channel and then gradually reduces to no significant enhancement near the exit of the channel.

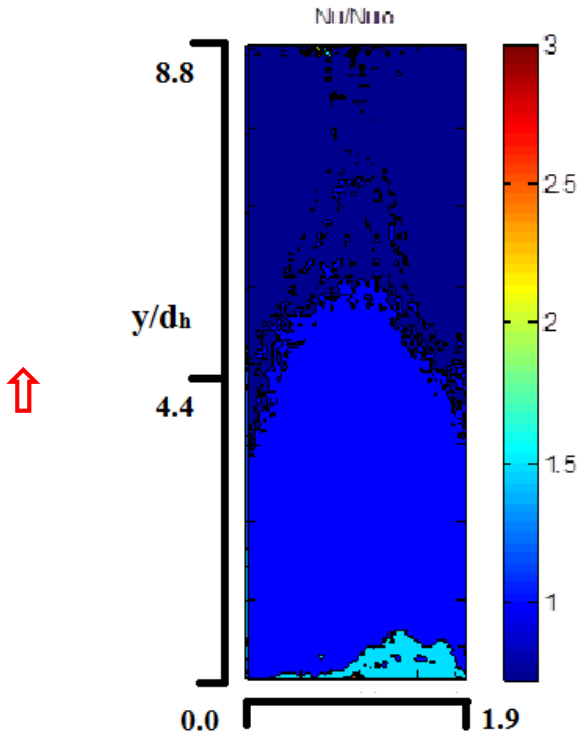

Figure 7-10: Heat Transfer Enhancement (Nu/Nu_o) for a Smooth Slot Channel, Re = 10k ($h_{avg.}$ ~ 40).

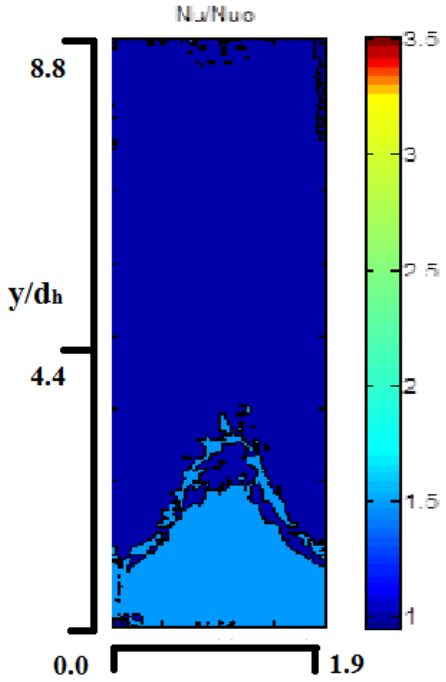

Figure 7-11: Heat Transfer Enhancement (Nu/Nu_o) for a Smooth Slot Channel, Re = 25k ($h_{avg.}$ ~ 75).

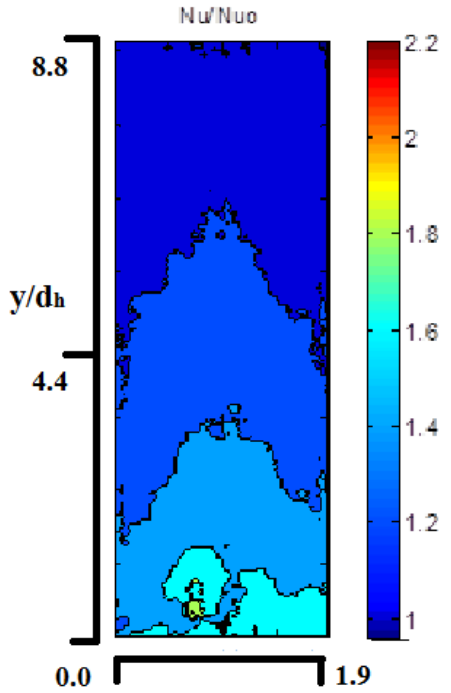

Figure 7-12: Heat Transfer Enhancement (Nu/Nu_o) for a Smooth Slot Channel, Re = 40k ($h_{avg.}$ ~ 127).

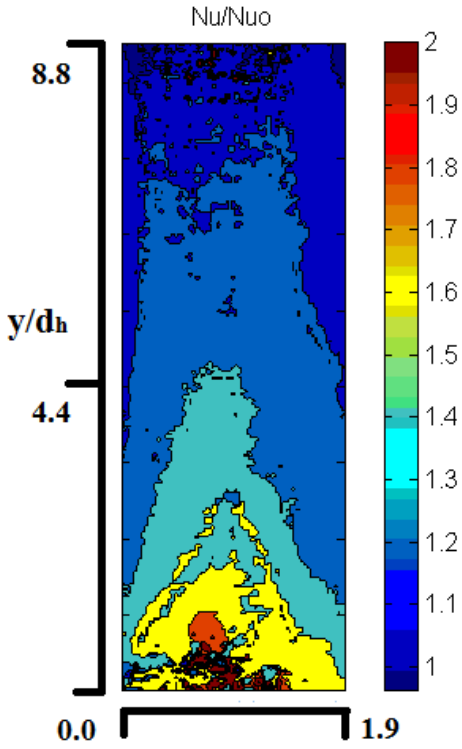

Figure 7-13: Heat Transfer Enhancement (Nu/Nu_o) for a Smooth Slot Channel, Re = 50k ($h_{avg.}$ ~ 160).

Single Helix – Axial Inlet

Plots of the normalized Nusselt number are presented for the single helix with axial flow entry in Figure 7-14. In reviewing the plot of Re = 10k in Figure 7-14, it is noted that as the fluid enters the channel minimal enhancement is apparent prior to the fluid contacting the first helix of the trip strip.

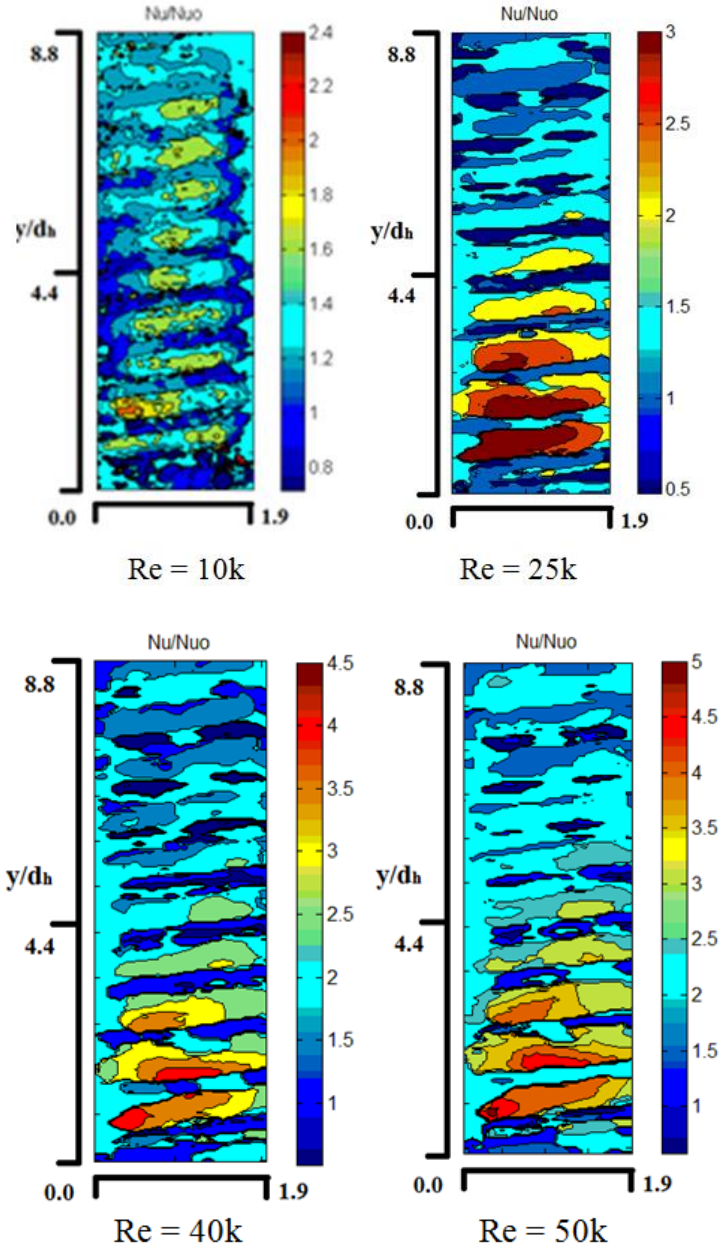

Figure 7-14: Heat Transfer Enhancement (Nu/Nu_o) for a Single Helix with Axial Entry at various Reynolds Numbers.

The enhancement quickly improves once the first helical strip is encountered and values of Nu/Nu_o 1.8 are noted locally in the channel. As the flow progresses the effect of the enhancement is reduced and stabilize to a range of 1.3 near the exit of the channel. The mean Nu/Nu_o for this configuration is 1.10, with an overall thermal performance factor of 1.10 at Re=10,000.

As the Reynolds number was increased to 25,000 and beyond, the same trend as in the 10,000 Reynolds number case was observed. For the 25,000 Reynolds number case the overall mean thermal performance increased to 1.71 with a mean heat transfer enhancement value of 1.62. As expected, the same lack of significant enhancement is noted at the entry in the figure. The enhancement sharply increases following the first trip strip to values of greater than three and maintain local values in excess of 1.5 throughout the channel to the exit, but these local areas diminish in size as the flow progresses through the channel.

As the Reynolds number is increased to 40,000 and 50,000 the increase in mean overall thermal performance increases significantly to 2.34 and 2.66, respectively. As seen in Figure 7-14, a small region of an enhancement value of five is noted after the first trip strip and diminishes as in previous plots. Very small regions of high Nu/Nu_o values exceeding two are noted near the exit.

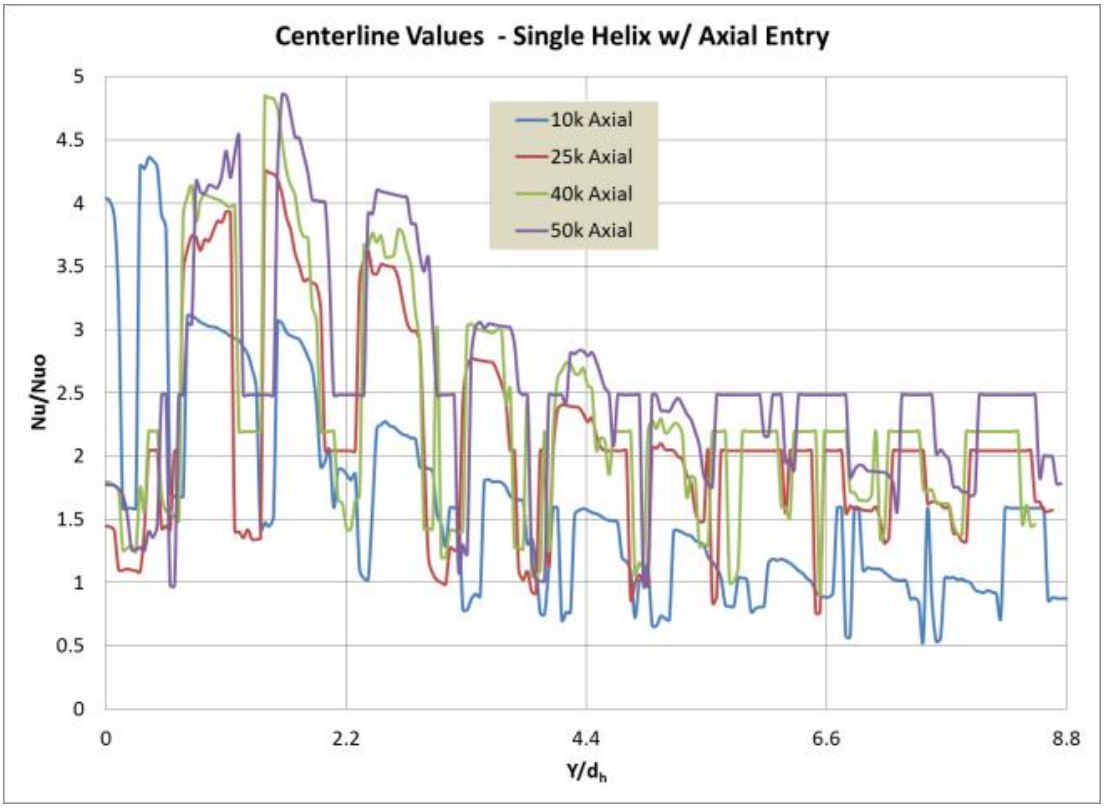

Figure 7-15: Line Plots of Centerline Values of Nu/Nu_o vs. Position along the Flow Path Axis for the Single Helix with Axial Entry.

One way to compare the performance of this grouping of test is to plot the centerline values of Nu/Nu_o vs. position along the flow path. Figure 7-15 shows all four single helix tests superimposed onto a single graph. The peaks occur in between the trip strips and the valleys indicate the location of the trip strips. Wide peaks indicate localized uniformity of heat transfer enhancement.

Single Helix – 90 Degree Inlet

Converting the test piece from the axial entry with a 0.5" radius to the 90 degree entry involves changing the entry adapter. The air will now enter the test piece as shown in Figure 7-1. The air must make two 90 degree turns prior to entering the main channel of the test piece. This creates substantial turbulence, which leads to high heat transfer enhancement at the channel entry.

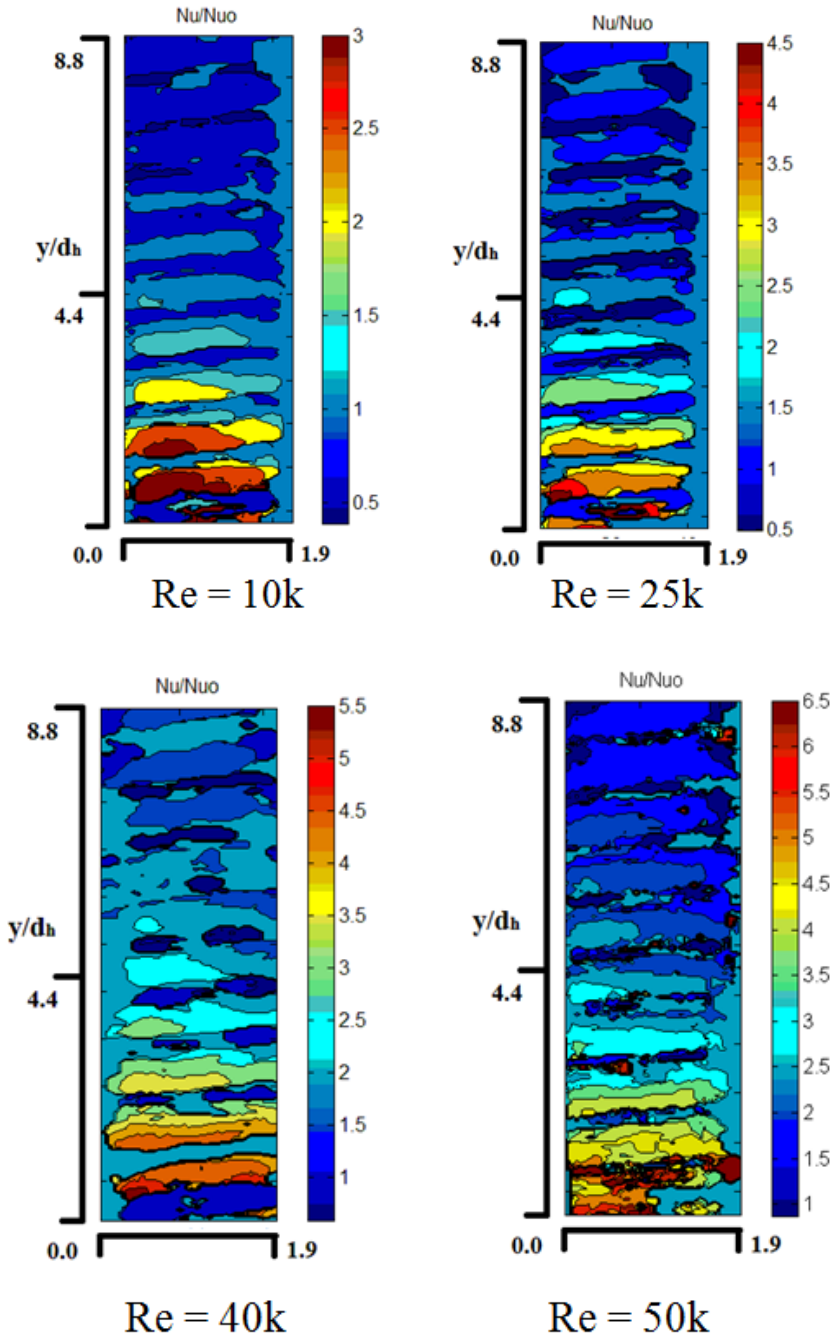

Figure 7-16: Heat Transfer Enhancement (Nu/Nu_o) for a Single Helix with 90 Degree Entry at various Reynolds Numbers.

Much higher enhancement values are observed at the entry when the 90 degree entry configuration is used in conjunction with the single helix trip strips. There is increased turbulence

caused by the two opposing flow regimes as the air enters the main slot shaped channel. High heat transfer values are apparent before the flow encounters the first trip strip. This initial turbulence enhances the heat transfer characteristics throughout the rest of the channel.

The color contour plots in Figure 7-16 show the heat transfer enhance in the channel when the single helix trip strips are used in conjunction with fluid flow entering the channel at a 90 degree angle relative to the main channel flow direction. The channel averaged heat transfer enhancement values are 1.26 for the 10,000 Reynolds number case and 2.46 for the 25,000 Reynolds number case. The overall thermal performance values are 0.93 for the 10,000 Reynolds number tests and 1.36 for the 25,000 Reynolds number test.

At the higher Reynolds numbers the heat transfer enhancement values did not show much higher values than the Re = 25k case. The Re= 40k average Nu/Nu_o value was slightly less than that of the Re=25k case at 2.35 and the Re = 50k value is 2.85. However, when pressure losses are taken into account the overall thermal performance values were markedly higher than the Re = 25k case with OTP values for the Re = 40k test of 1.52 and for the Re = 50k test an OTP value of 1.84.

In all cases the heat transfer distribution along the entire channel was not uniform, with values near the entry typically two to three times higher than values near the channel exit.

The centerline values of Nu/Nu_o are shown in Figure 7-17. In many cases the centerline plots may be a better indicator as to the uniformity of heat transfer enhancement.

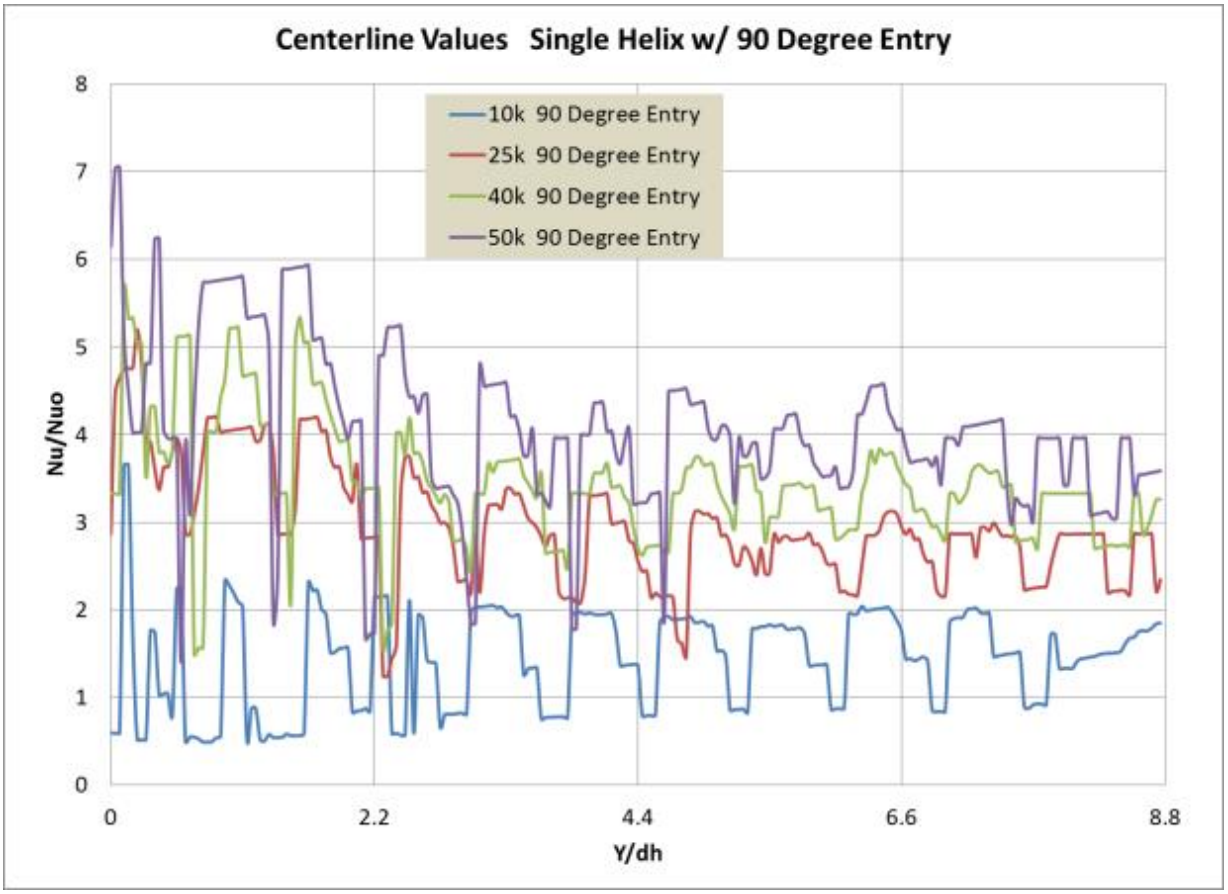

Figure 7-17: Line Plots of Centerline Values of Nu/Nu_o vs. Position along the Flow Path Axis for the Single Helix with 90 Degree Entry.

Double Helix – Axial Inlet

Figure 7-4 shows the layout of the double helix trip strips. Even though the spacing of the strips is maintained at a pitch of 0.75", each separate strip has its individual pitch of 1.5". This allows turbulence created on one wall by the inclusion of a trip strip in the flow path to influence the flow stream on the opposite wall of the test piece.

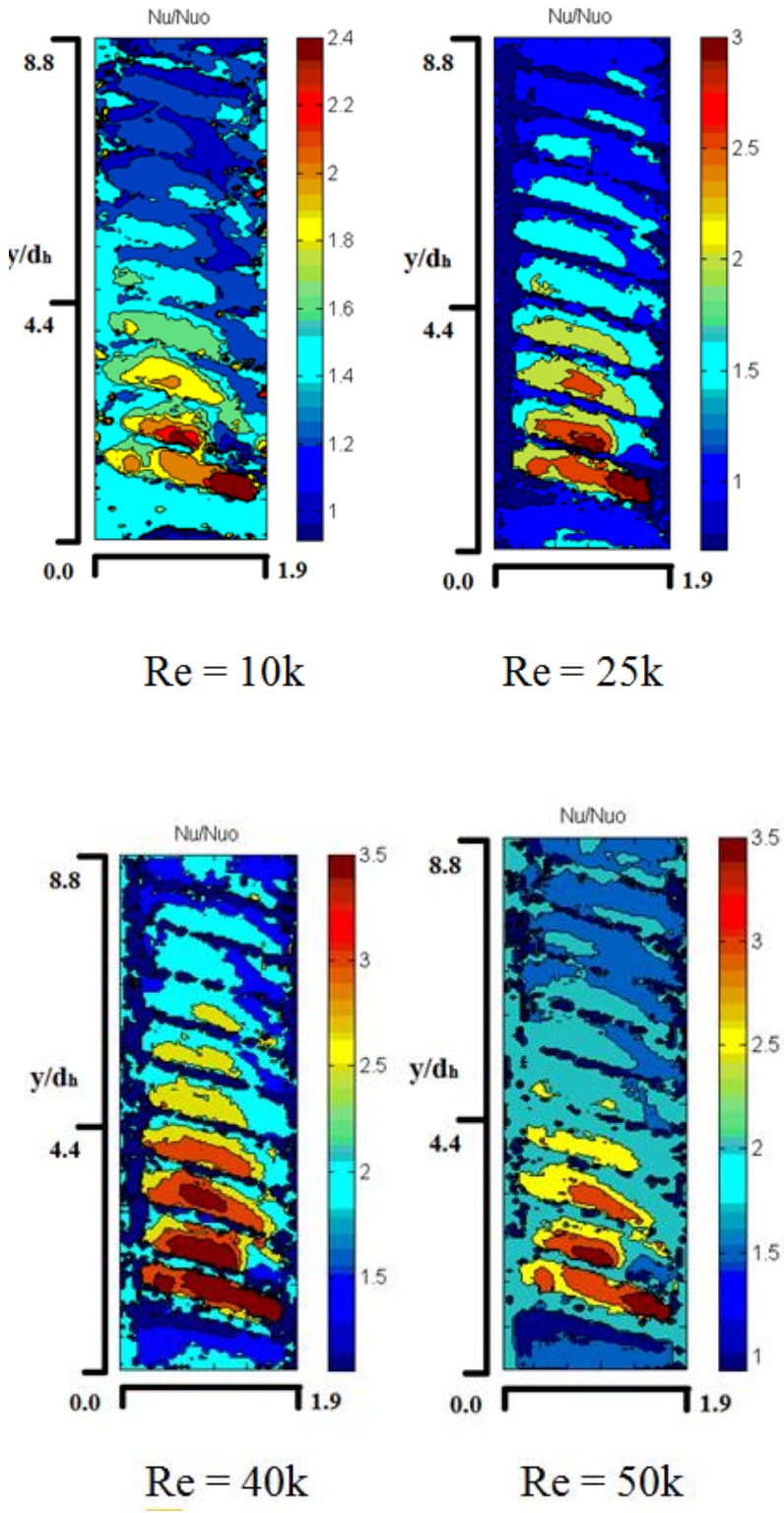

Figure 7-18: Heat Transfer Enhancement (Nu/Nu_o) for a Double Helix with Axial Entry at various Reynolds Numbers.

The double helix trip strip configuration exhibited the best heat transfer enhancement and the best overall thermal performance values of all three trip strips tested. Figure 7-18 shows the color contour plots of Nu/Nu_o vs. position along the flow path for all four Reynolds numbers tested with the axial entry. The tendency of high Nu/Nu_o local values occurring just after the first trip strip are present here also.

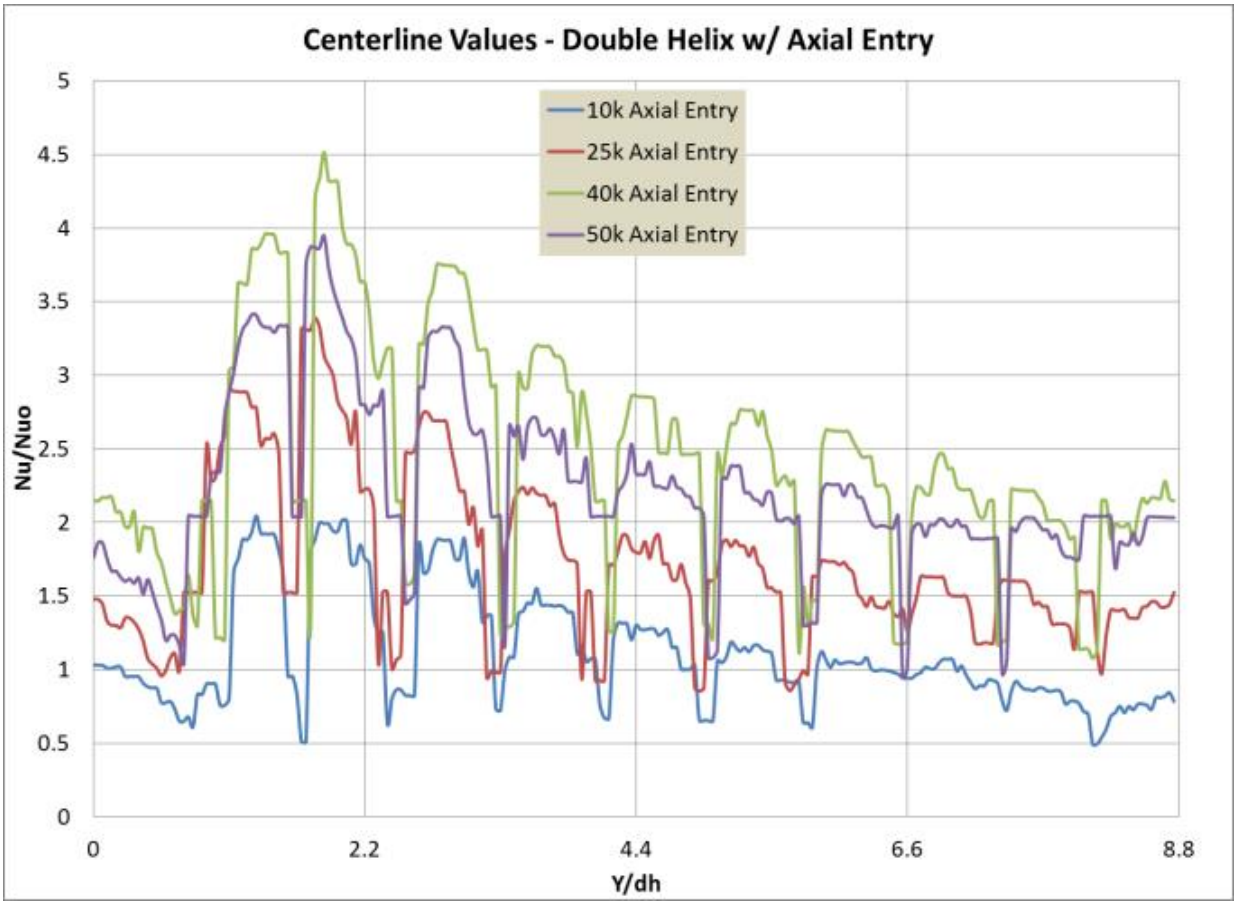

Figure 7-19: Line Plots of Centerline Values of Nu/Nu_o vs. Position along the Flow Path Axis for the Double Helix with Axial Entry.

Double Helix – 90 Degree Inlet

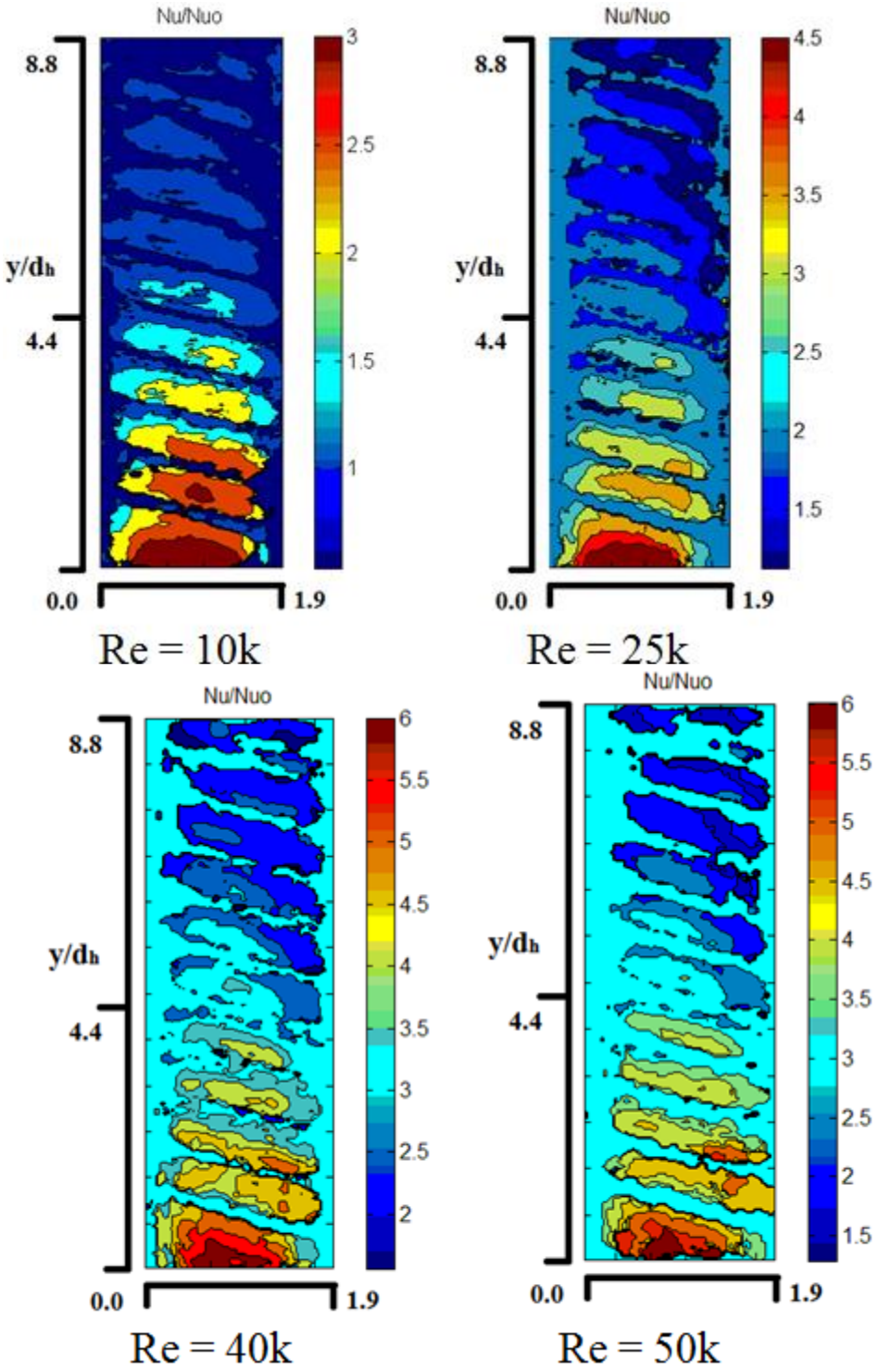

Figure 7-20: Line Plots of Centerline Values of Nu/Nu_o vs. Position along the Flow Path Axis for the Double Helix with 90 Degree Entry.

Test results yield a heat transfer enhancement value of 1.48 for Re = 10k, 1.53 for Re = 25k, 2.15 for Re = 40k, and 2.04 for Re = 50k. The overall thermal performance was very high with values of 1.45, 1.29, 1.73, and 1.59 for Reynolds numbers of 10k, 25k, 40k, and 50k, respectively.

The centerline values of Nu/Nu_o are shown in Figure 7-19. For the higher Reynolds number cases, Nu/Nu_o values of greater than two are maintained throughout the channel.

The double helix combined with the 90 degree entry configuration had superior heat transfer enhancement to all other combinations tested. The heat transfer distribution in the channel was the most uniform of all tests, especially at the higher Reynolds numbers. This is shown in the images in Figure 7-20.

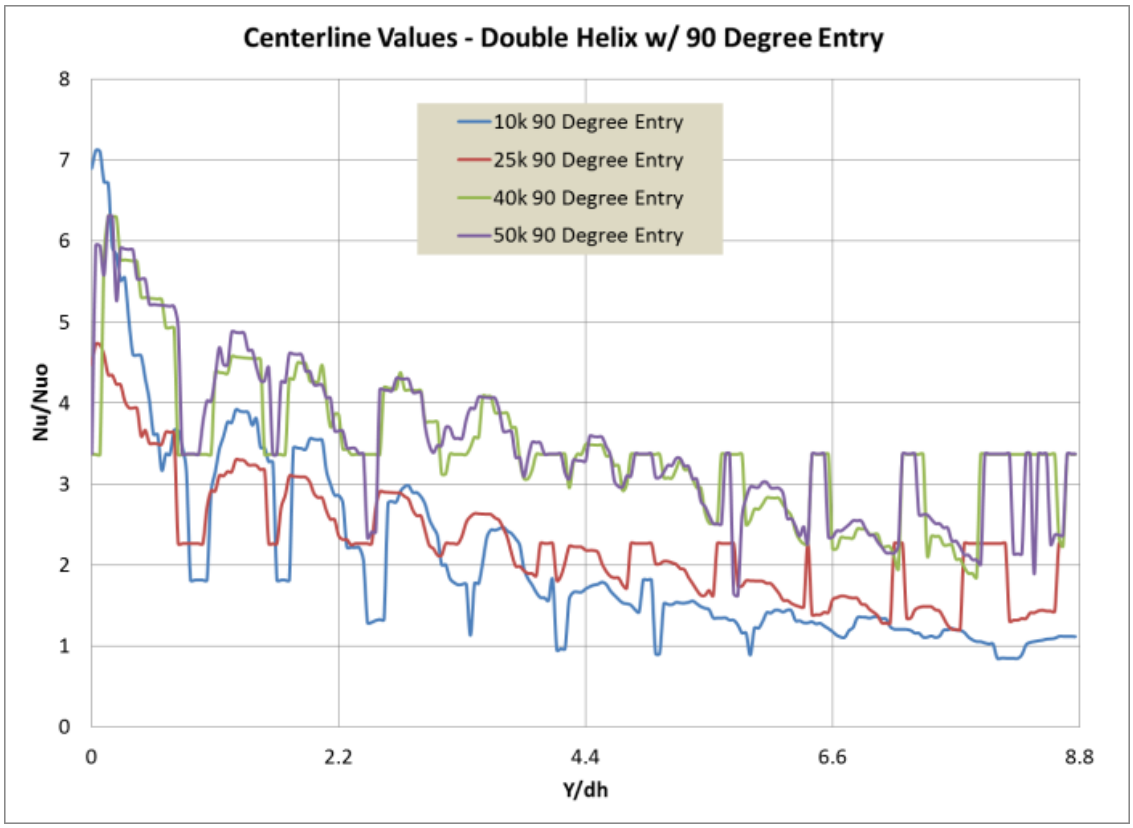

Figure 7-21: Line Plots of Centerline Values of Nu/Nu_o vs. Position along the Flow Path Axis for the Double Helix with 90 Degree Entry.

Nu/Nu_o values for the Re = 10k test were 2.05, which is considerably higher than the 1.48 value for the double helix strips used in conjunction with the axial entry. The values of the normalized Nusselt numbers for the Re= 25k, Re = 40k, and Re = 50k tests were 2.26, 3.37 and 3.37, respectively. The overall thermal performance (OTP) values were also the highest of the various test configurations with values of 1.21, 1.23, 1.89, and 1.95 for the 10k, 25k, 40k, and 50k Reynolds number test, respectively.

The centerline values of the double helix, 90 degree entry configuration are shown in Figure 7-21. At the higher Reynolds numbers the ribs, which act as thin fins, conducted enough of the heat onto the outer wall to substantially add to the overall performance. This can be seen by observing the small amplitude between the peaks and valleys in the centerline plots.

Pentuple Helix - Axial Inlet

The complexity of the trip strip profile can be seen in the transparent view of the test piece utilizing the pentuple trip strips in Figure 7-5. The pitch of the strips remains at 0.75", but each individual strip has a pitch of 3.75". This causes the angle of the individual strips to be at a 64 degree angle relative to the flow path. This strategy creates a chaotic path for the fluid which resulted in a more equal distribution of heat transfer in the channel. The penalty was the increase in pressure loss.

The images in Figure 7-22 detail the Nu/Nu_o behavior using the pentuple trip strip arrangement with the fluid entering the channel axially. Other than the initial high heat transfer areas at the beginning of the channel, the remainder of the channel exhibits a more uniform distribution than all of the other configurations tested.

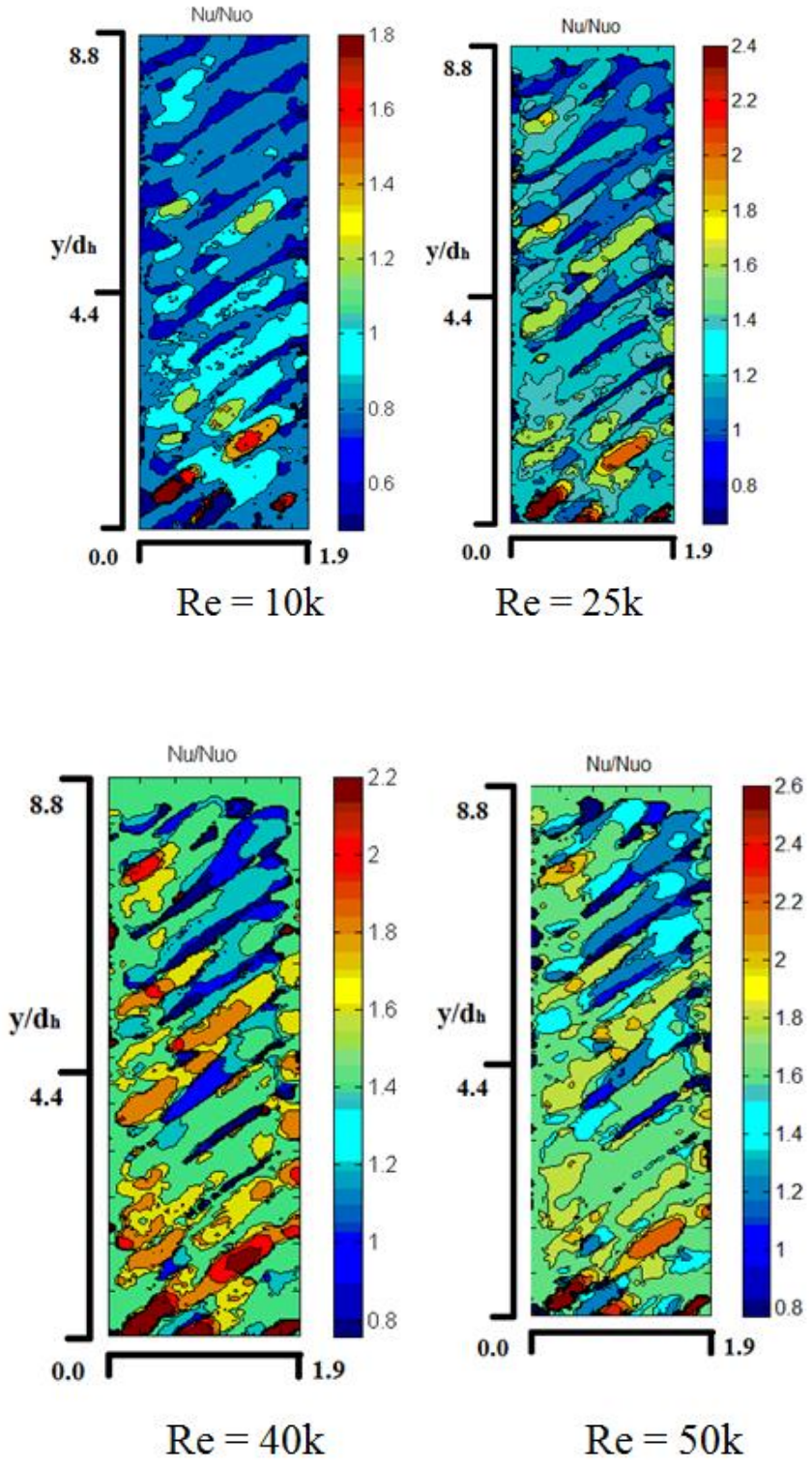

Figure 7-22: Heat Transfer Enhancement (Nu/Nu_o) for a Pentuple Helix with Axial Entry at various Reynolds Numbers.

The 50,000 Reynolds number test provided the best results for this configuration yielding a channel averaged normalized Nusselt value of 1.63, which translated to an OTP value of 1.26. The other configurations had values of Nu/Nu_o of 1.01, 1.33, and 1.63 for Re = 10k, Re= 25k, and Re = 40k, respectively. Consequently, the pressure losses proved to negate any obvious advantages to these configurations with OTP values of 0.98 for the 10,000 Reynolds number cases, 1.03 for the 25,000 Reynolds number cases, and 1.18 for the 40,000 Reynolds number cases.

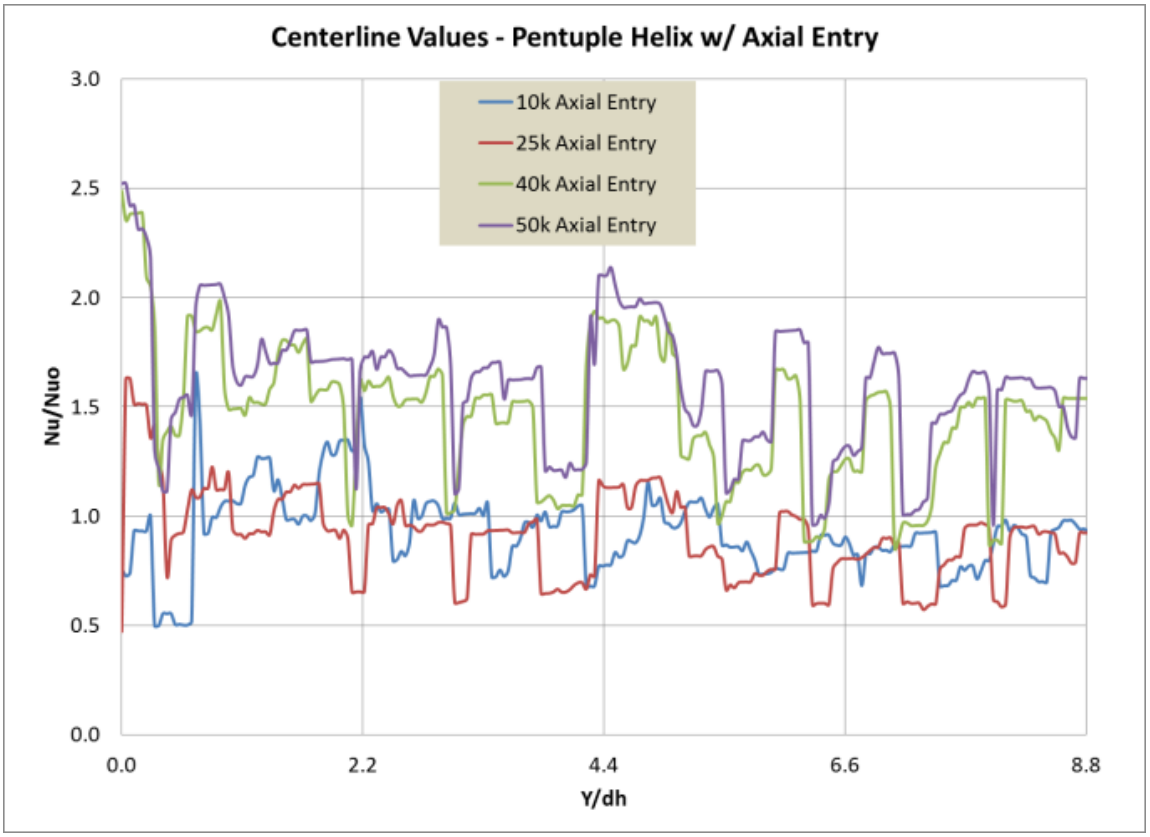

Figure 7-23: Line Plots of Centerline Values of Nu/Nu_o vs. Position along the Flow Path Axis for the Pentuple Helix with Axial Entry.

The centerline values shown in Figure 7-23 depict a relatively uniform trend of values for all Reynolds numbers, with the 40,000 and 50,000 Reynolds number test showing the best results in the pentuple helix test.

Pentuple Helix – 90 Degree Inlet

Except for the high localized heat transfer areas near the entrance to the channel, the 90 degree inlet test using the pentuple helix displayed similar results to that with the axial entry regime. As shown in Figure 7-24, the distribution of heat transfer was reasonably uniform when compared to the other two trip strip strategies.

The channel averaged heat transfer enhancement (Nu/Nu_o) values ranged from 1.17 for the Re = 10k test to 2.32 for the Re = 50k test. The Re = 25k test presented a value of 1.44 and the Re = 40k test a value of 1.96. When considering these values alone without the penalty of the pressure loss, they seem quite good at the higher Reynolds numbers. When the pressure losses are incorporated using Equation 7 the OTP values yield 1.20 for Re = 50k and 1.04 for Re = 40k. The lower Reynolds numbers came in with OTP values of 0.77 for Re = 10k and 0.75 for Re = 25k. This configuration would only benefit applications where pressure loss is not a primary consideration.

The centerline values of Nu/Nuo are shown in Figure 7-25. The downward trend in values as the flow goes from the test piece entry to the exit is typical, as energy is lost along the flow path. This is typical of every trip strip type turbulence enhancer. With side jets however, this problem can be overcome by varying the size of the jets along the flow path such that a higher blowing ratio is obtained further down the flow path. This is one advantage offered by side jets that is not possible with trip strips.

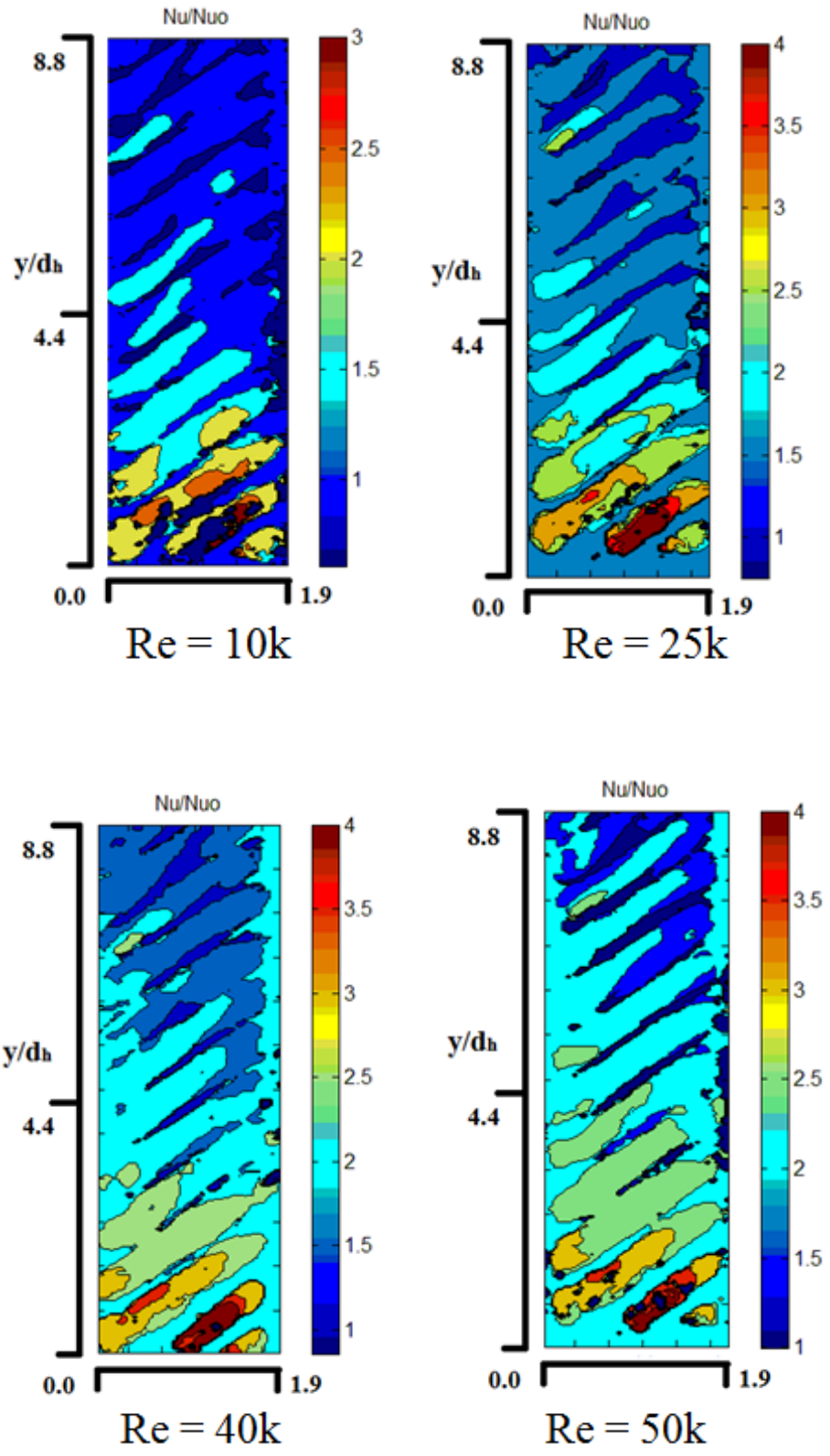

Figure 7-24: Heat Transfer Enhancement (Nu/Nu_o) for a Pentuple Helix with 90 Degree Entry at various Reynolds Numbers.

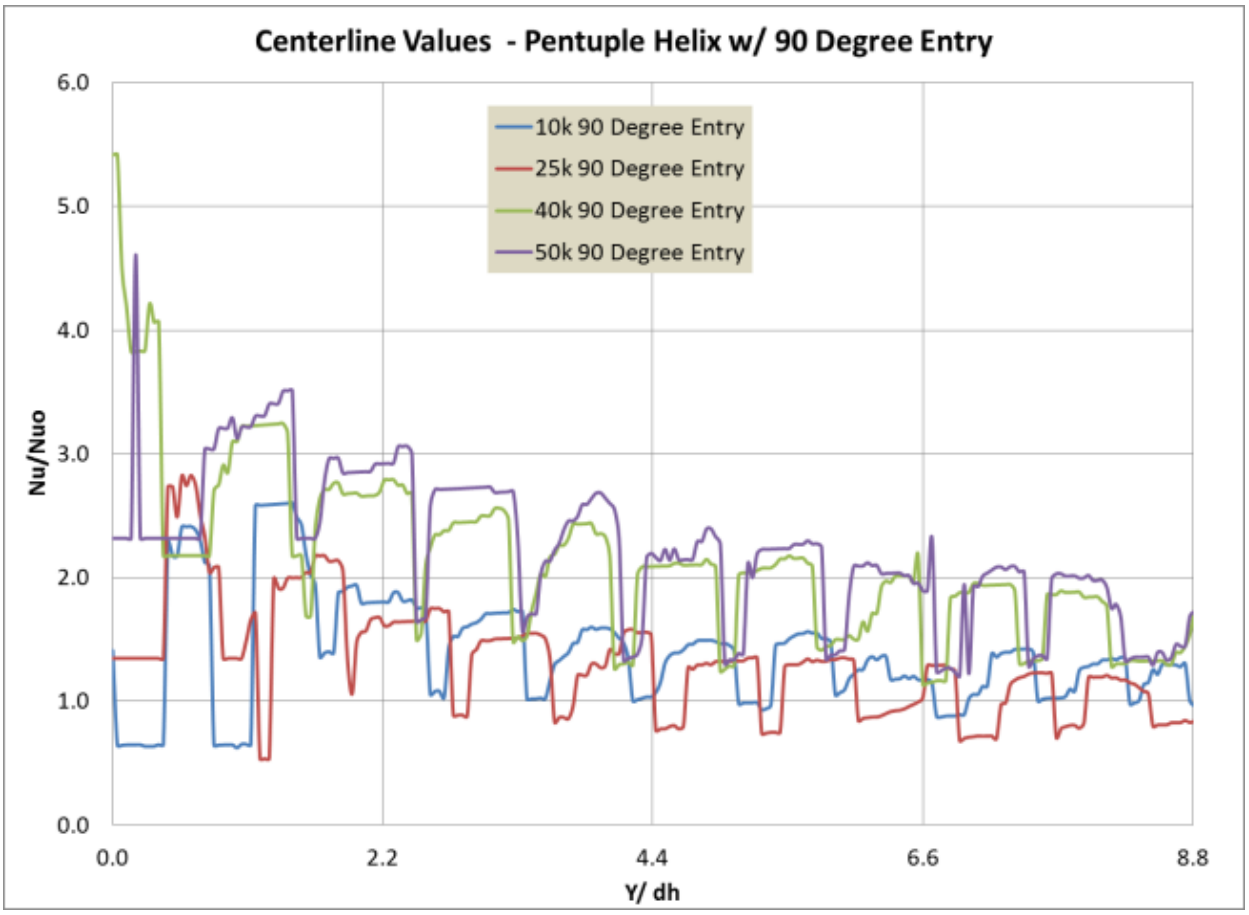

Figure 7-25: Line Plots of Centerline Values of Nu/Nu_o vs. Position along the Flow Path Axis for the Pentuple Helix with 90 Degree Entry.

When pressure losses are considered the Nu/Nu_o values presented in Figure 7-26 can be used in Equation 7 to obtain OTP values. Figure 7-27 summarizes the OTP values verses Reynolds number for all three trip strip strategies and both entry flow regimes. When the data points are connected using a curve fit the same cyclical trends seem to form.

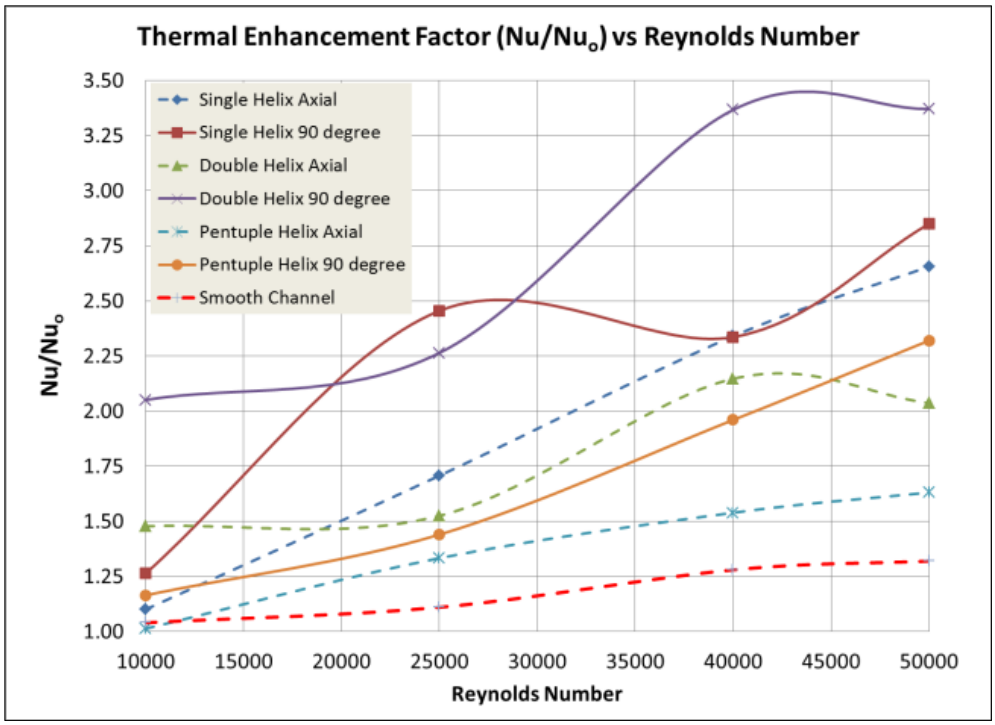

Figure 7-26: Thermal Enhancement Factor vs. Reynolds Number for all Seven Configurations Tested.

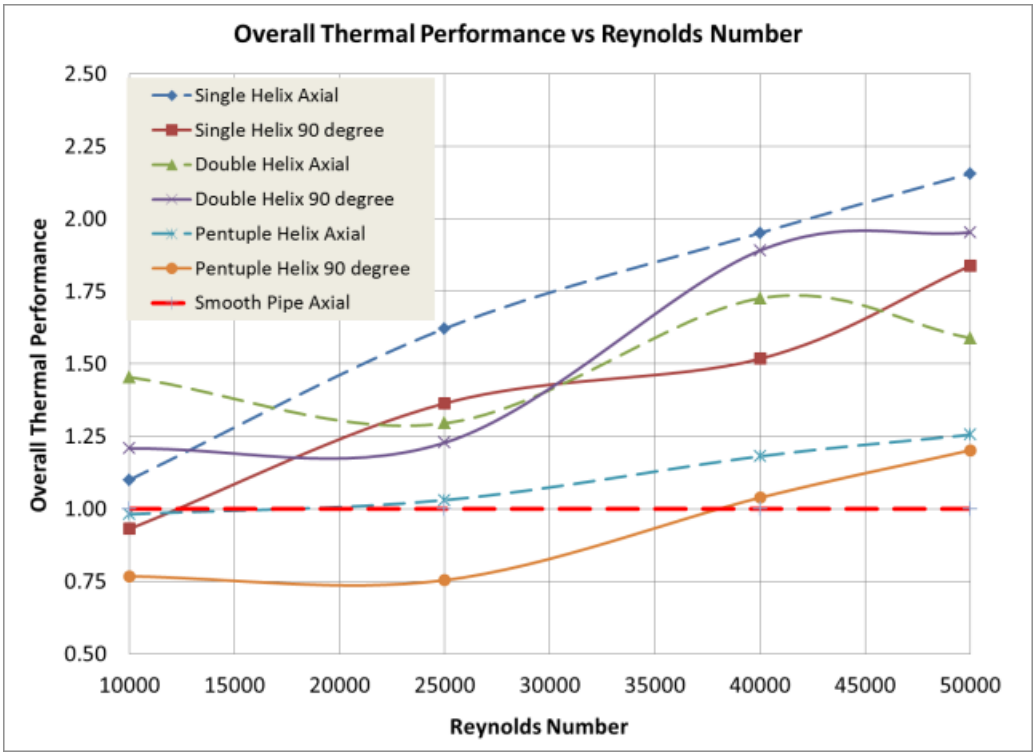

Figure 7-27: Overall Thermal Performance vs. Reynolds Number for all Seven Configurations Tested.

Experimental Uncertainty and Error

An accurate assessment of uncertainty in liquid crystal measurement of heat transfer coefficients is essential because many factors affect the TLC results. A large number of studies have concluded that a properly performed test yields mean uncertainty of up to 11.0% for values of h, and up to 9% for temperatures. Smith [19], et al, compiled a table summarizing uncertainty studies of h and T when narrow band TLC methods were used. Thermocouple accuracy and repeatability are large contributors to uncertainty as well as illumination spectral effects. The wall mounted thermocouples were used to compensate for this effect and resulted in a 0.2° C temperature correction.

Some parameters that should be included in the uncertainty analysis include fluid density, fluid velocity, mass flow rate, material properties of the test piece, thermocouple accuracy, calibration of the TLC, and time.

The fluid density, fluid velocity, and mass flow rate uncertainties can be lumped together into the uncertainty in measuring the Reynolds number. The calibration of the TLC and the thermocouple accuracy can also be lumped into a category of “temperature”. The uncertainty of the material properties and time are of less significance, but should not be ignored.

The overall relative uncertainty can be determined by using the Kline and McClintock method. Kline and McClintock [17] suggested the description of uncertainty by specifying the

mean of the readings, along with an uncertainty interval based on certain predefined odds. Each variable should thus be reported as shown in the equation below:

$$U = [(u_1)^2 + (u_2)^2 + \ldots.]^2 \qquad \text{(Eq. 8)}$$

Where:

U is the overall uncertainty

u is the uncertainty in the measured value (i.e. +/- 2 degrees)

Table 1 lists the items and uncertainty percentage used in the calculations of uncertainty in the experiments.

Table 7-1 : Variables used to determine experimental uncertainty.

Variables	Uncertainty (%)
Kinematic viscosity of air, μ	±2.9
Thermal conductivity of air, k_a	±3.0
Thermal conductivity of PC, k_t	±4.6
Thickness of liquid crystal, d_t	±3.5
Air mass flow rate, kg/s	±3.0
Liquid crystal temperature, TLC	±0.27
Air temperature, T_b	±3.0
Test Piece wall temperature, T_w	±2.5

It is not unusual to have uncertainty values in the range of 5% - 6% in TLC experiments. The overall uncertainty will depend on the accuracy of the equipment used and data obtained during the experiment.

A minimum of two of each tests was conducted to evaluate the repeatability of each test. Heat transfer values typically were repeatable within 3% for tests for Reynolds numbers of 10k and increased to 6% for Reynolds numbers of 50k. Estimates of the uncertainty in the Nusselt number parallel that of heat transfer coefficients.

Conclusion

There exists a substantial heat transfer benefit because of the opposing passages and 90 degree turn at the inlet of the slot shaped when compared to the axial entry and a smooth round pipe of equal hydraulic diameter. The pressure losses are upward of three times higher in the case of the higher Reynolds numbers tested. Despite these higher pressure losses, the enhancement gained by the high turbulence at the entry continued to aid the heat transfer in the entire channel and was enough to yield superior overall thermal performance values in the case of the double helix.

The test did not yield the same results for the single and pentuple helix configurations. The axial entry was better than the 90 degree entry for all Reynolds numbers tested with the single helix. The results with the pentuple helix were about the same for the axial entry and the 90 degree entry tests. The pentuple helix only performed about as well as the smooth channel when overall thermal performance values are compared. But, the pentuple helix exhibited a more uniform heat transfer distribution in the channel when used in conjunction with the 90 degree entry.

A plot of the data points seem to indicate cyclical trends are present in both Nu/Nu_o and OTP values that follow changes in Reynolds number.

Chapter 8 – Jets with Radial Flow Entry with Various Blowing Ratios

Introduction

Heat transfer results for a given slot shaped channel with a 3:1 aspect ratio and jets issuing from side walls are presented. Two different jet configurations are used as a means to enhance turbulence in the main flow stream. The Reynolds numbers investigated range from 10,000 to 50,000 and are based on the mean velocity of the fluid at the channel inlet for the slot shaped channel without enhancement, or when swirl-jets are used, the equivalent mass flow rates at the exit of the main channel. Blowing Ratios, defined as the mean side jet velocity verses the mean main channel velocity, ranged from 8.6 to 30.2. This heat transfer enhancement strategy has proven to be effective in round channels.

A transient technique combined with Duhamel's superposition theorem was used to obtain the heat transfer coefficient distributions. Narrow-band liquid crystals were used to map the transient surface temperatures and were combined with thermocouples that measured the center-line air temperatures along the flow path in the main channel. The results of the passage with jet enhancements were compared to the smooth slot channel, without any type of heat transfer enhancements. The tests results reported in this paper show mean heat transfer enhancement values ($Nu/Nu_{o\ smooth}$) greater than 4.2 and low normalized friction factors. Thermal performance factors ranged from 1.55-3.69 for the various configurations studied. These results show significant improvements over other types of heat transfer enhancement

methods currently used in the mid-span section of turbine blades.

Configurations Studied

A 3:1 AR single passage channel with a hydraulic diameter, $d_{h,}$ of 0.0248m and an L/d_h of 8.7 is chosen for this study.

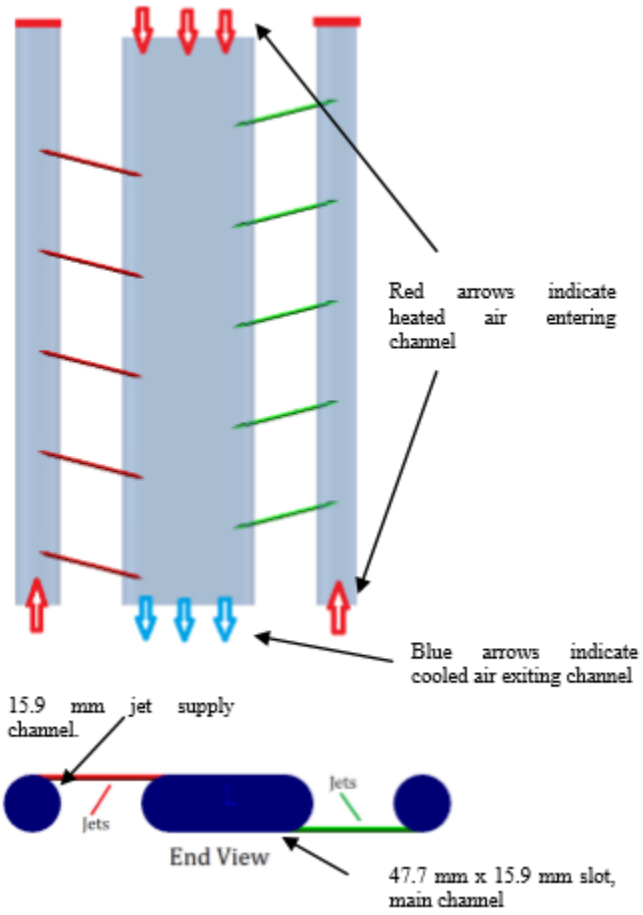

Figure 8-1 : Top and end view of typical fluid passages.

The configurations investigated to enhance heat transfer include fluidic-swirl-generation strategies where swirl is generated by introducing tangential jets along the side walls of the main coolant passage. Figure 8-2 shows the generic flow path of the fluid.

The two fluidic swirl-generation configurations are shown in figure 8-3, where the different configurations are shown and labeled as A and B.

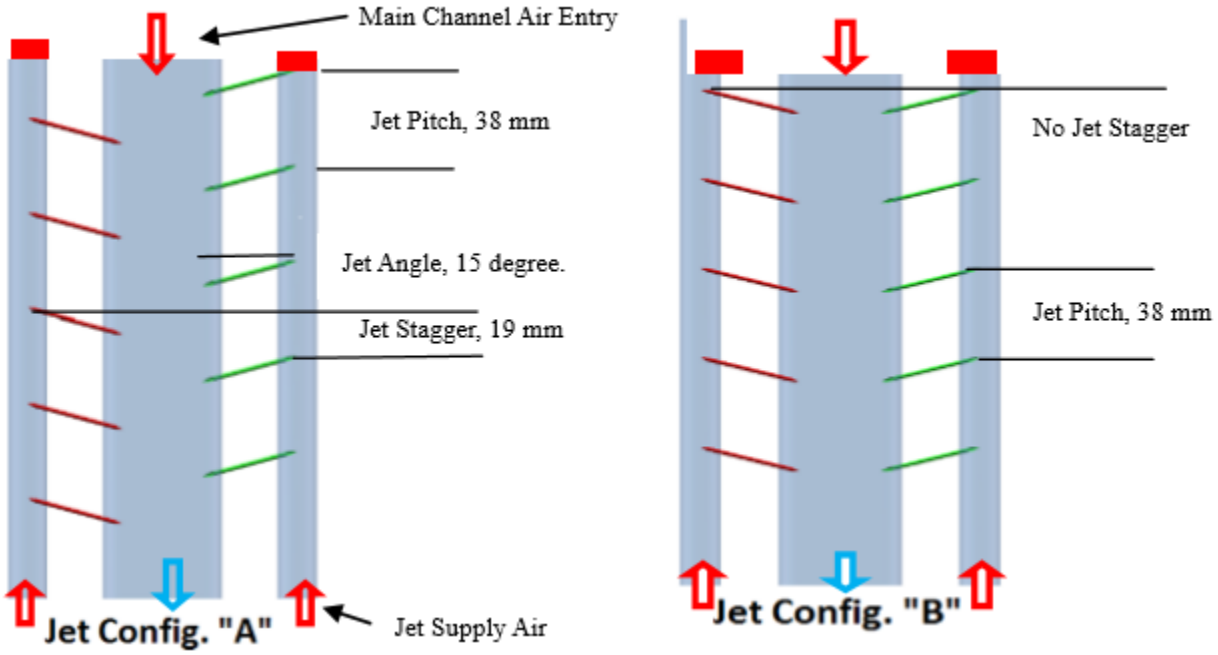

Figure 8-2 : Jet Configuration Schemes

In both configurations, air enters the main channel radially through a 3:1 AR slot shaped passage as well as through tangential side jets introduced through several holes placed axially along the neighboring (side) channels. Flow through the side-channels feeding the jet-holes was opposite to the main channel flow direction. The side-jets are introduced tangential to the main flow to produce a swirling motion, and are oriented at a 15 degree angle to the streamwise direction. In addition to the swirl, the jets are angled towards the main flow to generate counter-shear and associated turbulence. In figure 8-2, the red and green lines indicate the location of the jets entering the main channel. The pitch and offset of the jets are described in detail in the

experiments section. The tangential jet from the left is introduced along the top surface of the channel while the tangential jet from the right is introduced at the bottom of the channel. The two configurations differ in the relative offset between the left and right jets.

A channel-average blowing ratio, jet velocity to main channel velocity, was varied in each test. The average blowing ratio was calculated based on the measured mass flow rates in the main channel and the side channels, and is an average value across all the jet-holes. The individual jet-blowing ratio may vary from hole to hole depending on the pressure drop across the holes.

The minimum blowing ratio selected was a value that created a high enough jet exit velocity to ensured that the jet penetrated the main flow field to the other side, and potentially created an impingement effect. As a basis for comparison and normalization, an equivalent smooth-channel case with no swirl-enhancement was considered, with a mass flow rate equivalent to the sum of the main and side channel mass flow rates exiting the main channel for the swirl-enhanced cases. The total mass flow rate combined with the hydraulic diameter of the main channel was used to define the Reynolds number of the flow. The results of all tests presented in this paper are compared (normalized) with the non-enhanced smooth channel designated by $Nu_{o\ smooth}$.

Experiments

Experimental Apparatus

A simulated clear polycarbonate airfoil was built that incorporates a strategy for inducing swirl motion in the internal passages of an airfoil. The main cooling channel is slot shaped with an

aspect ratio of 3:1, with a height of 15.9 mm and a width of 47.6 mm. The overall length of the slot channel is 216 mm, not including a 12 mm radiused entry and 12mm radiused exit portion of the channel.

The side-jets that produce swirl are fed through outer passages that run parallel to the main slot shaped channel. These passages are 15.9 mm in diameter and the diameter of the jet at the entrance to the main channel is 1.6 mm. The flow into the jet supply channels was not through flow and could only exit through the jets (see figure 8-2). The jets were spaced 38 mm apart along one side. In configuration "A", the jets located on the opposite wall were offset by 19 mm relative to each other. In configuration "B" the jets were aligned (no offset) relative to each other along both walls of the main channel. The red and green lines indicate jet locations and sides. In each case the temperature at the entry of the respective channels at the beginning of the tests was maintained within two degrees Celsius of each other.

Initial static testing was performed using 25 thermocouples strategically placed in the passage of the channel. A smooth channel with no swirl inducement strategies was tested first, and the results of normalized heat transfer enhancement and pressure losses were used to compare against all tests with swirl enhancements. Testing with thermocouples as well as liquid crystal techniques will provide a more detailed account of heat transfer enhancement in the passage.

Heated air enters the test piece via a long diffuser section through a 12 mm radiused entry and exits the single flow slot shaped channel in an identical fashion. Upon exiting the channel the air is routed through a small plenum, then finally exits through two 18 mm holes to the atmosphere. The main channel inner walls are coated with a specially prepared thermochromic liquid crystal (TLC) substance which turns green at a nominal temperature of 35^0C. Two thin film thermocouples

are attached to the walls, one near the entry and one near the exit of the main channel. These will be used to confirm the accuracy of the TLC. Five fine wire thermocouples are placed, equally spaced, in the center of the main channel flow stream. The thermocouples are wired directly to a Labview thermocouple data acquisition system. The thermocouples have a resolution of 20 Hz and the data acquisition system is set to read thermocouple data at 15 Hz.

Two Canon SD430 wireless cameras are securely mounted on each side of the test piece. The cameras are set to record video images at 15 Hz. The thermocouple data acquisition system and the video cameras are synchronized via cold cathode fluorescent lamps (CCFL) that are used to illuminate the TLC and are triggered by a switch attached to one of the two air bypass valves.

Prior to the start of a test, heated air is allowed to bypass the test section. Once the bypassed heated air temperature has stabilized at approximately 80^{o} C preparations for the start of a test begins. The test piece is also maintained at room temperature for an extended period prior to the start of a test to ensure a uniform initial temperature.

Two separate heaters were used. One heater was used to heat air entering the main slot channel and the other was used to heat air entering the two outer jet supply channels. Two separate flow meters were used to control the mass flow rate of air entering each channel. As stated, the combined mass flow rate at the exit of the test piece is used to determine an equivalent Reynolds number for comparison with tests that do not utilize jets. The heated air from each heater is bypassed and allowed to stabilize prior to the start of a test. It is desirable to have the air entering each channel to be the same throughout the entire test.

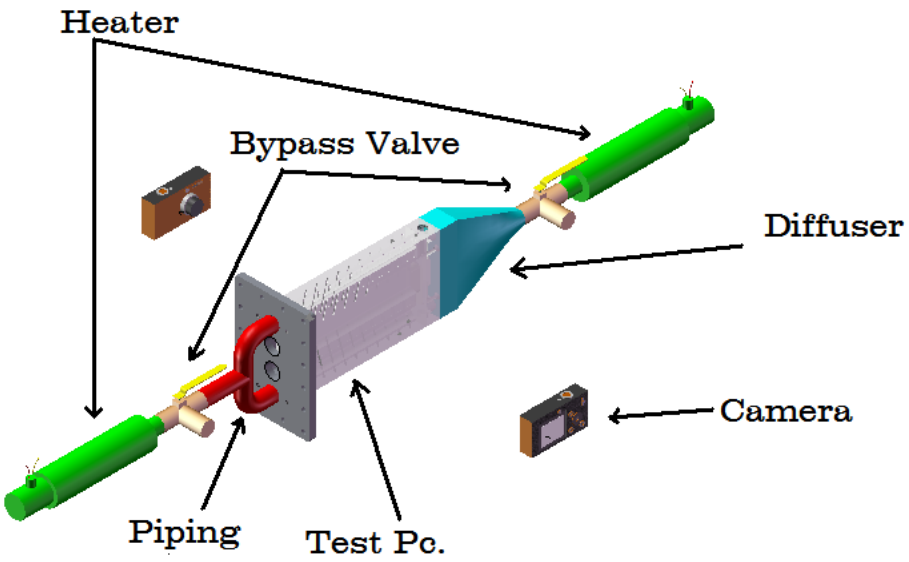

Figure 8-3 : Basic layout of test apparatus

This is quite a difficult task due to heat losses in the apparatus being somewhat different as the heated air travels from the individual heaters to the channel inlets. Thermocouples located at the entry of each channel monitor the temperature of the air entering the channel. Temperature differences of two degrees Celsius between the main and outer channel inlets were considered to be in the acceptable range for testing. Repeat testing using inlet air temperature differences as high as ten degrees Celsius were performed to better understand this effect.

To begin a test, the thermocouple data acquisition system is activated and the cameras begin recording. Then a bypass valves are closed allowing heated air to enter the test piece. Video images and thermocouple temperature readings are stored for post processing. The basic layout of the test apparatus is shown in figure 8-4.

Heat Transfer Coefficients

The local heat transfer coefficients across a liquid crystal coated target surface can be obtained using the 1-D transient heat conduction model of a semi-infinite solid with a convective boundary condition as given by:

$$\frac{\partial T}{\partial t} = -k\frac{\partial^2 T}{\partial x^2} \tag{1}$$

with boundary and initial conditions:

$$T(x = o, t = 0) = T_i$$

$$T(x = 0, t \to \infty) = T_m \tag{2}$$

$$T(x \to \infty, t) = T_i$$

$$-k\frac{dT}{dx}\Big|_{x\to 0} = h(T_w - T_\infty)$$

where, h is the surface heat transfer coefficient, T_w is the time-varying wall surface temperature and T_∞ is the time-varying local bulk (for internal flows) temperature. This is measured in the present work using suspended centerline thermocouples at several axial locations. These suspended thermocouples acquire temperature changes throughout each test. The data is used to produce a curve fit of the centerline temperatures vs. time along the entire main channel. The temperature vs. time equation is then associated with each column of pixels in the video image. Therefore, each column of pixels (flow stream is along rows) has an associated time vs. temperature array of data.

The solution for the surface temperature response with time is:

$$\frac{T_w - T_i}{T_\infty - T_i} = 1 - exp\left(\frac{h^2\,\alpha t}{k^2}\right) erfc\left(\frac{h\sqrt{\alpha t}}{k}\right) \quad (3)$$

A single transient test using the liquid crystal method described earlier is used. Each pixel value is examined for its peak in local intensity. The intensity value is used in conjunction with a specifically written MATLAB program to determine the corresponding temperature. By measuring the corresponding time required for the surface temperature to reach this temperature, the local heat transfer coefficient can be determined.

The 1D semi-infinite solid assumption must be satisfied. In order to satisfy the semi-infinite assumption, the transient temperature must not penetrate through the thickness of the polycarbonate during the test duration. This is achieved by using a sufficiently thick test piece of low thermal conductivity and diffusivity (0.201 W/mK and 0.1046 x10^{-6} m^2/s for polycarbonate respectively). For the one-dimensional heat transfer assumption to be satisfied, conduction should only occur normal to the surface with all lateral conduction effects neglected. The test piece may actually experience some lateral conduction, but it is assumed that the dominant temperature gradient is in the direction perpendicular to the surface, and lateral effects are negligible.

Although the initial temperature of the polycarbonate is uniform at ambient temperature, the incoming fluid temperature is higher and not a linear step increase. This is accounted for through

the modification of the previous equation by Duhamel's superposition theorem, which represents the temperature change as a series of steps described by:

$$T - T_i = \sum_{i=1}^{N} \left[1 - exp\left(\frac{h^2}{k^2}\, \alpha(t - \tau_i) \right) erfc\left(\frac{h}{k} \sqrt{\alpha(t - \tau_i)} \right) \right] \Delta T_{m,i} \quad (4)$$

where τ is the time step for each temperature step, $\Delta T_{m,i}$ is the temperature difference between each temperature step and the initial temperature, T_i. α, and k are characteristic of the polycarbonate plate. In the cases where heat transfer enhancements using jets are incorporated, the air temperature at the entry of the main channel and the jet channel at the beginning of the tests were maintained within two degrees Celsius. The temperature of the fluid exiting the jets as expansion occurred is not known, but is assumed to be taken into account when the main channel centerline temperature vs. time data is obtained.

Pressure Tests

A pressure tap is located at each end of the main channel, and in the case of air flowing through the jet supply channels, additional pressure taps are located at each end of the outer jet channels (see figure 8-5). In order to obtain accurate and consistent results, pressure measurements were taken during steady state adiabatic tests.

Flow meters were positioned before the heaters each supply channel. The mass flow rate at the exit of each flow meter and pressure, temperature, and cross section area at the entry of each

channel was used to determine velocities, densities, and associated Reynolds numbers, where applicable.

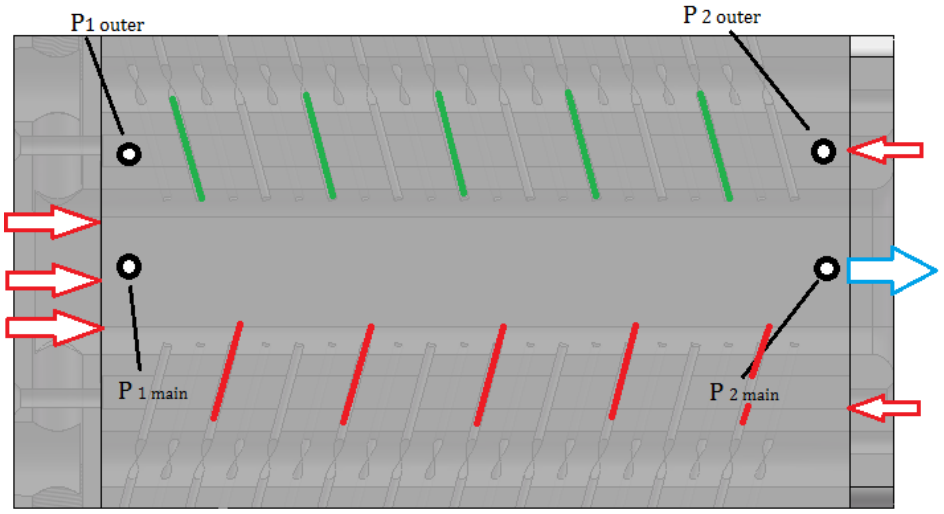

Figure 8-4 : Pressure tap locations used for pressure loss calculations

Pressure drops along the main channel and outer channels are recorded and used to determine friction losses. The following equation is used to determine friction loss in each channel:

$$f = 2\, d_h\, \frac{\Delta P}{L \rho U^2} \tag{5}$$

Velocities are calculated based on flow rates and channel cross section area. The friction losses in each channel are proportional to one over the square of the velocity as determined by the mass flow rate. When testing with jet enhancements the mass flow into each channel can be used to determine the total combined friction loss by using the following equation for friction loss in parallel flow:

$$1/\sqrt{f_{total}} = \frac{1}{\sqrt{f_1}} + \frac{1}{\sqrt{f_2}} + \frac{1}{\sqrt{f_3}} \quad (6)$$

where f_1 is the friction loss in the main channel and f_2 and f_3 are the losses in the two outer jet supply channels. Friction losses in the actual jets are not taken into consideration.

When jet configurations were used the combined overall mass flow rates were used to compare the plain smooth channel (no enhancements) to that of the jet enhanced channel. Table 8-1 below shows the mass flow rates when jet configurations "A" or "B" were used along with a 17.5:1 blowing ratio. In this case the percentage of mass flow rate through the jets ranged from 23% to 34%, The ratio of mass flow rates varied with each blowing ratio with high blowing ratio tests having as much as 45% of the total mass flow entering the main channel through the side jets.

Table 8-1 : Mass flow rates for Jet Configuration "A" and "B" with 17.5:1 Blowing Ratio

	Mass Flow Rate (kg/s)	
Reynolds Number	Main	Outer (Both)
10,000	0.00402	0.00140
25,000	0.00825	0.00531
40,000	0.01658	0.00507
50,000	0.02085	0.00619

In order for these configurations to work in a practical environment there must exists a pressure differential between the flow exiting the turbine blade, usually through film cooling holes, and the local pressure outside of the blade. A safety margin must be established to prevent high temperature

combustion gases from entering the interior of the blade. The concept of Back Flow Margin (BFM) is shown in Equation 7. A typical value of 20-30% margin must be maintained.

$$\%BFM = \frac{P_{int} - P_{ext}}{P_{ext}} * 100\% \quad (7)$$

Pressure taps located at or near the entry and exit of the main channel as well as the entry and exit of the jet channels were used to determine the differential pressure at each jet. The values for a blowing ratio of 17.5:1 are shown in Table 8-2 and were calculated based on the actual jet locations with the test piece set up in configuration "A". The "B" configuration showed similar results. A ~10-12% pressure drop exists between the first and last jet. This was typical throughout the range of blowing ratios.

Table 8-2 : Pressure between outer (P_2) and Main Channel (P_m) at various jet locations, Configuration "A" with 17.5:1 blowing ratio.

	$P_o - P_m$ (kPa)			
Jet Position	Re ~10k	Re ~25k	Re ~40k	Re~50k
1(Main Channel Entry)	11231	35529	60621	65547
2	10857	34562	59429	63659
3	10477	33582	57739	61969
4	10098	32605	56049	60183
5 (Main Channel Exit)	9716	31622	54358	58394
Max. Delta P (kPa)	1515	3907	6263	7154

Experimental Uncertainty and Error

An accurate assessment of uncertainty in liquid crystal measurement of heat transfer coefficients is essential because many factors affect the TLC results. A large number of studies have concluded that a properly performed test yields mean uncertainly of up to 11.0% for values of h, and up to 9% for temperatures. Smith [19], et al, compiled a table summarizing uncertainty studies of h and T when narrow band TLC methods were used. Thermocouple accuracy and repeatability are large contributors to uncertainty as well as illumination spectral effects. The wall mounted thermocouples were used to compensate for this effect and resulted in a 0.2° C temperature correction.

Heat transfer values typically were repeatable within 3% - 5% for tests with Reynolds numbers up to 25,000 and blowing ratios below 20. The repeatability values increased to 8% from higher Reynolds numbers or higher blowing ratios. As reported in the literature, current estimates of the uncertainty in the Nusselt number are approximately 10%.

Results and Discussion

Overall Heat Transfer and Friction

The initial tests were performed with a smooth slot shaped channel with no heat transfer enhancements. The results of these tests showed heat transfer coefficients similar to the standard smooth pipe results noted by the Dittus-Boelter equation near the exit of the channel and somewhat higher values near the entrance of the channel, due to entry effect. The mean values of the heat transfer coefficient (h) and Nusselt number (Nu) over the entire channel were used as the standard for the remainder of testing. Thus, all references to Nu in this paper are listed as $Nu/Nu_{osmooth}$.

Values of mean $Nu/Nu_{o\ smooth}$ vs. Reynolds numbers for all blowing ratios of jet configuration “A” are shown in figure 8-6 and for jet configuration “B” in figure 8-7. The results show the effectiveness of the jet configurations are extremely high ($Nu/Nu_{o\ smooth} \sim 4$) for both configuration “A” and “B” in a wide variety of blowing ratios. At Re =10k, configuration B performed much better than configuration A. This may be due to the interaction of the opposing jets in B having a larger influence on the cross flow in the main channel as opposed to the offset jets used in configuration A .

At 25,000 Reynolds numbers, both configurations performed well and both experienced a dip in values with blowing ratios near 15:1. Multiple tests were performed using the B configuration near the 10 and 15 blowing ratio values to see if this anomaly could be repeated and explained. The results in figure 8-7 show that repeated testing provided similar results.

As the Reynolds number increases the increased momentum of main channel fluid overcomes the momentum of fluid coming from each individual jets at lower blowing ratios and tends to direct the fluid leaving the jet downstream. The effect of the opposing jets interacting to increase turbulence is reduced at these lower blowing ratios.

The Re= 40k tests performed the best in configuration A with several Nu/Nu_{smooth} values near or above 4.0 in all of the higher blowing ratios tested. In the B configuration the Re = 40k tests were nested in the mid-range of all tests performed in the B configuration. The offset jets in configuration A are the likely reason for the exceptional performance. Overall, the A configuration tests were better performers when compared to the B configuration tests.

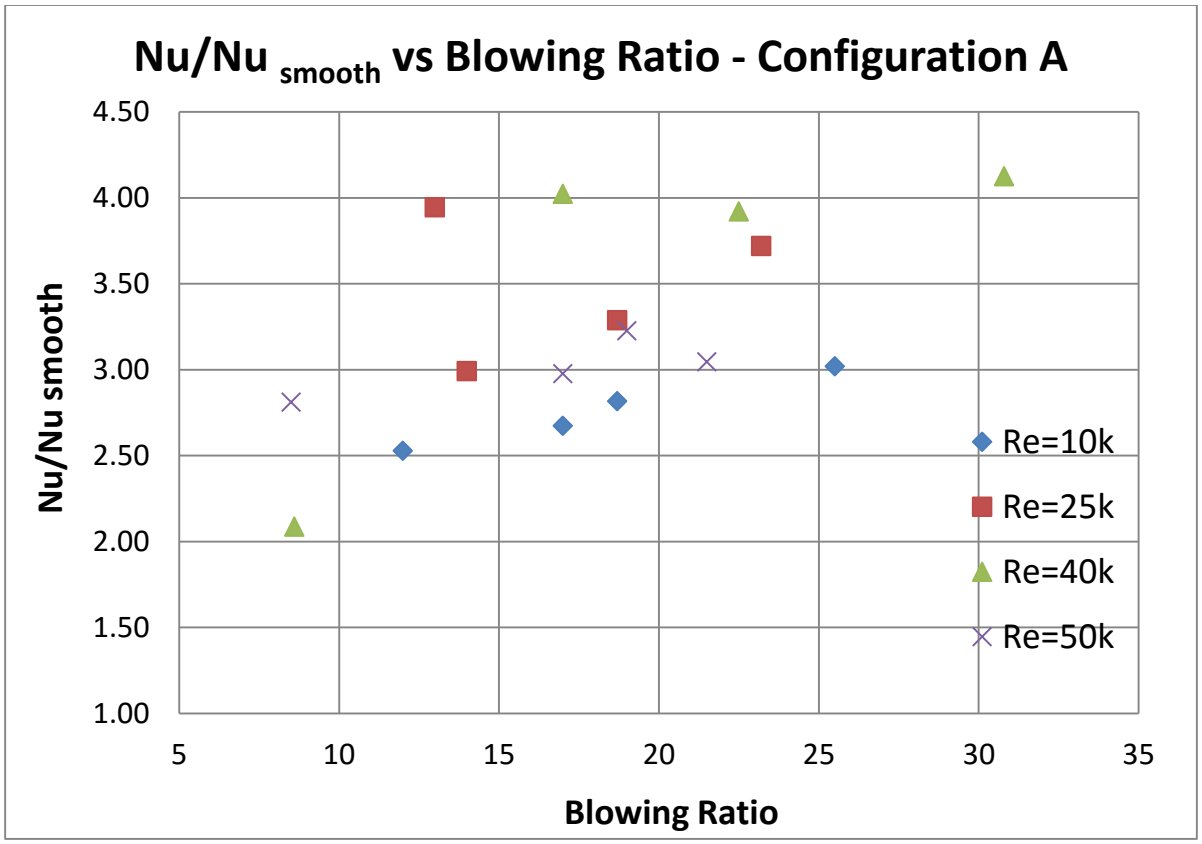

Figure 8-5: Heat Transfer Enhancement values for Configuration “A”.

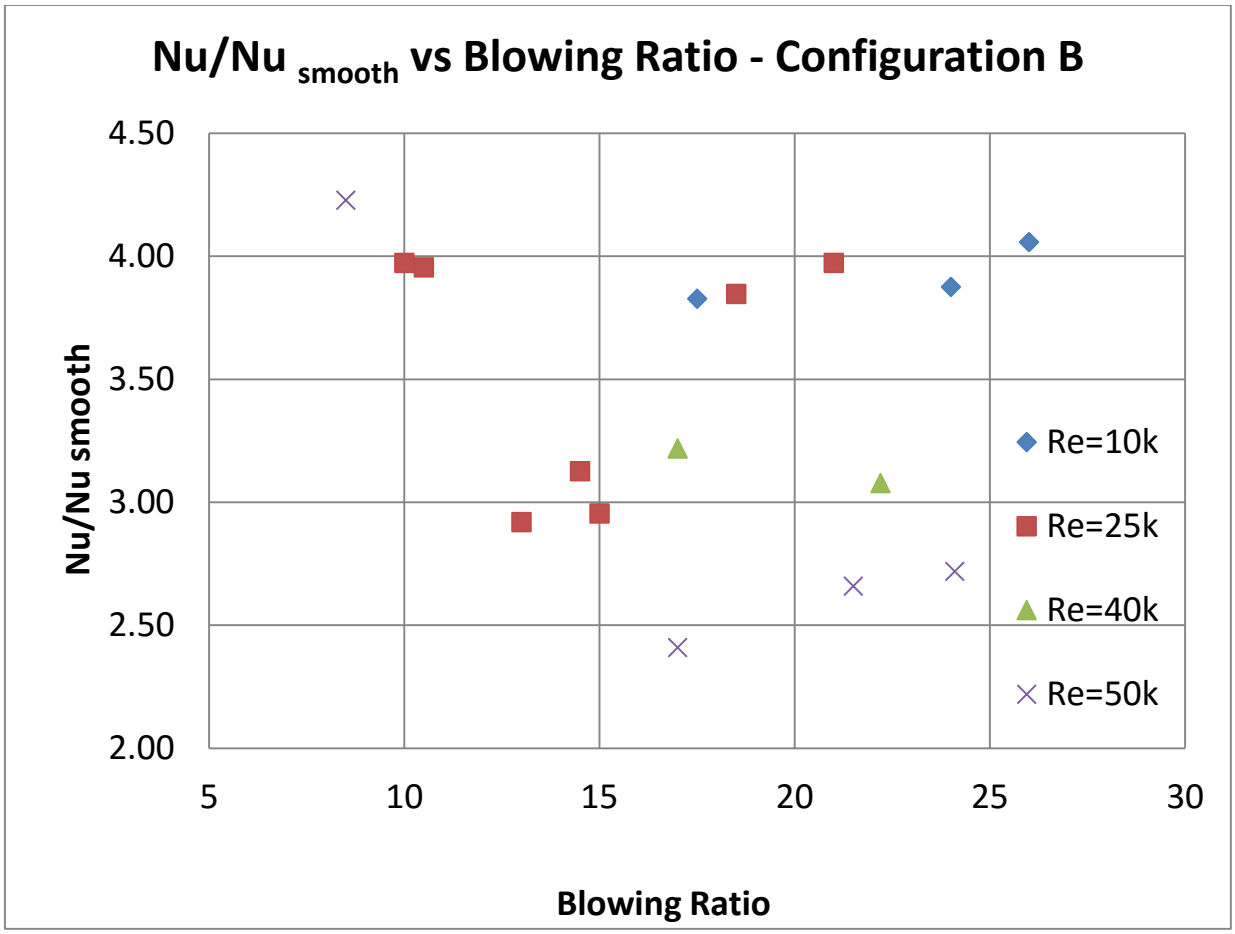

Figure 8-6 : Heat Transfer Enhancement values for Configuration “B”.

The normalized friction factor for all the swirl-jet cases are relatively low for all cases tested when compared to published data employing trip strips in rectangular channels, which are typically found to be in the 5-10 range for turbulated channels of turbine blades. The various swirl-jet case plots appear to be insensitive to Reynolds numbers and ranged from ~1.0 to 2.7. It should be noted that the friction factor for the tests utilizing the jet enhancements is a combination of friction factors in the main channel and two outer jet supply channels (Eq. 6).

Equation 7 is used to determine the thermal performance of each test. It is important to note that the values of Nu are an area averaged value that takes into account the entire test section between entry and exit pressure taps, not just the developed region.

$$\text{OTP} = \frac{Nu}{Nu_{o\ smooth}} \div \left(\frac{f_{total}}{f_{o\ smooth}}\right)^{1/3} \tag{7}$$

A plot of the calculated values summarizes the results in figure 8-8 for the A configuration jets and figure 8-9 for the B configuration jets. As expected from the previous plots, the jet configuration "A" performs extremely well at blowing ratios above 10 and extremely well at Re= 25k and Re = 40k. It should be noted that typical values reported in the literature for turbulated channels range between 1-1.5, and values higher than 1.5 are considered to be very good configurations for enhancing heat transfer without the associated friction penalty. The swirl-jet configurations tested here lead to numbers in the 1.5-3.5 range, with the vast majority of tests yielding values in the 2.5 to 3.5 range, over a reasonable Reynolds numbers of 10,000-50,000. These configurations should therefore be considered promising.

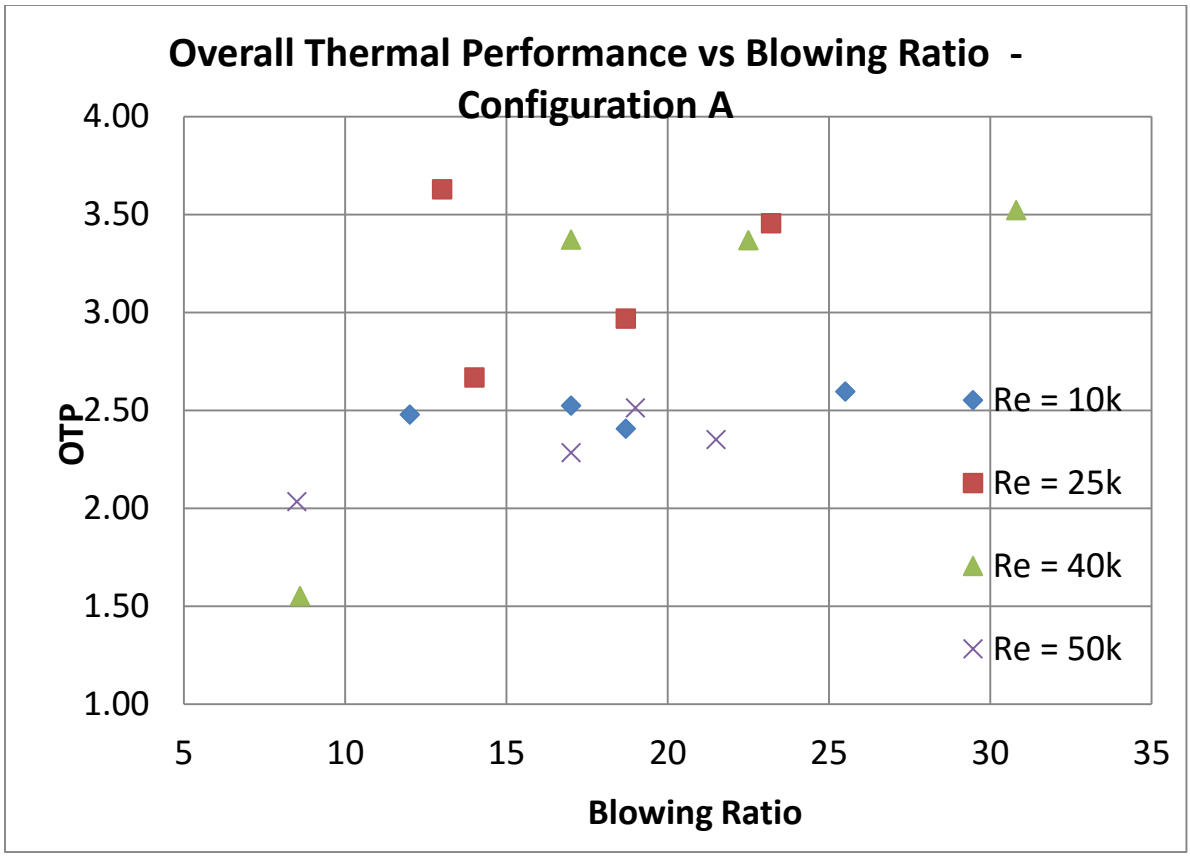

Figure 8-7 : Overall Thermal Performance values for Configuration "A".

Configuration B also showed very good OTP values for the Re = 10k, 25k, and 40k tests. The tests performed at Re=50k, at high blowing ratios, were some of the lowest performers with values between 2.0 and 2.25.

Jet velocities play an important role in swirl-enhancement. As blowing ratios and Reynolds numbers increased, so did the average exit velocity in the jets. Table 8-3 summarizes the velocity for each combination of tests. The jet exit velocities ranged from a low of 62 m/s to a high of 337 m/s as the blowing ratios spanned values of 8.6 to 30.8. These are average jet velocities. In a typical low blowing ratio tests the jet velocity would drop by 3- 5 m/s from the first jet to the last. In the

highest blowing ratio tests the jet velocity would reduce by as much as 18 m/s from the first jet to the last jet. Table 8-3 shows the average jet velocity for each tests.

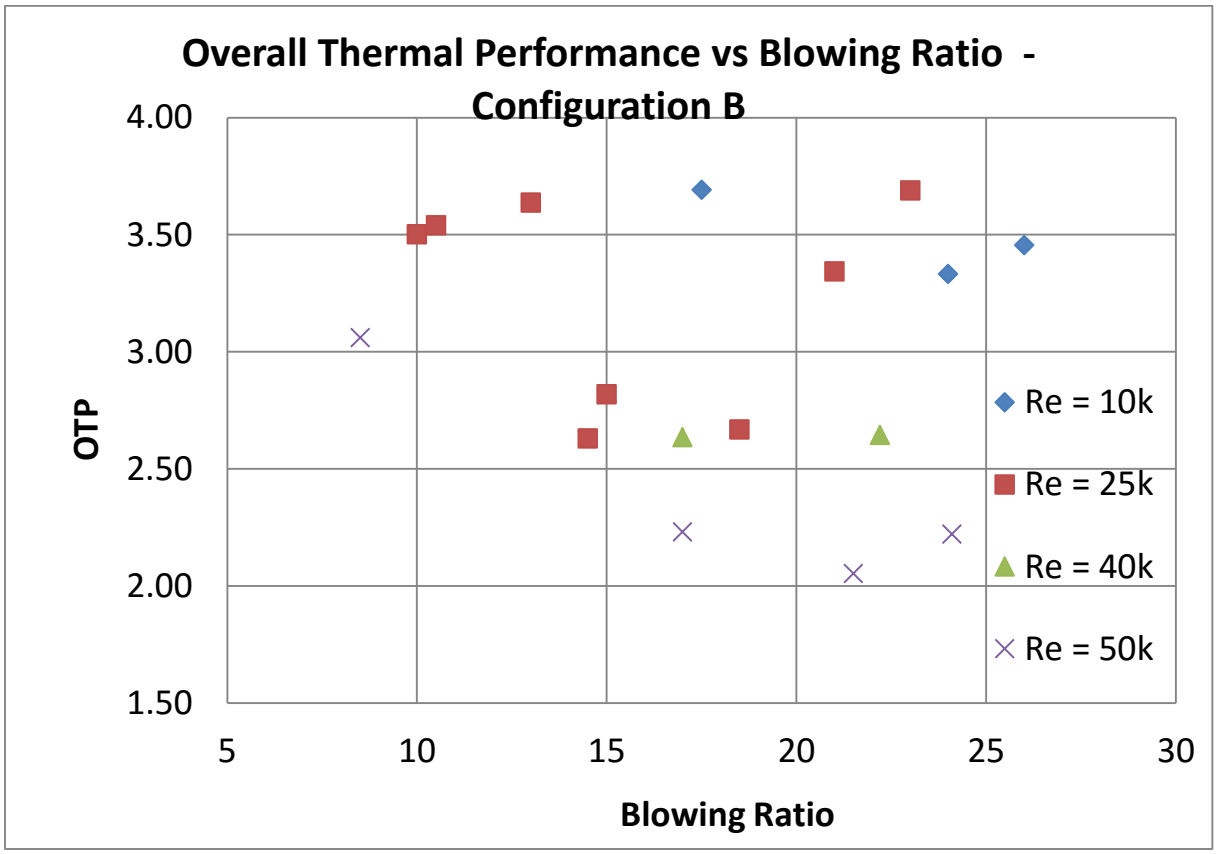

Figure 8-8 : Overall Thermal Performance values for Configuration “B”.

Table 8-3 : Average jet exit velocity values for Configurations A and B

Configuration A		
Re x 10^{-3}	B.R.	Jet Vel. (m/s)
10	12	62
10	17	77
10	18.7	83
10	25.5	99
25	13	141
25	14	169
25	18.7	208
25	23.2	255
40	8.6	192
40	17	290
40	22.5	329
40	30.8	343
50	8.5	207
50	17	312
50	19	321
50	21.5	329

Configuration B		
Re x 10^{-3}	B.R.	Jet Vel. (m/s)
10	17.5	79
10	24	93
10	26	102
25	10	120
25	10.5	133
25	13	141
25	14.5	175
25	15	178
25	18.5	205
25	21	223
25	23	252
40	17	290
40	22.2	327
50	8.5	207
50	17	312
50	21.5	329
50	24.1	337

Heat Transfer Contour Plots

For comparison purposes Nu/Nu_o plots of the slot shaped channel with a 12mm radiused entry and air entering thorough a straight entry is shown in figure 8-10. The Nu/Nu_o values are 1.04, 1.11, 1.28, and 1.32 for Re=10k, 25k, 40k, and 50k respectively.

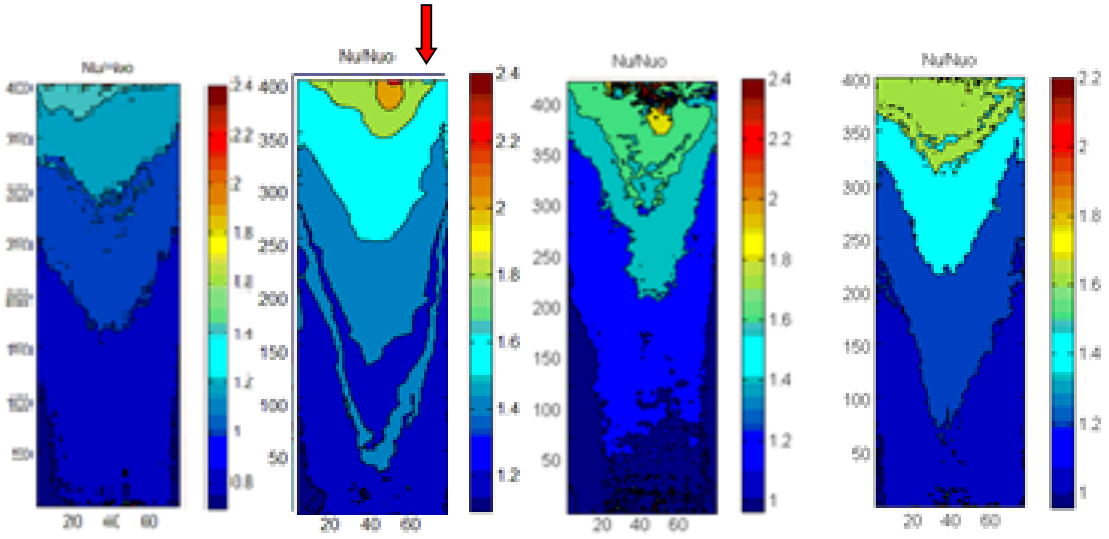

Figure 8-9 : Nu/Nu_o plots for the slot shaped channel with a straight entry for Re = 10k, 25k, 40k, and 50k respectively.

Jet-Swirl Configuration A:

This series of test examined the heat transfer enhancement characteristics when high blowing ratio jets were introduced into the main channel flow. Reynolds numbers ranged from 10,000 to 50,000. The diameter of each jet was 1.6 mm and provided an effective p/d ratio of 12:1, which is a commonly used ratio in the trip strip tests. The b/d ratio was 0.1. Air enters the main channel through two separate paths. One end of the slot shaped channel is connected to a diffuser from which the initial main channel air enters. Additionally, tangential side jets introduce air through neighboring channels. The offset of jet on any single side of the test piece is 38 mm. Jet holes on the opposite side are staggered by 19 mm. Details of configuration A is shown in figure 8-3.

Figure 8-11 shows the Nu/Nu_o plots of jet configuration A at an equivalent total mass flow to that of a Re = 10k, 25k, & 40k, respectively, in the smooth non-enhanced slot shaped channel

with a blowing ratio of 17. The jets on the opposing side are staggered in relation to the jets as shown in figures 8-3. At Re = 10k, the jet flow impinges on the surface of the main channel and cause very high local heat transfer enhancement, up to twelve in the main channel entry region. The enhancement values adjacent to each jet stream are much lower, especially near the entry, but as the flow proceeds through the channel the mixing quality improves with increasing crossflow, and there exists a more even distribution of heat transfer enhancement along with high local impingement values. The jet flow tends to cause swirl motion of the jet fluid and the main stream fluid seems to tumble as it encounters the high velocity jet fluid.

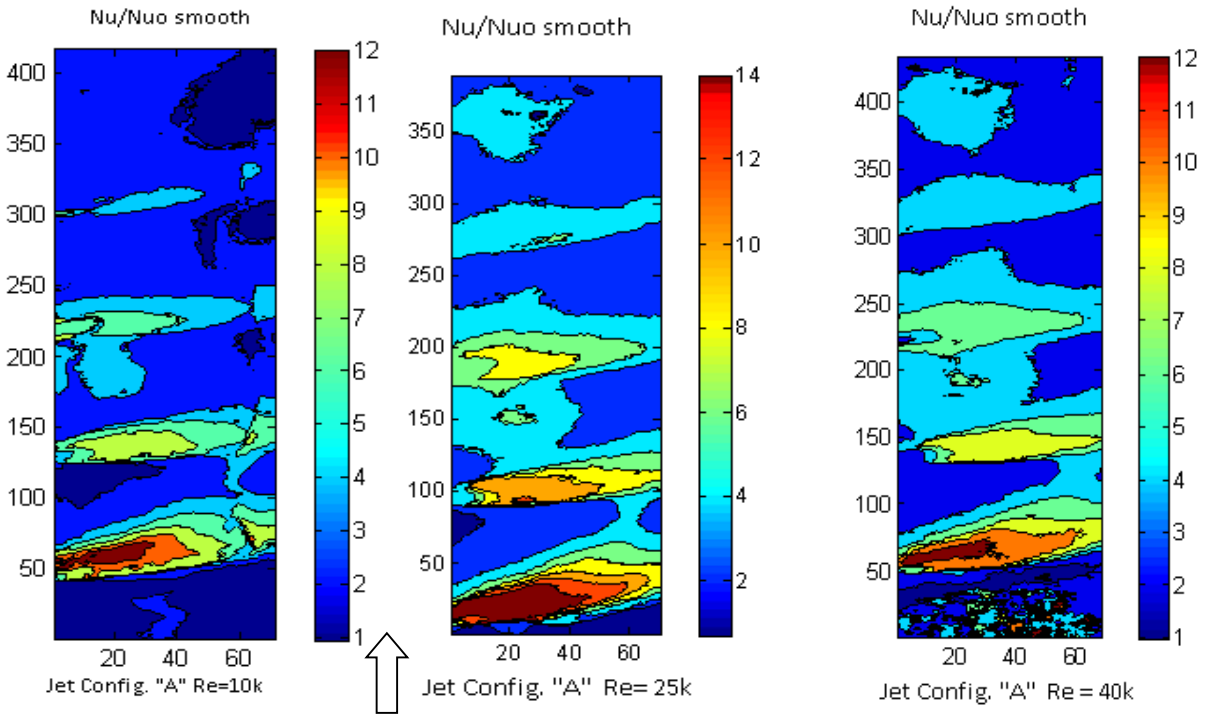

Figure 8-10 Figure 8-11: $Nu/Nu_{o\ smooth}$ jet configuration “A”, Re = 10k, 25k, & 40k, w/ B.R. = 17

The combination of swirl and tumble leads to the high heat transfer enhancement in this configuration. It is important to note that the jets continue to add mass into the main channel as

the fluid progresses from the entry to the exit and that the total mass does not equal to mass flow rate of the Re=10k flow of the smooth channel until near the exit of the channel. This explains why the enhancement levels are higher at the channel inlet where the local channel flow rate and average velocity are the lowest along the length of the channel. Therefore the local jet to channel flow velocity ratio is the highest at this entry location.

At a Reynolds number of 25k and 40k, figure 11 displays similar attributes to those discussed for Re = 10k. Large local areas with Nu/Nu_o values exceeding 4 are noted throughout the channel and continue to the channel exit. At Re=25k, for example, the overall mean thermal performance value is 2.97 with a Nu/Nu_o value of 4.05. The normalized friction factor remains low at 1.87. These values offer a significant improvement over the helical trip strips and most other published data related to heat transfer enhancement in the mid-span region of turbine blades.

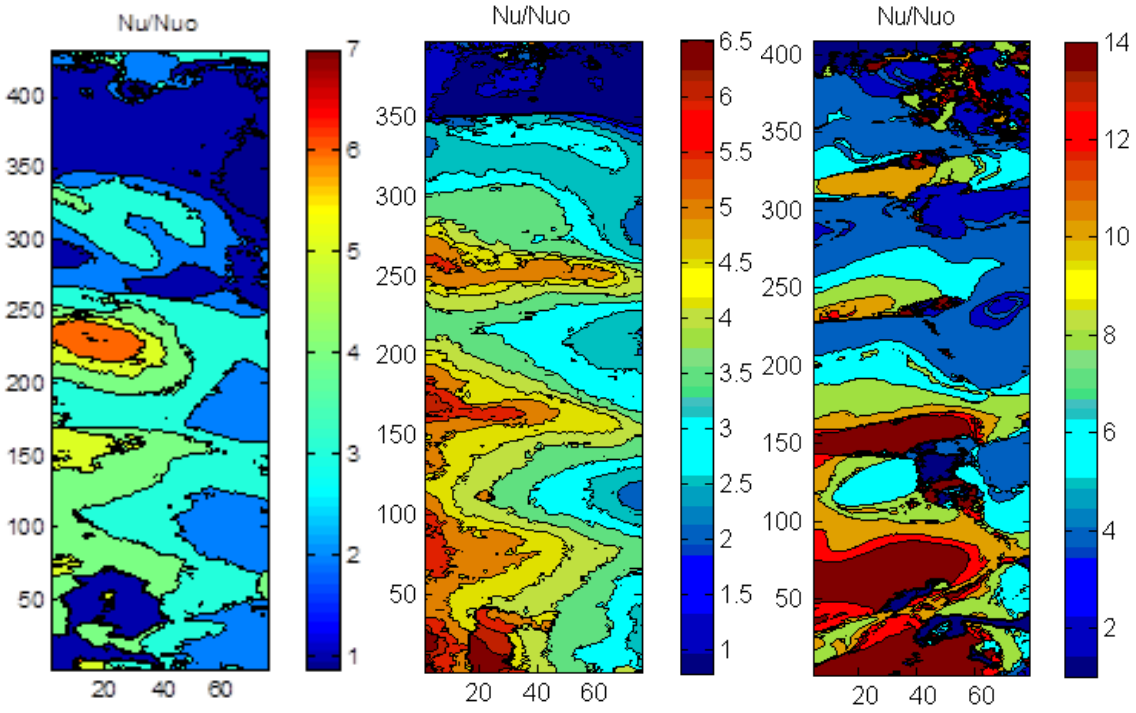

Figure 8-11 : Nu/Nu_o Jet Configuration "A", Re = 10k, w/ B.R. = 12, 18.7, & 25.5

Figure 8-12 shows the Nu/Nu_o color contour plots for jet configuration A, an equivalent Reynolds number of 10,000 and three different blowing ratios. The center plots, BR = 18.7 displays the overall best heat transfer distribution and yields an overall thermal performance value of 2.41. The overall thermal performance value for the 25.2 blowing ratio was slightly higher, at 2.60, but the distribution is not as uniform.

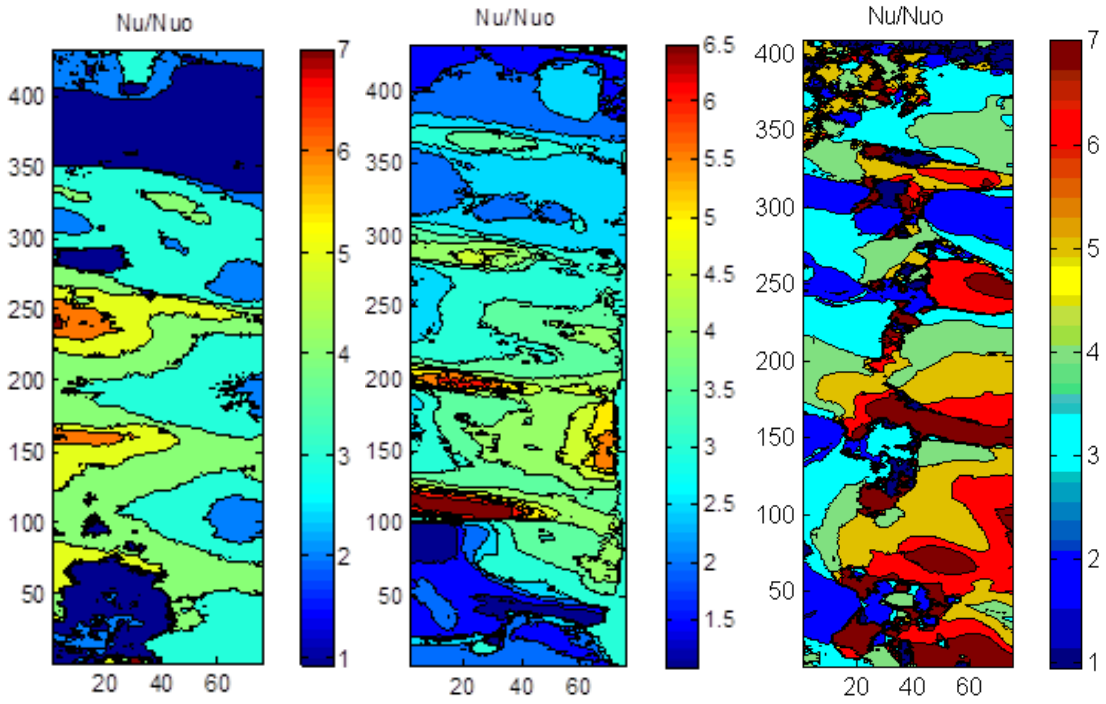

Figure 8-12 : Nu/Nu_o using Jet Configuration "A", Re = 25k, w/ B.R. = 14, 18.7, & 23.2

As the effective Reynolds number increased the OTP values increased. In figure 8-13 three blowing ratio color plots are shown. The highest blowing ratio provided the best OTP value of 3.46 along with highly turbulent regions throughout the channel. The 18.7 blowing ratio plot had an OTP of 2.97. The lower blowing ratio plot appears to have a large section of low heat transfer which severely affect the overall thermal performance.

Good heat transfer distribution is observed in the high blowing ratio color plots in figure 8-14. At Re = 40k the increasing main channel velocity interacts with the high velocity side jets to provide the best overall heat transfer distribution of any of the tests performed.

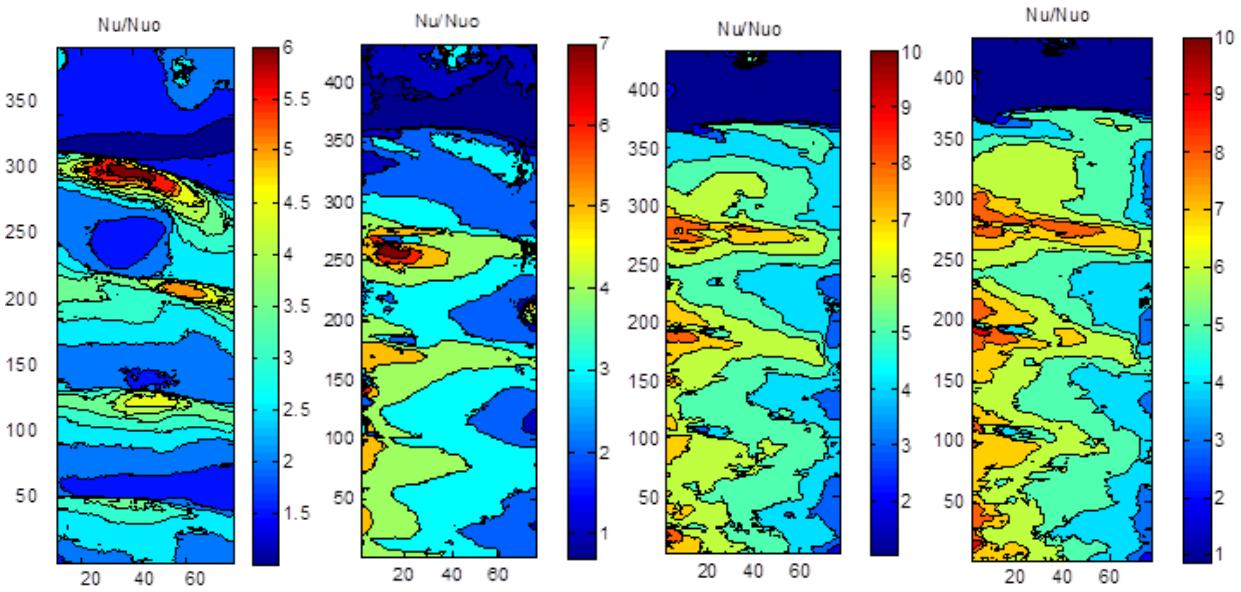

Figure 8-13 : Nu/Nu_o for Jet Configuration "A", with B.R. = 8.6, 13, 22.5, and 30.8

The normalized Nusselt number is 4.13 for the 30.8 blowing ratio tests and the OTP value is 3.52. The 22.5 blowing ratio tests displayed similar results with a normalized Nusselt value of 3.92 and an OTP of 3.37. The OTP values for the BR = 13 and the BR = 8.6 tests were 3.37 and 1.55 respectively.

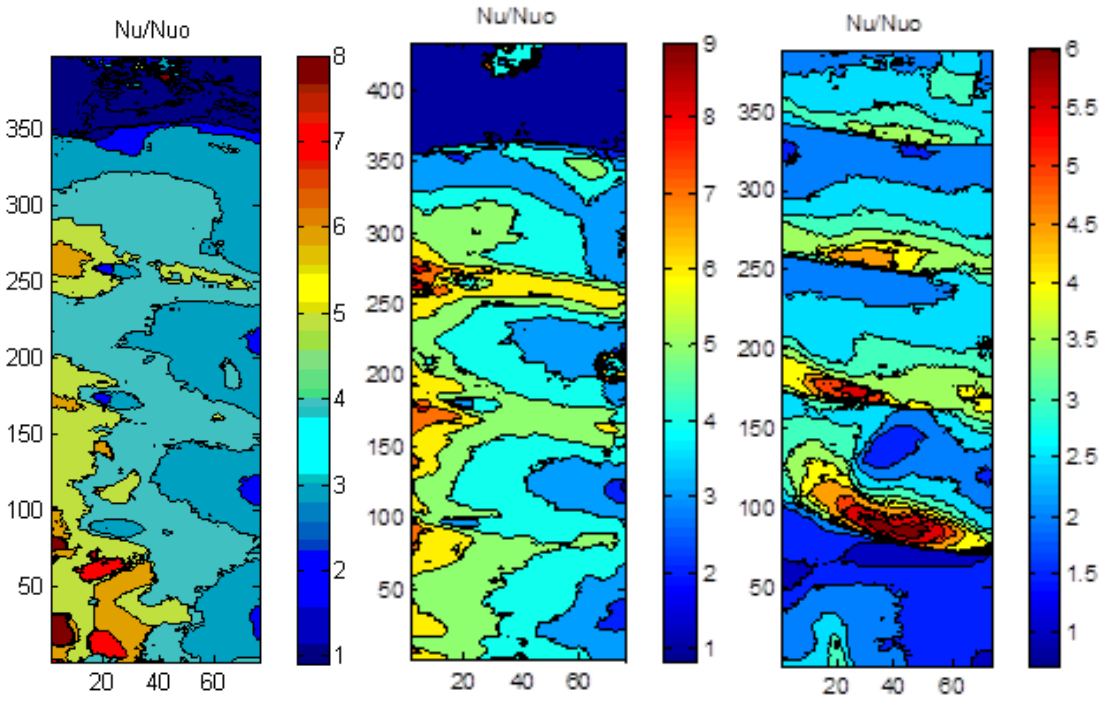

Figure 8-14 : Nu/Nuo with Jet Configuration "A", Re = 50k, with B.R. = 21.5, 19, and 8.5

The Re=50k tests yielded OTP results that were similar. At BR = 21.5 the OTP was 2.35, while the results of BR = 19 were 2.51, and the BR = 8.5 tests showed an OTP value of 2.03. The distribution was generally good for all tests performed at Re = 50k.

Jet-Swirl Configuration B:

The jet layout in configuration B is shown in figure 8-3. The spacing between jets was the same as configuration A, at 38 mm, but the opposing jets were directly across from one another. Whereas the jets in configuration A, in an idealized fashion, caused the jets to create a continuous helical swirl as the high velocity jets of air proceeding through the main channel, the jets in

configuration B caused the jets to cross one another on opposite walls of the main channel. Therefore, the patterns of heat transfer distribution are somewhat different.

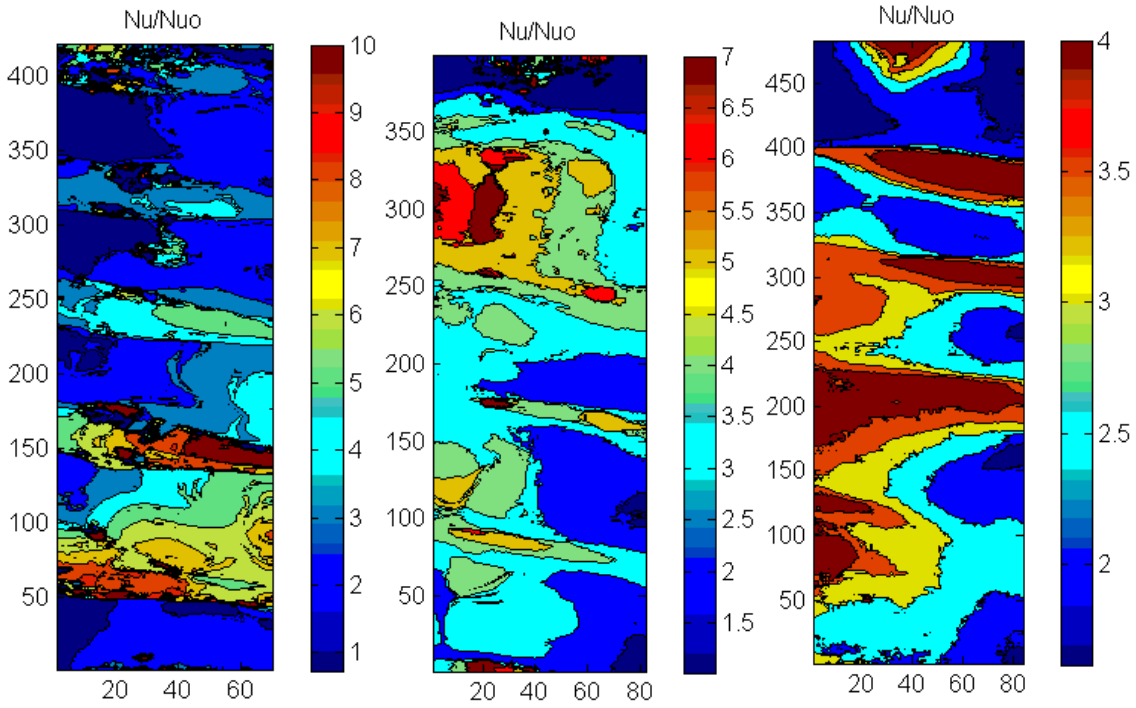

Figure 8-15 : Nu/Nu_o for Jet Configuration "B", Re = 10k, with B.R. = 17.5, 24, and 26

Figure 8-16 displays the color contour plots of 10,000 Reynolds number tests with high blowing ratios of 17.5, 24, and 26 respectively. The overall thermal performance values are 3.69, 3.33, and 3.46 respectively. These values are very high, but the heat transfer distribution is not very good.

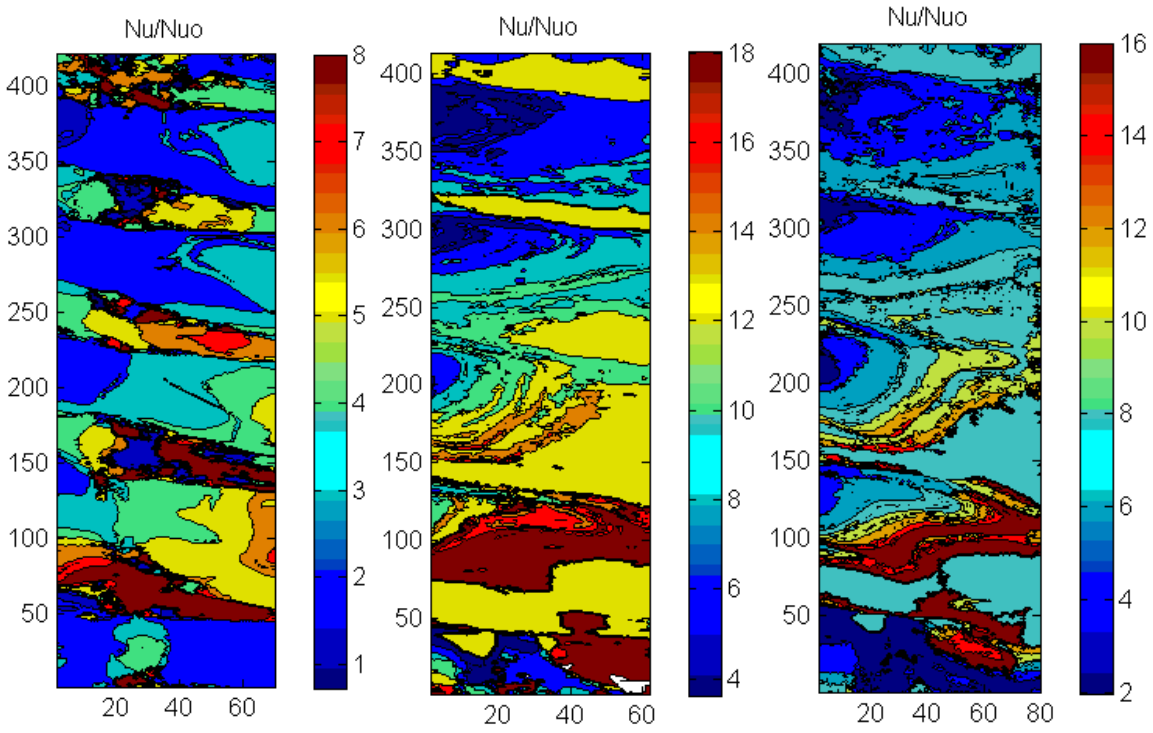

Figure 8-16 : Nu/Nu_o for Jet Configuration "B", Re = 25k, with B.R. = 13, 15, and 21

Increasing the Reynolds number to 25,000 helped the distribution and provided good overall thermal performance values of 3.64 for BR = 13, 2.82 for BR = 15, and 3.34 for BR = 21. The pressure losses for the BR = 15 tests were slightly higher than the other two tests. This contributed to the lower OTP value.

Conclusion

A series of tests were performed to determine heat transfer enhancement characteristics of a slot shaped channel, with jets issuing from side channels, using two different jet configurations and a multitude of blowing ratios. The resulting values of overall heat transfer enhancement,

normalized friction factors, and overall thermal performance were compared to a smooth slot employing no enhancements.

The jet configurations show a substantial improvement in mean heat transfer enhancement values when compared to published results for mid-span cooling techniques which usually utilize trip strips. Configuration A in this study shows extremely good values for overall thermal performance with a value of 3.63 at a Reynolds number of 25,000 and a blowing ratio of 13. Configuration B also performed well with the maximum overall thermal performance value of 3.69 at a Reynolds number of 25,000 and a blowing ratio of 23.The normalized friction factor remained below 2.5 for all tests using jet enhancements. Generally, the higher the blowing ratios resulted in better overall heat transfer distribution in the channel for jet configuration A. Jet configuration B did not show an even heat transfer distribution in most tests.

Chapter 9 – Jets with 90 Degree Axial Flow Inlet

Introduction

A heat transfer analysis was performed on a uniquely designed multi-channel passage consisting of a slot shaped channel with a 3:1 aspect ratio and two additional channels, located adjacent to the main slot shaped channel. Small round jets connect the outer channels to the main channels at a 15 degree angle relative to the main channel flow direction and at a position tangent to the floor/roof of the main channel. Flow entering the multi-channel passages is directed into the main channel through orifices that reduced the pressure in the main channel, thereby causing high velocity flow through the jets. The flow leaving the orifices continues through a 90 degree entrance into the main channel. The resulting flow through the side jets and main channel causes high shear flow along the roof and floor of the channel where the jet flow enters the main channel, swirl motion as the high velocity side jet flow enters the main channel flow at an angle relative to the main flow direction, and high turbulence regions as the lower velocity main channel flow tumbles when coming in contact with the high velocity jets issuing from the side channels.

The heat transfer characteristics were compared to the slot channel with a 90 degree inlet with no additional heat transfer enhancements. Four different jet configurations are presented along with three different orifice diameters.

The Reynolds numbers investigated range from 10,000 to 50,000 and are based on the mean velocity of the fluid at the channel inlet for the slot shaped channel without enhancement; or when swirl-jets are used, the equivalent mass flow rates at the exit of the main channel. The varying

orifice sizes contributed to changes in blowing ratio, which is defined as the mean side jet velocity verses the mean main channel velocity.

Thermochromic liquid crystal techniques were used combined with Duhamel's superposition theorem to obtain heat transfer coefficients and Nusselt numbers. The results yield average Nusselt numbers for the entire main channel as high as 13.6. Pressure losses, mainly due to the orifices, were high but the overall performance shows significant improvements when compared to other heat transfer enhancement methods in turbine blade mid-span regions.

Configurations Studied

A 3:1 single passage slot shaped channel with a hydraulic diameter d_h of 0.0248m and a L/d_h of 8.7 is chosen for this study. The various configurations investigated to enhance heat transfer include several fluidic-swirl-generation configurations where the swirl is generated by introducing tangential jets along the side walls of the main coolant passage at a 15 degree angle relative to the main channel flow direction (Figure 9-2).

High pressure air is introduced into two round 15.9 mm diameter outer channels. Some of the air is directed through orifices; before entering the main 15.9 mm high by 47.7 mm wide slot shaped channel through a 90 degree entry angle. The air in the outer jet supply channels feed the 1.6 mm diameter jets. This results in a d/b ratio of 0.1, a typical effective ratio used for trip strip heat transfer enhancement.

A typical fluidic swirl-generation configuration is shown in figure 9-2. The end view image shows the two round outer jet feed channels with red upper jets and green lower jets supplying air to the main channel along a path that is tangent to the upper and lower walls of the main channel.

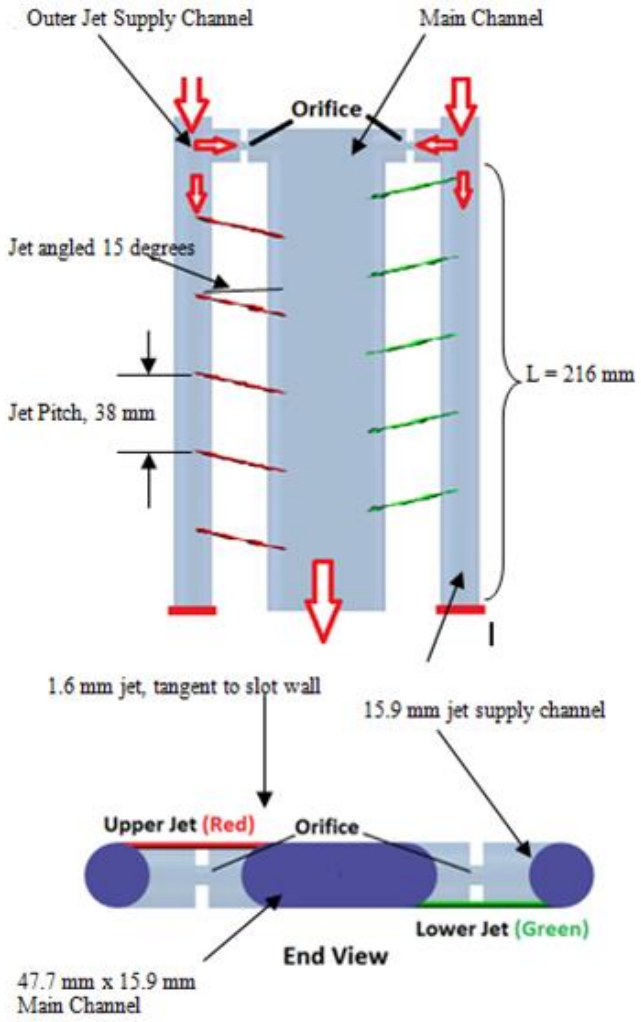

Figure 9-1 : Top and End View of Typical Fluid Passages

The location of the two orifices, one on either end of the entry to the main channel, is also shown. The orifices were removable and testing was performed with orifices of 3.18 mm, 3.94 mm, and 4.76 mm diameters. The ends of the outer jet supply channels are blocked. Therefore, all air entering the jet supply channels must exit through the jets.

Four different jet configurations were tested, each with three different diameter orifices. The jet diameter remained the same for all tests at 1.6 mm.

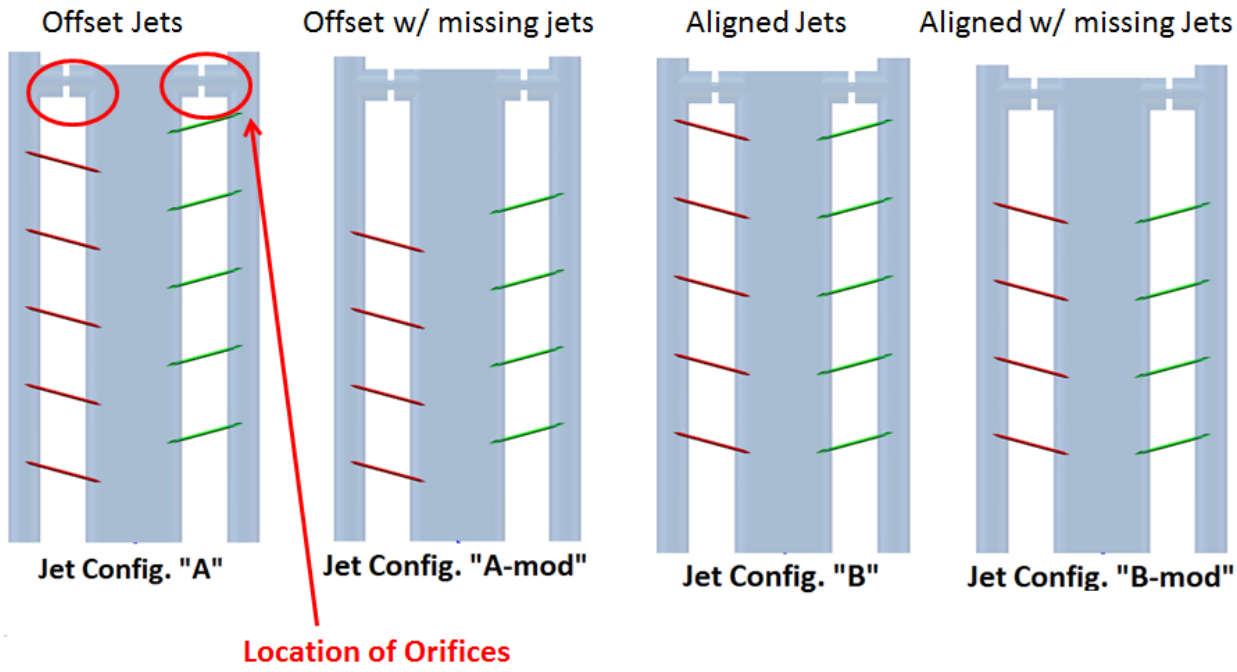

Figure 9-2 : Four Different Fluid Passage Configurations

The four jet configurations tested are shown in figure 9-3. Jet configuration “A” uses five jets issuing from each jet supply channel. In this configuration, the jets are staggered across from one another by 19 mm. The resulting ratio of jet stagger (pitch) to jet diameter is 12. Again, this value has shown to be an effective pitch to trip strip height ratio when trip strip enhancements are used. Jet configuration “A-mod” is the same as configuration “A”, except the first series of jets are blocked. Configuration “B” also has five jets issuing from each side. The main difference between configuration “A” and “B” is that the jets are aligned across from one another. Configuration “B-mod” differs from configuration “B” by having the first series of jets blocked.

In addition to the four configurations listed above a series of baseline tests were performed with the orifices removed and all jets blocked. This configuration tests the heat transfer enhancement of a smooth slot shaped channel with a 90 degree entry. Main channel Reynolds numbers of 10k, 25k, 40k, and 50k were tested and this configuration was used to normalize all tests performed with jets and orifices.

A channel-average blowing ratio, jet velocity to main channel velocity, varied with each orifice diameter. The average blowing ratio was calculated based on the measured pressure drops in the main channel and the side channels, and is an average value across all the jet-holes. The individual jet-blowing ratio may vary from hole to hole depending on the pressure drop.

Large values of blowing ratios were needed to ensure that the jet penetrated the main flow field to the other side, and potentially create an impingement effect. The total mass flow rates combined with the hydraulic diameter of the main channel were used to define the Reynolds number of the flow. The results of all tests presented in this paper are compared (normalized) with the non-enhanced smooth channel designated by $Nu_{9o\ smooth}$.

Experiments

Experimental Apparatus

A simulated clear polycarbonate airfoil was built that incorporates two strategies for inducing swirl motion in the internal passages of an airfoil. The main cooling channel is slot shaped with and aspect ratio of 3:1, with a height of 15.9 mm and a width of 47.6 mm. The overall length

of the slot channel is 216 mm, not including the 90 degree transition entry and radiused exit portion of the channel.

The side-jets that produce swirl are fed through outer passages that run parallel to the main slot shaped channel. These passages are 15.9 mm in diameter and the diameter of the jet at the entrance to the main channel is 1.6 mm. The flow into the jet supply channels was not through flow and could only exit through the jets. In configurations “A” and “B” the jets were spaced 38 mm apart along one side. In configuration “A”, the jets located on the opposite wall were offset by 19 mm relative to each other. In configuration “B” the jets were aligned (no offset) relative to each other along both walls of the main channel. The “A-mod” and “B-mod” configurations had the first series of jets blocked. Figure 3 shows the jet spacing and stagger. The red and green lines indicate jet locations and sides.

Initial testing was performed using 25 thermocouples strategically placed in the passage of the channel. A smooth channel with no swirl inducement strategies was tested first, and the results of normalized heat transfer enhancement and pressure losses were used to compare against all tests with jet swirl enhancements. Testing with thermocouples as well as liquid crystal techniques will provide a more detailed account of heat transfer enhancement in the passage.

Heated air enters the test piece via two outer jet supply channels and exits the single flow slot shaped channel. Upon exiting the channel, the air is routed through a small plenum, then finally exits through two 18 mm holes to the atmosphere. The main channel inner walls are coated with a specially prepared thermochromic liquid crystal (TLC) substance which turns green at a nominal temperature of 35^0C. Two thin film thermocouples are attached to the walls, one near the entry and

one near the exit of the main channel. These will be used to confirm the accuracy of the TLC. Five fine wire thermocouples are placed, equally spaced, in the main channel flow stream. These thermocouples measure the main channel centerline air temperature. The thermocouples are wired directly to a Labview thermocouple data acquisition system. The thermocouples have a resolution of 20 Hz and the data acquisition system is set to read thermocouple data at 15 Hz.

Two Canon SD430 wireless cameras are securely mounted on each side of the test piece. The cameras are set to record video images at 15 Hz. The thermocouple data acquisition system and the video cameras are synchronized via cold cathode fluorescent lamps (CCFL) that are used to illuminate the TLC and are triggered by a switch attached to an air bypass valve.

Prior to the start of a test, heated air is allowed to bypass the test section. Once the bypassed heated air temperature has stabilized at approximately 80^{o} C preparations for the start of a test begins. The test piece is also maintained at room temperature for an extended period prior to the start of a test to ensure a uniform initial temperature.

As stated, the combined mass flow rate at the exit of the test piece is used to determine an equivalent Reynolds number for comparison with the baseline tests that do not utilize jets or orifices.

To begin a test, the thermocouple data acquisition system is activated and the cameras begin recording. Then a bypass valve is closed allowing heated air to enter the test piece. Video images and thermocouple temperature readings are stored for post test processing. The basic layout of the test apparatus is shown in figure 4.

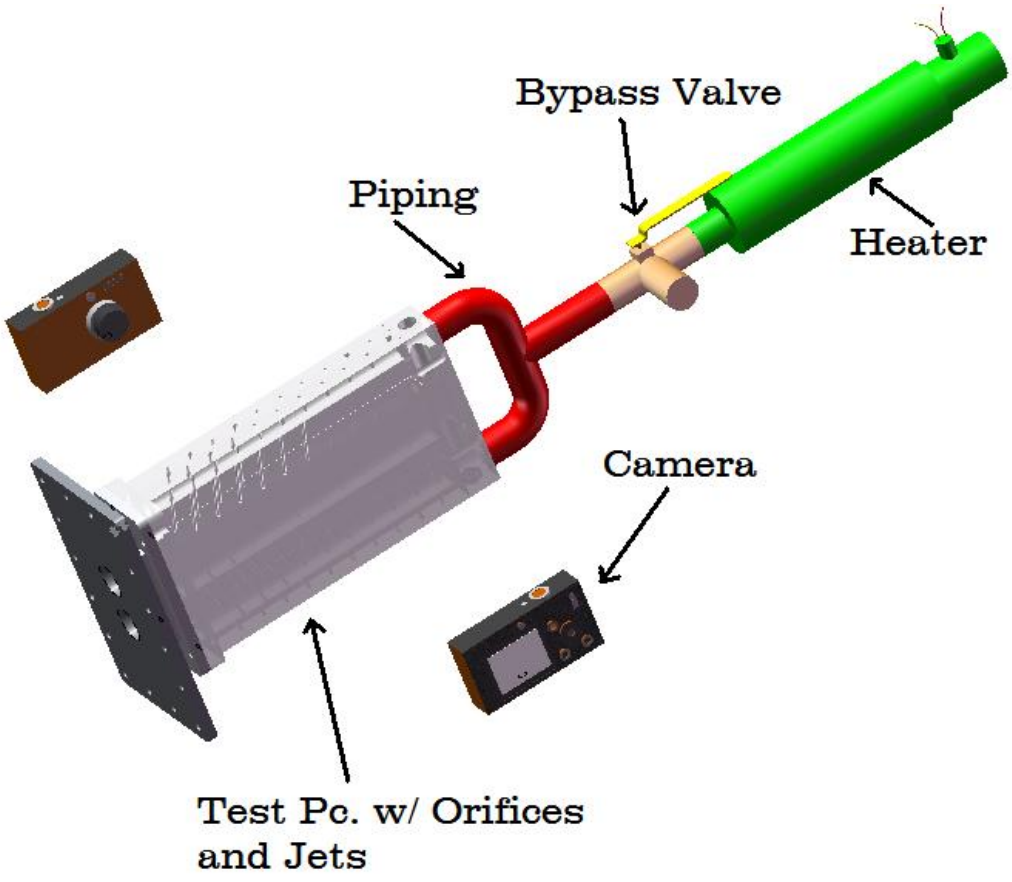

Figure 9-3 : Basic Layout of Test Apparatus

Heat Transfer Coefficients

The local heat transfer coefficients across a liquid crystal coated target surface can be obtained using the 1-D transient heat conduction model of a semi-infinite solid with a convective boundary condition as given by:

$$\frac{\partial T}{\partial t} = -k \frac{\partial^2 T}{\partial x^2} \tag{1}$$

with boundary and initial conditions:

$$T(x = o, t = 0) = T_i$$

$$T(x = 0, t \to \infty) = T_m \qquad (2)$$

$$T(x \to \infty, t) = T_i$$

$$-k \frac{dT}{dx} \Big|_{x \to 0} = h(T_w - T_\infty)$$

where, h is the surface heat transfer coefficient, T_w is the time-varying wall surface temperature and T_∞ is the time-varying local bulk (for internal flows) temperature. This is measured in the present work using suspended centerline thermocouples at several axial locations. These suspended thermocouples acquire temperature changes throughout each test. The data is used to produce a curve fit of the centerline temperatures vs. time along the entire main channel. The temperature vs. time equation is then associated with each column of pixels in the video image. Therefore, each column of pixels (flow stream is along rows) has an associated time vs. temperature array of data.

The solution for the surface temperature response with time is:

$$\frac{T_w - T_i}{T_\infty - T_i} = 1 - exp\left(\frac{h^2 \alpha t}{k^2}\right) erfc\left(\frac{h\sqrt{\alpha t}}{k}\right) \qquad (3)$$

A single transient test using the liquid crystal method described earlier is used. Each pixel value is examined for its peak in local intensity. The intensity value is used in conjunction with a specifically written MATLAB program to determine the corresponding temperature. By measuring the corresponding time required for the surface to reach this temperature, the local heat transfer coefficient can be determined.

The 1D semi-infinite solid assumption must be satisfied. In order to satisfy the semi-infinite assumption, the transient temperature must not penetrate through the thickness of the polycarbonate during the test duration. This is achieved by a sufficiently thick test piece of low thermal conductivity and diffusivity (0.201 W/mK and 0.1046 $x10^{-6}$ m^2/s for polycarbonate respectively). For the one-dimensional heat transfer assumption to be satisfied, conduction should only occur normal to the surface with all lateral conduction effects neglected. The test piece may actually experience some lateral conduction, but it is assumed that the dominant temperature gradient is in the direction perpendicular to the surface, and lateral effects are negligible.

Although the initial temperature of the polycarbonate is uniform at ambient temperature, the incoming fluid temperature is higher and not a linear step increase. This is accounted for through the modification of the previous equation by Duhamel's superposition theorem, which represents the temperature change as a series of steps described by:

$$T - T_i = \sum_{i=1}^{N} \left[1 - exp\left(\frac{h^2}{k^2} \alpha(t - \tau_i) \right) erfc\left(\frac{h}{k} \sqrt{\alpha(t - \tau_i)} \right) \right] \Delta T_{m,i} \quad (4)$$

where, τ is the time step for each temperature step, $\Delta T_{m,i}$ is the temperature difference between each temperature step and the initial temperature, T_i, α, and k are characteristic of the polycarbonate plate. The temperature of the fluid exiting the jets as expansion occurred is not known, but is assumed to be taken into account when the main channel centerline temperature vs. time data is obtained.

Pressure Tests

A pressure tap is located at each end of the main channel and at each end of the outer jet supply channels. In order to obtain accurate and consistent results, pressure measurements were taken during steady state adiabatic tests. The pressure differential between the inlet of the jet supply channel and the inlet of the main channel was used to determine the percentage of mass flow that entered the main channel, with the mass flow through the orifice calculated using equation 5. The orifices were manufactured to ISO 5167 standard dimensions and the mass flow through the orifice was calculated using the standard equation for compressible non-choked flow through an orifice as shown in equation 5.

$$\dot{m} = C\ A_2\ P_1 \sqrt{\frac{2\ M}{Z\ R\ T_1}\left(\frac{k}{k-1}\right)\left[(P_2/P_1)^{2/k} - (P_2/P_1)^{(k+1)/k}\right]} \tag{5}$$

Flow meters were positioned before the heater which supplied heated air to each jet supply channel. The mass flow rate at the exit of the flow meter and pressure, temperature, and cross

section area at the entry of each channel was used to determine velocities, densities, and associated Reynolds numbers, where applicable.

Pressure drops along the main channel and outer channels are recorded and used to determine pressure losses. Normally, friction losses are calculated and used to determine overall thermal performance. The orifices in the flow path prevent the use of friction factors and associated friction losses used to determine the overall thermal performance. The alternative was to use the overall pressure loss in the test piece and compare the pressure losses in the various configurations to that of the smooth slot channel without jets or orifices as shown in equation 6.

$$\Delta P/\Delta P_{90smooth} \tag{6}$$

The generally accepted method for calculating the overall thermal performance (OTP) is shown in equation 7,

$$OTP = \frac{{}^{N_u}/_{N_{uo}}}{\left({}^{f}/_{f_o}\right)^{1/3}} \tag{7}$$

where, N_u/N_{uo} is the heat transfer enhancement, f is the overall friction loss in the test piece, and f_o is the overall friction loss in a smooth pipe of the same hydraulic diameter.

The relationship between friction loss and pressure loss is shown in equation 8.

$$f = 2\, d_h \frac{\Delta P}{L\, \rho\, U^2} \tag{8}$$

The complexity of the flow passages, along with the absence of a friction loss factor associated with flow through an orifice was cause to modify the equation used to determine the overall thermal performance. For these tests, equation 9 was used to calculate the overall thermal performance (OTP).

$$\text{OTP} = \frac{\frac{N_u}{N_{u\ 90\ smooth}}}{\left(\frac{\Delta P}{\Delta P_{\ 90\ smooth}}\right)^{1/3}} \qquad (9)$$

In this equation the $N_{u\ 90\ smooth}$ value is the Nusselt number associated with flow through the test piece without the orifices installed and flow through all jets blocked. The value $\Delta P_{90\ smooth}$ is the pressure loss in the same plain test piece. The pressure tap locations are shown in figure 9-5. All heat transfer enhancement values reported were normalized to the same standard slot shaped channel with a 90 degree entry.

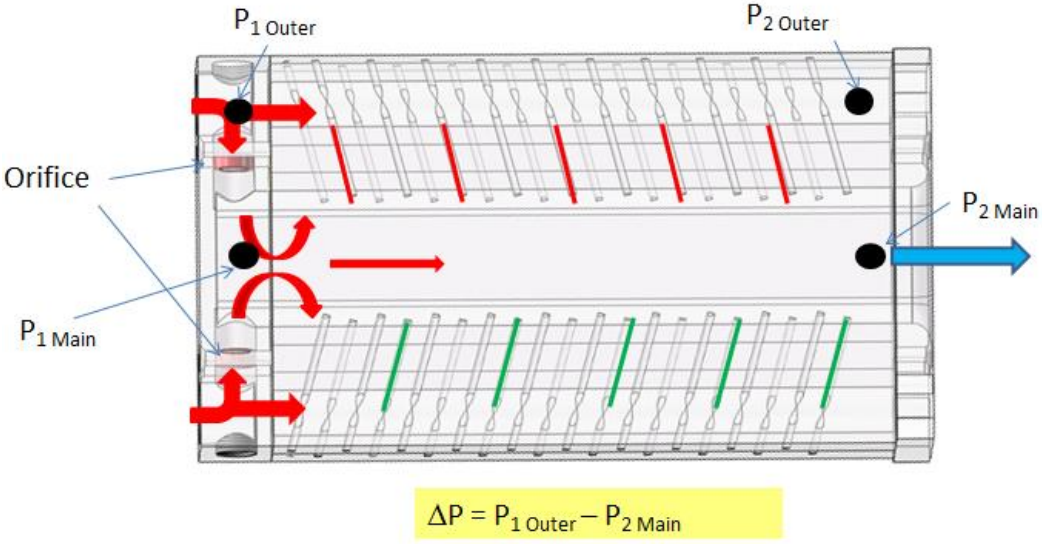

Figure 9-4 : Pressure tap locations used for pressure loss calculations

Experimental Uncertainty and Error

An accurate assessment of uncertainty in liquid crystal measurement of heat transfer coefficients is essential because many factors affect the TLC results. A large number of studies have concluded that a properly performed test yields mean uncertainly of up to 11.0% for values of h, and up to 9% for temperatures. Smith [19], et al, compiled a table summarizing uncertainty studies of h and T when narrow band TLC methods were used. Thermocouple accuracy and repeatability are large contributors to uncertainty as well as illumination spectral effects. The wall mounted thermocouples were used to compensate for this effect and resulted in a 0.2^{o} C temperature correction.

A minimum of two of each test was conducted to evaluate repeatability. Heat transfer values typically were repeatable within 3% -5% for tests with Reynolds numbers up to 25,000 and repeatability of 5%-8% with Reynolds number tests up to 50,000. As reported in the literature, current estimates of the uncertainty in the Nusselt number are approximately 10%.

Results and Discussion

The angle and location of the jets and orifices provide several positive heat transfer effects. The high velocity air issuing from the jets placed tangent to the walls of the main channel creates a shear flow phenomenon as the air travels along the walls of the main channel. This effect is very similar to that seen in impingement heat transfer. As the air passes through the orifices, which oppose each other near the entry of the main channel, the pressure significantly reduces and the velocity increases. The high velocity air from each end collides and creates high turbulence at the 90 degree channel entry.

The position of the jets in configuration “A” and “A-mod” is such that the high velocity jet flow continues across the main channel, then proceeds around the end walls of the slot shaped channel. This jet flow, likely severely weakened, then encounters the high velocity jet stream exiting from the succeeding jet on the opposite wall. The yellow helical path shown in figure 9-7 shows the idealized flow phenomenon. Additionally, when the low velocity main channel air engages the high velocity jets in cross flow, the low velocity main channel air tumbles over the high velocity jets which act as pseudo-helical trip strips. The turbulence intensity grows as the main channel air proceeds along the flow path. Figure 6 shows this idealized phenomenon as increasing spirals attached to the yellow helical strips in the figure.

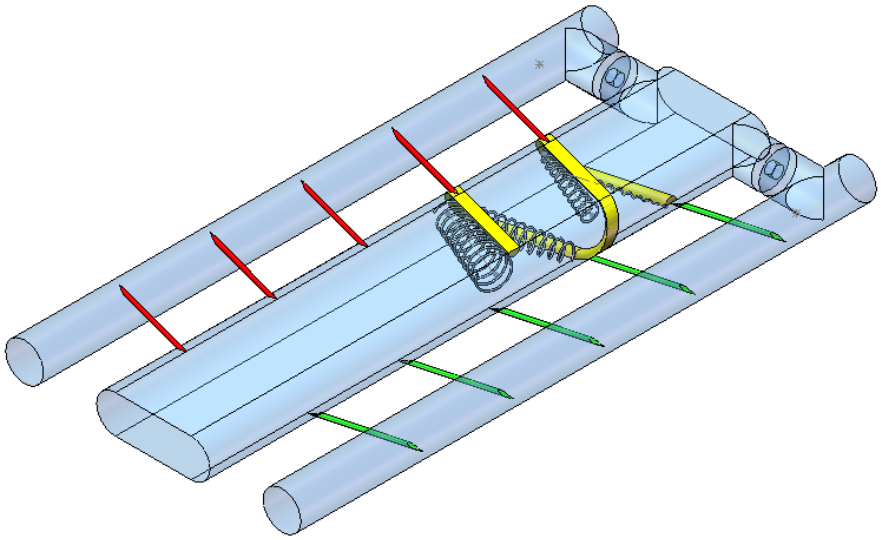

Figure 9-5 : Concept of swirl and tumble created by angled jets on each side of a slot shaped channel

Jet configurations “B” and “B-mod” offer a different swirl and tumble phenomenon, as the opposing jets are not offset.

In order for these configurations to work in a practical environment there must exists a pressure differential between the flow exiting the turbine blade, usually through film cooling holes, and the local pressure outside of the blade. A safety margin must be established to prevent high temperature combustion gases from entering the interior of the blade. The concept of Back Flow Margin (BFM) is shown in Equation 10. A typical value of 20-30% margin must be maintained.

$$\%BFM = \frac{P_{int} - P_{ext}}{P_{ext}} * 100\% \qquad (10)$$

The pressure loss ratio (see equation 6) values for each configuration and associated orifice diameter are shown in table 9-1. The □P values are the pressure losses that occur from the outer jet supply channel inlet (the high pressure side of the orifice) minus the main channel exit pressure. Because of the equal number of jets in configuration “A” and “B”, and in “A-mod” and “B-mod” the pressure loss values are the same for the associated orifice diameter.

The pressure loss values are within reason for preventing back flow in many turbine engines for which published data is available, with the possible exception of the 40k and 50k Reynolds number values with the 3.18mm orifices and the A/B-mod configuration where the total pressure loss values where 74 kPa and 60 kPa respectively and the 50k Reynolds number values with the 3.94mm orifices with the A/B-mod configuration which reached as high as 62 kPa.

Table 9-1 : Ratio of pressure loss ($\Delta P/\Delta P_{smooth}$) for each configuration and orifice diameter.

Smooth Channel w/ 90 deg. Inlet (3.18mm Orifice)		
Reynolds Number (10^3)	$\Delta P_{A\text{ or }B} / \Delta P_{smooth}$	$\Delta P_{A\text{-mod or B-mod}} / \Delta P_{smooth}$
10	52.8	67.6
25	54.1	70.0
40	49.2	66.5
50	45.1	59.7

Smooth Channel w/ 90 deg. Inlet (3.94mm Orifice)		
Reynolds Number (10^3)	$\Delta P_{A\text{ or }B} / \Delta P_{smooth}$	$\Delta P_{A\text{-mod or B-mod}} / \Delta P_{smooth}$
10	39.9	44.0
25	39.3	37.9
40	38.1	35.9
50	43.9	41.6

Smooth Channel w/ 90 deg. Inlet (4.76mm Orifice)		
Reynolds Number (10^3)	$\Delta P_{A\text{ or }B} / \Delta P_{smooth}$	$\Delta P_{A\text{-mod or B-mod}} / \Delta P_{smooth}$
10	19.6	22.0
25	20.3	25.1
40	21.2	25.9
50	18.6	23.3

There exists a substantial heat transfer benefit with the opposing passages and 90 degree turn at the inlet of the slot shaped channel when compared to a smooth round pipe of equal hydraulic diameter. Figure 9-7 shows the normalized Nusselt number (Nu/Nu_o) plots for the slot shaped channel with three different entry setups, all with an equivalent Reynolds number of 10,000. The first one labeled “case 1” is a color contour plot of the slot shaped channel with an axial flow entry path and a 12.5 mm radiused entry. The normalized channel averaged Nusselt

number is 1.04. The pressure loss is very low, almost not existent. This configuration yields an OTP of 1.01.

The second plot labeled “case 2” is the slot shaped channel with a 90 degree entry, all jets blocked, and no orifices installed in the opposing entry channels. The entry channels are 15.9 mm diameter round passages. The velocity at the inlet is much higher than in case “1”, but still very low when compared to the entry velocity with orifices installed. As indicated in the plot, the effect of the fluid interaction of the opposing passages leads to Nu/Nu_o values near 6 at the inlet. The normalized channel averaged Nusselt number is 1.93 and the overall thermal performance is 0.87.

In “case 3”, two 3.18 mm orifices were installed in the opposing entry channels. As expected, the heat transfer enhancement is very high near the inlet of the channel due to the high velocity colliding air streams that direct air into the main slot shaped channel. The velocity through the orifice is approximately 323 m/s and results in local Nu/Nu_o values of 12 near the entry of the channel.

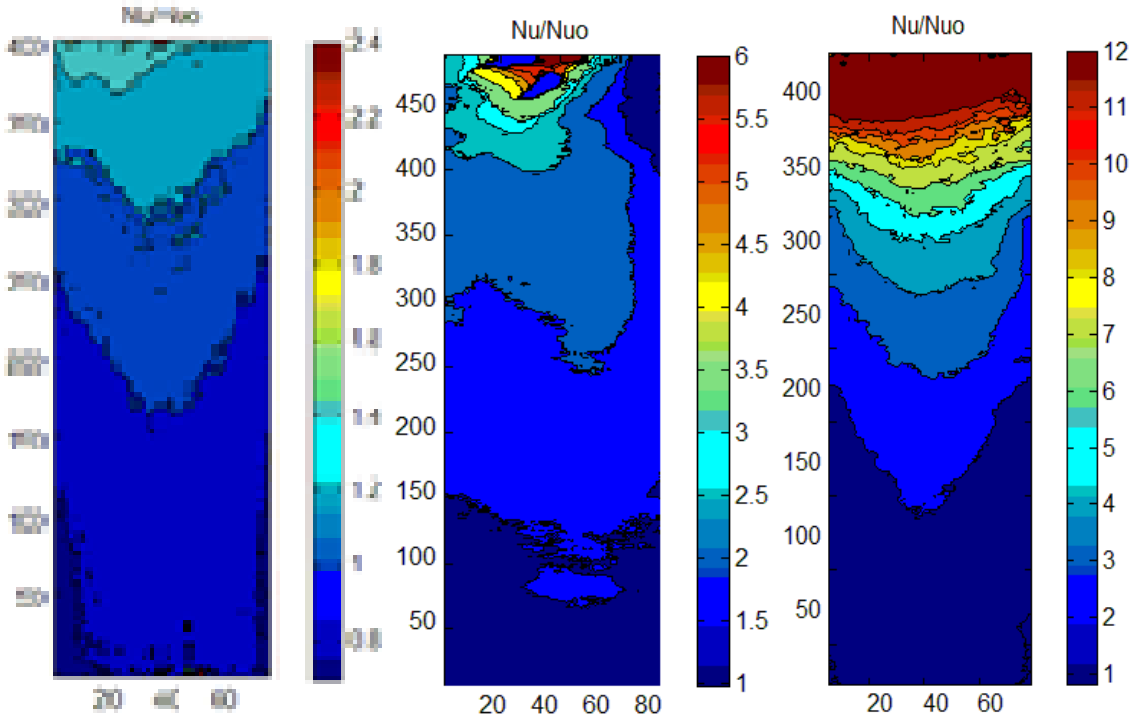

Figure 9-6 : Nu/Nu_o color contour plots for Re_{eq} =10k for; Case 1), axial inlet w/ radiused entry, Case 2), 90 degree inlet w/o orifices and blocked jets, Case 3), 90 degree inlet with 3.18mm orifices and blocked jets.

The high turbulence reduces as the flow progresses through the channel and the Nu/Nu_o values are near 1.0 at the exit of the channel. The normalized Nusselt number for this configuration is 4.85. The pressure losses are extremely high in this case and the OTP is a mere 0.29. The high heat transfer performance at the entry of the channel was the primary cause for testing in the A-mod and B-mod configurations. The hypothesis was that the orifices would create enough turbulence near the channel entry that jets would not be needed.

With the orifices and jets installed, calculations determined the distribution of mass flow through the jets and through the orifices. The mass flow rate associated with each Reynolds

number and percent mass flow through the jets for the various orifice diameters and jet configurations are shown in table 9-2. The mass flow through the entry of the main channel varied from about 20 % - 40%, depending on the test configuration and Reynolds number.

Table 9-2 : Percent mass flow rates through jets

		% Mass Flow Through All Jets					
Reynolds Number	Total Mass Flow Rate (kg/s)	3.18 mm Orifice (A, B)	3.94 mm Orifice (A, B)	4.76 mm Orifice (A, B)	3.18 mm Orifice (Amod, Bmod)	3.94 mm Orifice (Amod, Bmod)	4.76 mm Orifice (Amod, Bmod)
10,000	*0.00543*	73.1%	62.9%	61.3%	70.2%	60.3%	58.0%
25,000	*0.01353*	77.6%	70.1%	68.2%	73.2%	67.3%	64.3%
40,000	*0.02165*	79.0%	73.0%	70.4%	76.1%	72.3%	67.5%
50,000	*0.02706*	79.3%	75.7%	72.5%	78.4%	74.6%	69.2%

The average jet velocities were determined by using the average of the outer channel entrance and end pressures as well as the main channel entry and exit pressures. The difference in jet velocity from the first jet to the last jet is not shown in detail, but is calculated to be as small as 3 m/s in the case of the 4.76 mm orifice in conjunction with a Re=10k, to a difference of 21 m/s in the case of the 3.18 mm orifice in conjunction with a Re=50k. The blowing ratio (BR), which is defined as the ratio of the average jet velocity to the average main channel velocity, and the average jet velocity are shown in table 9-3.

Nu/Nu_o plots are provided for several of the configurations tested. The channel averaged $Nu/Nu_{90\ smooth}$ and overall thermal performance (see equation 9) values are indicated for each plot.

Table 9-3 : Average jet velocity and blowing ratio

	Average Jet Velocity, m/s and (Blowing Ratio)					
Reynolds Number	**3.18 mm Orifice (A, B)**	**3.94 mm Orifice (A, B)**	**4.76 mm Orifice (A, B)**	**3.18 mm Orifice (Amod, Bmod)**	**3.94 mm Orifice (Amod, Bmod)**	**4.76 mm Orifice (Amod, Bmod)**
10,000	73 (36)	55 (10)	42 (9)	92 (40)	66 (16)	50 (15)
25,000	183 (36)	114 (12)	73 (10)	201 (44)	114 (16)	87 (15)
40,000	221 (36)	182 (17)	116 (14)	268 (44)	211 (19)	129 (15)
50,000	269 (40)	222 (19)	131 (14)	291 (41)	243 (20)	154 (16)

In figure 9-8, the color plots show the Nu/Nu_o distribution for the four different configurations using the 3.18 mm orifices near the main channel entry (see figure 2) tested at a mass flow rate equivalent to a Reynolds number of 10,000 in the plain slot shaped channel with the benefit of jets and entry orifices. The "B" and "A-mod" configurations show good heat transfer distribution, which is an important aspect of a properly designed blade. The $Nu/Nu_{90\ smooth}$ values are 2.67, 5.83, 5.64, and 2.56 for the A, B, A-mod, and B-mod configurations, respectively. However, when pressure losses are taken into consideration, the overall thermal performance (OTP) values are 0.71, 1.55, 1.39, and 0.63 for the A, B, A-mod, and B-mod configurations, respectively. When compared to other traditional mid-span heat transfer configurations, such as trip strips, etc. the only configuration in figure 9-8 that indicates a comparable performance is configuration B. Figure 9-9 shows the results of the 3.94 mm orifices tested at an equivalent Reynolds number of 10,000.

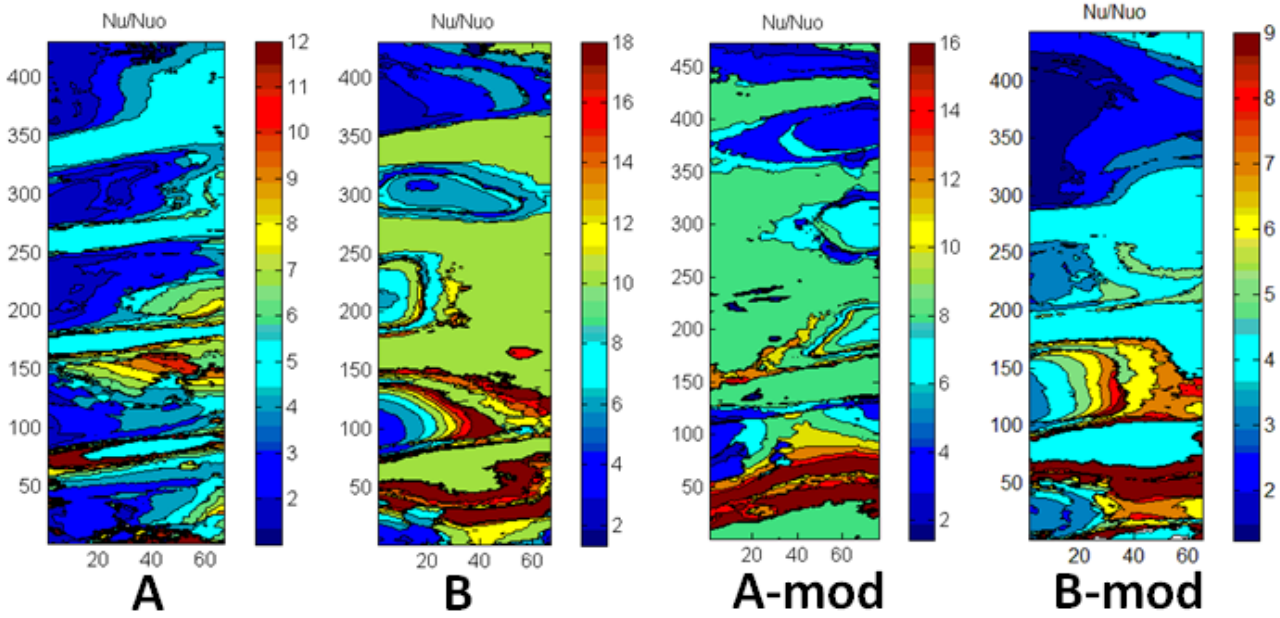

Figure 9-7 : Nu/Nuo plots with 3.18mm orifices, Re_{eq}= 10k

The heat transfer distribution is not as uniform as those shown in figure 9-8 but some of the configurations had beneficial values of OTP. The $Nu/Nu_{90\ smooth}$ values were 4.40, 4.75, 2.30, and 5.80 and OTP values were 1.29, 1.39, 0.65, and 1.64 for the A, B, A-mod, and B-mod configurations, respectively. It should be noted that the jet velocities are very low in the Re=10k tests. When compared to traditional heat transfer enhancement techniques used in the mid-span region only the B-mod configuration performs well, but has a large region with low performance.

As the jet velocities became higher, accompanied with high blowing ratios, the OTP values improved. Figure 9-10 shows color plots of Nu/Nu_o for tests performed with 3.18 mm orifices and mass flow rates equivalent to that of a Re=25k tests with the plain channel. The $Nu/Nu_{90\ smooth}$ values were 9.62, 10.68, 8.18, and 7.26, and OTP values were 2.55, 2.83, 1.99, and 1.76 for the A, B, A-mod, and B-mod configurations, respectively.

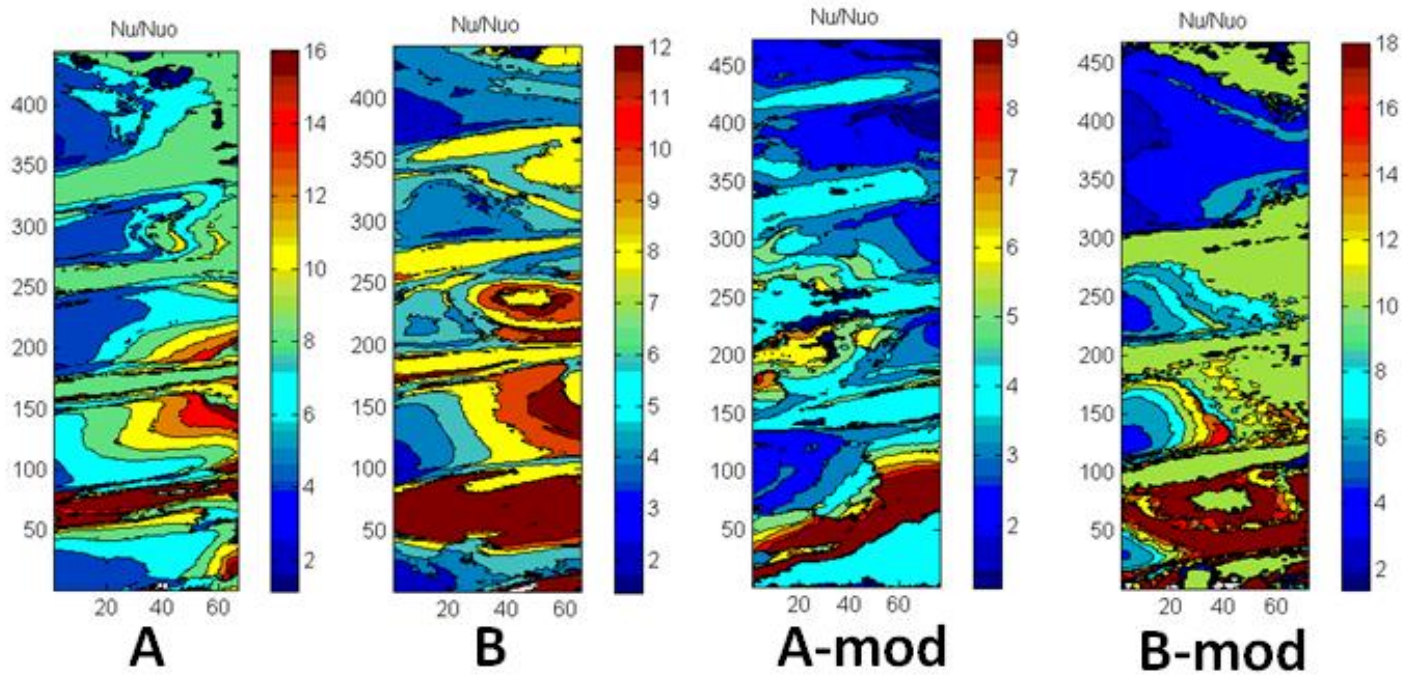

Figure 9-8 : No/Nu_o plots with 3.94mm orifices, Re_{eq} = 10k

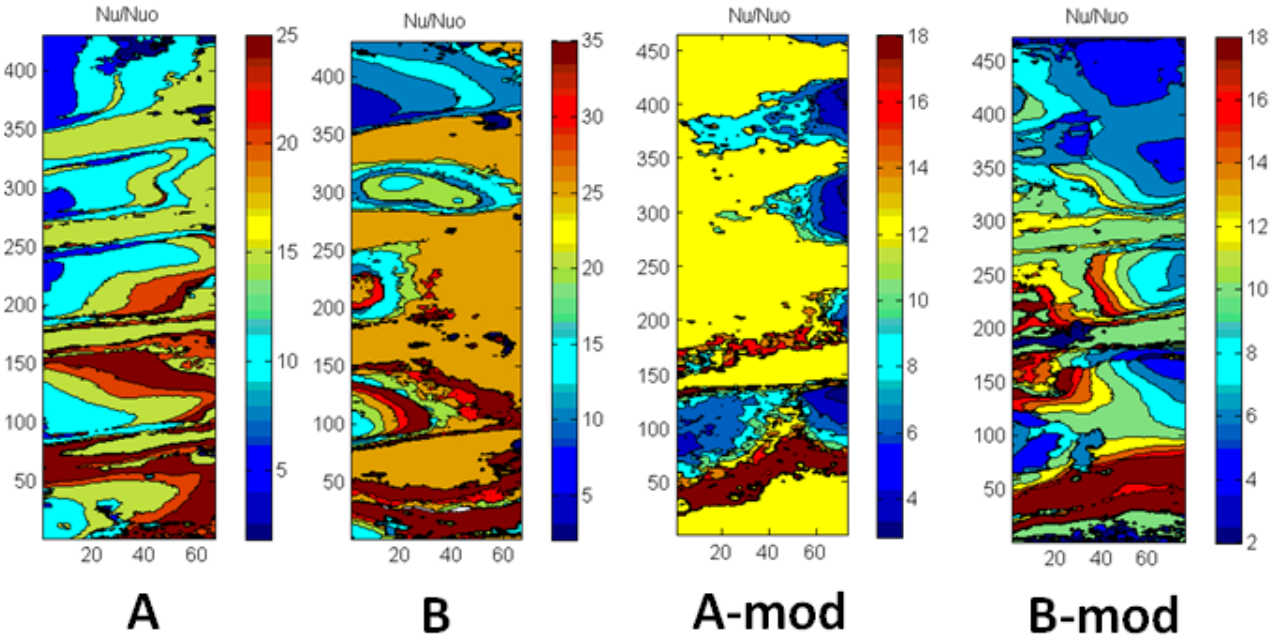

Figure 9-9 : Nu/Nu_o plots with 3.18mm orifices, Re_{eq}= 25k

The B and A-mod configurations showed very good heat transfer distribution.

When the largest orifices were used the blowing ratio was less than half of those with the smallest orifices and the jet velocities were significantly reduced. The $Nu/Nu_{90\ smooth}$ values for the largest, 4.76 mm orifices tested at Re=25k were 6.15, 3.30, 5.49, and 3.70 and the OTP values were 2.25, 1.21, 1.87, and 1.26 for the A, B, A-mod, and B-mod configurations, respectively. Figure 9-11 shows the color contour plots for this scenario. In this case configuration A has the best OTP and reasonable good distribution throughout the entire main channel.

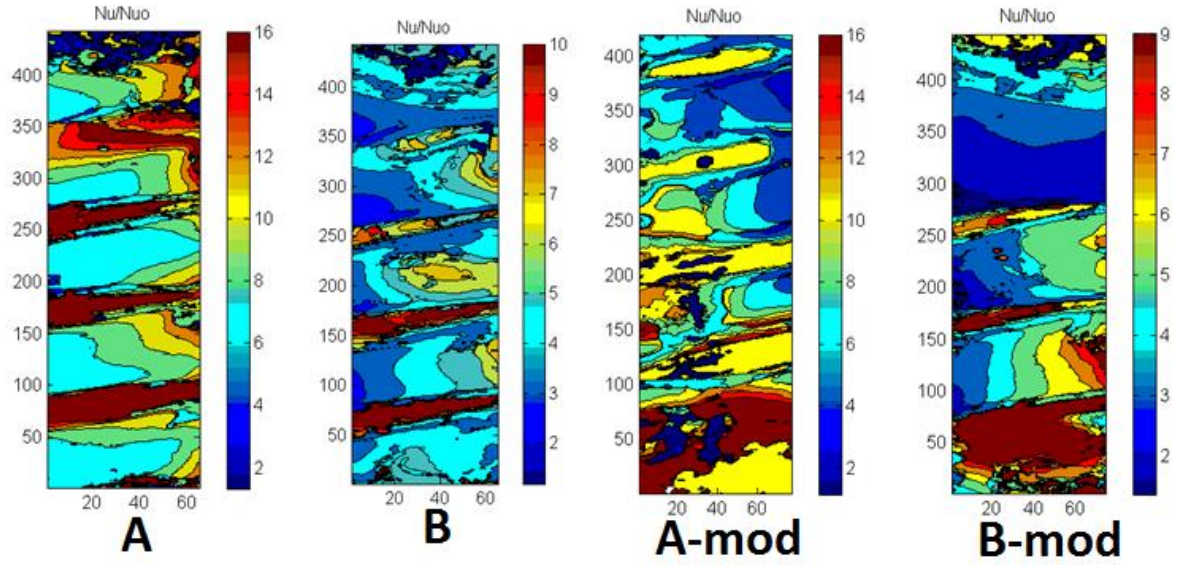

Figure 9-10: Nu/Nu_o plots with 4.76mm orifices, Re_{eq}= 25k

The data obtained and color plots in figure 9-12 shows the values of $Nu/Nu_{90\ smooth}$ were 6.44, 5.10, 5.72, and 7.60, and OTP values were 1.92, 1.52, 1.73, and 2.30 for the A, B, A-mod, and B-mod configurations, respectively. The high heat transfer zones near on one end of the channel contributed to the high OTP of the B-mod configuration. The distribution was better for the A configuration.

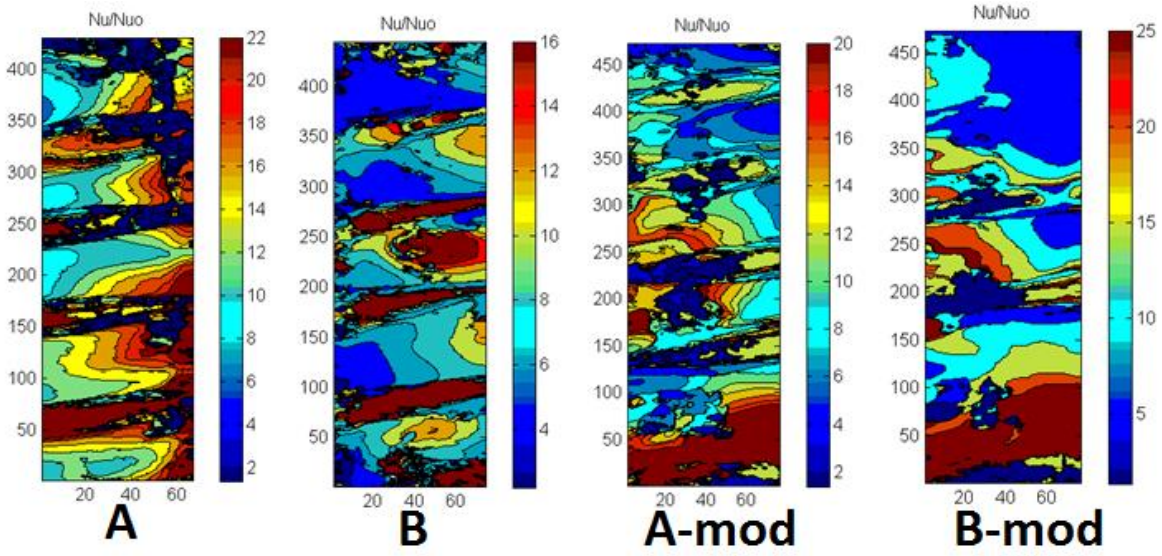

Figure 9-11 : No/Nu_o plots with 3.94mm orifices, Re_{eq} = 40k

At the highest Reynolds number tested and the largest orifices, the blowing ratios ranged from 10 to 19 and the jet velocities ranged from 131 m/s for configurations A and B, and 154 m/s for configurations A-mod and B-mod. The values of $Nu/Nu_{90\ smooth}$ were 4.19, 5.75, 5.43, and 5.24, and OTP values were 1.58, 2.17, 1.90, and 1.83 for the A, B, A-mod, and B-mod configurations, respectively. The color contour plots in figure 9-13 show that configuration B provides good reasonably even distribution throughout the channel.

A summary of the $Nu/Nu_{90\ smooth}$ values are presented in the data points of figure 9-14. The data clearly shows the superior performance of several combinations of orifice and jets at the equivalent Reynolds number of 25,000.

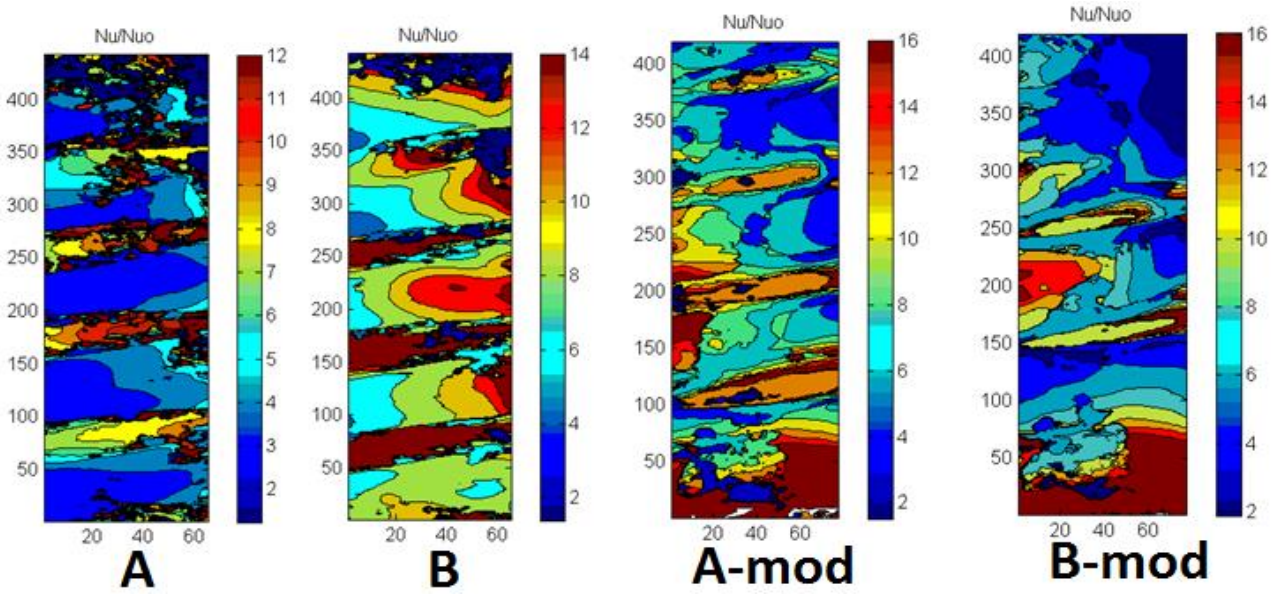

Figure 9-12 : Nu/Nu_o plots with 4.76mm orifices, Re_{eq}= 50k

This is not surprising, as the d/b and p/d values used were chosen based on testing performed with trip strips that performed well at Reynolds numbers near 25k, using similar ratios.

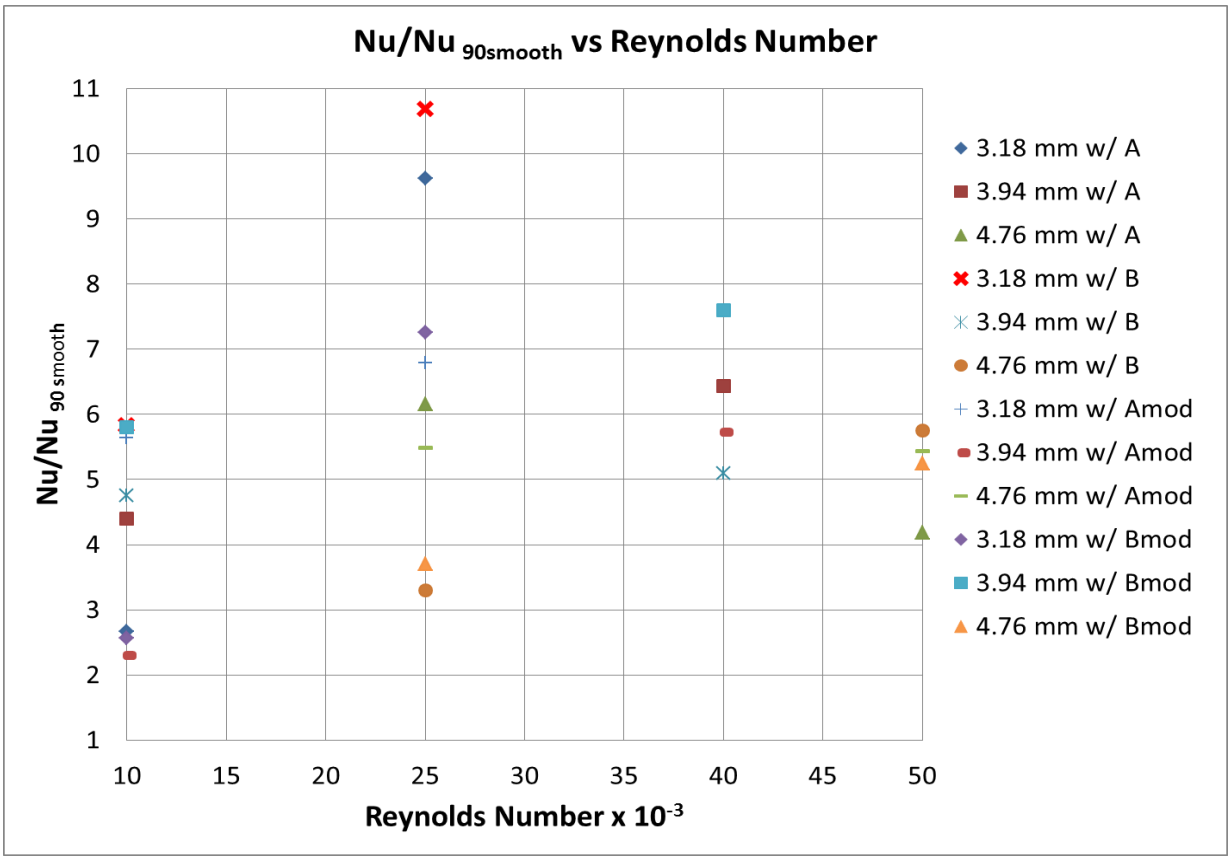

Figure 9-13 : Nu/Nu $_{90smooth}$ vs. Reynolds number for all orifices and configurations

If the values in figure 9-14 were viewed without considering the pressure losses, most tests configurations would appear superior to trip strips and other mid-span heat transfer enhancement techniques. But the pressures losses incurred in each of these tests were substantial, as shown in Table 9-1. Equation 9 was used to calculate the overall thermal performance. The result of merging the data in figure 14 with the pressure loss ratios in table 1 are displayed as overall thermal performance values (OTP) in figure 15. All of the 10,000 Reynolds number tests were low performers, while most of the higher Reynolds number test yielded OTP values above 1.5.

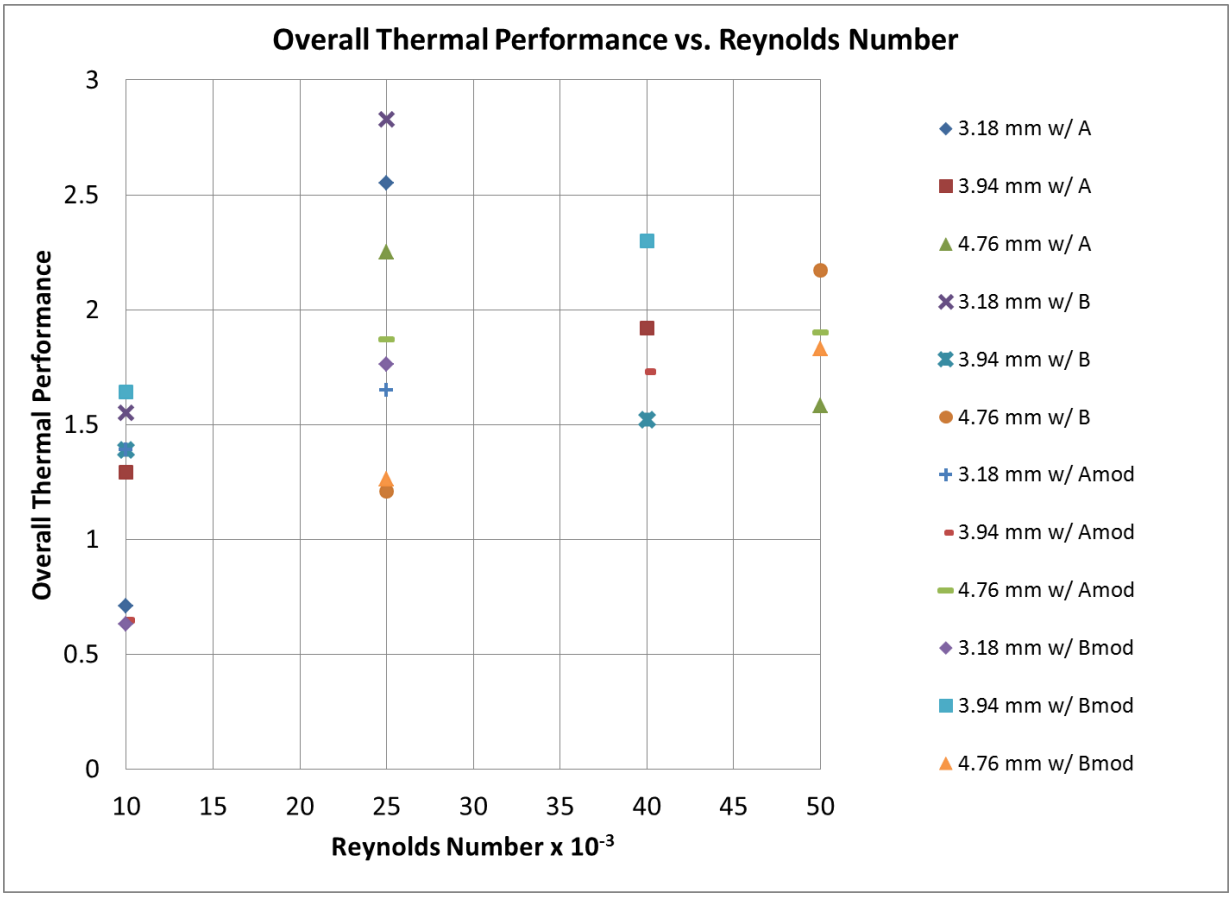

Figure 9-14 : OTP vs. Reynolds number for all orifices and configurations

The low velocity jets and orifices of the Re=10k tests showed reasonable good heat transfer distribution, but did not perform well when pressure losses were included. The Re = 25,000 tests performed the best with the 3.18mm orifices.

Conclusions

The heat transfer properties of a new and unique multi-channel passage, consisting of a 3:1 aspect ratio slot shape channel with jets issuing from each side and circular outer channels that connected the outer channels to the main channel, was tested for a range of mass flow rates and

associated equivalent Reynolds numbers of 10,000 to 50,000. The high velocity side jets entered the main channel flow at a 15 degree angle relative to the main flow direction at average blowing ratios ranging from 9 to 40 and average jet velocities ranging from 42 m/s to 291 m/s. As the main channel flow entered the channel from a 90 degree inlet, the flow encountered high velocity jets issuing along the walls of the slot channel. In addition to the jets having a shearing/impingement type affect along the floor at the exit of the jet, the jets ideally acted as pseudo-trip strips for the main channel fluid contacting the jets stream in cross flow.

High turbulence zones are noted in each test performed, with the downside being the high pressure losses in the channel. Overall Thermal Performance (OTP) values as high as 2.83 are reported and many of the various configuration show good heat transfer distribution throughout the main channel. This concept offers a new alternative for turbine blade designers as long as an acceptable back flow margin (BFM) can be maintained.

Chapter 10 – General Summary and Conclusion

The goal of these studies was to examine existing heat transfer enhancement strategies and performance in existing mid-span regions of first stage turbine blades and offer improvements using unique and untested combinations of heat transfer enhancements.

After careful examination of recent publications and patents, variations of two basic heat transfer enhancement strategies were tested. A slot shaped channel was selected, which differs from the standard rectangular shaped channel in most published journals. The aspect ratio of the channel and the ratio of aspect ratio to length was typical of other mid-span cooling tests used in recent publications.

One strategy was the implementation of unique shaped trip strips wound in a helical fashion along the main fluid channel. A variety of spiral configurations were used, along with a variety of ways to allow the fluid to enter the main channel passage. The range of Reynolds numbers tested was 10,000 to 50,000. The spiral pitch to trip strip height was determined from the published literature that yielded the best results for the Reynolds number range used in these tests.

The second strategy is to use jets issuing from side channels along the floor of the slot shaped channel to introduce a high velocity shear condition. The issuing jets would be angled into the crossflow air in such a fashion as to introduce a continuous swirling motion as the jet air progresses through the channel. It is proposed that the jets issuing along the floor of the passage could act like a trip strip and cause the main channel air to tumble as it comes in contact with the high velocity jets. Figure 11-1 shows a generic view of the fluid passages (transparent), the general shape of the

spiral wound trip strips (yellow), and the general location and angle of jet passages (red and green) that connect to high pressure outer channels.

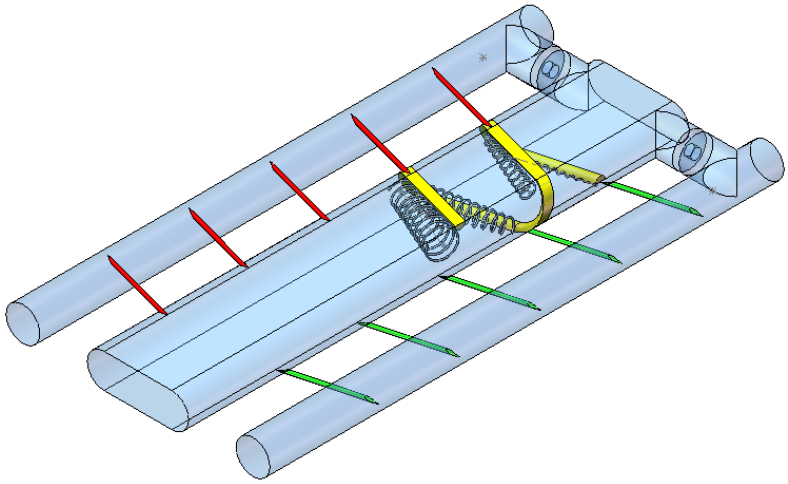

Figure 10-1 Generic view of fluid channels and heat transfer enhancement strategies used.

Narrow band Thermochromic Liquid Crystal (TLC) techniques were used along with Duhammel's superposition equations to determine local heat transfer coefficients (h) at every pixel of images taken during a dynamic heat transfer test. The heat transfer coefficient values were converted to normalized Nusselt values (Nu/Nu_o) used well established techniques. Friction loss measurements were taken and used to determine normalized friction loss measurements (f/f_o). The combination of normalized Nusselt values and normalized friction loss values are combined to calculate an Overall Thermal Performance (OTP) value. In all cases studied, heat transfer enhancement values were compared to the slot shaped channel with smooth walls and no additional heat transfer enhancements. Ultimately, this OTP value can be compared to existing cooling strategies to determine the optimal design.

The first series of tests are described in Chapter 6. These tests use a double helix trip strip and various orientations of side jets, labeled as configuration A, B, C, and D. Configurations C and D proved not to be of great benefit. The flow into the outer jet supply channels were controlled

independently from the main channel flow, with an equivalent exit mass flow from the main channel equal to that of the mass flow without any side jet flow. Configurations A and B showed good results, with A resulting in an Nu/Nu_o value of 4.83 at Re = 40k and OTP values of 2.46 at Re = 40k, and 2.97 at Re = 25k. Configuration B had similar results that were a little lower.

The trapezoid shaped trip strips displayed good uniform heat transfer coefficient values along the flow channel with Nu/Nuo values of 2.36 at Re = 10k and 3.02 at Re = 50k. The normalized friction values were 8.66 and 4.1 for Re = 10k and Re = 50k respectively.

With insight garnered from tests performed in Chapter 6, modified versions of the spiral trapezoid trip strips were studied using one additional variation of how the heated air entered the main flow channel. The radial entry configuration used in Chapter 6 test was used and a new dual path 90 degree entry was tested. The results are presented in Chapter 7. The two 90 degree entry paths provided a more turbulent mixture entering the main channel. Tests were performed using a single, double, and pentupule helix trapezoid shaped trip strip. Because of the high friction associated with the pentupule helix configuration, it performed very poorly at low Reynolds numbers. In some cases the performance was worse than a smooth unaided channel. The single helix design performed the best, especially at higher Reynolds numbers and offer an OTP value just over 2.0 at Re = 50k with the axial entry configuration and just under 2.0 at Re = 50k for the 90 degree entry configuration.

The tests performed and described in Chapter 8 were an extension of the original tests in Chapter 6, using high velocity jets issuing from separate side channels. In this series of tests, only the two best performing jet configurations A and B were used. The new variable introduced was a

number of different jet velocities were used, which resulted in a variety of "blowing ratios" (average jet velocity vs. main channel average velocity). The blowing ratios were controlled by the two independent air supply sources. Configuration A in this study shows extremely good values for overall thermal performance with a value of 3.63 at a Reynolds number of 25,000 and a blowing ratio of 13. Configuration B also performed well with the maximum overall thermal performance value of 3.69 at a Reynolds number of 25,000 and a blowing ratio of 23. The normalized friction factor remained below 2.5 for all tests using jet enhancements. Generally, the higher the blowing ratios resulted in better overall heat transfer distribution in the channel for jet configuration A. Jet configuration B did not show an even heat transfer distribution in most of the tests performed.

Visual studies of the tests performed in Chapter 8 showed that uniformity of heat transfer improvements were possible if the flow of the side jets into the main channel were altered. Additionally, it would be preferential if the entire flow could be controlled using a single source of heated air. In Chapter 9, the introduction of various sized orifices used to control the flow of air into the main channel were installed. Also, two new jet configurations were tested. These are referred to as Jet Configuration A-mod and B-mod. These new jet configurations essentially remove the first set of jets at the start of the main flow channel. The average blowing ratios ranging from 9 to 40 and average jet velocities ranging from 42 m/s to 291 m/s. As in all cases using the side jets, there are high pressure losses in the channel. Overall Thermal Performance (OTP) values as high as 2.83 are reported and many of the various configuration show good heat transfer distribution throughout the main channel. This concept offers a new alternative for turbine blade designers as long as an acceptable back flow margin (BFM) can be maintained.

In summary, the series and variation in test performed using trapezoid shaped trip strips and various blowing ratio configurations using jets issuing from separate side channels resulted in improvements in overall thermal performance, when compared to existing technology. As a refresher, the equation for overall thermal performance is shown below.

$$\frac{Nu}{Nu_{o\,smooth}} \div \left(\frac{f_{total}}{f_{o\,smooth}}\right)^{1/3} = \text{Overall Thermal Performance}$$

Using the data in Figure 2-6, the OTP of a select number of current heat transfer configurations can be obtained. Some prominent configurations OTP values are noted in Figure 10-1. Although not all of the various combinations of OTP were calculated, the seemingly more beneficial configurations offered OTP values as high as 2.45, with others near 2.0.

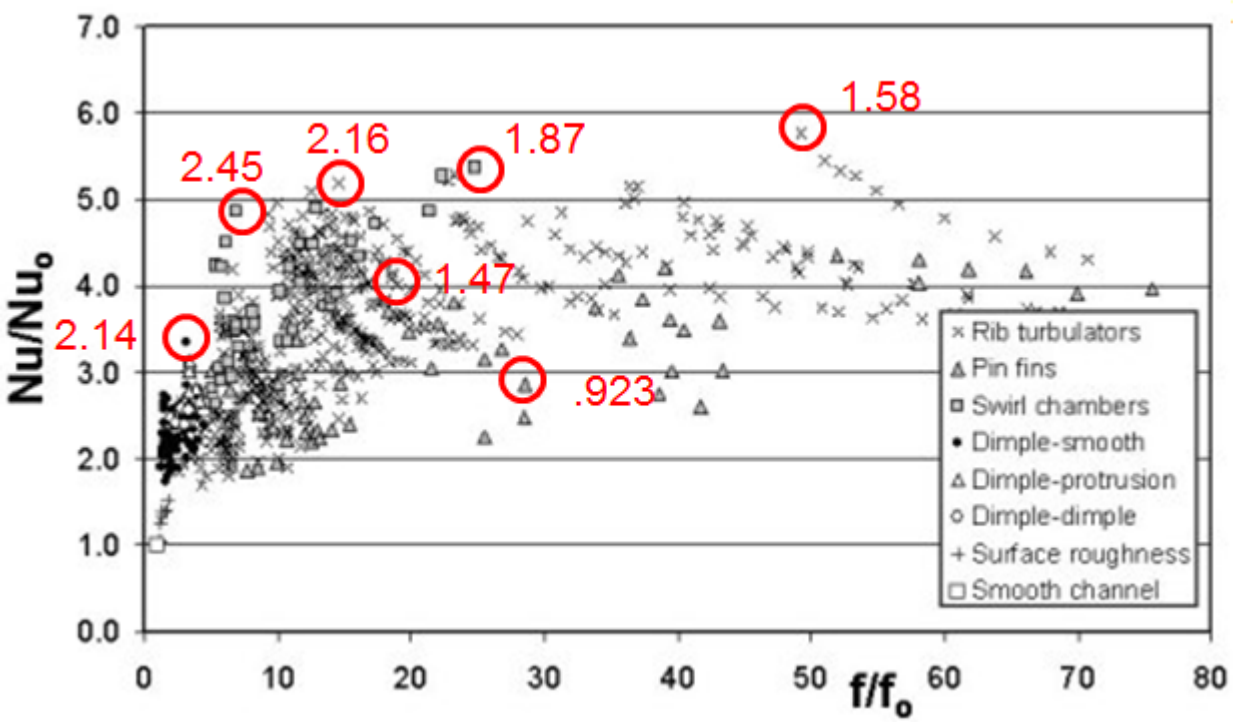

Figure 10-10-2: A modified version of Figure 2-6 showing calculated values of Overall Thermal Performance (OPT) of some of the heat enhancement strategies currently being reported in various publications.

Select OTP values from the testing performed in this study are superimposed onto the same Figure 2-6 in Figure 10-3. OTP values as high as 3.69 are reported and many other select test results exceed the best performance of other current heat enhancement strategies.

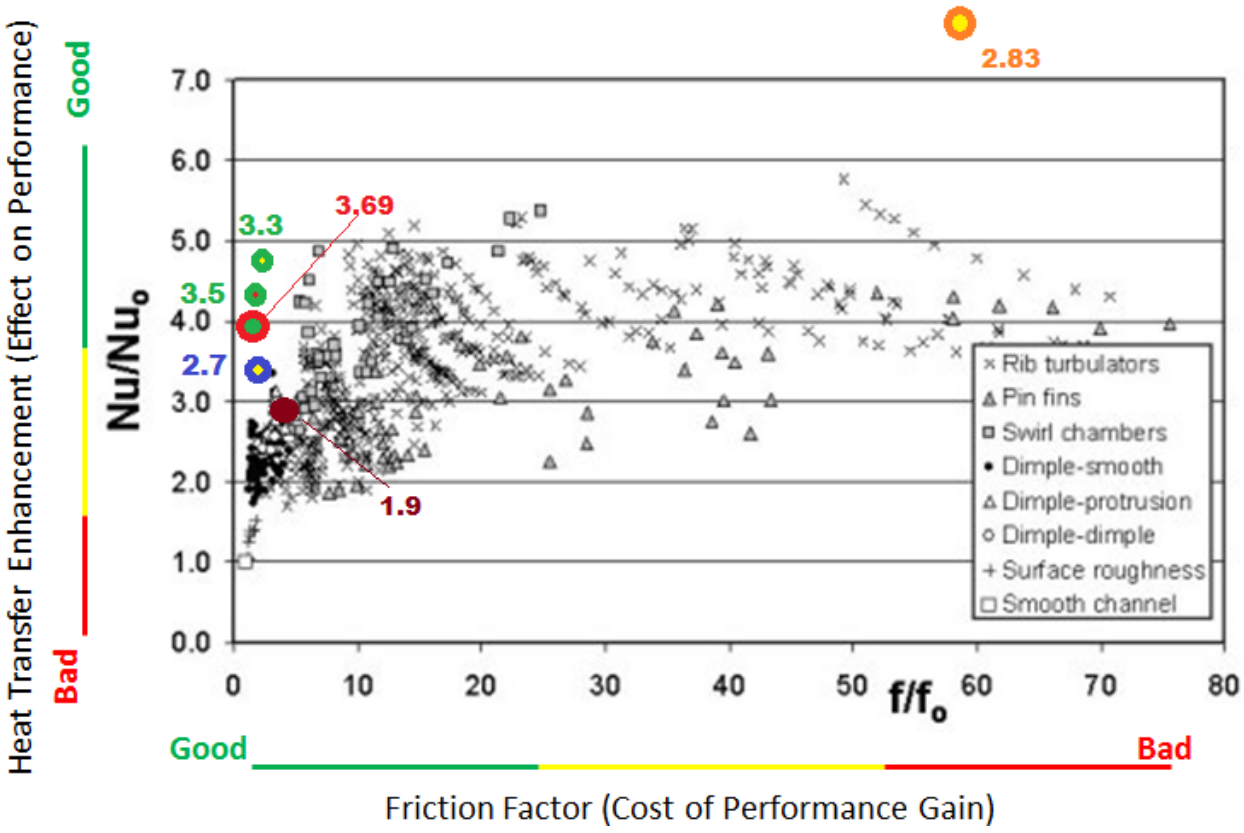

Figure 10-3 A modified version of Figure 2-6 showing calculated values of Overall Thermal Performance (OPT) for the best heat transfer strategies in the slot shaped channel.

References

1. Wagner, J. H., Johnson, B. V., Graziani, R. A. and Yeh, F. C., 1992, "Heat Transfer in Rotating Serpentine Passages With Trips Normal to the Flow", *J. Turbomachinery, Trans. ASME*, 114, pp. 847-857.

2. Obaid Younossi, Military Jet Engine Acquisition, Rand Corporation, 2002

3. R. C. Wilcock, The Effect of Turbine Blade Cooling on the Cycle Efficiency of Gas Turbine Power Cycles, Journal of Engineering for Gas Turbines and Power, JANUARY 2005, Vol. 127

4. Bernard L. Koff, Gas Turbine Technology Evolution: A Designer's Perspective, JOURNAL OF PROPULSION AND POWER, Vol. 20, No. 4, July–August 2004

5. Phil Ligrani, Internal Cooling – Surface Heat Transfer Augmentation, http://ligrani.com/Research/Groups/internalcooling.html

6. *The Investigation of Heat Transfer in Cooled Blades of Gas Turbines.* Goreloff, V., Goychengerg, M., and Malkoff, V. 1990. 26th Joint Propulsion Conference. AIAA Paper No. 90-2144.

7. J-C Han, S. Dutta, and S Eddak. Gas Turbine Heat Transfer and Cooling Technology. Taylor & Francis, New York, 2000.

8. Smith Eiamsa-ard, Pongjet Promvonge, Enhancement of heat transfer in a tube with regularly-spaced helical tape swirl generators, Solar energy, 2005, vol. 78, nº 4, page 89

9. İrfan Kurtbaş, Heat transfer augmentation by swirl generators inserted into a tube with constant heat flux, International Communications in Heat and Mass Transfer 36 (2009), 865–871

10. Hedlund, Ligrani, et-al, Heat Transfer and Flow Phenomena in a Swirl Chamber Simulating Turbine Blade Internal Cooling, Journal of Turbomachinery, Vol. 121, OCTOBER 1999, 804-813

11. G. Tanda, Heat transfer in rectangular channels with transverse and V-shaped broken ribs, International Journal of Heat and Mass Transfer 47 (2004) 229–243.

12. Kyung Min Kim, Pressure drop and thermal performance in rotating two-pass ducts with various cross rib arrangements, Heat Mass Transfer (2008) 44:913–919

13. C. Thianpong, Thermal characterization of turbulent flow in a channel with isosceles triangular ribs, International Communications in Heat and Mass Transfer 36 (2009) 712–717

14. Smith Eiamsa-ard, Pongjet Promvonge, Enhancement of heat transfer in a tube with regularly-spaced helical tape swirl generators, Solar energy, 2005, vol. 78, no 4, page 89

15. Experimental Investigation of Local Heat Transfer in a Square Duct with Various-shaped Ribs, Lei Wang, Bengt Sunden, Heat Mass Transfer, 2007, Vol. 43, pp. 759-766.

16. Koonlaya Kanokjaruvijit, Heat transfer correlations of perpendicularly impinging jets on a hemispherical-dimpled surface, International Journal of Heat and Mass Transfer (2010) .

17. Describing Uncertainties in Single-Sample Experiments, Kline, S. J., and F. A. McClintock: , Mech. Eng., p. 3, January 1953

18. Fundamentals of Heat and Mass Transfer, Incropera, DeWitt, 5th Edition, pp. 271, 2002.

19. Temperature sensing with thermochromic liquid crystal. C.R. Smith, D.R. Sabatino, and T.J. Praisner, Experiments in Fluids, Vol. 30, pp. 190-201, 2001.

Vita

Del Segura is currently attending graduate school at Louisiana State University in the School of Engineering in pursuit of a Ph. D. in Engineering where he maintains a 3.75 GPA at LSU. As of the fall of 2009, sixty three graduate credited hours have been completed. He was awarded a Masters of Science in Mechanical Engineering degree from Tulane University in 2004 and a Bachelor of Science degree in Mechanical Engineering from University of Southwestern Louisiana in 1992. He is currently a registered Professional Engineer in the state of Illinois where he worked in various management positions in New Model Development, Engineering and Development, and Quality Control for Mitsubishi Motor Manufacturing of America.

The research completed at Tulane University resulted in three published peered reviewed papers in the fields of Robotics and Controls, and Climatology. Additional projects completed at Tulane included the study and design of insulation systems for deep sea pipelines. This study was funded by ABB in The Netherlands and is considered proprietary. No publications were allowed in this study.

Del currently presides as Chairman of Innovention Toys, LLC, a company that he founded along with two other partners in 2005. Innovention Toys has amassed over $4 M in sales in the last four years. He owns an engineering consulting firm and does consulting work for various industries including the oil & gas industry, automotive industry, sports industry, and marine industry. He also is an advisory board member of EVAOS, an alternative energy aftermarket automotive company. Other notable projects include a consulting project which resulted in the proof of concept designs

for a low earth orbit fuel shuttle system for Lunar Transportation Systems, a NASA sub-contractor that will be used for the next generation lunar landing programs.

He currently resides in Covington, LA with his wife Sun Chaney Segura, M.D. and his daughter, Tia who was born in 2008. He is the co-owner and driver of a two competitive National Hot Rod Association race cars and has held nine national records during his racing career.